A study of the freezing of binary mixtures of hard colloidal spheres

Hunt, Neil Andrew

Award date:
1999

Awarding institution:
University of Bath

A STUDY OF THE FREEZING OF BINARY MIXTURES OF HARD COLLOIDAL SPHERES

submitted by Neil Andrew Hunt

for the degree of PhD

of the University of Bath

1999

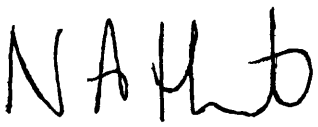

ProQuest LLC
789 East Eisenhower Parkway
P.O. Box 1346
Ann Arbor, MI 48106-1346

SUMMARY

The fluid-solid phase behaviour, of binary mixtures of essentially hard colloidal particles, with diameter ratios α = 0.42, 0.52 and 0.72, was investigated. The particles consisted of almost identical spherical cores of poly(methyl methacrylate) (PMMA), sterically stabilised by thin macromolecular layers and were suspended in a near refractive index matching mixture, of decalin and carbon disulphide. Particles were synthesised in a single-stage dispersion polymerisation and the size and polydispersity were measured by transmission electron microscopy and dynamic light scattering.

The binary crystal structures formed, were identified by means of "powder light crystallography". Depending upon the proportion of the two components, mixtures underwent an entropically driven freezing transition, into one of at least four different stable crystalline phases: irregularly stacked close packed crystals of A or B and the AB_2 and AB_{13} superlattice phases. At each size ratio, near the limits of extreme composition, fluid / A and fluid B phase coexistence was found. Also, at each size ratio, an amorphous region was found at intermediate compositions, the size of which increased with decreasing number ratio.

In mixtures prepared with diameter ratios α = 0.42 and 0.72, at least three different types of freezing behaviour were found. In mixtures with a diameter ratio α = 0.52, five distinct types of fluid-solid phase behaviour were observed. At this diameter ratio, both the AB_2 and AB_{13} superlattice structures were found, at different suspension compositions.

The observed phase behaviour, of mixtures prepared with diameter ratios α = 0.42 and 0.52, is compared with computer simulation phase predictions. The observed behaviour of mixtures with a diameter ratio of α = 0.72, is compared with the theoretical phase diagram, for the freezing of a mixture of hard spheres with size ratio α = 0.75, which are assumed to be immiscible in the solid phase.

CONTENTS

ACKNOWLEDGEMENTS

First and foremost, I would like to thank Dr. Paul Bartlett for his help, energy and enthusiasm. I am particularly grateful for the time he has given to read the thesis and the suggestions he has made. I would also like to thank Dr. Gareth Price for making available his polymer chemistry facilities and those in the lab, David, Phil, Roger and Simon.

CHAPTER 1

1. INTRODUCTION

1.1. Colloidal Dispersions

Since the earliest days of civilisation, when the ancient Egyptians prepared colloidal inks and pigments, the properties of colloidal systems have been exploited. Modern colloid technology has a wide range of practical applications, in many areas of industry, from biotechnology and pharmaceuticals, to paints and cosmetic preparations.[1] Many biological systems are also colloidal in nature. Colloid science has an extensive history. In 1828, Robert Brown investigated the nature of the erratic motion of pollen grains suspended in water.[1] In 1845, Selmi made what were then called demulsions of sulphur and silver halides.[2] Probably the first systematic investigation began in 1856, when Faraday made extensive studies of colloidal gold.[2] In 1861 Thomas Graham identified the colloidal state.[2] In 1910 the molecular basis of Brownian motion was settled, by Perrin's experimental observations and the ground breaking theory of Einstein, which were published almost simultaneously.[2] However, it was not until the 1940s that a detailed theory of colloidal stability was given. This was the classical DLVO theory, after Derjaguin and Landau, and Verwey and Overbeek.[3] These authors proposed the idea that the interparticle potential, between two charged colloidal particles, could be represented as the sum of the attractive and repulsive components.

Much progress has been made over the last thirty years, as a range of 'model' colloidal systems has been developed. These systems consist of particles with well-defined shape, size and interactions (see section 1.4). As a result of the availability of model colloidal systems, the investigation of colloids as atomic

analogues has also developed significantly over the last thirty years. The phase behaviour, structure and dynamics of such systems is increasingly the subject of investigation by both experimental and theoretical methods.[4] Such systems also provide a method for the study of fundamental problems in statistical mechanics, such as crystallisation.[5] Model systems have greatly increased our knowledge of colloidal suspensions.

In the present work, we are mainly concerned with the phase behaviour and structure of model hard sphere colloids. Over the last twenty years or so synthetic chemical methods have been developed, which have made it possible to prepare almost monodisperse, spherical colloidal particles, stabilised against flocculation by a thin layer of polymeric material chemically grafted onto the particle surface.[6,7] In a good solvent for the coating, the interaction potential is essentially hard sphere in nature (see section 1.4). Suspensions of almost equal sized colloidal particles have been studied increasingly in recent years. Such suspensions exhibit many of the physical features of simple atomic and molecular fluids. For example, they exhibit a freezing transition and at higher concentrations glass formation.[8] There is much interest in the fundamental properties of hard sphere suspensions as colloids. Also, as hard sphere atoms do not exist, these systems have provided a major step forward in providing an experimental method of investigating the hard sphere model.[9] In binary mixtures of two different sized suspensions of hard sphere colloids, superlattice structures have been observed.[10,11] As hard spheres have no attractive part in their pair potential, all phase behaviour observed in hard sphere systems is driven by entropic effects.

Particles are usually considered to be colloidal in nature if they have at

least one dimension in the range 1 nm to 1μm, although any definition is imprecise.[5] Colloidal particles are expected to be significantly larger than the molecules of the suspension medium, but sufficiently small that the particulate Brownian motion is not dominated by effects such as gravitational settling. A detailed discussion of colloid-atom analogues has been given by Pusey.[5] Colloidal particles are equivalent to atoms, in that they can reach thermal equilibrium through Brownian motion. In fact, under suitable experimental conditions, colloidal suspensions exhibit analogues of all the common states of atomic systems: gas, liquid, crystal, alloy and even glass. The equilibrium properties of such suspensions can be treated in terms of the physical theories originally developed for the study of simple fluids. To a good approximation the liquid, in which the particles are suspended, can be regarded as an inert thermal reservoir. The solution theories, of McMillan and Mayer, and Kirkwood and Buff, can then be used to obtain the solvent-mediated potential of mean force. This force is derived, from all the forces acting upon the colloidal particles.[12,13] The potential of mean force is a complicated function, of all the particle positions $\{r_j\}$ and is usually approximated as the sum of pair potentials, $V(|r_j - r_k|)$.[5] For spherical particles these are taken to be isotropic,

$$U[\{r_j\}] = \sum_{j>k} V(|r_j - r_k|). \qquad (1.1)$$

For hard sphere systems, with short ranged interactions, the assumption of a pairwise additive potential is expected to be reasonable.[5] The equilibrium thermodynamic properties, of a suspension of colloidal particles, are then essentially equivalent to those of an assembly of atoms interacting via a potential

of the same form. The effective pair potential is the input for statistical mechanics. Hence, statistical mechanical concepts, together with theories developed for simple atomic fluids and solids can be applied, to calculate such properties as the phase behaviour and structure of colloidal dispersions.

Colloidal particles are up to 10^3 times larger than atoms. As a result, the number density $\rho = N / V$, of a typical colloidal system, is $\sim 10^9$ times smaller than that of its atomic counterpart. However, the free energies, per particle, of a colloidal crystal and an atomic solid are similar.[5] Hence, the lower number density of a colloidal system results in colloidal solids, which are $\sim 10^9$ times weaker than their atomic counterparts. This weakness means that, for example, when a sample containing colloidal crystals is agitated, the crystals are readily disrupted by shearing forces and a metastable fluid is formed. As a consequence of the large structural relaxation times of colloids, the metastable phase will often take a macroscopic time to recrystallise (from seconds to months). Therefore, the structure and dynamics of the metastable states, of colloidal systems, can be studied in detail. Fundamental non-equilibrium processes, such as crystallisation[14] and the glass transition[5,15] can be investigated. Also, experiments which would be difficult, if not impossible, with atomic systems can be carried out using colloidal systems.

The spheres in the classical hard sphere model are all exactly the same size. However, colloidal particles almost invariably have a distribution of sizes. This size distribution $P(R)$ can be usefully described by the polydispersity,[5]

$$\sigma = \frac{\left(\overline{R^2} - \overline{R}^2\right)^{1/2}}{\overline{R}} , \qquad (1.2)$$

where,

$$\overline{R^n} = \int R^n P(R) \mathrm{d}R \,. \qquad (1.3)$$

The lattice constant of colloidal crystals is of the order of the wavelength of visible light. Hence, colloidal crystals are iridescent, due to the Bragg diffraction of light from the ordered structure. As the wavelength of light is comparable to the colloidal dimensions, light scattering is the most commonly used technique to study colloidal systems. X-ray and small-angle neutron scattering provide complementary information. In static (or conventional) light scattering, the average intensity of scattered light is measured as a function of angle. This is analogous to the diffraction of X-rays in the study of atomic systems. In both cases, the scattering pattern contains information about the time-averaged structure in the scattering volume. By contrast, in dynamic light scattering, the fluctuating intensity at a particular scattering angle is monitored as a function of time, giving information on the motion of particles contained in the scattering volume. Small-angle neutron scattering (SANS) is especially useful, for the study of colloidal mixtures, as the different scattering lengths of the proton and deuteron can be exploited.[16,17] Much information can of course be obtained, by direct visual observation of colloidal samples. Optical microscopes have also been used, although only for sufficiently dilute samples.[18] In recent years scanning laser confocal microscopy has allowed access to colloidal particles, deep in the bulk of turbid samples.

1.2. Colloidal Stability

1.2.1. Intermolecular Forces

The existence of forces of attraction between non-polar atoms and molecules, has been well known since the pioneering work of van der Waals in 1873.[19] However, their origin was not understood until 1930, when London gave an explanation in terms of quantum mechanics.[19] London realised that the electron clouds of non-polar atoms and molecules exhibit fluctuations in charge density, giving rise to an oscillating dipole moment. Although the time average of this dipole moment is zero, the fluctuating electromagnetic field that is generated polarises any nearby neutral atom or molecule, inducing in it a dipole moment. The interaction between the two fluctuating dipoles, results in an attractive force between the two atoms or molecules. The time average of this force is finite and this is the non-polar van der Waals force, which is always present between any two bodies of matter. This complex coupling depends on the contrast in the frequency dependent dielectric function, between the particle and the solvent.[11] In the case of two neutral atoms A and B, separated by a distance r, the range and magnitude of this interaction can be estimated as follows. If atom A has an instantaneous dipole of moment $\mu = a_o e$, this creates an electric field E at atom B. This field polarises atom B and induces an instantaneous dipole μ', of magnitude $\alpha_p E$, where α_p is the electronic polarisability of atom B. The polarisability is given by the expression[19]

$$\alpha_p = 4\pi\varepsilon_o a_o^3, \qquad (1.4)$$

where a_o, in terms of the Bohr model of the atom, is the shortest distance between a proton and an orbiting electron, the first Bohr radius. At this radius the Coulomb energy $e^2 / 4\pi\varepsilon_o a_o$ is equal to $2h\nu$. Hence,[19]

$$a_0 = \frac{e^2}{2(4\pi\varepsilon_0)h\nu}, \tag{1.5}$$

where h is Planck's constant and ν is the orbiting frequency of the electron. The interaction between the two dipoles gives rise to an attractive interaction, between atoms A and B. The energy of this interaction, in a vacuum, is given by[19]

$$V_A(r) = \frac{-\mu^2 a_0}{(4\pi\varepsilon_0)^2 r^6} = \frac{-(a_0 e)^2 \alpha_p}{(4\pi\varepsilon_0)^2 r^6}. \tag{1.6}$$

Using equation 1.5 for a_o and equation 1.4 for α_p, equation 1.6 above can be rewritten as[19]

$$V_A \approx \frac{-\alpha_p^2 h\nu}{(4\pi\varepsilon_0)^2 r^6}. \tag{1.7}$$

Apart from a slightly different numerical factor, this equation is the same as that derived by London in 1930, by means of quantum mechanics.[19] For the dispersion interaction between two identical atoms or molecules, London's classical equation is[19]

$$V_A(r) = \frac{-C_{disp}}{r^6} = -\frac{(3/4)\alpha_p^2 h\nu}{(4\pi\varepsilon_0)^2 r^6}. \qquad (1.8)$$

At separation r, the attraction between the atoms is directly proportional to the inverse sixth power of the separation. The interaction potential $V(r)$, between a pair of atoms or molecules, is illustrated schematically in figure 1.1.

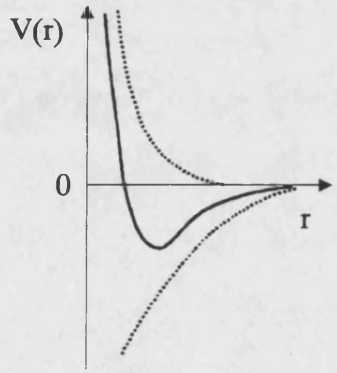

Figure 1.1. The interaction potential $V(r)$ between two molecules separated by a distance r. The total interaction potential (solid line) is the sum of the van der Waals attraction and the steep Born repulsion (dashed lines).

1.2.2. Interparticle Forces

The van der Waals interaction between two macroscopic particles can be calculated, to a first approximation, by assuming that every atom in one particle interacts with every atom in the other, according to a van der Waals pair potential. By summing the attractions, between all interparticle pairs of atoms, the total attraction is obtained. For a collection of atoms, such as a colloidal particle, the cumulative effect is a relatively long-range attractive interaction of

~10 nm. The energy of attraction (in a vacuum) between two identical spherical particles, was determined by Hamaker on the basis of pairwise additivity, to be[19]

$$V_A(r) = -\frac{A}{6}\left[\frac{2R^2}{r^2-4R^2}+\frac{2R^2}{r^2}+\ln\left(\frac{1-4R^2}{r^2}\right)\right], \qquad (1.9)$$

where R is the particle radius and r is the centre-to-centre particle separation. A is the Hamaker constant, which is determined by the material properties of the particles and suspension medium. The conventional Hamaker constant is defined as[19]

$$A = \pi^2 C_{disp}\rho_1\rho_2, \qquad (1.10)$$

where C_{disp} is the coefficient in the atom-atom pair potential. ρ_1 and ρ_2 are the number of atoms, per unit volume, in the two particles. A is typically in the range 10^{-21} - 10^{-19}J, at room temperature.

In theory the attractive potential at touching ($r = 2R$) is infinite. However, the Born repulsive force, due to the interpenetration of electron clouds, contributes a significant repulsion near contact. Hence the interparticle potential has a very deep minimum at $r = 2R$, the depth of which is many times greater than the thermal energy k_BT. Unless an additional repulsive force is provided, coagulation will occur due to these strong short-range attractions. To generate stable dispersions, a mechanism is required that will produce a potential energy barrier, of adequate height to prevent the system passing into the deep potential minimum. Two practically useful methods, with which this can be achieved, are

steric stabilisation and electrostatic repulsion.

1.2.3. Steric Stabilisation

It has long been known empirically that particulate dispersions can be stabilised by the addition of polymers. Probably the earliest recorded example is the use of naturally occurring polymers by the Chinese and Egyptians, in the preparation of inks over 2000 years ago.[1] The prevention of coagulation of a colloidal system, by coating the particles with layers of flexible polymer, is known as steric stabilisation.[2] A wide range of polymer types may be used and the coating can be physically adsorbed on the particle surface, or chemically bonded to it. Colloidal stabilisation by natural or synthetic polymers is utilised in many industrial products and processes.[2] Steric stabilisation is equally effective in both aqueous and non-aqueous dispersion media. However, the repulsive electrostatic forces, of the type generated in aqueous media, are not generally available for stabilising particles in non-polar organic solvents. Hence, steric stabilisation is essential for non-aqueous colloidal dispersions.

In order to provide stabilisation, the polymeric layer must prevent the particles from approaching one another, to a distance where the van der Waals attractive forces become significant. This can be achieved in a good solvent, with a sufficiently thick, compact layer. The thicker the layer, the greater the distance between the particles and hence the more stable the dispersion. The minimum layer thickness is determined by the particle size and the magnitude of the Hamaker constant. If the polymeric layers are not displaced, when the particles collide and the interaction between the layers is purely repulsive, then the

dispersion will be stable.[20] This is shown in figure 1.2.

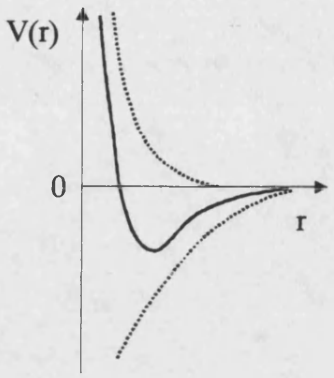

Figure 1.2. Schematic potential energy curve of the interaction between two sterically stabilised particles (solid line). The upper dashed line represents the (nearly) hard sphere repulsive potential and the lower line denotes the van der Waals attractive potential.

It has been determined, experimentally, that the most effective steric stabilisers are amphipathic block or graft copolymers.[6] These consist of two chemically bound homopolymer components, a lyophobic anchor polymer and a lyophilic stabilising chain. The anchor units attach to the particle surface, preventing desorption of the stabiliser during Brownian collisions. These units are ideally insoluble in the dispersion medium. The stabilising polymer chains are soluble in the dispersion medium, extending out into the medium, away from the particle surface. If the dispersion medium is a good solvent for the stabilising moieties, then the polymer-solvent interactions are favoured and interparticle repulsion results. However, if the dispersion medium is a poor solvent, then the polymer-polymer interactions are favoured and interpenetration of the polymer chains occurs, until prevented by the elastic repulsion of the chains.

Homopolymers can also be used to impart steric stability. However, they are relatively ineffective, due to the opposing requirements that the dispersion medium be a good solvent to impart steric stabilisation, but a poor solvent to ensure effective adsorption of the stabiliser onto the particle surface. Instability often occurs in dispersions with a homopolymer stabiliser, due to the lateral movement, or desorption, of the polymer chains.

While electrostatically stabilised dispersions are at best thermodynamically metastable, sterically stabilised systems can be thermodynamically stable. Providing that the steric stabiliser is securely anchored to the particle and surface coverage is complete, the stability of sterically stabilised dispersions is determined by thermodynamic factors. When two polymer covered particles approach sufficiently close, that the outer segments begin to overlap, the free energy change ΔG that takes place is influenced by factors such as temperature, pressure and solvent composition. If ΔG is positive then the polymer-polymer interaction is unfavourable and the particles are sterically stable. If ΔG is negative then the interaction is favourable and flocculation occurs. At the θ-point the free energy change is zero and there is no interaction.

As usual ΔG may be expressed in terms of the corresponding enthalpy ΔH and entropy ΔS changes, so that $\Delta G = \Delta H - T\Delta S$. If, as the chains interpenetrate, there is a reduction in the polymer-solvent interaction and an increase in the polymer-polymer interaction, then ΔH will be positive. ΔS will be positive, if there is a reduction in the number of configurations that the polymer chains may adopt as they overlap. If both ΔH and ΔS are positive, then the dispersion will be entropically stable and will flocculate if heated above the θ-

temperature. If both ΔH and ΔS are negative, then the dispersion will be entropically stabilised and will flocculate if cooled below the θ-temperature. If ΔH is positive and ΔS negative, then the dispersion may be stable at all accessible temperatures. At room temperature and pressure, entropic stabilisation is more common in non-aqueous media, whereas enthalpic stabilisation occurs more often in aqueous dispersions. A correlation between the θ-temperature and flocculation has been established.[20]

Quantitative theories of steric stabilisation are complex.[20,21] The interparticle interactions depend on the density of polymer coverage, at the particle surface and whether the polymer is physically adsorbed from solution, or chemically grafted onto the particle. The quality of the solvent is also an important factor. Because of the wide variety of possible systems, a theory of steric stabilisation has not been established which has the same generality as that of charge stabilisation. Two main problems remain unresolved, prediction of polymer conformations at the particle surface, together with the thermodynamics of the interaction of the two steric barriers. However, the steric forces between surfaces with end-grafted chains are now reasonably well understood, both theoretically and experimentally. This is because such systems are relatively simple to define. The theories are only sufficiently developed for interactions in θ and worse than θ-solvents. In a simple system the steric interaction occurs between two polymer covered surfaces, where each molecule is permanently attached to the surface at one end. At low surface coverage, if there is no interaction between neighbouring chains, then each chain will interact with the opposite surface independently of the other chains. In a θ-solvent the repulsive energy per unit area, between two such surfaces, is approximately exponential

over the distance $D = 9R_g$ to $D = 2R_g$ (where R_g is the radius of gyration of the polymer) and is given by[19]

$$W(D) = 2\Gamma k_B T e^{-D^2/4R_g^2} + \ldots \approx 36\Gamma k_B T e^{-D/R_g} \quad (1.11)$$

or

$$W(D) \approx 36 k_B T e^{-D/R_g} \text{ per molecule,} \quad (1.12)$$

where Γ is the number of polymer chains per unit area. Γ may be expressed in terms of the average separation, s, of the grafted chains at the particle surface, by $\Gamma = s^{-2}$. Equation 1.12 is accurate only at low surface coverage ($s > R_g$) when the layer thickness, L, is equal to R_g. As the surface coverage is increased the distance between the chains is reduced and they extend away from the surface, further than R_g. The repulsion then occurs over a greater distance than that predicted by equation 1.12. In a θ-solvent the thickness of the layer varies according to $L \alpha M^{\nu}$. At low coverage $\nu = 0.5$ and at high coverage $\nu = 1$. In a good solvent the layer thickness has been given by[19]

$$L = \frac{nl^{5/3}}{s^{2/3}} = \Gamma^{1/2} R_F^{5/3}, \quad (1.13)$$

where n is the number of polymer segments and l is the effective segment length. At high surface coverage ($s < R_g$) the repulsive pressure, between two interpenetrating surfaces, is given by the Alexander-de Gennes equation as[19]

$$P(D) \approx \frac{k_B T}{s^3} [(2L / D)^{9/4} - (D / 2L)^{3/4}], \text{ for } D < 2L \quad (1.14)$$

In a good solvent for the coating, the polymer-polymer interaction and hence the repulsive interaction between two particles increases from near zero, as the polymeric layers begin to overlap, to many k_BT over distances of a few nanometers.[5] Thus it is possible to sufficiently reduce the depth of the potential minimum, to give a stable system.

If the particles and the suspension medium have the same frequency-dependent polarisabilities, then $A = 0$.[5] Hence, if the refractive indices of the particles and the suspension medium are matched (at the frequency of visible light), then the van der Waals attractions are expected to be negligible. When the spheres are close to touching,[5]

$$\lim_{r \to 2R} V_A(r) = \frac{-A}{12} \frac{R}{r - 2R}. \qquad (1.15)$$

In this case the interaction potential can be approximated by that of hard spheres, as illustrated in figure 1.3.

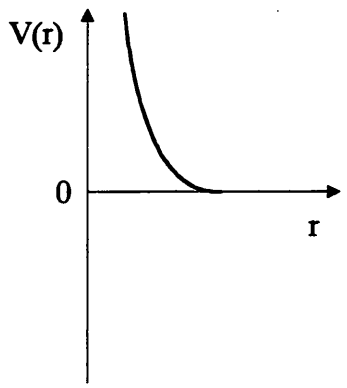

Figure 1.3. Schematic potential energy curve for the interaction between two sterically stabilised colloidal particles, dispersed in an index-matching medium.

1.2.4. Charge Stabilisation

Colloidal particles dispersed in polar (e.g. aqueous) media usually carry a surface charge. This may be acquired by several mechanisms, including ionisation of surface groups and ion adsorption and dissolution. This charge influences the distributions of ions around the colloidal particle. Oppositely charged ions (counter-ions) are attracted towards the surface, while similarly charged co-ions are repelled away. Thermal motion causes the counter-ions to be distributed in a diffuse manner. Hence, there is an ionic atmosphere surrounding each particle, which forms an electrical double layer with the surface charge. The total charge in the double layer, in which there is an excess of counter-ions, is just balanced by the surface charge. When two charged colloidal particles approach each other, the diffuse parts of the electrical double layers interpenetrate giving rise to a repulsive force, which can prevent particle coagulation. The range of the repulsion depends on the charge on the particle and on the electrolyte concentration.

An important advance, in the development of a quantitative description of colloidal systems, was the evaluation of the potential of mean force for charged colloidal particles. This is the classical DLVO theory, which was developed independently by Derjaguin and Landau, in 1941 in the Soviet Union, and Verwey and Overbeek, in 1948, in the Netherlands.[3] According to this theory, colloid stability is determined by a balance of the van der Waals' attraction (V_A) and the electrical repulsion (V_R). The theory assumes that the ions in the diffuse part of the double layer are point charges, distributed according to a Boltzman distribution. The electrical potential is then calculated, by the application of

Poisson's equation. The resulting Poisson-Boltzman equation is solved by making the Debye-Huckel approximation. This method leads to the DLVO expression, for the interaction energy of two charged particles surrounded by electrolyte. Two extreme conditions are distinguished, according to the particle size and the thickness, $1 / \kappa$, of the double layer.

If the charged particles are assumed to be spherical, when the radius (R) is large and the double layer is thin ($1 / \kappa$ is small) $\kappa R >> 1$ and the electrostatic repulsive potential is given by V_R

$$V_R = \frac{\varepsilon R \Psi_0^2}{2} \ln\{1 + \exp[-\kappa(r - 2R)]\}, \qquad (1.16)$$

where r is the centre-to-centre separation of the particles, ε is the dielectric constant of the solvent and Ψ_o is the surface potential.

If the charged particles are small and the double layer thickness is large, $\kappa R << 1$ and

$$V_R = \frac{\varepsilon R \Psi_0^2}{r} \{\exp[-\kappa(r - 2R)]\}. \qquad (1.17)$$

As $\kappa \rightarrow 0$ and the distance between the two particles $(r - 2R)$ becomes small, equation 17 may be approximated by

$$V_R = \frac{\varepsilon R^2 \Psi_0^2}{r}. \qquad (1.18)$$

The thickness of the double layer is then given by

$$\frac{1}{\kappa} = \left(\frac{\varepsilon k_B T}{8\pi n e^2 Z^2} \right)^{1/2}. \qquad (1.19)$$

The total potential energy (V_{total}) between two colloidal particles is given by,

$$V_{total} = V_{attractive} + V_{repulsive}. \qquad (1.20)$$

One possible type of potential energy curve, representing the interaction between two charge stabilised colloidal particles, is shown in figure 1.4.

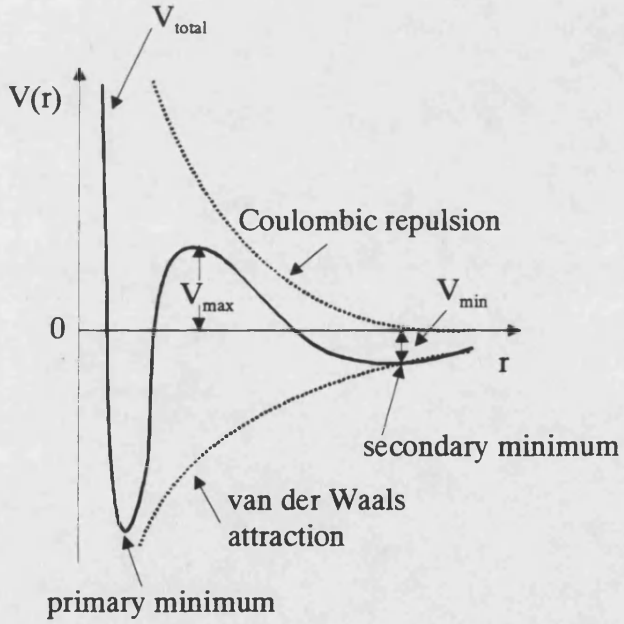

Figure 1.4. Schematic potential energy curves, for the interaction between two charge stabilised colloidal particles.

The total potential energy curve has a repulsive energy maximum (V_{max}) and a secondary minimum, (V_{min}). When two particles approach each other they may overcome the repulsive barrier V_{max}, in which case they are strongly attracted and the potential energy falls rapidly into the primary minimum. The lower the barrier height V_{max}, the more likely it is that the particles will approach close enough to irreversibly aggregate. If the barrier is considerably larger than the thermal energy k_BT, of the particles, then few particles will make contact and the dispersion will be stable. The DLVO theory predicts that an energy barrier of 15 to $20k_BT$ will be sufficient to produce a stable system.

The shape of the total potential energy curve varies, according to the ionic strength of the dispersion medium. At low ionic strengths the potential energy curve often has a high repulsive barrier (V_{max}). If this barrier is greater than the thermal energy k_BT of the system, then the dispersion will be thermodynamically stable. At moderate ionic strengths, the potential energy curve may develop a secondary minimum. In this case the dispersion will be thermodynamically metastable. If the depth of the minimum is several k_BT, reversible flocculation can occur. As the concentration of electrolyte is increased, the thickness of the double layer rapidly decreases. At high ionic strengths the repulsive barrier becomes negligibly small, leading to irreversible flocculation in the primary minimum (V_{min}). The effect of concentration, on the shape of the potential energy curve, is illustrated in figure 1.5 below.

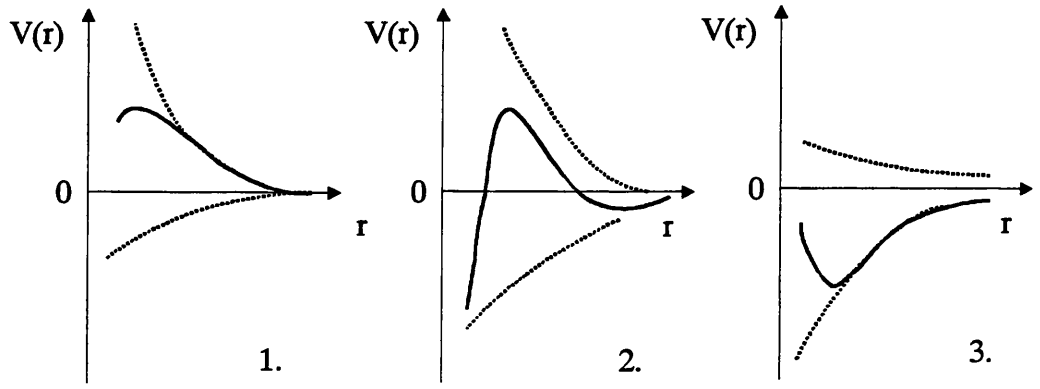

Figure 1.5. The effect of concentration on the potential energy curve, of the interaction between two charge stabilised particles. 1. At low electrolyte concentrations the dispersion is stable. 2. At intermediate concentrations, a secondary minimum develops. 3. At high concentrations the dispersion flocculates.

1.3. Colloid Phase Behaviour

1.3.1. Introduction

The thermodynamic properties (phase behaviour, structure etc.) of a suspension of colloidal spheres, are determined by the form of the interparticle potential. The nature of this potential varies greatly, according to the properties of the particles and suspension medium. In the case of a typical stable suspension, the form of the interparticle potential usually resembles that of the Lennard-Jones potential of atoms.[5] Hence, colloidal suspensions can demonstrate a range of equilibrium phase behaviour, similar to that of a one phase atomic system. If the interparticle potential is carefully controlled, colloidal systems can, for example, exhibit both gas-liquid and liquid-solid phase transitions.[22] However, although the interaction potential of non-metallic atoms is assumed to

be temperature and density independent, the interparticle potential of suspended colloidal particles is often a strong function of temperature, concentration and other suspension conditions. For example, the van der Waals and specific coating interactions, of sterically stabilised colloids, can both be temperature dependent. In the case of a charge stabilised suspension of colloidal spheres, the screening parameter κ varies with temperature. Also, the interaction potential can vary strongly with the addition of free polymer.

In the theoretical consideration of the thermodynamic properties of colloidal suspensions, the liquid in which the particles are suspended can, to a good approximation, be regarded as an inert thermal reservoir. Hence, as far as its thermodynamic properties are concerned, a suspension of identical colloidal spheres can often be treated as a one-component system.[5] The interparticle potential of the colloidal particles can then usually be determined, by the application of the solution theories of McMillan and Mayer, and Kirkwood and Buff.[12,13] From this interparticle potential, using statistical mechanics together with simple liquid and solid state theories, the equilibrium properties can be calculated.

While the suspension medium may be regarded as an incompressible continuum, if it is also assumed that the suspended particles are incompressible then the colloidal suspension is studied under conditions of constant volume. This differs from the more usual experimental situation, where the limiting factor is one of constant pressure. The phase diagram of a one-component colloidal suspension is often represented in a 'pressure-density', or osmotic pressure (Π) - volume fraction (ϕ), form. The osmotic pressure Π of a colloidal suspension is analogous to an atomic fluid's pressure P.

As mentioned previously, if a colloidal suspension and a one-phase atomic system both have an interaction potential of the same form, then the thermodynamic properties of each should be closely analogous. However, the dynamic properties of suspended colloidal particles are fundamentally different from those of atomic materials, being described by the Langevin equation rather than by Newton's second law.[5] Nevertheless, at long times, where the particles or atoms have undergone numerous collisions, notable similarities between the dynamics of both systems have been found.[5,23]

Most of the experimental investigations, of colloidal phase behaviour, have been carried out in the supercritical region of the phase diagram. This contrasts with the case of atomic systems, where the supercritical phase can only be obtained at very high pressures. Examples of colloids whose observed behaviour is supercritical include sterically stabilised particles, in a refractive index-matched suspension medium, where the van der Waals attractions are minimised and small charged stabilised particles, suspended in a medium of relatively low ionic strength. Hence, in the phase diagrams of such systems, there are no distinct gas and liquid phases. Below the freezing concentration (ϕ_f), the samples exist as a colloidal fluid (with gas and liquid being identified with the same state). As the volume fraction is increased, the osmotic pressure rises until crystallisation begins at the freezing concentration (ϕ_f). As has been noted elsewhere, an attractive part in the pair potential is not required for the formation of colloidal crystals.[5] Between the freezing (ϕ_f) and melting (ϕ_m) concentrations, colloidal fluid and crystalline phases coexist. Crystallisation is complete at the melting concentration (ϕ_m) and as the volume fraction is increased, the osmotic pressure rises and the crystalline phase is compressed. In order to investigate

experimentally the phase behaviour of a colloidal system, several samples are usually prepared spanning a range of concentration.[8]

At the critical point, the temperature of a colloidal system is such that the kinetic (thermal) energy of a particle is of approximately the same magnitude as the interparticle attraction energy. With care, colloidal systems can be prepared which have both critical (T_c) and triple point (T_p) temperatures, near room temperature.

1.4. Model Systems

As was mentioned in section 1.1, the study of well-characterised 'model' suspensions of colloidal spheres, over the last twenty years, has greatly increased our knowledge of the behaviour of colloids. Some of the most commonly encountered model systems are poly(methyl methacrylate) / PHSA, polystyrene and silica colloids. These model systems all consist of well-characterised and reproducible suspensions of nearly monodisperse particles. The characteristics of these systems are discussed below.

1.4.1. Polystyrene

The first commonly used model colloidal system was an aqueous suspension of charge stabilised polystyrene spheres, synthesised by emulsion polymerisation. In this system, which has been studied increasingly over the last 30 years, the spherical colloidal particles consist of a large number of entangled polystyrene chains. Each chain starts and ends with a hydropilic group (such as -

KSO_4^-) and the arrangement of the chains is such, that the end groups are located mainly at the surface of the particles. When the particles are dispersed in a medium like water, with a high dielectric constant, the surface groups ionise and each particle acquires a large negative charge. The counter-ions (usually H^+) discharged by the particles, together with ions present in the dispersion medium, form part of an electrical double layer around each particle. The double layers provide the particles with colloidal stability. In this system the strength and range of the double layer repulsive interaction can be easily controlled experimentally, by varying the ionic strength of the suspension medium (the screening parameter κ, which controls the range of the repulsion, is determined by the ionic strength of the dispersion medium).

Concentrated suspensions of polystyrene particles appear opaque, due to the strong multiple scattering of light. This is because of the difference between the refractive index of colloidal polystyrene ($n \sim 1.61$) and that of possible dispersion media ($n \sim 1.33$). X-rays and neutrons are scattered more weakly by colloidal polystyrene and so are suitable for investigating more concentrated samples ($\phi \geq 0.3$). Until recently, the analysis of such systems using light scattering techniques was only practical at low volume fractions ($\phi \leq 10^{-3}$).[5] However, the index-matching difficulties have been overcome by the synthesis of charged polytetrafluoroethylene copolymer (PFA) particles, which have a lower refractive index ($n \sim 1.36$).[24] Using a mixture of liquids as the dispersion medium (e.g. glycerol and water), accurately index-matched samples can be readily prepared. These can be studied by light scattering, up to much higher volume fractions than was previously possible in the non index-matched system.

Suspensions of colloidal polystyrene spheres can be synthesised, with a

low polydispersity ($\sigma \sim 0.01$), provided that the average particle diameter is greater than 100 nm. Systems composed of particles smaller than this generally have a higher polydispersity.

Not long after the first suspensions of colloidal polystyrene were prepared, iridescence was observed in concentrated samples, due to the Bragg diffraction of visible light from ordered structures. Since then colloidal polystyrene has been investigated in increasing detail. Subcritical behaviour of charged particles is expected to occur only in a restricted range of suspension conditions. Most of the studies of the phase behaviour have been carried out in the supercritical region.[5] The calculations of Robbins *et al.*, together with the experimental results of Monovoukas and Gast and Sirota *et al.*, have provided a reasonably qualitative description of the supercritical phase behaviour of hard sphere colloids.[25,26,27]

Robbins *et al.* calculated the phase behaviour of charged particles, interacting through a Yukawa potential, based on molecular dynamics simulations.[25] The predicted phase diagram is illustrated in figure 1.6 below.

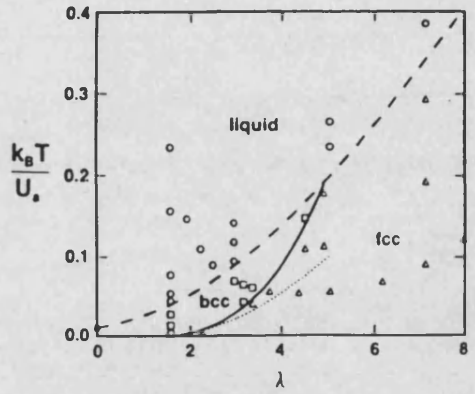

Figure 1.6. From Robbins *et al.*[25] Predicted phase diagram for particles interacting through a Yukawa potential. Circles - fluid, squares - bcc crystal, triangles - fcc crystal. The dashed line indicates the fluid-crystal boundary and the solid line the bcc-fcc boundary.

U_a is the energy of interaction of two particles, separated by the mean interaction separation, $a = \rho^{-1/3}$ and $\lambda = \kappa a$ is the product of this distance and the screening parameter. At $T = 0$ the stable solid is that with the lowest potential energy. The bcc-fcc boundary, at $T > 0$, is determined by the calculation of free energies. The bcc crystal has a higher entropy than the fcc structure and so is thermodynamically stable up to $\lambda \approx 5$. For higher values of λ, the fcc structure is thermodynamically favoured. For sufficiently strong interparticle interactions, the colloidal particles freeze into a body-centred cubic (bcc) or face-centred cubic (fcc) crystal structure.

Monovoukas and Gast studied the phase behaviour of a reasonably well-characterised suspension of polystyrene spheres, of diameter 134 nm, suspended in potassium chloride solutions.[26] They mainly studied samples at low ionic strength and volume fraction. The results are shown in figure 1.7 below.

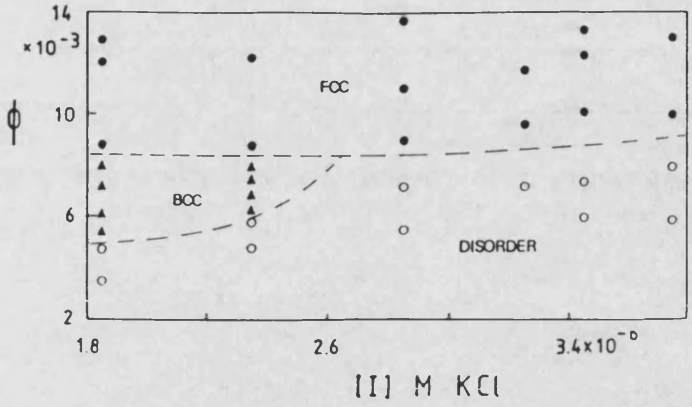

Figure 1.7. From Monovoukas and Gast.[26] Experimental phase diagram of charged polystyrene spheres, of radius 67 nm, as functions of volume fraction and electrolyte concentration. 'Disorder' indicates the fluid phase.

Monovoukas and Gast mapped these experimental results onto the theoretically predicted phase diagram of Robbins *et al.*, as shown in figure 1.8.

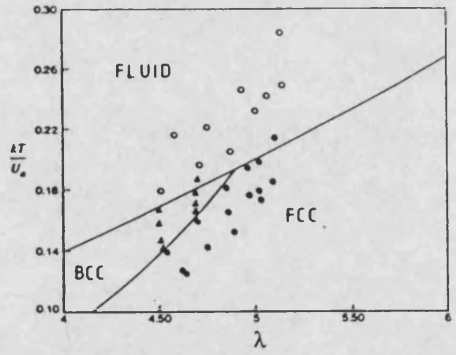

Figure 1.8. From Monovoukas and Gast.[26] Mapping of the experimental data of figure 1.7, onto the theoretical predictions of figure 1.6. The solid lines are the phase boundaries taken from figure 1.6.

The agreement, between experimental and theoretical results, is reasonably good.

Sirota *et al.* investigated the phase behaviour of suspensions of polystyrene particles, of diameter ~92 nm, suspended in a methanol-water mixture.[27] These authors observed coexisting fcc and bcc crystals. The phase behaviour observed was similar to that predicted by Robbins and co-workers, although the observed freezing transitions were found to occur at lower particle concentrations than predicted. Sirota *et al.* suggested that this could be due to the relatively high particle concentration used in the experiment.

Hence, an important property of model polystyrene systems is the ability to be able to change the range of the interparticle repulsion, from slightly larger than the particle diameter to many diameters, simply by changing the ionic strength of the dispersion medium.

1.4.2. Silica

Possibly the most commonly used model system is colloidal silica. Initially, colloidal silica is synthesised as a charge stabilised colloid. In this form colloidal silica is less useful than colloidal polystyrene. Hence, it is usually modified to provide sterically stabilised particles.[5] The most widely used stabiliser consists of stearyl chains, grafted onto the surface of the particles. The length of the stearyl chain is up to ~2 nm.[28]

In a good solvent for the coating, the repulsive interaction between the particles is expected to increase from zero (on the first overlap of the stabiliser layers) to many k_BT, over a distance of up to 1 nm. As this distance is considerably less than the particle diameter, the interparticle potential is very close to that of hard spheres.

These particles can be synthesised with a range of radii, from ~10 nm to ≥ 500 nm and polydispersities from 0.2 for the smallest particles, reducing to ~0.02 for the larger particles. The refractive index of the particles is $n \approx 1.45$.[28]

Colloidal silica ($n \approx 1.45$) can be prepared using a range of index-matching liquids. The resulting suspensions, which remain almost transparent up to high volume fractions, can be studied using light scattering techniques.

The sub-critical phase behaviour of the stearyl-silica system was investigated in a study by Edwards and co-workers.[29] In this work, particles of various diameters (d = 50 – 265 nm) were suspended in n-pentane, n-hexane and n-heptane. In several samples, phase separation was observed upon increasing and decreasing the temperature, with respect to room temperature. Above room temperature, the temperature at which phase separation was observed, varied according to the particle size and the solvent. The results obtained by these authors are shown in figure 1.9.

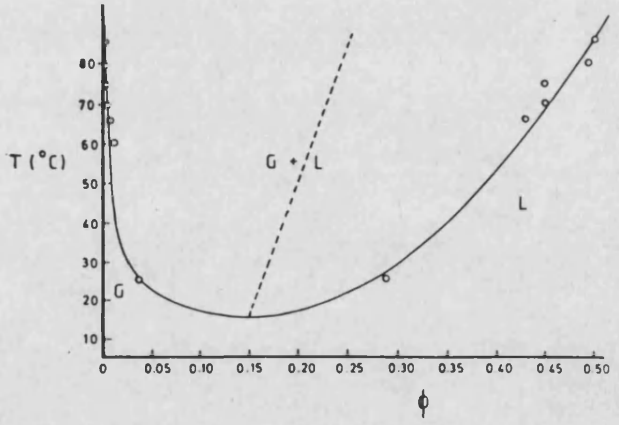

Figure 1.9. From Edwards *et al.*[29] 'Gas-liquid' coexistence of stearyl silica particles of radius 138 nm in hexane, as a function of temperature and volume fraction.

Edwards *et al.* suggested that this behaviour is a gas-liquid transition, which is caused by van der Waals attractions between the particles. These attractions increase in magnitude as the temperature is increased, due to the decreasing density of hexane and the resulting growing difference between the polarisabilities of the particles and the liquid.

Below room temperature, Edwards *et al.* observed that phase separation was far less dependent on particle size and solvent type and could not be explained in terms of van der Waals forces.

It is possible to prepare index-matched suspensions of colloidal silica in a range of liquids, whose refractive indices are close to those of the particles. These suspensions can be studied using light scattering techniques, as the suspensions remain almost transparent even at high volume fractions. In a solvent such as cyclohexane, which is a good solvent for the coating, the repulsive interaction between the particles is expected to increase from zero (on the first overlap of the stabiliser layers) to many k_BT over a distance of ~1 nm.[28] Hence, the interparticle potential appears to be very close to that of hard spheres. If these silicas are dispersed in a liquid that is a poor solvent for the coating, specific coating-coating interactions can occur, which results in a short ranged attraction. In this case the particles can be considered to be sticky hard spheres.[28] Also, away from the exact index match, van der Waals attractions can become significant.

1.4.3. Poly(Methyl Methacrylate)

The system used in the present work was a well-characterised model colloidal system, synthesised in a one-step dispersion polymerisation.[7] It has been extensively investigated, in a number of previous studies[2-9] and consists of similarly sized spherical cores of amorphous poly(methyl methacrylate) (PMMA). These are sterically stabilised by a 'comb' stabiliser, consisting of poly(12-hydroxystearic acid) (PHSA) linked to a copolymer 'backbone' of methyl methacrylate and glycidyl methacrylate. The 'backbone' is attached to the particle surface and the PHSA 'teeth' project into the dispersion medium, as shown in figure 1.10.

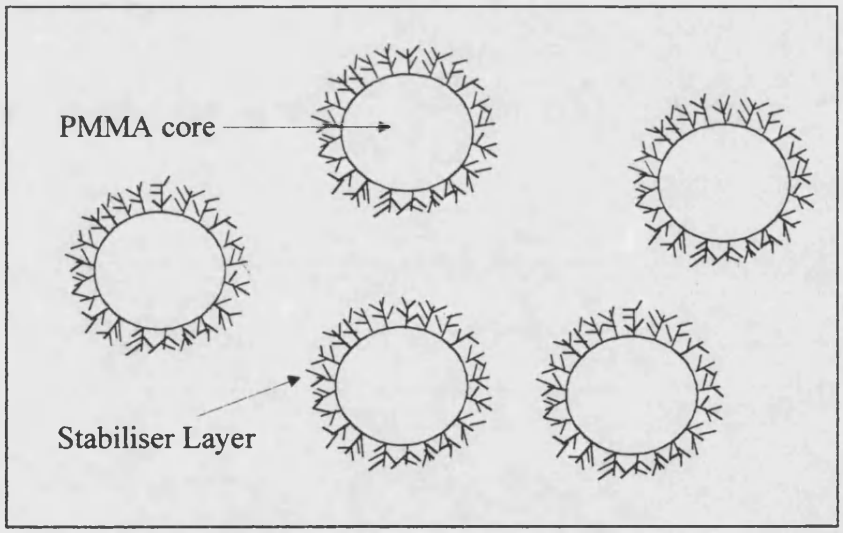

Figure 1.10. Schematic diagram of poly(methyl methacrylate) (PMMA) colloidal particles, sterically stabilised by a thin layer of poly(12-hydroxystearic acid) (PHSA).

Colloidal PMMA particles of low polydispersity can be synthesised, in hydrocarbon media, in a single-stage dispersion polymerisation reaction. For particles with diameters greater than ~300 nm, the polydispersity is typically less than $\sigma = 0.08$. The refractive index, of the PMMA cores, is $n \approx 1.49$. Index-matched suspensions can be prepared by suspending the particles, in a mixture of decahydronapthalene (decalin) and carbon disulphide. This provides nearly transparent samples, which can be studied by direct observation and light scattering methods, even at high volume fractions. By matching the dispersion medium and particle refractive indices, the attractive van der Waals forces are minimised. In a non-polar medium the electrostatic effects should be negligible. Hence, the interparticle potential should be purely repulsive, arising only from the compression of the densely packed PHSA stabiliser molecules. The length of these molecules is typically ~10 nm, which is comparable to the range of the van der Waals attraction. The high chain density, at the particle surface, ensures that the repulsive interaction increases from zero to many k_BT, over a distance of 2 – 3 nm[10]. This distance is small in comparison with the core diameter of the particles (typically at least 150 nm) hence, to a good approximation, the particles interact like hard spheres. The assumption of a hard sphere interaction is supported by a number of previous experiments, on one-component suspensions of this type.[8] The phase behaviour and structure of hard sphere colloids is discussed further in chapter 2.

1.5. Colloid-Polymer Systems

It has long been known, experimentally, that the addition of a small amount of a non-adsorbing random coil polymer, to an initially stable suspension of spherical colloidal particles, can induce an effective attraction between the particles. If this attraction is strong enough, phase separation (depletion flocculation), into colloid-rich and colloid-poor phases, can occur. The depletion attraction between colloidal particles is an entropic effect. This phenomenon is of fundamental interest and considerable technological importance. The first theoretical treatment of the depletion mechanism, in a colloid polymer mixture, was the simple, but useful, geometrical model proposed some decades ago by Asakura and Oosawa (AO) and also later independently by Vrij.[30,21] The AO model is based on the fact that the free energy, in a hard sphere system, is entirely entropic and depends on the volume accessible to the centre of each particle. For hard spheres, the Helmholtz free energy ($F = U - TS$) is determined by the entropy. Hence, $F = T$(constant - S). The only contribution to the internal energy is kinetic, which is strictly proportional to the temperature.[28] In the AO model, the polymer molecule and colloid particles are assumed to behave as hard spheres, of diameter σ_p and σ_c respectively. However, the diameters are assumed to be non-additive, so while the polymer molecules interact as hard spheres with the colloid particles, they interpenetrate each other freely. Hence, $\sigma_{pc} > (\sigma_{pp} + \sigma_{cc}) / 2$ where σ_{pc} is the distance of closest approach of particles of colloid and polymer. The centres of mass, of the polymer molecules, are excluded from a spherical region or depletion zone around each colloid particle, of radius $(\sigma_p + \sigma_c) / 2$. The key point of this model is that, although the colloidal particles cannot

overlap, their depletion zones can. The overlap of the depletion zones, of two particles, increases the total free volume for the polymer molecules in the sample as a whole. The entropy of the system is increased and there is an effective attractive potential, which drives the two colloidal particles together.

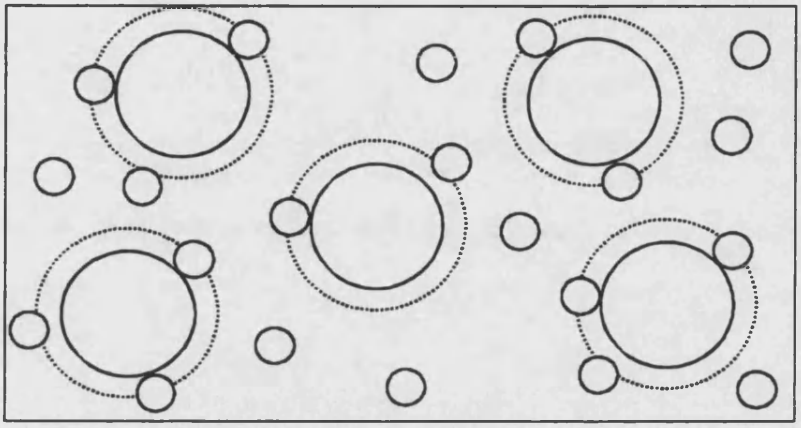

Figure 1.11. A schematic diagram of the Asakura and Oosawa (AO) geometric depletion model.[30] The dashed lines around the large particles indicate depletion zones, from which the centres of the small particles are excluded.

An alternative, but equivalent, argument is that when the surface-surface separation of two colloidal particles becomes less than the diameter of a free polymer coil, σ_p, the polymer molecules are excluded, from the overlapping depletion zones between the particles. However, the polymer molecules can still approach the remainder of the particle surfaces and the colloidal particles experience an anisotropic osmotic pressure. This gives rise to an effective attractive potential between the particles. In either case, on the basis of this simple but useful idea, Asakura and Oosawa estimated the potential of the depletion force, at the limits of low particle concentration, to be,[30]

$$V_{cc}(r) = \infty \qquad \text{for } r < \sigma_c$$

$$-\frac{4}{3}\pi n_p k_B T[\sigma_{pc}^3 - \frac{3}{4} r\sigma_{pc}^2 + \frac{1}{16} r^3] \qquad \text{for } \sigma_c < r < 2\sigma_{pc} \qquad (1.21)$$

$$0 \qquad \text{otherwise}$$

A useful property of the depletion potential is that its depth is determined by the polymer concentration and its range by the molecular weight of the added polymer. Hence, the potential is 'tuneable' experimentally.

The depletion potential still applies in the low density limit, when the second component is a micelle, or small particle of the same kind. In the case of an asymmetric mixture of hard sphere colloids, the interaction diameter is then additive and $\sigma_{pc} = (\sigma_{pp} + \sigma_{cc}) / 2$ (see chapter 6). While the AO model provides useful expressions for the depletion potential, the internal degrees of freedom of the polymer molecules are neglected.

In order to investigate the phase behaviour of colloid and polymer mixtures, a more sophisticated treatment of the depletion force is required. Statistical mechanical theories, of colloid-polymer mixtures have been developed, which take into account the polymer internal degrees of freedom. The first such analysis was proposed by Feigin and Napper,[31] followed by the self-consistent field theory of Joanny and co-workers.[32] More recently, phase diagrams were calculated by Gast *et al.* and Vincent *et al.*, who used an 'effective potential' approach.[33,34,35] In this method, the statistical mechanical technique known as perturbation theory, is used to calculate the equilibrium properties of the system. The interaction potential between two particles is split into a reference potential, of known properties and a perturbation potential. In the simplest theory [33,34] the hard sphere potential is used as the reference potential and the perturbation potential is the depletion

attraction induced by the added polymer,

$$U(r) = U_{hs}(r) + U_{depl}(r). \qquad (1.22)$$

The topology of the phase diagrams calculated using this method[33,34], for a suspension of hard spheres in an ideal polymer solution, depends sensitively on the size ratio $\alpha = R_g / R$. R_g is the radius of gyration of the polymer and R is the radius of a colloidal particle. For $\alpha < 0.3$ only fluid-solid coexistence is expected. However, for $\alpha > 0.3$ a liquid-gas transition, with a critical point and a triple point, is predicted. These predictions agree qualitatively with the observations of Sperry, who pioneered the experimental study of colloid-polymer mixtures.[36]

The effective potential approach does not allow for the partitioning of the polymer between coexisting phases.[37] The polymer concentration is assumed to be the same in each phase. Recently, Lekkerkerker and co-workers proposed an alternative theoretical method, where the phase behaviour of a colloid-polymer mixture is considered in terms of the free energy of the whole system.[37] Unlike the effective potential approach, this method does allow for the partitioning of polymer between phases. In the simplest approximation, the colloidal particles are assumed to interact as hard spheres and the polymer molecules are treated as interpenetrating coils, whose centre of mass cannot approach closer than a distance R_g, from the surface of a colloidal particle. Consequently, the polymer is excluded from a spherical shell, of radius $(R + R_g)$, around each colloidal particle. In the theory of liquids, this description corresponds to the asymmetric non-additive hard sphere model, which was first suggested by Widom and Rowlinson for the study of liquid-vapour transitions.[38] In order to calculate the

free energy of this model, Lekkerkerker *et al.* used a simple statistical mechanical approach, working initially in the grand canonical ensemble.[37] Integration over the polymer degrees of freedom was performed exactly, leading to a potential of mean force of the form[28]

$$U = V_c - \Pi_p(\mu_p)V_{free}(r_c), \tag{1.23}$$

where V_c is the interaction potential of the two isolated colloid particles. Π_p is the osmotic pressure of a pure polymer system and is a function of the polymer chemical potential μ_p. V_{free} is the total free volume accessible to the polymer molecules and is a function of the colloid particle positions, r_c. Using a van der Waals mean-field approximation, the Helmholtz free energy (F) of the mixture can be expressed as[28]

$$F = F_c(N_c,V) + F_p(N_p,V_{free}), \tag{1.24}$$

where $F_c(N_c,V)$ is the free energy of N_c hard spheres, in a volume V. $F_p(N_p,V_{free})$ is the free energy of a pure polymer, of N_p molecules, in the volume not occupied by the hard spheres (V_{free}). The overlapping of depletion zones increases V_{free}. This increases the entropy of the polymer molecules and lowers the free energy of the colloid-polymer mixture. Figure 1.12, from Pusey and Poon and co-workers, shows the phase diagrams of colloid-polymer mixtures, which were calculated using this approach.[28]

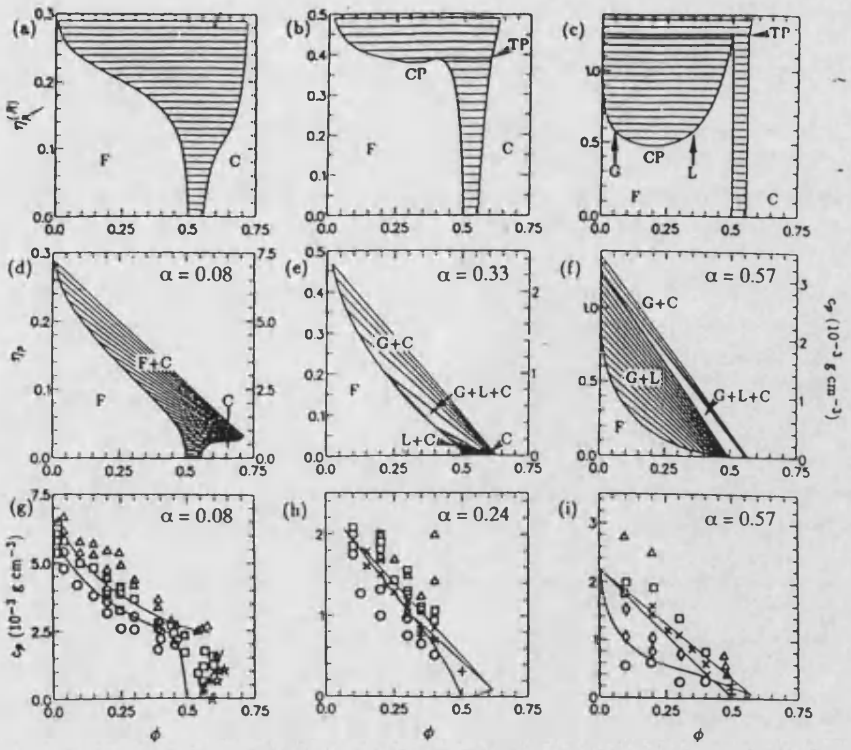

Figure 1.12. Phase diagrams of colloid-polymer mixtures, from Pusey and Poon *et al.*[28] (a)-(c) Theoretical phase diagrams in the ϕ - η_p^* plane, for size ratios α = 0.08, 0.33 and 0.57. η_p^* is the polymer volume fraction in the free volume left by colloids at a volume fraction of ϕ. (d)–(f) Predicted phase diagrams (a)-(c) translated into the experimentally accessible ϕ - η_p plane, where η_p is the polymer volume fraction. (g)-(i) Experimental results for comparison with (d)-(f), with observed phases: ○, single-phase fluid; □, fluid (or gas) + crystal; X, gas + liquid + crystal; ◇, gas + liquid; +, liquid + crystal; Δ, gel, or no visible crystallites; ∗, fully crystalline; ★, glass.

In figures (a)-(c), the colloid volume fraction ϕ is plotted against $\eta_p^{(R)}$, the polymer concentration in a reservoir of pure polymer solution, in equilibrium with the

system. Without polymer ($\eta_p^{(R)} = 0$) the hard sphere freezing and melting transitions are recovered. For $\alpha \leq 0.32$ a fluid-solid transition only is expected and the region of coexistence is broadened by the addition of polymer. For $\alpha \geq 0.32$ critical and triple points are predicted. This is in qualitative agreement with the predictions of the effective potential approach mentioned earlier.[33,34] Ilett *et al.* translated these diagrams (a-c) into an experimentally accessible form, by plotting the colloid volume fraction ϕ against the dimensionless polymer concentration η_p.[39] For $\alpha \leq 0.32$ fluid-solid coexistence is predicted, but oblique tie lines imply marked partitioning of polymer between the phases.[37] For $\alpha \geq 0.32$ the triple lines of graphs (b) and (c) become triangular regions of three phase coexistence.

In order to investigate these theoretical predictions, Pusey, Poon and co-workers performed a number of experiments, using a model colloid-polymer mixture (discussed in reference 28). The system used consists of PMMA particles, sterically stabilised by a thin layer of PHSA (see section 1.4) and non-adsorbing random coil polystyrene, dispersed in a cis-decalin. Diagrams (g), (h) and (i) show the results of an experimental investigation, of the phase behaviour of this system, at size ratios $\alpha = 0.08$, 0.24 and 0.57. These results largely confirm the theoretical predictions, illustrated in graphs (a), (b) and (c).

In a recent study, the phase behaviour of nearly hard sphere polystyrene latices, suspended in aqueous solutions of hydroxyethyl cellulose (a non-adsorbing polymer), was investigated.[40] The phase diagrams produced are similar in topology to those determined experimentally, by Pusey, Poon and co-workers.[28]

1.6. Phase Separation at Hard Walls

To make progress theoretically, the phase behaviour of hard sphere colloids is generally considered within a boundless environment. This differs to the usual experimental situation, where such systems are spatially restricted.[28] In experiments using suspensions of almost monodisperse PMMA spheres, Pusey and Poon observed an iridescent 'sheen' on the walls of samples, at volume fractions just below the freezing transition ($\phi_f = 0.494$).[28] These authors attributed this phenomenon, to the formation of an ordered phase at the walls of the sample (wall crystallisation). Although more detailed experimental investigation, using one-component hard sphere systems, has yet to be carried out, computer simulation studies have found similar behaviour.[41,42] In these studies, it was found that wall crystallisation occurred, in a system of monodisperse hard spheres, when the bulk volume fraction was $\phi = 0.486$, which is below the bulk freezing transition ($\phi_f = 0.494$) and in quantitative agreement with the observations of Pusey and Poon.[28]

The effect of a hard, flat, wall on the phase behaviour of binary mixtures of hard spheres has recently been investigated, using both experimental and theoretical methods.[43,44] Experimentally, Kaplan *et al.* studied the phase behaviour of mixtures of charge stabilised polystyrene spheres, screened so that they interacted approximately as hard spheres. An ordered phase was observed to precipitate on the walls of the sample, at volume fractions as low as 0.2. However, bulk crystallisation was not observed at higher sample concentrations. Kaplan and co-workers explained these results in terms of the simple geometrical argument, first advanced by Asakura and Oosaka to explain phase separation in

colloid-polymer mixtures.[30] Kaplan *et al.* suggested, that just as there is a depletion zone around each large particle, from which the centres of the small particles are excluded, a hard, flat, wall also has a depletion zone. The overlap of the depletion zones of the large particles and the wall induces a deletion attraction between the wall and the particles and a monolayer of hard spheres forms at the wall. Recently, an experimental study by Dinsmore and co-workers found that, at volume fractions below that at which bulk freezing occurs, a fluid monolayer, consisting mainly of hard spheres, formed at the sample wall.[45] As the volume fraction was increased the fluid at the wall was observed to freeze, due to the depletion attraction between the large spheres. These results are in qualitative agreement with the recent theoretical calculations of Poon and Warren. These authors predicted that wall crystallisation will occur, in hard sphere mixtures, prior to bulk crystallisation.[44]

CHAPTER 2

2. HARD SPHERE COLLOIDS

2.1. Introduction

An assembly of identical hard spheres is one of the simplest classical models. Nonetheless, hard sphere systems exhibit much the same range of equilibrium phase behaviour, as is observed in simple atomic systems. The possibility of a freezing transition in an assembly of hard spheres, was predicted by early theoretical work.[46] The freezing transition was first observed, in the computer simulation study of Alder and Wainwright.[47] It was then quantitatively investigated, in a computer simulation study, by Hoover and Ree.[46] It was found that as the concentration is increased, an assembly of identical hard spheres undergoes a first-order freezing transition, to form a crystal with a close-packed structure. Hence, an attractive part in the pair potential is not required for the formation of hard sphere crystals. Since the potential energy of a hard sphere system is the same for all particle configurations, the freezing transition is driven by entropy alone. Early computer simulation experiments[47] and theoretical calculations also suggested, that sufficiently rapid compression should transform a hard sphere system, into a dense metastable amorphous (or glass) state. More recently, Woodcock identified a glass transition, from computer simulation studies, at $\phi_g \approx 0.58 \pm 0.02$.[48] The glassy state was found to persist up to the maximum packing fraction.

2.2. One-Component Phase Behaviour

The phase behaviour and structure of assemblies of hard spheres can be investigated experimentally, using 'model' suspensions of spherical colloids. As discussed in the introduction, well-characterised model colloidal spheres can now be prepared, whose interaction is a close approximation to that of hard spheres. One of the first experimental studies, of the freezing transition of hard sphere colloids, was carried out by Kose and Hachisu.[18] In this investigation, an approximate hard sphere interaction was obtained by using cross-linked poly(methyl methacrylate) colloidal particles dispersed in benzene. Suspensions with a variety of concentrations were prepared and crystallisation was observed to occur in several samples, confirming the predictions of the theoretical work. In a subsequent study, Pusey and van Megen investigated the phase behaviour of hard sphere colloids in some detail, using the PMMA / PHSA system used in the present work.[8,49] The interaction potential, of the PMMA spheres in this system, is predominantly steep and repulsive.[8] Samples were prepared in a range of concentration, spanning both the freezing and glass transitions. Coexisting fluid and crystalline phases were observed and the phase diagram was determined.[8] The spherical PMMA colloidal particles used in this study were suspended in a mixture of decahydronapthalene (decalin) and carbon disulphide. The relative proportion of decalin and CS_2 was chosen to provide a suspension medium, with a refractive index close to that of the particles ($n \sim 1.50$). The resulting 'index-matched' particles were nearly transparent, even at high volume fractions. Hence, they could be studied, by both light scattering and direct observation, without problems of multiple scattering arising. Also, because of the refractive

index matching, the van der Waals attractions between the particles are minimised and the interparticle interaction is predominantly steep and repulsive.[8] The study reported by Pusey and van Megen, together with a number of subsequent experiments (reviewed in reference 5) on one-component suspensions of this type, has established that the interaction between the particles is well approximated by that of hard spheres.

The phase behaviour of a monodisperse system of hard spheres is determined by the volume or packing fraction

$$\phi = \frac{4}{3}\pi R^3 \rho, \qquad (2.1)$$

where R is the particle radius and ρ is the number density N / V. The phase behaviour of the PMMA / PHSA, decalin / CS_2 system was investigated in the present work, by preparing samples with a range of volume fractions spanning the phase coexistence region. First, the samples were shaken in order to shear-melt any colloidal crystals present. The resulting metastable fluids were then left undisturbed and observed at regular intervals. Crystals were observed hours or days after mixing. The phase diagram was determined, by measurement of the crystal volume of each sample. The phase diagram of PMMA hard colloidal spheres is illustrated in figure 2.1.

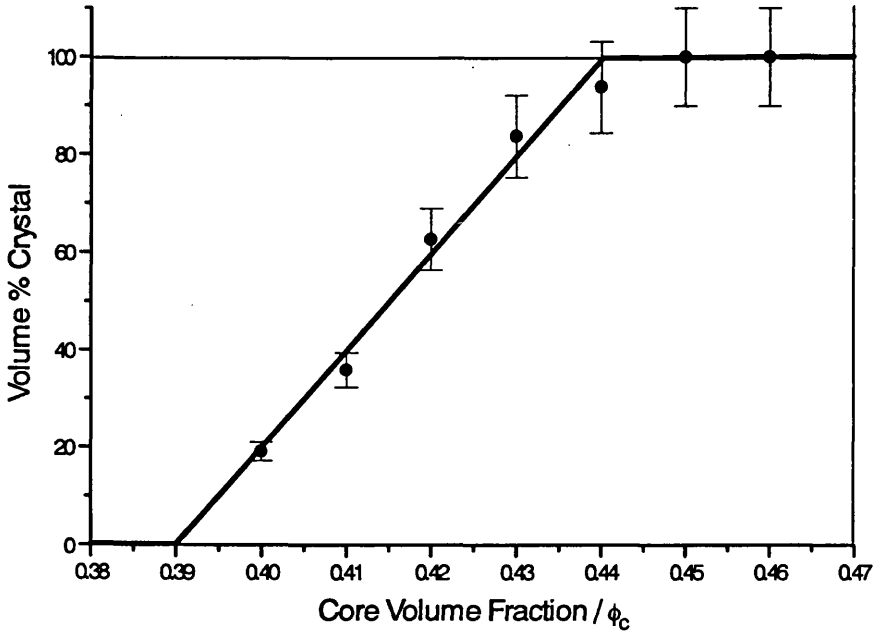

Figure 2.1. Phase diagram of hard colloidal PMMA spheres (sample DMM7), with the crystalline fraction of the sample volume plotted as a function of the core volume fraction.

Below the freezing volume fraction (ϕ_f), the samples exist as a colloidal fluid. Between the freezing and melting (ϕ_m) concentrations, colloidal fluid and polycrystalline phases coexist. In this region ($\phi_f < \phi < \phi_m$) Bragg reflecting crystallites are homogeneously nucleated. Nucleation occurs throughout the bulk of the sample, but not at the meniscus or cell walls. The crystallites that are formed settle under gravity and a distinct boundary can be observed, separating the lower polycrystalline phase from the upper disordered fluid phase. The position of the fluid-solid phase boundary is controlled, by competition between the rates at which crystallites nucleate and grow and gravitational compaction.[50] The observed melting concentration ϕ_m is very close to the hard sphere value of

$\phi_m = 0.545$. Above the melting concentration ϕ_m, but below the glass transition at $\phi_g \sim 0.58$, the stable phase is a colloidal crystal. In this region ($\phi_m < \phi < \phi_g$), the samples are completely filled with homogeneously nucleated crystallites. At concentrations above the glass transition ($\phi_g \sim 0.58$), crystallisation is suppressed and non-equilibrium behaviour is observed. In this region the only crystallisation that occurs is heterogeneously nucleated, at the meniscus and cell walls. Crystallisation by heterogeneous nucleation occurs at a much lower rate, than the homogeneously nucleated crystallisation observed at lower concentrations. Just above $\phi_g \sim 0.58$, large crystallites with irregular morphologies grow until the cell is full.[8] It has been shown that the glass transition coincides with a change in the mechanism of crystallisation.[50] As the concentration is increased, heterogeneous nucleation is reduced and occurs at the meniscus only, while the rest of the sample remains in an amorphous or glassy state. As the concentration is further increased, no heterogeneous crystallisation is observed. The samples remain in an amorphous state, up to close packing at $\phi = 0.7405$. Although the equilibrium state of the samples above the glass transition is crystalline, the colloidal particles in the metastable fluid phase do not have sufficient freedom of motion to form crystal nuclei.[50] The long distance diffusion is suppressed by the glass transition.

As calculated in the pioneering work of Bernal, the maximum volume fraction of an amorphous assembly of hard spheres is $\phi = 0.64$.[51] At this concentration, the random close-packed particles are confined by the surrounding particles. Hence, they have no free volume for local motions. The theoretical hard sphere value of $\phi = 0.64$, is close to the experimental value of $\phi \sim 0.66$ for the amorphous sediment formed, when samples are centrifuged rapidly enough to

avoid crystallisation.[5]

The crystal volume of each sample can be determined, by measurement of the height of the fluid-solid phase boundary. As illustrated in figure 2.1, extrapolation to 0% and 100% crystal then provides an estimate of the equilibrium freezing and melting concentrations. With larger colloidal particles, it is necessary to take into account the effects of gravitational settling. If the rate of sedimentation is greater than the rate of nucleation and growth of the crystallites, then the observed phase behaviour will be highly non-equilibrium.[52] In this case, in order to determine the equilibrium phase behaviour, either a time-averaged zero gravity method must be used[52] (see chapter 4), or a technique that involves measuring the changes in height of several distinct layers over a period of time.[53]

The carbon disulphide cosolvent used in the preparation of the refractive index-matched suspensions of PMMA, is known to penetrate the cores of the colloidal particles.[54] This causes the cores to swell, although the increase in radii is thought to be less than 3%.[54] As a result of this swelling and because of the incomplete characterisation of the stabiliser coating, the density of the composite core-shell particle is not known precisely. Hence, the volume fraction cannot be reliably calculated from the dispersion weight fraction. In the present work, as in previous studies, effective volume fractions were determined as follows. First, samples were prepared with a range of core volume fractions (ϕ_c) spanning the phase-coexistence region. Accurate core volume fractions ϕ_c were then calculated, from the measured suspension dry weight fractions and the literature value for the density of PMMA ($\rho_{PMMA} = 1.188 gcm^{-3}$). After the samples had reached equilibrium, the volume of crystal in each sample was measured.

Extrapolation to 0 to 100% crystal then provided the core volume freezing (ϕ_c^f) and melting (ϕ_c^m) concentrations. Hoover and Ree determined the hard sphere freezing volume fraction to be $\phi_{hs}^f = 0.494$ and the melting volume fraction to be $\phi_{hs}^m = 0.545$, from computer simulation experiments.[46] In the present work, the interparticle potential was assumed to be hard sphere and the core volume fraction, at which crystallisation first occurred (ϕ_c^f), was identified with the hard sphere value ($\phi_{hs}^f = 0.494$). All other core volume fractions were then scaled by the same factor, α, to provide effective hard sphere volume fractions, ϕ, where

$$\phi = \alpha \phi_c. \qquad (2.2)$$

This process allows the effective density of the composite core-shell particles to be accurately determined. Due to the higher proportion of the low density stabiliser in small particles, in comparison with larger particles, the effective density is a slowly increasing function of particle size.[5] The volume fraction of the crystal phase, at the melting transition, was identified with the lowest suspension concentration at which 100% crystal was observed. A comparison of the observed melting concentration with the value for hard spheres, determined by computer simulation, shows the two to be in good agreement.[5]

2.3. The Structure of One-Component Hard Sphere Colloidal Crystals

Although the very existence of a freezing transition, in a one-component assembly of hard spheres (with no attractive part in their pair potential), was initially the subject of vigorous debate[5], it is now generally accepted.[5,8,49] Since

the internal energy of an assembly of hard spheres is entirely kinetic, the formation of ordered structures is caused by entropy, which is normally imagined as a driving force for disorder. This apparent paradox may be resolved, by considering the two contributions to a system's entropy, the configurational entropy of the metastable fluid and the entropy associated with the amount of local free volume available to the spheres. As mentioned earlier, Bernal determined the maximum volume fraction of a random close-packed assembly of hard spheres to be $\phi_{rcp} \approx 0.64$.[51] At this concentration, the particles are touching and have no free volume for local motion. However, the particles of a close-packed crystal at the same concentration ($\phi \approx 0.64$) do have enough free volume for local motion. This is because the close-packed crystal is not fully compressed, until the volume fraction is increased to $\phi_{cp} = 0.7405$. The increase in local free volume, in going from a disordered fluid phase to the crystal, is associated with an increase in free volume entropy. However, the increase in long ranged order, on the formation of the crystal, is associated with a reduction in the configurational entropy. Hence, crystallisation occurs when the reduction in configurational entropy is more than offset, by the increase in the free volume entropy.

Although assemblies of hard spheres play an important role in the development of liquid state theory[55], the equilibrium hard sphere crystal structure remains uncertain. Because of the short ranged isotropic nature of the hard sphere potential, it is generally accepted that the structure should be close-packed. The two simplest close-packed arrangements, are the face-centred cubic (fcc) and hexagonal close-packed (hcp) structures. Both structures can be visualised in terms of the periodic stacking, of identical layers of hexagonally

arranged particles.[56] In either structure each layer can adopt one of three lateral positions. If a layer adopts the reference position A (figure 2.2a), then the layer stacked on top will be in position B if the centres of the particles of the layer are located above the interstitial sites in layer A.

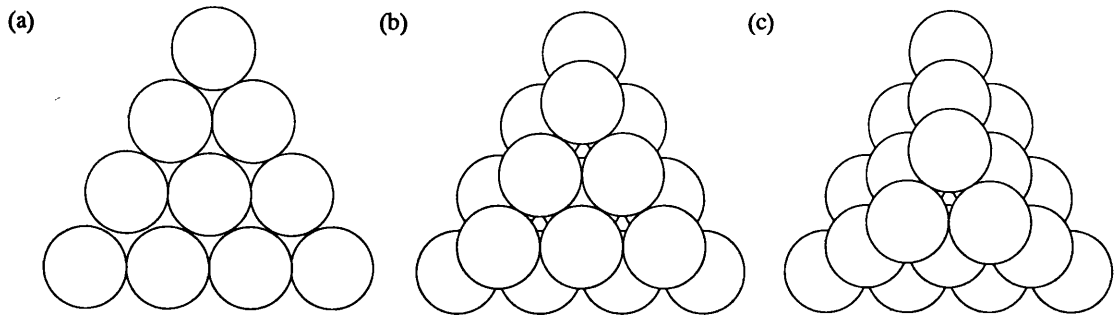

Figure 2.2. The stacking of hexagonal layers of hard spheres. (a) The reference layer A, (b) Layers A and B and (c) Layers A, B and C.

This corresponds to a lateral translation $(\boldsymbol{a} + 2\boldsymbol{b}) / 3$ of B relative to A, where $\boldsymbol{a}$ and $\boldsymbol{b}$ are hexagonal lattice vectors in the plane of the layers. The next layer in the stacking sequence will be in position C, if the particles of the layer are centred above the interstitial sites in layer B. This position corresponds to a lateral translation of $(2\boldsymbol{a} + \boldsymbol{b}) / 3$ of C, relative to A. The stacking sequence ABABAB... corresponds to a hcp structure, whereas the sequence ABCABC... corresponds to the fcc structure.

Initially, the equilibrium structure of the hard sphere crystal was generally assumed to be fcc. However several calculations[57,58,59] have indicated that the difference in free energy between the fcc and hcp structures is very small, no more than $2 \times 10^{-3} k_B T$, per particle. Hence, long-lived non-equilibrium states may easily be achieved. Recent computer simulations by Woodcock,

suggest that the fcc phase is favoured over the hcp phase, by a tiny but significant entropy difference.[60] Because this difference is so small, a high level of numerical accuracy was required and Woodcock found that fcc is more stable than hcp by only $5 \times 10^{-3} k_B T$, per particle, with a 20% uncertainty.[60] Woodcock proposed that the equilibrium hard sphere structure is fcc, although the free energies of structures with faulted stacking have not yet been determined. The small difference in energies between the fcc and hcp structures means that stacking faults readily occur. The local environment of the particles is very similar in both structures, as the first two shells of neighbouring particles are identical. Differences only occur in the third and successive neighbours. Both structures have the same density with a packing fraction of 74%.[18]

Pusey and co-workers found experimentally, that there appears to be a correlation between the structure and the rate at which the crystals have grown.[56] These authors noted that provided adjacent layers n and $n+1$ have different positions, close packing can be achieved. They also argued that for hard spheres, there is no reason to expect much 'communication' between the layers n and $n+2$.[56] Hence, structures may be formed with a degree of 'randomness' in the stacking, providing sequences such as ...ABCABCACB... The probability that the layers n and $n+2$ have different positions, can be defined by the stacking probability α, where $\alpha = 1$ corresponds to fcc, $\alpha = 0$ to hcp and $\alpha = 0.5$ to a completely random stacked close-packed (rcp) structure.[56]

In a sample, with a volume fraction $\phi = 0.535$, in which crystallisation was complete after 1 hour, Pusey and co-workers found crystals with almost completely random stacking ($\alpha = 0.5$). More dilute samples were then prepared,

in which crystal formation took up to several weeks. The colloidal crystals grown more slowly, while still containing many stacking faults, showed a tendency towards a fcc sequence of layers ($\alpha > 0.5$). The longer crystallisation took to complete, the closer the value of α was to 1. Pusey *et al.* suggested that, if the colloidal particles are assumed to be hard spheres, fcc could be the true equilibrium crystal structure but that, because of the small differences in the free energies of this and other possible structures, non-equilibrium states are easily formed.[56] However, they also noted that a small degree of polydispersity, or a slight deviation of the interparticle potential from the hard sphere form, could result in the fcc structure being favoured.

More recently, Verhaegh and co-workers investigated the structure of crystals of rhodamine labelled silica spheres, using fluorescence confocal scanning laser microscopy (CSLM).[61] The confocal optics allowed individual hexagonal layers of particles to be resolved in turbid samples. The layers were imaged one at a time and were identified as either A, B or C. This provided a direct measurement of the stacking probability α and the average value was calculated to be $\alpha = 0.4 \pm 0.2$. The large uncertainty, was a consequence of the poor statistics related to this method of studying crystal structures. The authors noted that random close stacking of the planes was found by direct observation.

Subsequently, Elliot *et al.* studied the structure of colloidal crystals, of sterically stabilised poly(methyl methacrylate) spheres, dispersed in an index-matching mixture of decalin and tetralin.[62] Images of polycrystalline samples were studied, by means of conventional phase-contrast optical microscopy. Elliot and co-workers found that some crystallites have facets in the focal plane, which display sequences of irregularly kinked lines. These authors related the number

of kinks, per unit length, to the stacking sequence. This gave an alternative, statistically more accurate method, for the direct determination of α. For crystals nucleating from a metastable fluid, with a volume fraction $\phi = 0.529$, a value of $\alpha = 0.60 \pm 0.07$ was found. This result is in agreement with the scattering results of Pusey *et al.*[56]

A study of colloidal crystallisation, under time-averaged zero gravity, has been reported by Bartlett and co-workers.[52] Using a simple experimental technique the effects of gravity were minimised, by the continuous slow rotation of the samples, at the rate of one revolution per day (see section 2.4.3 for further details). It was found that, in one-component suspensions of PMMA particles, the rate of crystallisation was normally greater than the rate of sedimentation. In this case the equilibrium phase behaviour can be determined reasonably accurately, under conditions of normal gravity.[52] In systems where the rate of crystal nucleation and growth was slower than the rate of gravitational settling, the behaviour observed on standing was highly non-equilibrium. Hence, shear induced distortion of the suspension microstate can give rise to non-equilibrium phases.[52]

Recently, the effects of gravity were eliminated by performing experiments in conditions of microgravity, aboard the Space Shuttle Columbia.[63] The aim of this study was to observe crystalline phases, grown without the influence of gravity, to determine whether either the convection or the viscous stresses of settling significantly change the crystallisation process. As mentioned earlier, colloidal crystals grown in normal gravity, with volume fractions just above $\phi_m = 0.537$, have a rcp structure with a tendency towards fcc ($\alpha > 0.5$).[56] However, a sample, which formed coexisting crystal and fluid phases under

normal gravity, was redispersed and allowed to reach equilibrium in microgravity conditions. Crystallisation occurred and the structure was found to be almost pure rcp. There was no trace of the fcc structure, found in colloidal crystals formed on Earth. This suggests that the tendency towards fcc found in normal gravity, could be a result of gravity induced stresses. However, in contrast to the ground based experiments, in which the crystals were small and compact, the microgravity crystals were larger and exhibited previously undetected dendritic growth.[63] Hence, while the rcp structure formed in microgravity conditions could be the true equilibrium structure, it could also be the result of non-equilibrium (dendritic) growth.

The local environment of the particles is very similar in both the fcc and hcp structures, as the first two shells of neighbouring particles are identical. Differences only occur in the third and successive neighbours. Both structures have the same maximum packing fraction ($\phi = 0.7405$).[26] These structures also have very similar equations of state.[64] The calculation of the relative stability, of the fcc and hcp phases, is a long standing problem in statistical physics. The difficulty is due to the very similar free energies of both structures. Calculations [65,66] and simulations[67-70] have yet to find a significant free energy difference between the two structures. Recently, Frenkel and Ladd used a (Einstein crystal) Monte Carlo simulation approach, to determine the free energy difference between fcc and hcp hard sphere solids, at volume fractions close to melting.[57] These authors found the Helmholtz free energy difference to be not significantly different from zero: $-0.001 \leq \Delta F \leq 0.002$. As was mentioned earlier, Woodcock recently investigated the relative stability of the fcc and hcp structures.[60,58] The single occupancy cell method, introduced by Hoover and Ree, was applied to calculate the free

energies of both the fcc and hcp crystal structures, via molecular dynamics (MD) simulations. Woodcock found a small difference in the reduced Gibbs free energy (in favour of fcc), which is equivalent to a difference in the reduced Helmholtz free energy of $\Delta F \equiv (F_{hcp} - F_{fcc}) / RT = 0.005(1)$, at the melting density. R is the gas constant, T is the absolute temperature and the number in parentheses is the estimated error in the last digit.

More recently, Bolhuis and co-workers noted that Woodcock's free energy difference is incompatible with the result of Frenkel and Ladd. These authors calculated the free energy difference between the fcc and hcp structures, both at the melting density and at close packing, using two different methods.[59] In simulations using the 'Einstein-crystal' method, the free energy difference at melting was found to be (in favour of fcc) $\Delta F = 0.00087(20)$ and at close packing $\Delta F = 0.00094(30)$. In simulations using a new 'multi-hamiltonian' method, the free energy difference near melting was $\Delta F = 0.00085(10)$ and $\Delta F = 0.0011(2)$ at close packing (in favour of fcc). Bolhuis *et al.* observed that the free energy differences, obtained using the two different methods, are essentially the same.

Subsequently, Woodcock published new free energy data (favouring the fcc structure), determined using the same method.[59] The free energy difference between the fcc and hcp structures was found to be $\Delta F = 0.0026 \pm 0.001$ at close packing. At melting, a value of $\Delta F = 0.0023(10)$ was obtained. Woodcock noted that although a quantitative difference remains, between his results and those of obtained using other methods, all the results predict that the fcc phase is more stable. Woodcock also determined preliminary results for a hybrid $(\text{-ABCAB-})_n$ structure. The results indicated that the hybrid structure is of intermediate stability, between the fcc and hcp structures.[58]

2.4. Binary Mixtures

2.4.1. Introduction

As mentioned previously, one-component assemblies of essentially hard spherical colloids have been studied in some detail. Initial experiments established the phase behaviour[8], particle dynamics[49], crystallisation[49] and glass formation.[5] However, less is known about the more complex thermodynamic and structural properties, of two-component mixtures of large (A) colloidal hard spheres and smaller (B) spheres. In comparison with a one-component system, a binary mixture of colloids has two additional variables to consider. First, the size ratio

$$\alpha = R_B / R_A, \tag{2.3}$$

where R_A and R_B are the diameters of the large and small spheres respectively, so that $\alpha \leq 1$. Since colloidal hard spheres can be prepared with a range of sizes, binary suspensions of almost any size ratio can be studied.[7] Secondly, the number ratio N_B / N_A, which corresponds to the proportion of A and B particles in the system. Hence, in the study of binary mixtures, a large parameter space must be covered.

Binary mixtures exhibit a much wider variety of phase behaviour than single component systems. In the fluid phase, colloidal A and B spheres are expected to be completely miscible if $\alpha > 0.3$. There are several possible solid phases: pure crystals of A or B, ordered colloidal alloys (superlattices) consisting

of interpenetrating lattices of each species, substitutional crystals in which the two species are distributed on a common lattice and binary glasses.

2.4.2. Superlattice Structures

It is somewhat surprising, that the first examples of colloidal crystals with superlattice structures were found by Sanders, in naturally occurring gem opal.[71] Common opal consists of a solidified array of similarly sized colloidal silica spheres, probably formed in an aqueous environment.[71] Since the lattice spacing is comparable to the wavelength of light, Bragg diffraction is responsible for their colourful appearance. The crystal structure is generally random stacked close-packed. However, in an electron microscopy study of a sample of Brazilian opal, Murray and Sanders observed crystalline arrangements of silica spheres, of two different sizes, R_A = 181 nm and R_B = 105 nm. This corresponds to a size ratio of $\alpha = 0.58$.[72,73] Two superlattice structures were identified, AB_2 and AB_{13}. The AB_2 structure consists of layers of hexagonally packed large A particles, stacked vertically, with the smaller B particles occupying the trigonal prismatic cavities between the A layers. The structure is illustrated in figure 2.3, with the unit cell shown in bold.

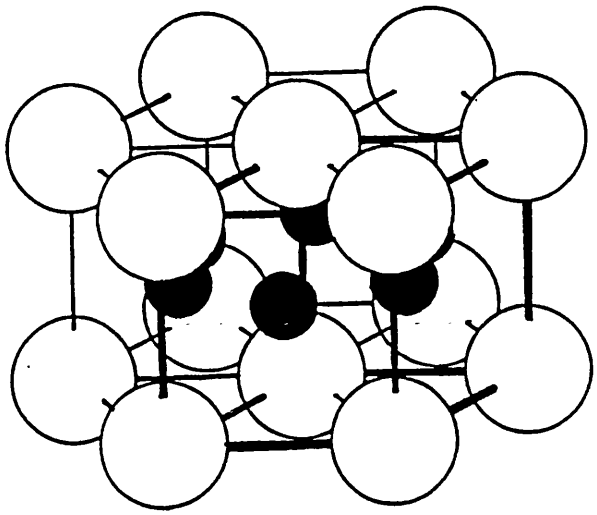

Figure 2.3. The AB_2 superlattice structure. Layers of hexagonally packed large A particles, are stacked vertically and interspersed with hexagonal layers of smaller B particles. From Yoshimura and Hachisu.[89]

The observed AB_2 structure is analogous to the structure found in a large number of borides and silicides, such as AlB_2 and $ErSi_2$. The AB_{13} structure is rather more complex and the full unit cell consists of 104 small spheres and 8 large spheres. The structure is constructed from a simple cubic lattice of large A particles with, at the cube centres of the lattice, a small B particle surrounded by twelve other small particles, forming a perfect icosahedron (shown in figure 2.4).

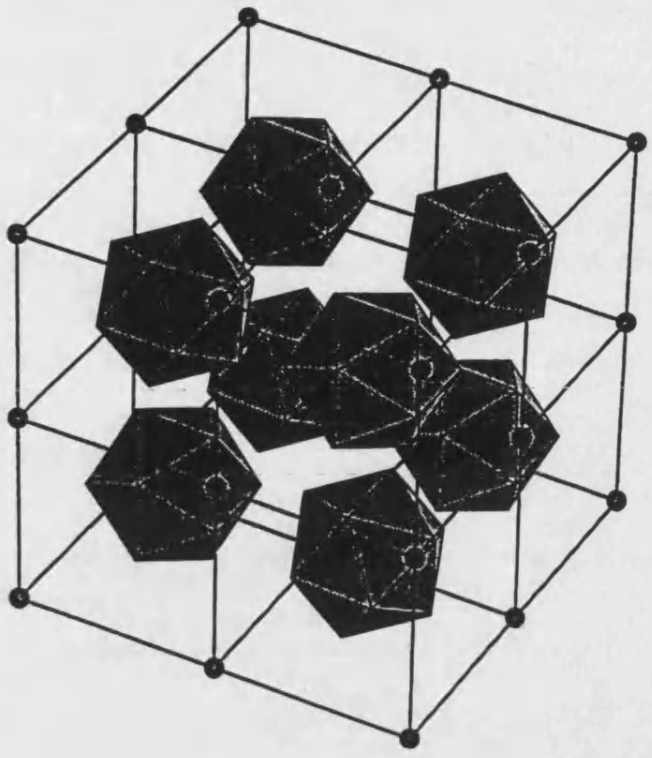

Figure 2.4. The AB_{13} superlattice structure.[74] The large A spheres are located at the corners of the face centred cubic unit cell, with the smaller B spheres at the vertices and centres of the shaded icosahedra. From Bartlett and van Megen.[74]

The full unit cell contains eight subcells and the icosahedra in adjacent subcells are rotated by 90^0 relative to each other. Atomic analogues of the AB_{13} structure include $NaZn_{13}$ and UBe_{13} among others.[74]

Murray and Sanders explained the formation of these complex superlattice structures, in binary hard sphere mixtures, on the basis of simple geometric packing arguments.[72,73] For the AB_{13} structure, this explanation required that the central small sphere in each icosahedron was shrunk by 9.8%, so that the small spheres are all in contact. These authors then argued that, at $\alpha = 0.58$, both the AB_2 and AB_{13} (with the slight deformation of the unit cell) structures when fully compressed have a total volume fraction ($\phi_A + \phi_B$), which is

higher than the volume fraction of a fully compressed close-packed crystal of identical hard spheres ($\phi = 0.7405$). At the lower concentrations, at which crystals are first formed ($\phi_A + \phi_B \sim 0.55$), the superlattice structures will have greater free volume contributions to their entropy, than the one-component crystals of pure A and pure B. Hence, Murray and Sanders determined, that the AB_2 and AB_{13} superlattice structures are more likely to form at $\alpha = 0.58$, than phase separated close-packed crystals of pure A and pure B.[73]

Subsequently, Hachisu and Yoshimura studied the formation of crystals, with superlattice structures, in binary mixtures of charge stabilised polystyrene spheres.[75] The crystals were studied directly, by optical microscopy and at least five different superlattice structures, including AB_2 and AB_{13} were identified. Effective interaction diameters were estimated, so that the results could be interpreted in terms of the packing of effective hard spheres. The samples were prepared using the following method. Initially, a binary colloidal glass was prepared in a sample cell, which could be viewed directly by an optical microscope. The sample was then diluted to a point where significant Brownian motion was observed, but the interparticle interaction remained sufficiently strong for crystallisation to occur. The sample was left undisturbed and crystals were observed to form over several days. The crystal structure was then studied using the microscope. Several binary mixtures, with an excess of small particles, were studied at a volume fraction $\phi_A + \phi_B \approx 0.1$. The high turbidity of the samples restricted observations of the crystals, to areas in close proximity to the cell walls, where surface effects could be important. Nonetheless, five different superlattice structures were observed. Effective interaction diameters were estimated, so that the results could be interpreted in terms of the packing of

effective hard spheres. These interaction diameters were between 50 and 100% greater than the diameters of the core polystyrene spheres, reflecting the long ranged nature of the screened Coulombic repulsion. AB_2 and AB_{13} phases were identified with the same structure as those found in opals, at similar size ratios, by Murray and Sanders. As mentioned earlier, atomic analogues of the AB_2 and AB_{13} structures include AlB_2 and $NaZn_{13}$ respectively. Hachisu and Yoshimura also identified three other superlattice structures. A second AB_2 phase was found, with atomic analogue $MgCu_2$. An AB_4 phase was found, with no known atomic analogue and an AB_5 phase with atomic analogue $CaCu_5$ was also identified. The range of effective size ratios, at which each structure was observed was as follows: AB_2 (AlB_2), $\alpha = 0.50 - 0.61$; AB_{13} ($NaZn_{13}$), $\alpha = 0.56 - 0.63$; AB_2 ($MgCu_2$), $\alpha = 0.77 - 0.84$; AB_4, $\alpha = 0.62$, AB_5, $\alpha = 0.72 - 0.75$.[75]

2.4.3. Phase Behaviour of Binary Mixtures

In neither of these important studies was the phase behaviour, nor the interparticle interaction, well-characterised. However, more recently Bartlett *et al.* have reported a detailed study, of the phase behaviour and structure of binary mixtures of colloidal hard spheres, with a size ratio $\alpha = 0.62 \pm 0.01$.[10] The particles consisted of PMMA cores, sterically stabilised by a thin layer of poly(12-hydroxystearic acid). Suspensions were prepared, using a near index matching mixture of decalin and carbon disulphide. As mentioned earlier, this PMMA / PHSA and decalin / CS_2 system is a well-characterised 'model' colloidal system. It is now generally accepted, that the interparticle potential is steep and repulsive and closely approximated by that of hard spheres.[5] The

particles used consisted of large A spheres of radius 321 ± 3nm and smaller B spheres of radius 199 ± 3nm.[10] The polydispersity of both, measured by dynamic light scattering and transmission electron microscopy, was found to be in the range 0.04 - 0.05. Thirty-five samples were prepared with total volume fractions ($\phi_A + \phi_B$) between 0.48 and 0.62, where crystallisation was expected to occur, at some fifteen different number ratios. As with a one-component system, crystallisation appeared to be homogeneously nucleated throughout the sample. The crystal structures were determined by 'powder light crystallography'. Also, several dried samples of the solid phase were studied, by scanning electron microscopy.

In these binary mixtures, Bartlett and co-workers found that when crystallisation occurred, it was generally much slower than in a single component system at the same volume fraction.[10] In a single component system, crystallisation within the phase coexistence region is often complete within hours or days of mixing, whereas in the binary mixtures crystallisation took weeks or months to complete. If the binary mixtures were left undisturbed, after vigorous agitation, the slow rate of crystallisation allowed gravitational settling to dominate the crystallisation process. As a result, dense, amorphous, sediments often formed. In order to observe the equilibrium phase behaviour, the rate of gravitational settling must be sufficiently low, in comparison with the crystal nucleation and growth rates, to allow crystallites to form and separate from any coexisting fluid, before significant sedimentation can occur. These authors overcame this difficulty, by using a simple experimental technique, that allowed conditions of effective zero gravity to be achieved, which greatly reduced the effects of sedimentation.[52] The influence of gravity was minimised by the

continuous slow rotation of the samples in the vertical plane, at a rate of one revolution per day. Hence, the sedimentation velocity, averaged over one rotation, of a particle relative to the sample cell, was zero. In effect, the samples were subject to conditions of time-averaged zero gravity. The shear forces, which arise due to the flows induced by the slow rotation of the cell, appeared to be sufficiently small that the Brownian motion and crystallisation of the particles was virtually unaffected.[12] Occasionally, the samples were removed from the rotator and studied, after which they were replaced.

The results of Bartlett *et al.* have recently been summarised by Eldridge and co-workers.[76] These authors used a computer simulation approach, to determine the phase diagram of a binary mixture of hard spheres, with size ratio 0.62. The phase diagram obtained is shown in figure 2.5. The samples prepared experimentally, by Bartlett *et al.* at $\alpha = 0.62$, are plotted on the diagram. If the liquid, in which the colloidal particles are suspended, is regarded as an incompressible thermal reservoir, then in terms of its thermodynamic properties, a binary mixture can be treated as a two component, A and B system. If the particles are also assumed to be incompressible, then a colloidal suspension is studied under conditions of constant volume. Hence, the phase diagram of binary mixtures at constant volume is naturally represented, in a form where the axes are ϕ_A and ϕ_B, the partial volume fractions of the components.[77] In this representation, mixtures of constant number ratio (N_B / N_A) lie along straight lines, which radiate from the origin, along which the total volume fraction $\phi_A + \phi_B$ varies. Mixtures with a fixed total volume fraction correspond to straight lines, which intersect the axes at 45°, along which the

number ratio varies.

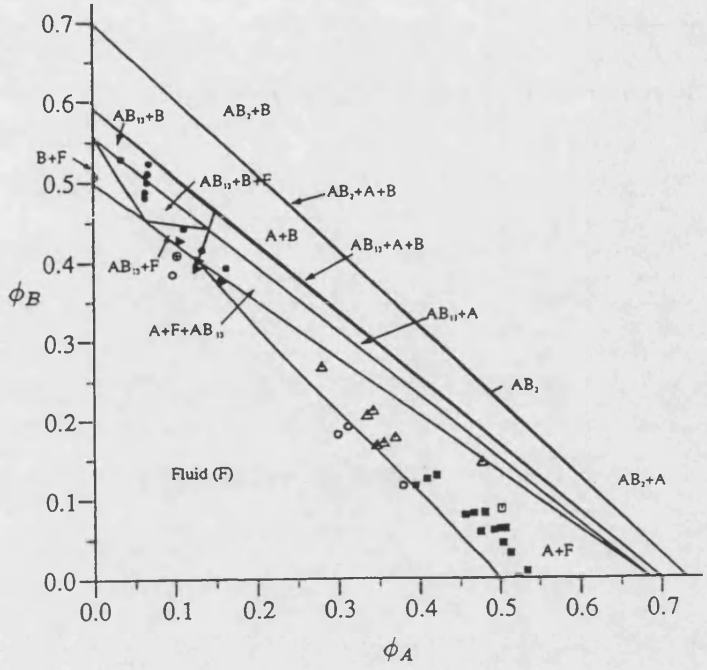

Figure 2.5. From Eldridge *et al.*[76] Experimental samples, of mixtures of hard sphere colloids with a size ratio $\alpha = 0.62$, with observed phases: ○, fluid (F); △, amorphous solid; ●, B; ▶, AB_{13} + B + F; ⊕, B + F; ■, A + F; □, A. The solid lines show the positions of the phase boundaries, calculated by Eldridge and co-workers, for a mixture of hard spheres with a size ratio $\alpha = 0.62$.

As predicted by previous work, a sample consisting only of component A crystallised rapidly, within a few days of mixing.[8] However, in samples where the A particles were the majority species, with a small content of B particles ($0 \leq N_B / N_A \leq 1.2$), the rate of crystallisation slowed significantly. Coexisting fluid and crystalline phases were found at equilibrium. It was observed that the greater the content of B particles in the mixture, the longer crystallisation took to complete. A sample, with a number ratio $N_B / N_A \approx 1.2$, took a month or two to

reach the equilibrium coexistence state. Both fluid and solid phases were analysed. The colloidal crystals were found to be almost pure A, while the coexisting fluid phase was enriched in B. Eldridge *et al.* suggested that the reduction in the rate of crystallisation, that occurs with the increasing B content of the mixture, is associated with the expulsion of greater numbers of B particles from the growing crystals of essentially pure A.[76]

Mixtures rich in B, with A as the minority species, $N_B / N_A \geq 16$, were also composed. After mixing, crystals of almost entirely B particles and coexisting fluid enriched in A particles formed. The rate of crystallisation was found to decrease markedly, with the increasing content of A particles. Hence, at number ratios $N_B / N_A \leq 1$ and $N_B / N_A \geq 16$ the A and B particles appear to be essentially immiscible in the solid phase.

By contrast, samples with number ratios in the range $1.2 \leq N_B / N_A \leq 4$, did not show crystallisation over several months of observation. The samples remained in equilibrium fluid or glassy states.

Possibly the most interesting phase behaviour was found in four mixtures, with number ratios in the range $10 \leq N_B / N_A \leq 16$. The sample with the highest total volume fraction formed crystals, of apparently pure B and coexisting fluid. However, the samples prepared at lower volume fractions were found to contain AB_{13}, B and coexisting fluid. A sample, with number ratio $N_B / N_A = 12.9$ and volume fraction $\phi = 0.533$, was found to contain crystallites after one day. Bartlett and co-workers identified the structure as random stacked close-packed B, from an analysis of the powder diffraction patterns. However, after three months an additional crystal phase was formed, with a diffraction pattern consistent with the AB_{13} structure. Subsequently, the amount of the AB_{13} phase

in the sample reached a peak after about six months, after which time the concentration slowly decreased. These authors suggested that, at this size ratio, the AB_{13} phase is metastable with respect to the coexisting B crystal and fluid. Hence, it is likely that kinetic factors are also important in determining which phases are found experimentally.

Bartlett and co-workers also investigated the phase behaviour and structural properties of binary hard sphere mixtures, with a size ratio $\alpha = 0.58$.[11] It was at this size ratio that Sanders and Murray observed the first colloidal superlattice structures in opal.[71] In their study, Bartlett *et al.* used particles with radii $R_A = 321 \pm 3$ nm and $R_B = 186 \pm 3$ nm. The polydispersity of both species was determined, by dynamic light scattering and transmission electron microscopy, to be 0.04 - 0.05. Twenty-five samples were prepared at various number ratios, at total volume fractions in the range $0.50 \leq \phi_A + \phi_B \leq 0.55$. Again, the effects of gravity were minimised by the continuous slow rotation of the particles, at a rate of one revolution per day. The solid phases were studied by dynamic light scattering. Several dried samples were also studied by scanning electron microscopy. The samples are represented in the phase diagram in figure 2.6.

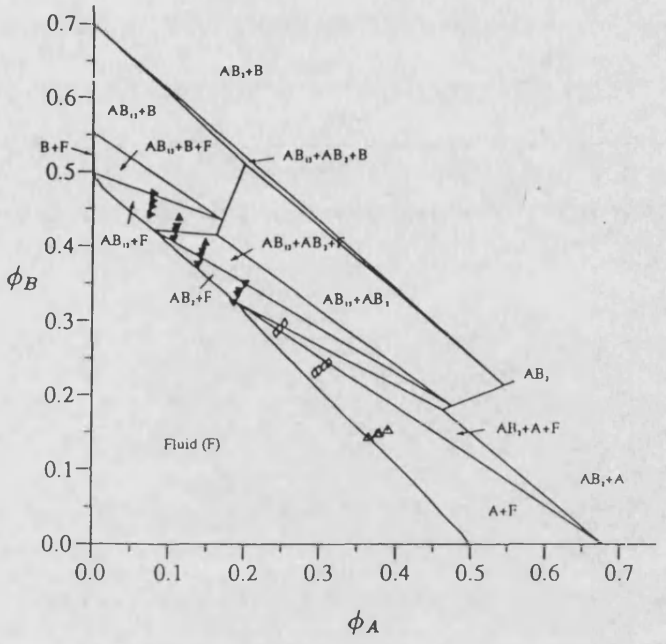

Figure 2.6. From Eldridge *et al.*[76] Mixtures of hard sphere colloids, prepared by Bartlett *et al.* with a size ratio $\alpha = 0.58$, with observed phases: ▶, AB_{13} + B + F; ▼, AB_{13} + F; ▲, AB_{13}; ◇, AB_2 + F; Δ, amorphous solid.[11] The solid lines show the positions of the phase boundaries, calculated by Eldridge and co-workers, for a mixture of hard spheres with a size ratio $\alpha = 0.58$.

As mixtures rich in A ($N_B / N_A \leq 1.2$) were expected to exhibit much the same behaviour as was found at $\alpha = 0.62$[10] (crystals of A and coexisting fluid), samples were not prepared in this region of the phase diagram. However, samples were prepared with $N_B / N_A = 2$. After several months, no crystallisation was observed and the samples remained amorphous. It was somewhat surprising that crystals of AB_2 did not form in suspensions with compositions corresponding to the AB_2 stoichiometry. However, in samples with $N_B / N_A = 4$ and $N_B / N_A = 6$ and $\phi_A + \phi_B$ between 0.52 and 0.557, coexisting crystal and fluid phases were observed, about five weeks after preparation. The crystal structure

was identified as AB_2 and the slow crystallisation process took up to three months to complete. AB_2 was found to form fastest from samples of composition $N_B / N_A = 6$. All the samples prepared at these compositions ($N_B / N_A = 4$ and $N_B / N_A = 6$) formed coexisting AB_2 and fluid, with the proportion of each phase varying with the total volume fraction of the sample.

The mixture with the highest total volume fraction, at both $N_B / N_A = 14$ and $N_B / N_A = 20$, appeared to form a solid phase composed entirely of AB_{13}. However, it is expected that it also contained some solid B, in either an amorphous or crystalline phase. The other samples prepared with compositions $N_B / N_A = 14$ and 20, together with all those at $N_B / N_A = 9$, formed coexisting crystals of AB_{13} and fluid. In comparison with the rate of crystallisation of AB_2, the formation of AB_{13} was rapid. In a suspension with $N_B / N_A = 20$ and $\phi_A + \phi_B = 0.538$, crystals of AB_{13} were visible within a few days of mixing and the crystallisation process was complete within three weeks. Also, in samples prepared at $N_B / N_A = 30$, coexisting crystals of AB_{13} and fluid were again observed. AB_{13} appears when it's not expected, while AB_2 seems to be reluctant to form.[76]

Bartlett and Ottewill reported a study, where colloidal PMMA particles were studied by a combination of small angle neutron scattering (SANS) and light scattering measurements.[16] Binary mixtures with a size ratio of 0.31 were prepared, by combining the large A particles, with $d = 315$ nm, with smaller B particles, with $d = 97$ nm, These authors noted that at this size ratio, the B particles are sufficiently small that they could occupy the interstitial sites of a crystal of large A spheres. In principle, a range of crystal structures could be formed, by either complete or partial occupancy of the vacant octahedral and

tetrahedral sites in an assembly of large spheres.[16] Full occupancy of the octahedral sites gives a crystal phase, with a structure equivalent to that found in NaCl. Murray and Sanders predicted a NaCl type structure at this size ratio, on the basis of simple packing arguments.[73] Bartlett and Ottewill emphasised the small sphere microstructure, by means of a contrast matching method. While the large spheres were fully hydrogenated, the small spheres consisted of deuterated cores and hydrogenated stabiliser layers. The particles were suspended in a mixture of cis-h_{18}-decalin and d_{18}-octane. The neutron scattering length density of the mixture was manipulated, by varying the relative proportions of the hydrogenated and deuterated hydrocarbons. Binary mixtures were investigated, with $N_B / N_A = 4$ and $\phi_A + \phi_B = 0.61$. The partial volume fractions were chosen so that the sample was within the fluid-solid phase coexistence region. Crystallisation of the small spheres was suppressed by the polydispersity, which was $\sigma = 0.13$. Five mixtures were studied at different suspension medium contrasts and after a day or so small crystals were visible, throughout each sample. SANS measurements were made on all the samples. These authors concluded that in each sample, the large spheres formed a close packed crystal, with a structure similar to that of the pure component crystals identified in binary mixtures, of comparably sized particles. The small particles are thought to be excluded from the large sphere crystal and instead form a coexisting fluid phase. No evidence for interstitial crystals was found.

In a subsequent study, Bartlett and Ottewill extended this work, to investigate the depletion mechanism in binary mixtures with $\alpha = 0.31$.[17] Five new mixtures were prepared, using the same colloidal suspensions as were used previously. The mixtures had number ratios in the range $1.4 \leq N_B / N_A \leq 5.7$. The

partial volume fraction of the large spheres was $\phi_A \sim 0.45$, while that of the small spheres was in the range $0.017 \leq \phi_B \leq 0.068$. The volume fractions of the large spheres, was chosen to be below the freezing transition, in order to ensure that the samples remained in the fluid state. The mixtures were studied using SANS and the small sphere microstructure was emphasised using the contrast matching technique. Evidence was found for the clustering of the large spheres, which supports the existence of a depletion force in an asymmetrically sized mixture of colloidal particles. No evidence for a fluid-fluid phase separation was found at this size ratio. (see chapter 6 for further details).

CHAPTER 3

3. SYNTHESIS

3.1. Introduction

Stable dispersions of micron and submicron polymer particles are often referred to as polymer colloids.[78] Such systems can be prepared using various particle polymerisation methods. The colloidal particles produced can be dispersed in either aqueous or hydrocarbon media. Both aqueous and non-aqueous polymer colloids are widely used commercially. Emulsion polymerisation[79] has been used to synthesise aqueous dispersions of polymer colloids since the late 1920s, while the first non-aqueous polymer colloids were synthesised in 1975.[6] As a result, knowledge of the behaviour of aqueous polymer colloids is further advanced, than that of polymer particles dispersed in non-aqueous media. Aqueous dispersions of well-characterised monodisperse particles have been available for use as 'model' colloidal systems over the last thirty years. During this time the study of these systems has greatly increased our knowledge, of the behaviour of aqueous polymer colloids. Less attention has been given to dispersions in non-aqueous media, although knowledge of the behaviour of such dispersions has steadily increased over recent years. Well-characterised dispersions of nearly monodisperse particles, in non-aqueous media, are now readily available. Thus, the behaviour of polymer particles dispersed in non-aqueous media is a research topic of considerable interest. Also, non-aqueous polymer colloids form an important proportion, of colloidal systems produced on an industrial scale.[78] These systems are key constituents of solvent based coatings, ion exchange resins and liquid chromatography columns. More

recently, applications in the biomedical field have been devised.

3.1.1. Dispersion Polymerisation in Non-Aqueous Media

Non-aqueous polymer colloids can be prepared, using a method known as dispersion polymerisation. The dispersion polymerisation process was originally developed, in order to synthesise colloidal polymer particles in non-polar liquids, such as aliphatic hydrocarbons.[6] The technique was developed by researchers at ICI Paints.[80] If a monomer is polymerised, which is soluble in the dispersion medium, then two situations may be considered. If the polymer formed is soluble in the dispersion medium, then the reaction is a solution polymerisation. However, if the polymer formed is insoluble in the dispersion medium, the reaction is known as a precipitation polymerisation. If an amphipathic block or graft copolymer is present, during the precipitation reaction, then well-defined colloidal particles are formed instead of an ill-defined precipitate.[80] This process has become known as non-aqueous dispersion polymerisation.[6] Unlike emulsion polymerisation, the reaction can be carried out using a wide variety of continuous phase dispersion media. Also, stable colloidal particles, with diameters between 0.1 and 15μm, have been prepared.[80] In principle, a range of monomers can be polymerised. However, only a few have been thoroughly investigated, examples of which include methyl methacrylate and styrene.[80] The synthesis of poly(methyl methacrylate) (PMMA) colloidal particles, by dispersion polymerisation, using methyl methacrylate as the monomer, a hydrocarbon dispersion medium and poly(12-hydroxystearic acid) (PHSA) as the stabiliser, has been extensively studied.[80-84] The stable monodisperse particles produced

constitute a well-characterised 'model' colloidal system, which is used in the present work. The system consists of spherical cores of amorphous PMMA, which are sterically stabilised by a graft copolymer consisting of a 'backbone' of methyl methacrylate, covalently linked to the particle surface and 'teeth' of poly(12-hydroxystearic acid) (PHSA) projecting into the dispersion medium.

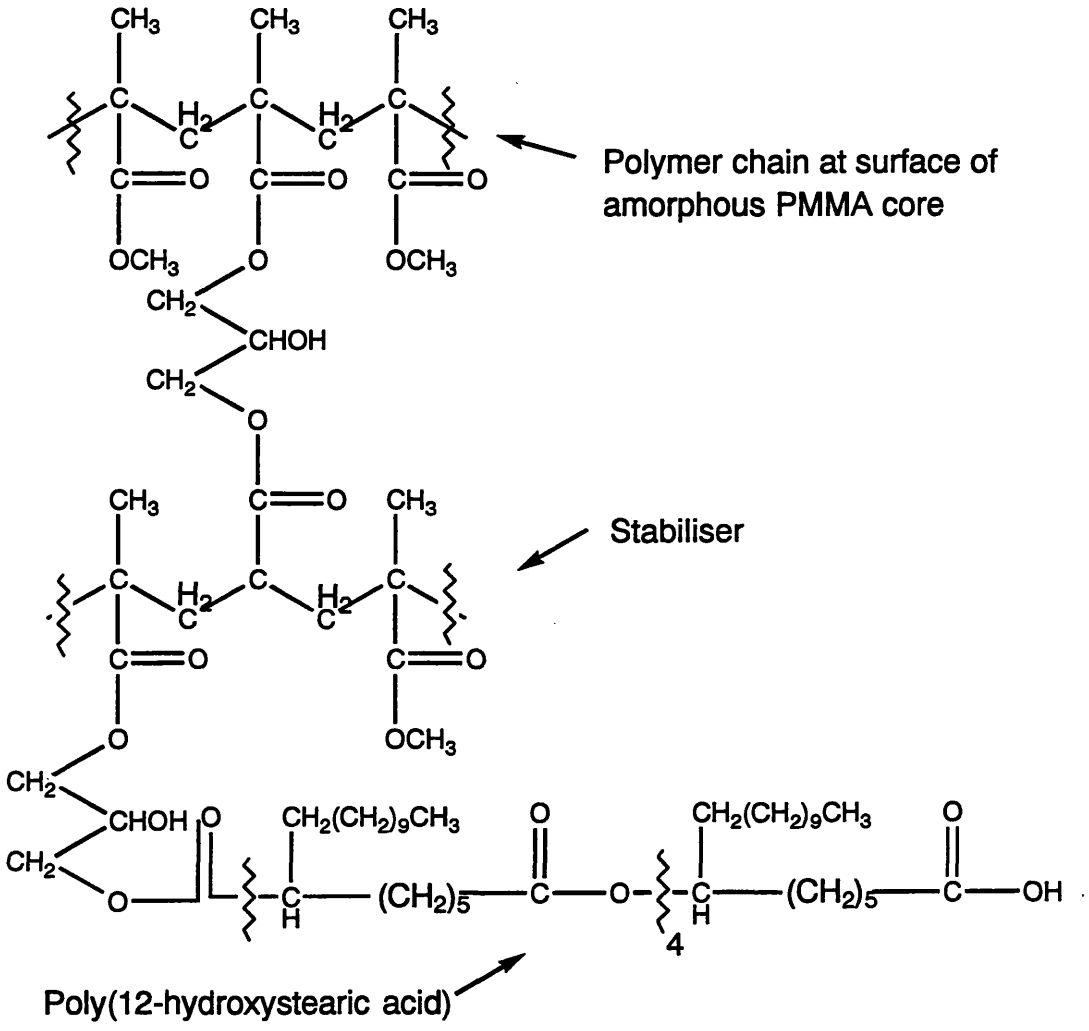

Figure 3.1. Structure of the poly(12-hydroxystearic acid) (PHSA) steric stabiliser, which is covalently linked to the PMMA particle surface.

The behaviour of the PMMA / PHSA system has been thoroughly investigated, in a range of previous studies (reviewed in reference 74). In an important publication, Antl and co-workers studied the effect of varying the initial concentration of methyl methacrylate, used in the dispersion polymerisation, on the size and stability of the latex particles produced. The initial monomer concentration was varied, between 5 and 50% (by weight) and a stabiliser concentration of 5%, by weight of the amount of monomer, was used. The results obtained by these authors are illustrated in figure 3.2.

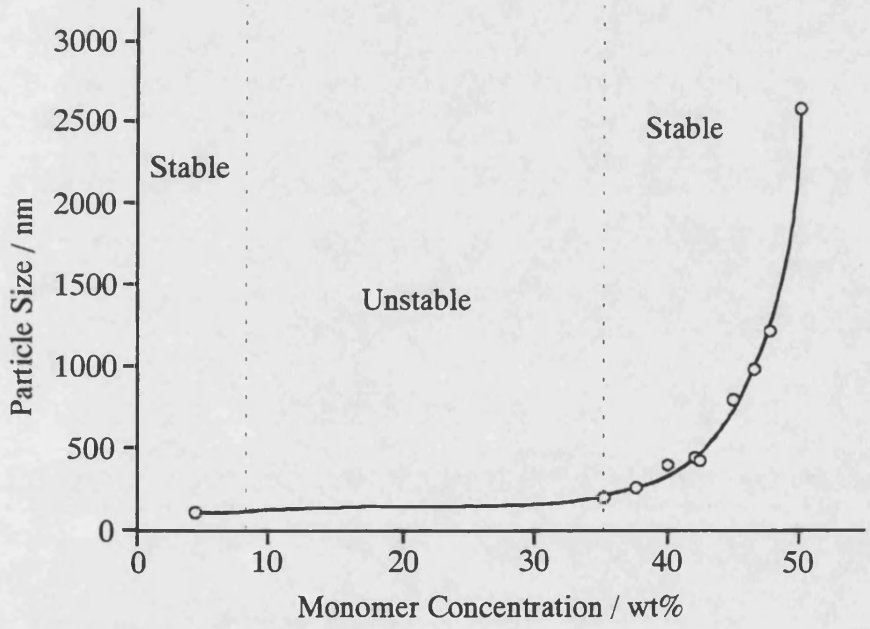

Figure 3.2. From Antl *et al.*[7] Graph of particle size (diameter) vs. monomer concentration, for the colloidal particles produced in dispersion polymerisation reactions. The stabiliser concentration was 5%, by weight of the amount of monomer.

Antl *et al.* observed three distinct regions, within the range of the initial

monomer concentration. Reactions carried out using a monomer concentration in the range 5 to 8.5% produced stable colloidal particles, with an average diameter approaching 80 nm. Analysis by electron microscopy, suggested that these particles were reasonably monodisperse.[7] When the initial monomer concentration was greater than 8.5%, but less than 34%, it was found that, although the dispersion formed was initially stable, coagulation occurred before the reaction was complete. Antl and co-workers observed, that as the initial monomer concentration was increased, from 35 to 50%, the particle size increased from 0.18 to 2.6μm.[7] The polydispersity (eqns. 1.2 and 1.3, chapter 1) of these dispersions was found to be very low. These authors suggested, that the mechanism of particle formation may differ at low and high monomer concentrations, with competition between the two mechanisms resulting in the formation of unstable latices, in the 8.5 - 35% monomer concentration range.[7]

The dramatic increase in the final size of the latex particles, on increasing the initial monomer concentration from 35 to 50%, is somewhat unexpected. If an equal number of particle nuclei are assumed to form, under similar reaction conditions, when the monomer concentration is increased from 35 to 50%, the volume of the particles produced should increase by 43%.[82] However, this corresponds to a change in diameter from 0.18 to 0.20 μm, which is two orders of magnitude smaller than the size increase observed experimentally.[82]

Clearly, increasing the initial concentration of monomer used in the reaction significantly effects the particle formation process. Antl *et al.* proposed that the size of the final particles is closely related to the solvency of the dispersion medium, for the polymer being formed.[7] The changes in solvency that occur, during the dispersion polymerisation, are a key consideration in

interpreting the process. As was mentioned earlier, the polymer formed by this type of reaction is insoluble in the dispersion medium, but is soluble in the monomer. Before the dispersion polymerisation is initiated, the reaction components form a clear homogeneous solution. Decomposition of the initiator produces free radicals, which undergo propagation to begin the polymerisation process. The growing polymer chains that form, are initially well solvated by the monomer. However, as the reaction proceeds and the monomer is polymerised, the concentration of monomer remaining is reduced. As the polymer is soluble only in the monomer, the solvency of the dispersion medium for the polymer decreases, as the reaction progresses. Approximately eight minutes after the reaction is initiated, the solvency of the dispersion medium for the polymer is reduced to the point where the polymer chains become insoluble. Polymer particles are then nucleated. The solvency of the dispersion medium for the stabiliser also decreases, during the reaction, as it too is soluble in the monomer. Hence, the stabiliser absorbs onto the surface of the newly formed nuclei, providing the nuclei with colloidal stability. These nuclei act as light scattering centres, which cause the reaction mixture to become opaque.

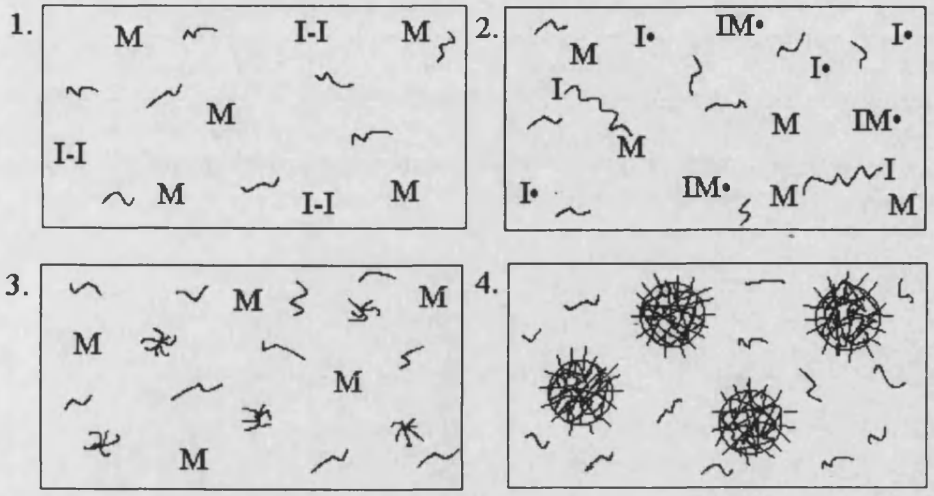

Figure 3.3. Schematic diagram of the dispersion polymerisation process: (1) the homogeneous reaction mixture, (2) the growing polymer chains, (3) the nucleation step and (4) the final latex particles.

Increasing the initial monomer concentration, affects the nucleation process in several ways.[80] First, the size of the initial nuclei produced, is thought to be related to the solvency of the dispersion medium. As the monomer concentration is increased, the greater is the solvency of the dispersion medium for the growing polymer. The better the solvency for the polymer, the longer the polymer chains can grow before nucleation occurs and the larger the final particles produced. Secondly, a reduction in the interfacial tension, causes the particle nuclei to be swollen by the monomer to a greater extent.[86] Also, the steric stabiliser is less efficient, when large amounts of monomer are present in the reaction medium, as the monomer acts as a solvent for the stabiliser. All of these affects are thought to contribute, to an increase in the average final size of the latex particles. However, this explanation does not account for the dramatic size increase observed experimentally, in going from the minimum to the

maximum monomer concentration.[7]

In a model by Morrison, Gilbert and Napper (reviewed in reference 80) coagulation is suggested to be an important part of the nucleation process. In this coagulative nucleation mechanism, it is proposed that the dispersion polymerisation starts with the growth of polymer molecules, which increase in length until the solubility limit is reached. The colloidally unstable entity, formed at this point, is referred to by the authors as a precursor.[80] Once the precursor is formed, several potential events can transpire, leading to the formation of colloidally stable latex particles. For instance, if the precursors collide, homocoagulation will occur with a concomitant increase in particle size. Growth can also result, by propagation of the polymer chain or stabiliser adsorption may take place. Finally, swelling with monomer could occur, with polymerisation then taking place within the particles. The nucleation process is complete, when the growing polymer chains are captured before becoming precursors.[81]

Pathmamanoharan and co-workers have recently reported a study, in which latex particles were prepared following the method of Antl *et al.*[83] The effect of varying the initial monomer concentration, used in the dispersion polymerisation, between 5 and 44% was investigated. These authors found that stable latex particles could be prepared, in the whole concentration range, providing sufficient stabiliser was used.[83] In initial experiments, the minimum stabiliser concentration needed, for the formation of stable monodisperse latex particles, was found to be between 10 and 28%, by the monomer weight, for initial monomer concentrations of 5 and 35%.[83] In these experiments, monodisperse particles, with radii between 40 and 900 nm, were obtained.[83] This is contrary to the results of Antl *et al.*, who found that when the stabiliser

concentration was increased beyond 5%, the polydispersity of the final latex particles (at 50% monomer) increased. Antl and co-workers suggested 5%, as the optimum level of stabiliser, for the nucleation and growth of monodisperse particles.[7]

Pathmamanoharan *et al.* did not find the unstable region, observed by Antl and co-workers. However, when the initial monomer concentration was varied between 8.5 and 34%, these authors found two distinct regions within the initial monomer concentration range. In the monomer range 32 - 44%, the final particle size was observed to increase dramatically, with increasing monomer concentration. In this region the stabiliser concentration was between 10 and 15%. This is similar to what Antl *et al.* found in the 35 - 50% monomer range, using 5% stabiliser throughout. In the 5 - 29% monomer range, Pathmamanoharan and coworkers observed that small particles formed. In this range a high concentration of stabiliser (between 26 and 28%) was required. These authors suggested that the high amount of stabiliser (10%) used in the 32 to 34% region, compared with the 5% used by Antl *et al.* could be a consequence of the short poly(12-hydroxystearic acid) chains present in the stabiliser.[83]

3.2. Experimental Section

3.2.1. Materials

Polymer colloids were prepared by dispersion polymerisation, using the following reagents. The monomer, methyl methacrylate (MMA) was supplied by Aldrich. Before use it was distilled under nitrogen, at low pressure (and at 40°C)

and then stored at 4°C. The methacrylic acid (MA) monomer was obtained from BDH Ltd and was used as received. The radical initiator, azo-bis-isobutyronitrile (AIBN), was purchased from BDH Ltd and before use was recrystallised, at a low temperature, from acetone. The solvents, hexane (Aldrich) and dodecane (Aldrich), were used as received, as was the chain terminator, octyl mercaptan (Fluka) and the base catalyst, diethanolamine (Aldrich). On completion of the synthesis, some latex samples were redispersed in decahydronapthalene (decalin), which was purchased from Aldrich and used as received. Three stabiliser samples were used, of which two consisted of poly(12-hydroxystearic acid) (PHSA) chains, linked to a copolymer backbone of methyl methacrylate and glycidyl methacrylate (GMA). Of these, one was obtained from Bristol University, while the other was synthesised during the present work (as described in section 2.2.6). The third stabiliser was obtained from ICI Paints and was a graft copolymer of PHSA and MMA. All three stabiliser samples were received as a 33% solution, in a mixture of butyl and ethyl acetate. Before use each sample was purified, first by precipitation in ice-cold methanol and then by drying under vacuum at 45°C, to yield a white powder. The powder was dissolved in dodecane to provide a 30wt% solution of the stabiliser, which was used directly in the dispersion polymerisation.

In addition to the MMA, AIBN and octyl mercaptan listed above, the following additional materials were required for the stabiliser synthesis. The PHSA-GMA precursor was obtained from ICI, as a 51wt% solution in acetates and was used as received. Glycidyl methacrylate (GMA) and the solvents, butyl acetate and ethyl acetate, were obtained from Aldrich and used as received.

3.2.2. Preparation of Polymer Latices

Spherical PMMA particles of low polydispersity were prepared in a single-stage dispersion polymerisation of methyl methacrylate, in the presence of an amphipathic stabiliser.[7] When the total mass of the reaction components was 65g, the dispersion polymerisation was carried out in a 250ml round bottomed flask. When the total mass was 650g, a 2-litre flask was used. For some of the 650g preparations, the reaction mixture was stirred using a mechanical anchor-type Teflon stirrer. This was set to rotate at 50rpm and the reactions were carried out under a nitrogen atmosphere.

Initially the monomer, initiator and stabiliser solution were weighed directly into the reaction vessel. Methacrylic acid and octyl mercaptan were then added, followed by the solvents hexane and dodecane (in 2:1 ratio). After stirring, to ensure a homogeneous reaction mixture, the flask was fitted with a vertical condenser and then submerged in an oil bath at 80°C. The reaction mixture was then allowed to reflux, for 2 hours. The 65g preparations were not stirred during this period, as previous work suggests stirring is not necessary for small reaction volumes.[7]

Upon heating, the dispersion polymerisation is initiated by the thermal decomposition of the free radical initiator (AIBN).

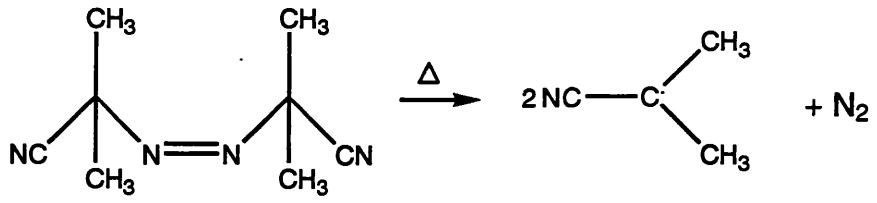

Figure 3.4. Thermal decomposition of the free radical initiator, azo-bis-isobutyronitrile (AIBN).

The initiator readily forms free radicals, because the homolytic cleavage liberates the very stable nitrogen molecule. Poly(methyl methacrylate) (PMMA) is formed in a free radical polymerisation reaction (figure 3.5). Initially the reaction mixture remains transparent, as the PMMA is soluble in the monomer (MMA).

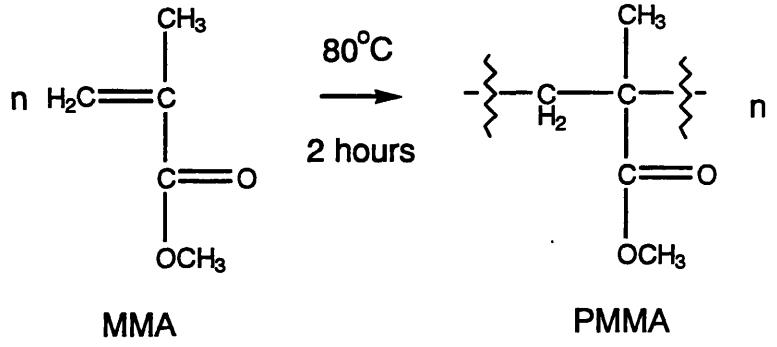

Figure 3.5. The free radical polymerisation of methyl methacrylate (MMA), to form poly(methyl methacrylate) (PMMA).

As the reaction proceeds, the monomer concentration decreases. At some critical molecular weight, the solvency of the reaction mixture is reduced to the extent that the growing polymer chains are no longer soluble. At this point they collapse

into a condensed state, forming polymer nuclei. As the solvency is also decreasing for the stabiliser, which has a PMMA backbone (figure 3.1), it adsorbs onto the surface of the newly formed nuclei. The PHSA 'teeth' of the stabiliser, which are soluble in the aliphatic hydrocarbons, impart colloidal stability to the nuclei. Hence, approximately 8 minutes after initiating the reaction, the formation of the nuclei, which act as light scattering centres, cause the reaction mixture to become opalescent. As was mentioned earlier, once nucleation has occurred, there are several possible events, which can occur, leading to the formation of colloidally stable particles.

The methacrylic acid in the reaction mixture is incorporated into the PMMA chains in a copolymerisation reaction (illustrated in figure 3.6).

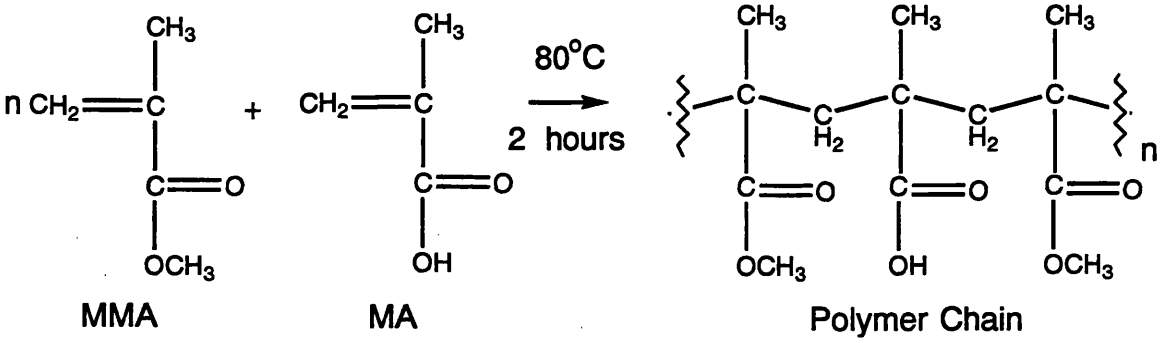

Figure 3.6. Copolymerisation of methyl methacrylate (MMA) and methacrylic acid (MA).

The kinetics of copolymerisation reactions can be described, in terms of the reactivity ratios r_1 and r_2. As the product r_1r_2 approaches zero, there is an increasing tendency towards alternating copolymers. However, as the product approaches 1, there is an increasing tendency towards random copolymers. In the

case of the copolymerisation of MMA and MA, at 60°C, the product r_1r_2 is 0.74, which suggests there will be a tendency towards random copolymerisation.[85]

3.2.3. The Locking Reaction

Whenever the particles were to be used in further studies and before size measurements were made, the 'locking reaction' was carried out. This was an esterification reaction, during which the stabiliser was covalently linked to the particle surface. The procedure is as follows. The condenser was arranged for distillation, in a horizontal position. Dodecane was then weighed into the flask, the amount being equivalent to the mass of hexane used in the polymerisation reaction. The hexane in the solution phase was removed by distillation. Diethanolamine, a base catalyst, was then added in the proportion of 0.2% of the total weight of the mixture. The temperature of the oil bath was raised to 120°C and the condenser returned to the vertical reflux position. The flask was submerged in the oil bath, then the reaction mixture was allowed to reflux overnight.

During the locking stage, the acid groups (arising from the incorporation of methacrylic acid into the growing polymer chain during the dispersion polymerisation) at the particle surface reacted with the epoxide groups on the stabiliser backbone, covalently linking the two.

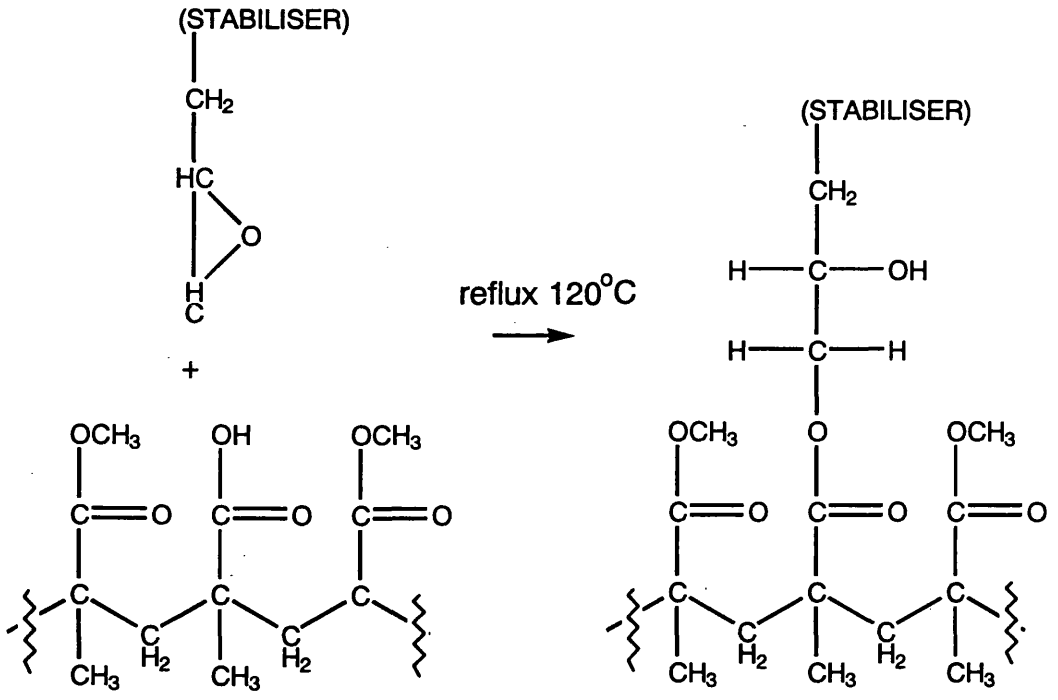

Figure 3.7. The 'locking' reaction.

3.2.4. Latex Purification Procedure

On completion of the locking reaction, the latex was filtered through glass wool into a clean screw-cap bottle. The latex was then purified by repeated centrifugation, at 25 °C. Latices consisting of colloidal particles up to ~500 nm in diameter were centrifuged at 6000 rpm for 1 hour, while those consisting of particles greater than ~500 nm in diameter were centrifuged at 4000 rpm for 1 hour. After centrifuging, the supernatant (containing excess stabiliser in solution) was decanted.[7] Clean dodecane was then added and the latex particles were resuspended, by agitating vigorously for 2 hours. Once redispersed, the particles were again centrifuged and the supernatant replaced with fresh dodecane. This process was repeated seven times. Stock dispersions were prepared, in both

dodecane and decahydronapthalene (decalin). When decalin was used, the centrifuge speeds were increased by 1000rpm, due to the higher density of decalin relative to dodecane.

3.2.5. Particle Characterisation

The size and polydispersity, of the PMMA cores of the colloidal particles, was determined by dynamic (DLS) and static light scattering (SLS) measurements in dilute suspensions. Transmission electron microscopy (TEM) was also used. Before size measurements were carried out, each sample underwent the locking reaction and was cleaned by repeated centrifugation. The characterisation methods used are discussed further in chapter 4.

3.2.6. Stabiliser Synthesis

As was mentioned earlier, the stabiliser used to impart colloidal stability to the amorphous PMMA particles consisted of a copolymer backbone of methyl methacrylate and glycidyl methacrylate, to which poly(12-hydroxystearic acid) was attached. The stabiliser was prepared using the following method, as described by Antl *et al.*[7] The first two stages were not carried out in the present work, as a sample of the PHSA-GMA stabiliser precursor was kindly donated by ICI Paints.

3.2.6.1. Poly(12-Hydroxystearic Acid) Synthesis

Initially, 12-hydroxystearic acid was refluxed at 150°C for two days, in the presence of a methane sulphonic acid catalyst. A condensation polymerisation reaction occurred and poly(12-hydroxystearic acid) (PHSA) was formed, with the elimination of water. The reaction is illustrated in figure 3.8.

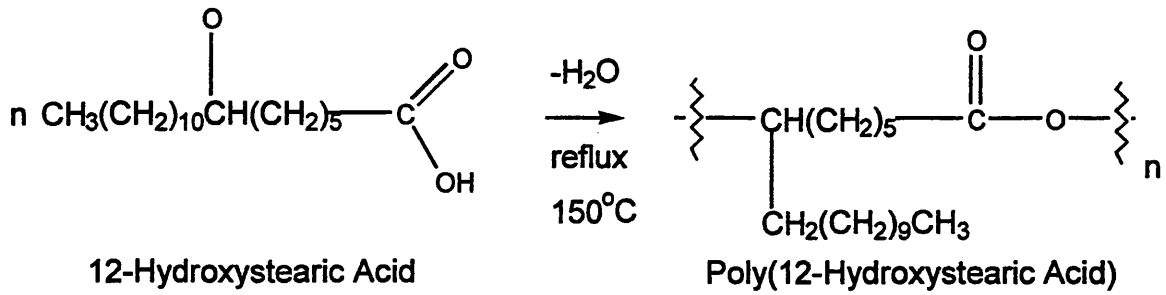

Figure 3.8. The condensation polymerisation reaction.

The reaction conditions are chosen so that the number average degree of polymerisation ($D_p = M_n / M_o$) approaches 5.

3.2.6.2. Stabiliser Precursor Synthesis

Next, poly(12-hydroxystearic acid) underwent a further reflux reaction, with glycidyl methacrylate (GMA), to produce the poly(12-hydroxystearic acid)-glycidyl methacrylate precursor.

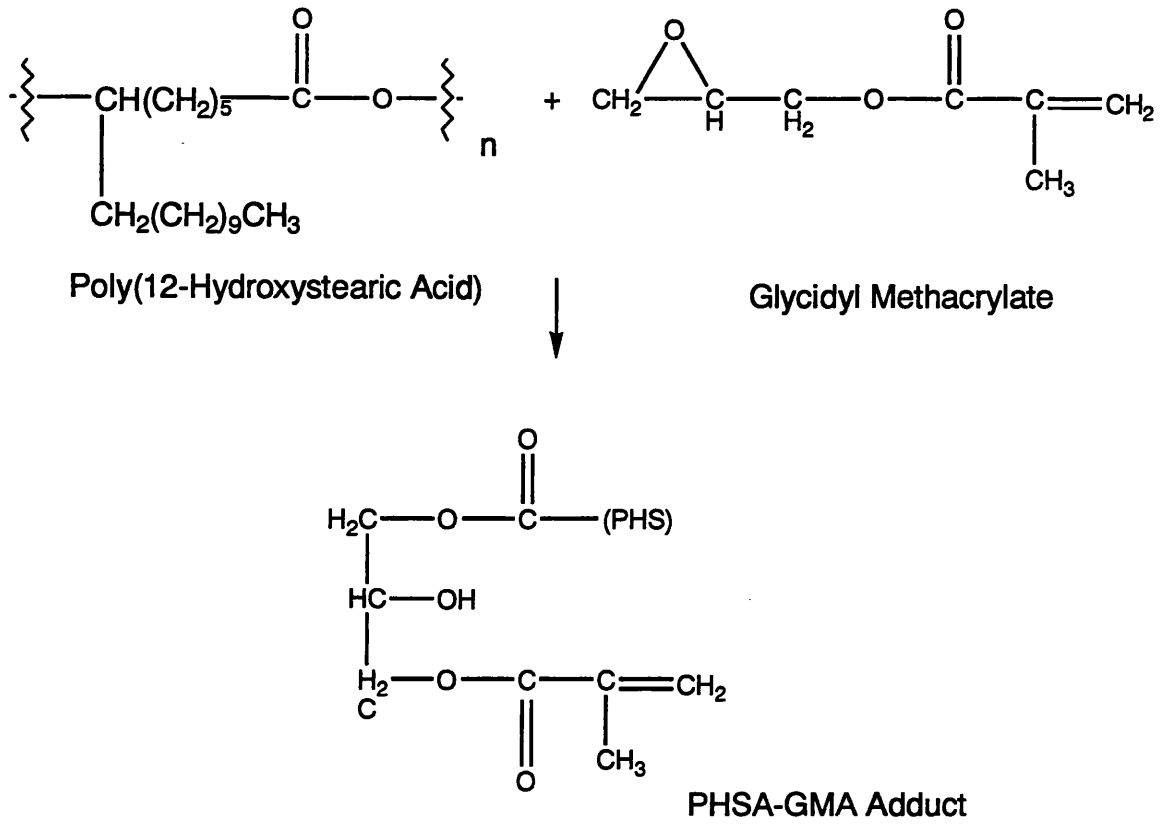

Figure 3.9. The formation of the PHSA-GMA adduct, the stabiliser precursor.

3.2.6.3. The Polymeric Stabiliser

The final stabiliser was prepared, in a copolymerisation of the PHSA-GMA adduct, or macromonomer, with methyl methacrylate and glycidyl methacrylate. A sample of the PHSA-GMA precursor was obtained from ICI Paints. The reaction reagents were used in the quantities shown in table 3.1.

Reactant	Mass Used (g)
Butyl acetate	125.0
Ethyl acetate	250.0
AIBN	0.5
Methyl methacrylate	225.0
Glycidyl methacrylate	25.0
PHSA-GMA precursor	485.0
Octyl mercaptan	0.5
AIBN	1.0

Table 3.1. The reactants used in the stabiliser synthesis.

125.0g of butyl acetate and 250.0g of ethyl acetate were weighed directly into a 2-litre, 6-necked, round bottom flask. 0.5g of the radical initiator (AIBN), which had previously been recrystallised from acetone, was added. The flask was then sealed and fitted with a condenser, arranged for reflux, together with a nitrogen bleed. A mechanical, anchor-type, Teflon stirrer was also fitted. The stirrer was set to 50rpm and the flask was immersed in an oil bath heated to 95°C.

Next, 1.0g of AIBN was added to 225.0g of methyl methacrylate (MMA), in a 1-litre beaker. The MMA had previously been distilled under vacuum, to remove the inhibitor. 25.0g of glycidyl methacrylate (GMA) and 485.0g of the PHSA-GMA precursor solution, was then added to the beaker. The precursor was supplied as a 51.0wt% solution in acetates. Hence, the 485.0g of this solution, contained 250.0g of the PHSA-GMA precursor. Finally, 0.5g of octyl

mercaptan was weighed into the beaker and the mixture was stirred.

When the acetates in the flask (in the oil bath) had reached 95°C, the mixture in the 1-litre beaker was added very slowly, over a period of approximately three hours. This was done using a motorised syringe, which slowly dispensed the mixture into the flask through a rubber septum. The contents of the flask were stirred throughout the reaction. When all of the mixture had been added to the acetates, the reaction was allowed to proceed under reflux for a further 2 hours. During this period the viscosity of the solution became noticeably greater. The solution was then left to cool overnight.

The reaction that occurs is a radical polymerisation, of the PHSA-GMA macromonomer with methyl methacrylate and a small amount of glycidyl methacrylate. The radical initiator is AIBN. The reaction is illustrated in figure 3.10 below.

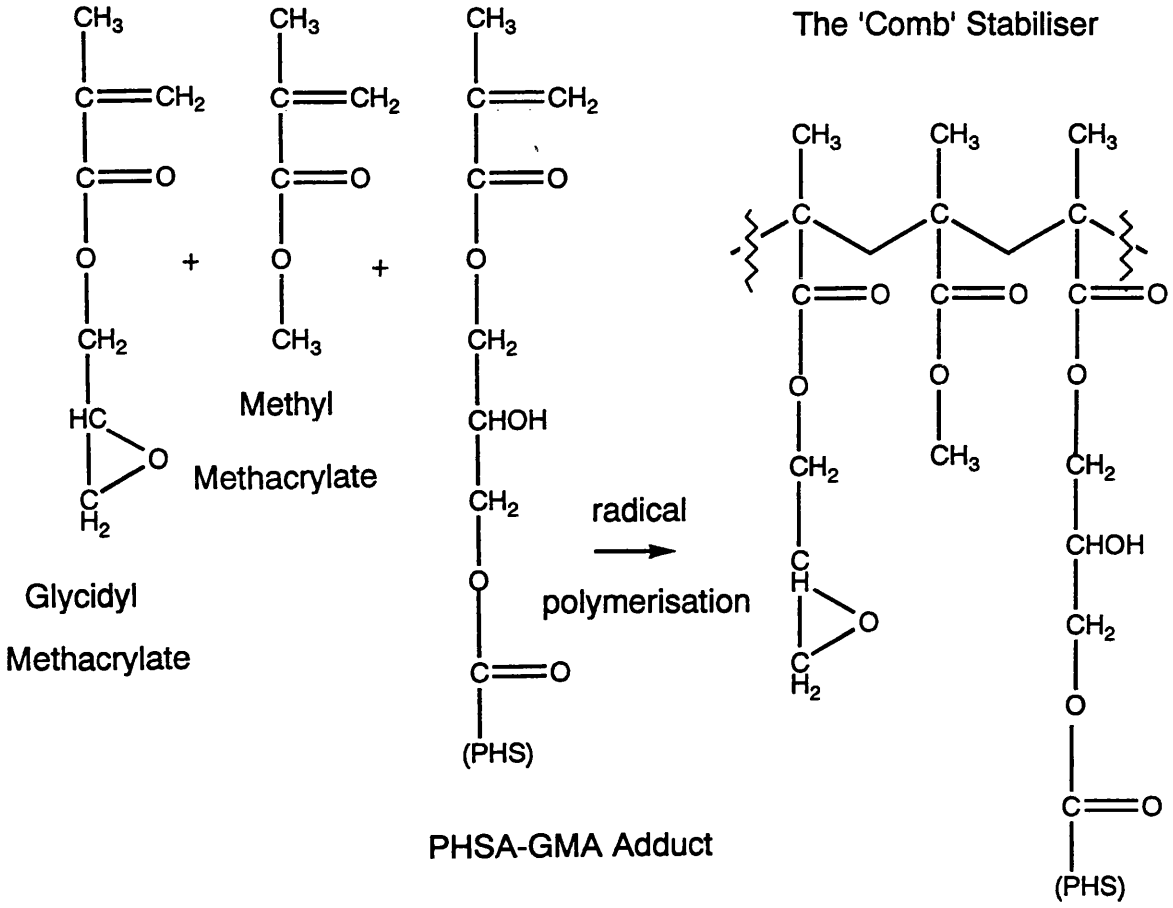

Figure 3.10. Synthesis of the stabiliser, in a radical copolymerisation of the PHSA-GMA adduct, with methyl methacrylate and glycidyl methacrylate.

The small amount of GMA that is added, is randomly incorporated into the growing polymer chain. This allows the stabiliser backbone to be covalently linked to the particle surface, during the locking stage (as explained in section 3.2.3). In order to make use of the stabiliser in further reactions, it was removed from the acetate solvents. A 30% (by weight) solution in dodecane was then prepared. First, the stabiliser was slowly added to excess ice-cold methanol. Then, the resulting precipitate was separated from the methanol, before being placed in a vacuum oven heated to 45°C. When the methanol, together with any

remaining solvent, had been removed, the solid formed was weighed into a flask containing a known amount of dodecane. The flask was then heated to 120°C in an oil bath and after stirring, a 30wt% solution of the stabiliser was produced.

3.2.7. GPC Analysis of Stabiliser Samples

Each of the stabiliser samples used in the present work, was analysed by means of gel permeation chromatography (GPC). The GPC system was calibrated with polystyrene and the universal calibration method was applied, using the data from an online viscometer. Thus, a system calibration was devised, of the logarithm (to base 10) of the product of molecular weight and intrinsic viscosity, versus retention time.

Using the combined GPC / viscosity approach, the weight average molecular mass ($\overline{M}_w$), number average molecular mass ($\overline{M}_n$), polydispersity index $\overline{M}_w$ / $\overline{M}_n$ and the Mark-Houwink parameters K and a were obtained for each stabiliser sample (table 3.2 below). Conventional GPC results were also calculated, using the refractive index response alone.

Stabiliser	$\overline{M}_w$	$\overline{M}_n$	$\overline{M}_n$ / $\overline{M}_n$	$\log K$	a
ICI	97400	19500	5.0	-2.78	0.43
	(70000)	(18000)	(3.8)		
Bristol	84033	14700	5.8	-2.50	0.38
	(62800)	(16000)	(3.9)		
Present	84000	17900	4.7	-2.68	0.42
	(65100)	(17700)	(3.7)		

Table 3.2. Combined GPC / viscosity results for the stabiliser samples in tetrahydrofuran. Conventional GPC results are shown in brackets and expressed as polystyrene equivalents.

Assuming the universal calibration is valid, the GPC / viscosity molecular weights given above should be the true molecular weights of the samples. The polystyrene equivalent weights, from conventional GPC, are consistently lower than those measured by the combined GPC / viscosity approach. Also, the Mark-Houwink parameter *a* is low. These observations suggest a low level of solvation and are consistent with a heavily branched polymer. A plot of the computed GPC / viscosity molecular weight distribution is shown in figure 3.11 below.

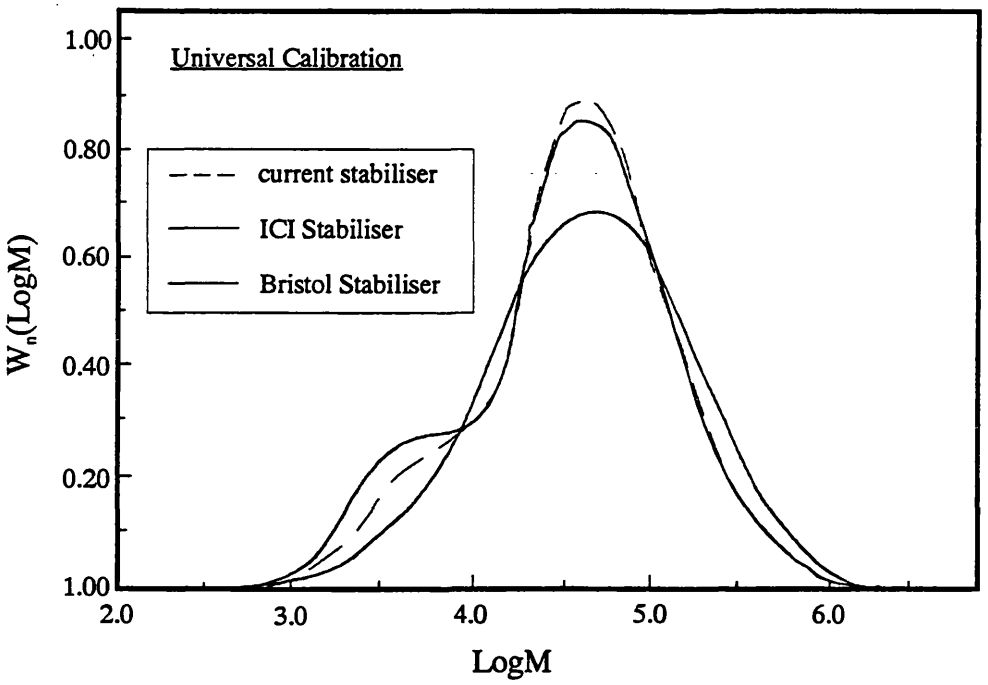

Figure 3.11. Plot of the computed molecular weight distribution, obtained from combined GPC / viscosity measurements.

The results indicate that the stabiliser sample synthesised in the present work, is similar in structure to the sample donated by Bristol University. The results also suggest that the stabiliser obtained from ICI Paints, is somewhat different in structure. This is consistent with the absence of glycidyl groups in this stabiliser, which are present in the copolymer backbone of the other two stabiliser samples.

3.3. Results

3.3.1. Preparation of Latex Particles using the Stabiliser Sample from ICI Paints

Single-stage dispersion polymerisation reactions were carried out, using the method described previously (section 3.2.2), in the presence of a stabiliser kindly donated by ICI Paints. This stabiliser was a graft copolymer of poly(12-hydroxystearic acid) and methyl methacrylate and was used as a 30% by weight solution in dodecane. Preparations were carried out, using the formulations given in table 3.3.

Sample	Monomer / wt%	Hexane / wt%	Dodecane / wt%	Stabiliser / wt%	Stabiliser / by wt% monomer
NHA	41.0	34.38	17.19	2.05	5.0
NHB	41.0	34.38	17.19	2.05	5.0
NHC	41.0	33.24	16.62	2.56	6.25
NHD	41.0	32.78	16.39	3.08	7.50
NHE*	41.0	29.82	14.91	4.10	10.0

*stable sample

Table 3.3. Summary of the samples prepared, using the stabiliser sample kindly donated by ICI Paints. In all the preparations, AIBN was 0.40 wt%, methacrylic acid 2.0 wt% on the monomer and octyl mercaptan 0.5 wt% on the monomer.

The reactions were carried out using a range of stabiliser concentrations. It was

found that latices prepared with 7.5% stabiliser in the reaction (by weight of the amount of monomer) or less were initially stable but coagulated, approximately 45 minutes after the dispersion polymerisation was initiated, forming a white solid. However, when the reaction was carried out using 10.0% stabiliser, a stable dispersion was produced. As was mentioned earlier, Antl and co-workers found the optimum concentration of stabiliser to be 5.0%, by weight of the monomer.[7] The stabiliser used by these authors, was a graft copolymer of poly(12-hydroxystearic acid), with methyl methacrylate and glycidyl methacrylate. The incorporation of glycidyl methacrylate into the stabiliser copolymer, could account for the difference in the minimum stabiliser concentration required to synthesise a stable latex. However, in another study, which was undertaken to prepare latex particles following the methods of Antl *et al.* (using the same reaction components), the minimum stabiliser concentration required for the formation of stable monodisperse latex particles was found to be 10.0% (by weight of monomer), with a monomer concentration of 35.0%.[83] The stabiliser used in this study, was similar in structure to the one used in the present work. It is possible that when the stabiliser contains glycidyl methacrylate groups, the glass transition temperature (T_g) of the stabiliser 'backbone' is lowered, making the stabiliser more flexible. Hence, it becomes more efficient and so less is required.

3.3.2. Preparation of Latex Particles using a Stabiliser Sample obtained from Bristol University

Colloidally stable polymer particles were prepared, by dispersion

polymerisation, following the method described in section 3.2.2. The formulations used are listed in table 3.4. The stabiliser was obtained from Bristol University (X190-243 / DJS1) and was a graft copolymer of poly(12-hydroxystearic acid), methyl methacrylate and glycidyl methacrylate. The stabiliser was used as a 30.0% (by weight) solution in dodecane.

Sample	Monomer / wt%	Hexane / wt%	Dodecane / wt%	Stabiliser / wt% by monomer
NH1*	41.0	34.38	17.03	5.0
NH2*	42.0	33.59	16.80	5.0
NH3*	47.0	26.69	14.85	5.0
NH4*	45.0	31.25	15.62	5.0
NH5*	50.0	27.34	13.67	5.0
NH6*	50.0	27.34	13.67	5.0
NH7*	45.0	27.34	13.67	5.0
NH10*	47.0	26.69	14.85	5.0

* stable sample

Table 3.4. Latex samples prepared using the stabiliser sample obtained from Bristol University (X190-243 / DJS1). Samples NH7 and NH10 were stirred.

The initiator (AIBN) was used in all the reactions at 0.40 wt%, together with methacrylic acid at 2 wt% (on the monomer) and octyl mercaptan at 0.5 wt% (on the monomer). Samples were successfully prepared, over a monomer concentration range of 41 – 50%. The stabiliser concentration for each reaction was kept at a constant 5.0% (by the weight of the monomer). The NH7 sample

was prepared with the addition of 5% butyl acetate. Also, during the preparation of samples NH6 and NH7, the reaction mixture was stirred at 50 rpm, under a nitrogen atmosphere. In each case, eight minutes after initiating the reaction, the translucent reaction mixture became opalescent. On completion of the reaction, after 2 hours, a stable colloidal dispersion was formed. Average particle diameters were obtained by dynamic light scattering (DLS) and are given in table 3.5.

Sample	Monomer / wt%	Mean Diameter / ± 10 nm
NH1	41.0	289
NH2	42.0	248
NH3	47.0	494
NH10	47.0	575

Table 3.5. Mean diameters, measured by dynamic light scattering (DLS), of colloidal particles prepared in a one-step dispersion polymerisation, with varying initial monomer concentrations.

As the initial monomer concentration used in the reaction is increased, from 41 to 47%, the average diameter of the latex particles formed becomes greater. The increase in size is of the order predicted by previous work.[7] Samples NH3 and NH10 were both prepared using a monomer concentration of 47%. The light scattering measurements indicated the average particle diameter of NH3 to be 494 nm and NH10 to be 575 nm. Hence, in terms of particle size the samples are similar.

The polydispersity, of the NH10 sample, was measured by DLS and a value of $\sigma = 0.08 \pm 0.01$ was obtained. Previous experiments have found that samples with $\sigma = 0.075$ crystallise slowly, in the phase coexistence region, but not above ϕ_m, while samples with $\sigma \approx 0.12$ do not crystallise at all.[5] Hence, in samples with polydispersities greater than the critical value of $\sigma_c = 0.08 - 0.12$, crystallisation is suppressed. As the polydispersity of the NH10 latex particles was less than the critical value, this sample was expected to be reasonably monodisperse. The phase behaviour was investigated and crystallisation was observed to occur rapidly in several samples, confirming the low polydispersity value.

Butyl acetate was used in the preparation of the NH7 latex, in order to investigate the effect of adding cosolvent to the reaction. In their studies Antl *et al.* added a mixture of butyl and ethyl acetate to all the dispersion polymerisation reactions carried out.[7]

In order to investigate the effect of stirring the reaction mixture, the NH5 preparation was repeated, whilst stirring under a nitrogen atmosphere.

3.3.3. Preparation of Latex Particles using the Stabiliser Sample prepared in the Present Work

Dispersion polymerisation reactions were carried out, using the stabiliser synthesised in the present work (section 3.2.6). This stabiliser was a graft copolymer of poly(12-hydroxystearic acid), glycidyl methacrylate and methyl methacrylate. A range of monomer concentrations were used, with samples being prepared according to the amounts given in table 3.6.

Sample	Monomer / wt%	Hexane / wt%	Dodecane / wt%	Stabiliser / by wt% monomer
NH9*	47.0	29.69	14.85	5.0
NH11	39.0	35.94	17.97	5.0
NH12*	43.0	32.81	16.41	5.0
NH13*	41.0	34.05	17.03	5.0
NH14	39.0	35.94	17.97	5.0
NH15	40.0	35.83	17.91	5.0
NH16	51.0	26.56	13.28	5.0
NH17	56.0	22.66	11.33	5.0
NH18*	51.0	26.56	13.28	5.0
NH19*	56.0	22.66	11.33	5.0
NH20	61.0	18.75	9.38	5.0
NH21	66.0	14.85	7.42	5.0
NH22*	51.0	26.56	13.28	5.0
NH23*	51.0	26.56	13.28	5.0
NH24*	48.5	28.52	14.26	5.0
NH25*	53.0	25.00	12.50	5.0
NH26*	47.5	29.30	14.65	5.0
NH27*	47.5	29.30	14.65	5.0
NH28*	47.5	29.30	14.65	5.0
NH29*	47.5	29.30	14.65	5.0

NH30*	53.0	25.00	12.50	5.0
NH31*	53.0	25.00	12.50	5.0
NH32*	60.0	19.53	9.77	5.0
NH33*	58.0	21.09	10.55	5.0
NH34*	62.0	17.97	8.98	5.0
NH35*	47.5	29.30	14.65	5.0
NH36*	45.0	31.25	15.62	5.0

*stable sample

Table 3.6. Formulations used in preparing colloidal particles, by a one-step dispersion polymerisation, with the stabiliser synthesised in the present work.

The initiator (AIBN) was used in all the reactions, at a constant 0.40 wt%. Methacrylic acid and octyl mercaptan were also used in all the reactions, at 2.0 and 0.5 wt% respectively, on the monomer weight. In each case the stabiliser concentration was maintained at 5.0% (by weight) on the monomer used. The reactions that produced stable samples are indicated.

The lower limit of the stable monomer range appears to be 41%. As can be seen from table 3.6, the NH13 sample was prepared using 41% monomer and formed a stable dispersion. The preparations carried out at lower monomer concentrations, NH11 and NH14 at 39% monomer together with NH15 at 40% monomer, all coagulated approximately 30 minutes after the dispersion polymerisation was initiated. In the opposite limit, stable samples include NH33, at 58% monomer, NH32, at 60% monomer and NH34, at 62% monomer. Suspensions NH20, at 61% monomer and NH21, at 66% monomer, were unstable. This indicates the upper limit of the stable monomer range, to be

approximately 61%. It was unexpected to find NH34 to be stable, at 62% monomer, while NH20 coagulated at 61%. This may be due to the closeness of both preparations, to the unstable monomer range.

Dynamic light scattering measurements indicated the average diameter of the NH9 colloidal particles to be 301 ± 10 nm, with the diameter of the NH10 latex particles being 575 ± 10 nm. As both were prepared at a monomer concentration of 47%, the size difference could be due to the different stabiliser used. The smaller diameter of the NH9 latex particles, produced using the stabiliser prepared in the present work, suggests that this stabiliser may be more efficient as it is able to stabilise a larger surface area. Hence, the smaller size of the particles of sample NH9 compared with those of NH10.

Samples NH18, NH22 and NH23 were all synthesised using 51.0% monomer in the reaction. Stable dispersions were produced and each was analysed, by both dynamic light scattering and transmission electron microscopy (TEM). The results obtained are given in table 3.7.

Sample	Mean Diameter (d) / nm		Polydispersity (σ)	
	DLS ± 10	TEM ± 30	DLS ± 0.01	TEM ± 0.02
NH18	812	797	0.12	0.09
NH22	691	728	0.08	0.07
NH23	680	726	0.08	0.08

Table 3.7. Dynamic light scattering (DLS) and transmission electron microscopy (TEM) measurements, of colloidal dispersions prepared using the stabiliser synthesised in the current work.

The results indicate that the latex particles, of samples NH22 and NH23, are very similar in diameter, while those of NH18 are slightly larger. These results are within the bounds of experimental error, for this type of reaction. The polydispersity values are reasonably low for the NH22 and NH23 samples, which suggests that crystallisation should occur. The polydispersity of the NH18 sample is at the upper limit of σ_c. Phase behaviour samples were prepared, using each dispersion, spanning a range of volume fractions. Those samples prepared with the NH18 dispersion, did not exhibit coexisting fluid and crystalline phases. However, in the samples prepared using the NH22 and NH23 latices, crystals were observed to form. In order for crystals to form, the particle polydispersity must be less than the critical value of $\sigma_c = 0.08 - 0.12$.[5] The observation of crystals in the phase behaviour samples, prepared using the NH22 and NH23 latices, suggests that the polydispersity of the particles of both samples is lower than σ_c. However, the absence of crystals in the NH18 samples, indicates that the polydispersity of this sample is above σ_c. These observations are in good agreement with the DLS and TEM measurements. Further size measurements are given in table 3.8 below.

Sample	Monomer / wt%	Mean Diameter (d) / ± 10 nm	Polydispersity (σ) / ± 0.01
NH9	47.0	301	0.04
NH12	43.0	293	0.06
NH13	41.0	305	0.32
NH18	51.0	812	0.09
NH19	56.0	1010	-
NH22	51.0	691	0.07
NH23	51.0	680	0.08
NH24	48.5	634	0.003
NH25	53.0	1042	0.007
NH26†	47.5	680	v. high
NH27†	47.5	661	v. high
NH28	47.5	397	0.04
NH29†	47.5	419	0.09
NH31†	53.0	916	0.07
NH35	47.5	500	0.05

† 650g synthesis.

Table 3.8. Dynamic light scattering (DLS) measurements, of the mean diameter (d) and polydispersity (σ), of colloidal particles prepared using various initial monomer concentrations and the stabiliser synthesised in the present work.

The polydispersity values are expected to be accurate, as crystals were observed in samples with measured σ values lower than σ_c. A graph of particle diameter vs. monomer concentration was plotted, using the data in table 3.8.

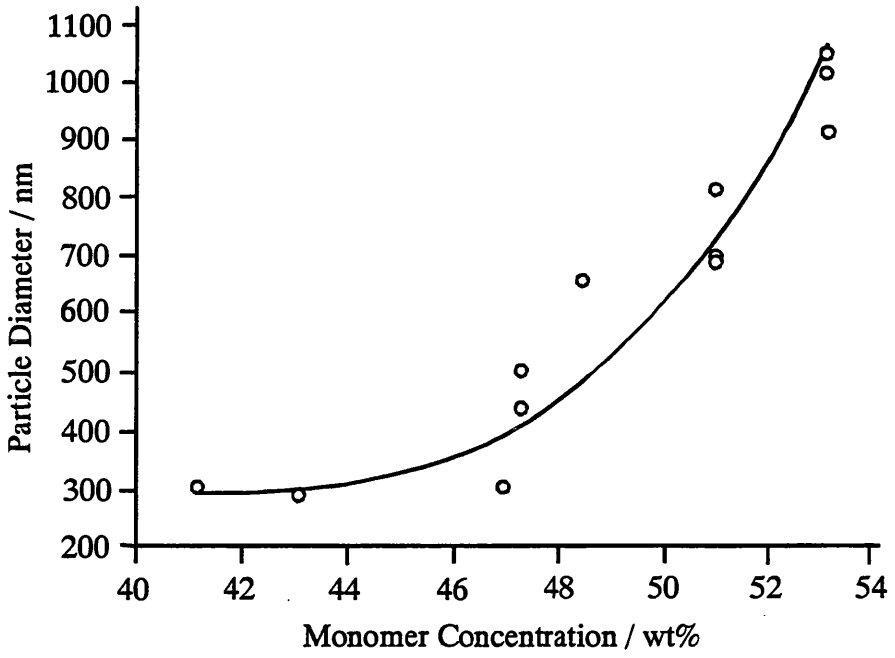

Figure 3.11. From present work, a graph of monomer concentration vs. particle diameter, for colloidal particles synthesised by dispersion polymerisation, using the stabiliser prepared in the present work at 5%, by weight of the amount of monomer.

This graph provides sufficient information, about the shape of the particle size / monomer concentration curve, to be able to predict reasonably accurately the size of the particles, which will be produced at a given monomer concentration.

In order to provide a more useful amount of latex particles, several syntheses were carried out with 650g of reaction components (as indicated in table 3.8). The first 650g synthesis was carried out using the same method, as was used for the 65g preparations. On completion of the reaction a stable latex was formed. However, it was subsequently discovered that the balance, used to weigh out the reaction components, was not working correctly. The synthesis was repeated (NH27) and a stable latex was produced. However, measurements

by DLS (see table 3.8) indicated the polydispersity to be greater than 0.12. Also, at 661 ± 10 nm the diameter of the latex particles was larger than expected, from previous results. In order to investigate whether the particles produced were influenced by the size of the synthesis, the NH27 preparation was repeated using 65g of reactants. A stable dispersion formed (NH28) and as shown in table 3.7, DLS measurements gave a particle diameter of 397 ± 10 nm, with a polydispersity of 0.08 ± 0.01. This is close to what would be expected, from the previous results. Samples with a range of volume fractions were prepared, using the NH28 suspension, spanning the phase coexistence region. Crystals were observed by eye, which suggested that the polydispersity was less than the critical value σ_c. The reaction was then repeated, using a larger amount of materials (650g) and the mixture was stirred throughout. A stable colloidal dispersion was produced (NH29) and dynamic light scattering measurements gave an average particle diameter of 419 ± 10 nm and a polydispersity of 0.09 ± 0.01. This diameter was very close to the measured diameter of NH28, although the polydispersity was higher. Phase behaviour samples were then prepared, using the NH29 dispersion, spanning a range of volume fractions. After being left undisturbed for several months, no crystals were observed, which appeared to confirm that the polydispersity was above σ_c. The final 650g preparation (NH31) was carried out using 53.0% monomer and was stirred throughout the reaction. As shown in table 3.8, the DLS measurements indicated the diameter of the particles to be 916 ± 10 nm and the polydispersity to be 0.07 ± 0.01. Samples with a range of volume fractions were then prepared. Crystals were observed to form, indicating that the polydispersity was below the critical value. The stability and low polydispersity of the particles, produced in this reaction (NH31),

suggests that it is necessary to stir the reaction mixture when preparing larger amounts of material.

3.4. Discussion

Spherical micron and submicron sized latex particles were prepared in a reproducible manner, in a single-stage dispersion polymerisation reaction.[7] These colloidal particles formed stable dispersions in hydrocarbon media. Three different stabiliser samples were used and reactions were carried out, using a range of initial monomer concentrations. Our initial goal was to prepare stable particles with a narrow distribution of diameters. The size and polydispersity of the colloidal particles were measured using dynamic light scattering. Measurements were also made by means of transmission electron microscopy.

Using a stabiliser kindly donated by ICI Paints, the minimum stabiliser concentration required, in the dispersion polymerisation, to produce a stable latex was 10% (by weight of the amount of monomer). The recipes used are given in the experimental section. By comparison, Antl and co-workers found 5% stabiliser to be the most favourable in this reaction.[7] However, there are two differences between the reaction conditions these authors report and ours. The first concerns the stabiliser, as our stabiliser did not contain glycidyl groups. The glycidyl groups in the stabiliser, used by Antl *et al.*, could lower the glass transition temperature (T_g) of the stabiliser 'backbone' making the stabiliser more flexible and efficient. Hence, less would be required to stabilise the particles and the minimum stabiliser concentration would be lower. Secondly, the use by these authors, of an ethyl acetate-butyl acetate cosolvent, will increase

the 'solvency' of the dispersion medium. As was mentioned earlier, this can have a significant effect on the dispersion polymerisation.

Using the stabiliser sample from Bristol University, stable latex particles were synthesised, with the initial monomer concentration in the range 41 - 50%. The formulations used are given in section 3.3.2. All the reactions were carried out using a stabiliser concentration of 5%, by the weight of the amount of monomer used. The structure of the stabiliser, is the same as that of the stabiliser used by Antl and co-workers.[7] These authors also carried out dispersion polymerisations, using 5% stabiliser. Further measurements are required, in order to investigate fully the effects of the addition of butyl acetate and of stirring the reactions, under a nitrogen atmosphere.

Using the stabiliser sample synthesised in the present work, preparations were carried out using a range of monomer concentrations. The recipes used are given in the experimental section. The stabiliser concentration was kept at a constant 5%, by weight of the amount of monomer used in the reaction. Again, this was the same stabiliser concentration as was used by Antl and co-workers.[7] The monomer concentration range, which produced stable latex particles was found to be 41 to 62%. Preparations carried out using an initial monomer concentration outside this range, produced unstable samples. Antl *et al.* observed the stable monomer range to be 35 to 50%, while Pathmamanoharan *et al.* found it to be 32 to 44%. These differences, in the stable monomer range, could be a consequence of differing reaction conditions. For example, as was mentioned earlier, Antl *et al.* used a cosolvent in the reaction.[7] In the present work, as the monomer concentration was increased from 41 to 62%, the final size of the particles increased from 301 nm to over 1 μm.

Each of the three stabiliser samples, was studied by means of combined GPC / viscosity measurements. The results suggested that the structure of the stabiliser from Bristol and the sample prepared in the present work, were similar. The results also indicated that the stabiliser sample from ICI was different to the other two stabiliser samples. These results are consistent with the absence of glycidyl groups in the ICI stabiliser, which are present in the other two samples.

Samples NH27 and NH35 were successfully prepared, using an initial monomer concentration of 47.5%, with a total mass of reaction components of 65.0g. Measurements by dynamic light scattering indicated the polydispersity of the particles to be less than $\sigma_c = 0.08 - 0.12$. This was confirmed by the crystallisation, of phase behaviour samples prepared using NH27. A reaction carried out using identical reaction components, but with a total mass of 650g, was found to have a polydispersity greater than 0.12. Also, crystals were not observed in the phase behaviour samples that were prepared. However, when the synthesis was repeated and the reaction mixture stirred throughout, under a nitrogen atmosphere, a stable sample of lower polydispersity was produced. A further reaction, carried out under identical conditions but with 53.0% initial monomer, was found to have a low polydispersity and crystals were observed to form. This suggests that stirring is required throughout the reaction, when larger 650g preparations are used. However, stirring does not appear to be necessary for 65g preparations.

CHAPTER 4

4. CHARACTERISATION

4.1. Introduction

Colloidal poly(methyl methacrylate) particles, sterically stabilised by thin layers of poly(12-hydroxystearic acid), were prepared in the present work in a one-step dispersion polymerisation reaction, as described in chapter 3.[7] After cleaning, by repeated centrifugation, the average particle size and polydispersity of dilute samples were measured by dynamic light scattering (DLS). Measurements were also made by transmission electron microscopy (TEM). The colloidal particles were also suspended in a refractive index matching mixture of decahydronapthalene (decalin) and carbon disulphide. This provided nearly transparent index-matched samples, which could be studied by both light scattering and direct observation.

4.2. Light Scattering

4.2.1. Introduction

A characteristic property of many colloidal fluids is the noticeable turbidity, which is a consequence of intense light scattering. The angular distribution, intensity and polarisation of the light scattered, from a colloidal dispersion, depend on the size and shape of the colloidal particles, the difference between the refractive indices of the particles and the medium and the inter-particle interactions. Light scattering measurements can therefore provide

valuable information about colloidal suspensions. The theoretical development of the subject has a long history, which began when Rayleigh developed the first rigorous theory for light scattering by small particles in 1871. Mie determined a general theory for light scattering by spheres in 1908. This theory was extended by Gans (1925), to include certain non-spherical shapes. Many others have made notable contributions to the subject. In 1940 experiments with conventional (or time-averaged) light scattering began. This involves measuring the average intensity of the scattered light, as a function of the scattering angle. The technique was developed further in 1960 with the invention of the laser, which provided an intense and well-collimated light source. However, more importantly, in the early 1960s, it was found that much more detailed information on suspensions and solutions could be obtained, by measuring the intensity fluctuations in the scattering from a continuous-wave laser. This lead to the development of a new technique, called dynamic light scattering (DLS), which uses the coherence of laser light to provide information about the dynamics of colloidal particles. The DLS approach is now generally used, to determine the size of colloidal particles. However, static, or conventional, light scattering remains an important technique for the investigation of colloidal crystal structures.

4.2.2. Conventional Light Scattering

If a beam of light is directed at a colloidal dispersion, some of the light is absorbed, some is scattered, while the remainder is transmitted through the sample undisturbed. According to classical electromagnetic theory, light can be

considered as the propagation of a fluctuating electric field, perpendicular to an associated magnetic field. When plane-polarised light falls on a colloidal particle, if there is a difference between the refractive index (n_1) of the particle and the refractive index (n_2) of the dispersion medium, the electric field induces a dipole moment. The magnitude of the dipole moment is determined by the polarisability (α_p) of the material. The dipole moment oscillates, at the frequency of the incident radiation, emitting secondary radiation of the same frequency in all directions. Hence, the particle becomes a scattering centre. The plane of the incident and scattered light define the scattering plane and the polarisation of the incident light is usually chosen to be perpendicular to this plane, using an appropriately placed polarising prism. The scattered light is then observed with the same polarisation at the detector. The basic light scattering arrangement is shown in figure 4.1.

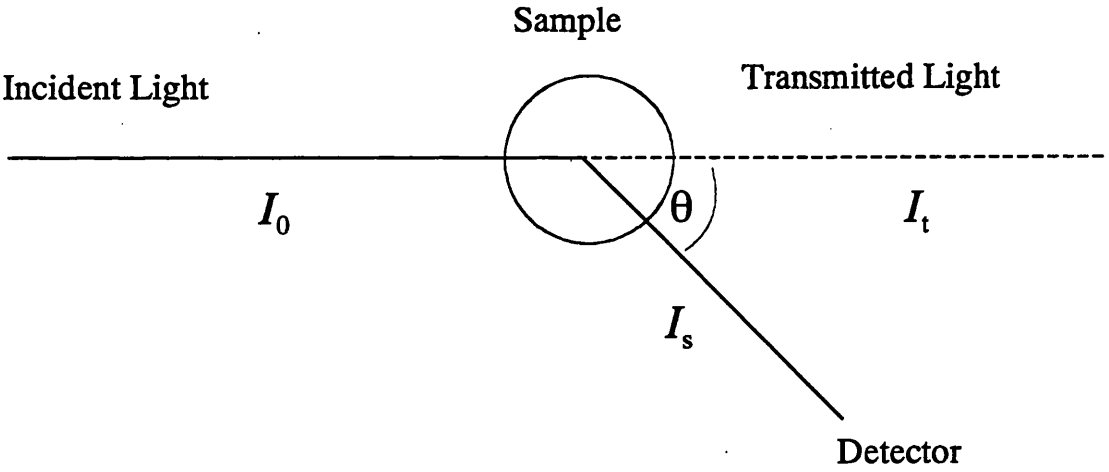

Figure 4.1. The basic light scattering experimental arrangement.

The paper represents the scattering plane, and I_o is the intensity of the incident light. I_s is the intensity of the light scattered, at an angle θ to the transmitted

beam, measured at a distance r from the scattering centre.

4.2.2.1. Rayleigh Scattering

For particles, of radius R, much smaller than the wavelength λ of the incident light ($R / \lambda << 1$), the theory originally developed by Rayleigh is applicable. The key point of this approach is that, as the particle is much smaller than the wavelength, the entire particle is subject to the same electric field, so the scattered light waves produced by the dipole oscillations are in phase. Rayleigh showed that the intensity I_R of the light scattered by an isolated particle, of radius much smaller than λ, is

$$I_R = I_0 \frac{16\pi^4}{r^2} \cdot \frac{R^6}{\lambda^4} \left(\frac{n^2 - 1}{n^2 + 2} \right)^2 \qquad (4.1)$$

where I_o is the intensity of the polarised incident light, λ is the wavelength (in the medium) and n is the refractive index ratio n_1 / n_2. The main points to note are, that I_R is independent of the scattering angle and depends on the refractive index difference $n_1 - n_2$. I_R becomes zero when $n_1 = n_2$. There is a very strong (sixth power) dependence on particle size R. The scattered intensity also depends on $1 / \lambda^4$, so that blue light ($\lambda \sim 450$ nm) is scattered more strongly than red light ($\lambda \sim 650$ nm).

4.2.2.2. Rayleigh-Gans-Debye Scattering

When the size of the scattering particle is comparable to λ, not all the regions within the particle experience the same electric field. Dipoles of varying magnitude are induced and the secondary radiation, emitted by the oscillating dipoles, is no longer in phase. In this case, for particles somewhat larger than the Rayleigh region, with a small relative refractive index difference $(n_2 - n_1)R / \lambda << 1$, a modification of the Rayleigh theory known as Rayleigh-Gans-Debye (RGD) can be used. This takes into account the interference, between the light scattered from different induced dipoles. In the RGD approximation, the modified scattering equation is

$$I_{RGD} = I_R \times P(\theta). \qquad (4.2)$$

$P(\theta)$ is a shape factor with properties $P(0) = 1$, $P(\theta) < 1$ for $\theta > 0$ and for $qR_g << 1$ then

$$P(\theta) = 1 - \frac{1}{3}(R_g q)^2 + \ldots \qquad (4.3)$$

where R_g is the particle's radius of gyration, a size measure for particles of arbitrary shape and q is the scattering vector (see eqn. 4.5).

4.2.2.3. Mie Scattering $(n_1 - n_2)R / \lambda \geq 1$

If the wavelength of light is comparable to the path length through the

scattering particle and the refractive index is higher than the medium, the incident light can be severely distorted on passing through the particle. The theory becomes rather complex, particularly when the absorption of light by the particle is considered. The problem of the propagation of an electromagnetic wave through a particle, which both scatters and absorbs, is a complicated one. It was solved by Mie in 1908, for spherical particles and subsequent work has extended the theory to particles of other shapes. For very large particles, $R >> \lambda$, a complex angular dependence of the scattered intensity is found. The Mie method may be used to predict the scattering intensity as a function of angle, offering a particle sizing technique above the Rayleigh region. It is possible to measure the size of monodisperse spherical particles up to ~2μm, by matching the experimental data to theoretical scattering profiles. However, the complexity of the scattering pattern limits the use of this method, to particles of very simple shape.

4.3. Dynamic Light Scattering

4.3.1. Introduction

Even when coherent (laser) light sources are used, the older time-averaged light scattering methods are limited to particles of simple shape and fairly uniform size, although modern computer methods have greatly expanded the range and accuracy of the procedures. Static light scattering, the measurement of time-averaged intensities of scattered light, remains an important technique for the investigation of colloidal crystal structures. However,

a much better general method, of determining the size of colloidal particles, is dynamic light scattering (DLS). As mentioned previously, the development of this technique followed shortly after the invention of the laser in 1960. The laser provides a monochromatic, coherent light source (the wave motion is in phase across the plane of propagating light), which results in phase relationships being maintained during the scattering process.

Dynamic light scattering is a general term, which also includes the techniques of quasi-elastic light scattering, intensity fluctuation spectroscopy, photon correlation spectroscopy, light-beating spectroscopy, homodyne and heterodyne spectroscopy. In the present work, we are concerned with the technique of photon correlation spectroscopy (PCS), which involves data processing by digital correlation.

4.3.2. Dynamic Light Scattering Theory

4.3.2.1 Introduction

When a laser beam is focused on a small volume of solution containing colloidal particles, the scattered light is seen as a random fluctuating 'speckle' pattern, consisting of bright and dark regions. The phase and polarisation, of the light scattered from any particle, is determined by its size, shape and composition. As the particles undergo random Brownian motion, the intensity fluctuates due to the interference of the phase modulated light, scattered from the different particles. The time scale of the fluctuations is determined by the time scale of the motion of the particles. Hence, the temporal fluctuations in the

scattered intensity, contain information about the dynamics of the colloidal particles. If a dilute suspension, containing N colloidal particles, is illuminated by laser light of wavelength λ, then the electric field induces a dipole in each particle. The magnitude of the dipole is proportional to the refractive index difference, between the particle and the dispersion medium. Each dipole oscillates, at the same frequency as the incident light and emits radiation in all directions. The scattering then consists of the superposition of these secondary electric fields. Constructive or destructive interference occurs, depending on the phases of the dipoles and on the phase changes, which occur between the sample and the detector. The amplitude of the instantaneous scattered electric field, observed at a point in the far field, is[5]

$$E(q,t) = \sum_{i=1}^{N} b_i(q) \exp[i\boldsymbol{q} \cdot \boldsymbol{r}_i(t)], \tag{4.4}$$

where $b_i(q)$ and $\boldsymbol{r}_i(t)$ are the scattering amplitude and instantaneous position of the ith particle. The magnitude of the scattering vector $\boldsymbol{q}$ is given by

$$q = |\boldsymbol{q}| = \frac{4\pi n_2}{\lambda} \sin\frac{\theta}{2}, \tag{4.5}$$

where λ is the wavelength of the laser light in a vacuum, n_2 is the refractive index of the medium and θ is the scattering angle. Each speckle subtends a small solid angle $(\lambda / V^{1/3})^2$ at the sample.[5] It can be shown that the instantaneous intensity of a speckle is[5]

$$I(q,t) = |E(q,t)|^2. \tag{4.6}$$

In dynamic light scattering the intensity is measured, for a given scattered field, as a function of time. A single fluctuating speckle in the scattered field illuminates a photomultiplier tube, which produces a temporally modulated signal. The photomultiplier output is passed through an amplifier-discriminator system, the output of which is a digital signal. This signal is processed by a digital correlator, that determines the time scale over which the fluctuations take place. From the data, the correlator generates the normalised second-order intensity autocorrelation function[87]

$$g^{(2)}_{(t,\, t+\tau)} = \frac{< I(t)I(t+\tau) >}{< I >^2}, \tag{4.7}$$

which represents the relationship between the average intensity at a time $(t + \tau)$ and at time τ. τ is the correlation time delay, the typical fluctuation time of the speckle pattern at the detector. As τ becomes large, the intensities become uncorrelated and $g^{(2)}_{(t,\, \tau\to\infty)}$ approaches 1. As τ approaches 0 the value of $g^{(2)}_{(t,\, \tau\to 0)}$ will depend on the exact properties of the field. As the scattered field, $E(q,t)$, represents the spatial Fourier component of q, DLS effectively follows the temporal evolution of a single spatial Fourier component of the sample's concentration fluctuations.[74] The first-order electric field autocorrelation function, at a point in space, is given by[87]

$$g^{(1)}_{(t,\, t+\tau)} = \frac{< E(t)E^*(t+\tau) >}{< I >}. \tag{4.8}$$

$g^{(1)}_{(t,t+\tau)}$ is the Fourier transform of the optical spectrum. It is assumed that the scattering volume (V) contains a large number of particles (N) and that the range of spatial correlations among the particles is much smaller than $V^{1/3}$.[74] Also, the motion of the particles is assumed to be sufficiently unrestricted, that a representative sample of spatial configurations are explored during the course of a measurement. In this case, the system is ergodic and the time average, indicated by the angular brackets in equations 4.7 and 4.8, is equivalent to an ensemble average.[74] For non-ergodic media, such as colloidal glasses, alternative DLS approaches have been developed. For an ergodic system, the scattered light field has Gaussian statistics and is specified completely by a knowledge of the first-order autocorrelation function. For Gaussian light, the normalised intensity and field autocorrelation functions may be expressed in terms of the Siegert relation,[87]

$$g^{(2)}(\tau) = B(1 + \beta \left| g^{(1)}(\tau) \right|^2), \tag{4.9}$$

where B is a baseline and β is the coherence factor, which takes into account deviations from ideal correlation. For non-Gaussian light this equation is not applicable and the intensity autocorrelation function contains information, which is not available from the field autocorrelation function.

For a dispersion of dilute non-interacting identical spheres, the electric field autocorrelation function is a single exponential,

$$\left| g^{(1)}(\tau) \right| = \exp(-\Gamma\tau), \tag{4.10}$$

where Γ is the decay constant, given by $\Gamma = q^2D$, where q is the scattering vector and D is the translational diffusion coefficient for the Brownian process. For spheres, D is given by the Stokes-Einstein relationship

$$D = \frac{k_B T}{6\pi\eta R_H}, \tag{4.11}$$

where k_B is the Boltzman constant, T is the temperature, η is the viscosity of the liquid and R_H is the hydrodynamic radius, the particle radius in solution.

In photon correlation spectroscopy, the normalised intensity autocorrelation function is measured. From this the field autocorrelation function $g^{(1)}(\tau)$ can be evaluated using equation 4.9. The diffusion coefficient of the particles can then be determined, from the exponential decay of the field autocorrelation function. First, by plotting (or fitting) ln $g^{(1)}(\tau)$ against τ, the decay constant, Γ, can be calculated from the gradient of the graph. Then, using the relation $\Gamma = q^2D$, D can be determined. Since the temperature T and viscosity η of the dispersion medium are both measurable quantities, the hydrodynamic radius of the particles can be determined using equation 4.11.

For polydisperse non-interacting particles, each particle size has a different scattered intensity and a different diffusion coefficient. In this case the field autocorrelation function is a sum of exponentials, one for each size of particle, weighted by the intensity scattered by each particle,

$$\left| g^{(1)}(\tau) \right| = \int_0^\infty G(\Gamma) \exp(-\Gamma\tau) d\Gamma, \tag{4.12}$$

where $G(\Gamma)$ is the intensity scattered by particles with a decay constant between Γ and $\Gamma + d\Gamma$. $|g^{(1)}(\tau)|$ is non-exponential and represents an average over the distribution of sizes. A variety of methods can be used, to obtain the desired information (the distribution of the decay times $G(\Gamma)$) from equation 4.12. Theoretically, this equation can be solved through the inversion of a Laplace transform. However, this procedure is very sensitive to statistical error in the data and large errors can arise, in the reconstruction of the particle size distribution. Mathematically, this is considered an ill-conditioned problem. Nonetheless, in recent years the problem has received much attention and meaningful results have been obtained. There are now a variety of Laplace transform methods, which can be used to determine an approximation to the real distribution of decay times. The most commonly used approaches include the method of nonnegative least squares, singular value analysis and maximum entropy. These methods usually involve some means of limiting the possible solutions to the problem. Equation 4.11 can also be solved by non-Laplace techniques. For narrower distributions, the method of cumulants is one of the simplest approaches.

4.3.2.2. The Method of Cumulants

The cumulant method has the advantage of obtaining information, about the form of $g^{(1)}(\tau)$, without *a priori* knowledge of the form of the function. The method involves fitting the logarithm of the normalised field autocorrelation function, to a polynomial in powers of the correlation time delay. The log of the field autocorrelation function can be expanded, as a power series in τ (the

correlation time delay), to give

$$\ln g^{(1)}(\tau) = -Aq^2\tau + \frac{B}{2}q^4\tau^2 + \ldots, \tag{4.13}$$

where each term represents a 'statistical moment' of successively higher order. $\kappa_1 = -Aq^2$ is the first cumulant, $\kappa_2 = \frac{B}{2}q^4$ is the second cumulant and so on. The coefficients A, B, etc. are related to moments of the particle size distribution. For spherical Rayleigh scatterers, the first cumulant corresponds to the 'average' diffusion coefficient,

$$A = \frac{k_B T}{6\pi\eta} \cdot \frac{\overline{R^5}}{\overline{R^6}}. \tag{4.14}$$

The normalised second cumulant yields a mean-squared deviation from this average, B / A^2, which is a measure of the width of the particle size distribution. This also provides an indication of the departure of $g^{(1)}(\tau)$ from a single exponential.

$$\frac{B}{A^2} = \frac{\overline{R^6 R^4}}{\left(\overline{R^5}\right)^2} - 1. \tag{4.15}$$

The cumulant expansion is valid for small τ and sufficiently narrow $g^{(1)}(\tau)$. The power-series expansion is generally truncated to two or three terms, as in practice it is difficult to measure cumulants higher than the second. Hence, the cumulants

method gives no information on the form of the distribution function. However, the cumulant expansion algorithm is fast and easy to implement, which is usually done using the appropriate computer software.

4.3.2.3. Multi-Angle Dynamic Light Scattering

Dynamic light scattering is widely used, to accurately measure the particle size in colloidal systems. However, determining the nature of the particle size distribution is more difficult. Methods such as cumulant analysis or Laplace transformation of the data, obtained at a single scattering angle, are commonly used. However, these methods become unreliable for samples with a polydispersity less than 0.2. Pusey and van Megen have reported an alternative approach, in which polydispersities as low as $\sigma = 0.01$ can be measured.[88] In this technique more information is obtained, about the particle size distribution, by conducting photon correlation spectroscopy as a function of the scattering angle. As the angular dependence, of the intensity of light scattered by an individual particle, changes according to the particle size, changing the scattering angle for a polydisperse sample causes the particle size distribution to be sampled differently.[88] The colloidal particles are assumed to be homogeneous spheres, which fulfil the Rayleigh-Gans-Debye (RGD) criterion. For an individual particle, the form factor is given by[88]

$$P(q) = \frac{9}{(qR)^6}(\sin qR - qR\cos qR)^2, \qquad (4.16)$$

where R is the particle radius and q is the scattering vector. The scattered

intensity, at angle θ, for a dilute suspension of such particles is[88]

$$I(q) = \int_0^\infty R^6 P(qR) G(R) \mathrm{d}R, \qquad (4.17)$$

where $G(R)$ is the normalised particle size distribution.

Methods based on measurements at a single scattering angle, measure the composite distribution $R^6P(qR)G(R)$, rather than just the particle size distribution $G(R)$. Hence, a measurement at a single angle is of little use. To make progress Pusey and van Megen analysed the field autocorrelation function of the scattered light, by the method of cumulants, over a range of angles. At each angle, the effective diffusion coefficient $D_e(q)$ was obtained from the first cumulant κ_1 (the initial slope of the log of the field autocorrelation function). $D_e(q)$ is the intensity-weighted average diffusion coefficient

$$D_e(q) = \frac{-\kappa_1}{q^2} = \frac{\int R^6 P(qR) D(R) G(R) \mathrm{d}R}{I(q)}, \qquad (4.18)$$

where $D(R)$ is given by equation 4.11. Pusey and van Megen calculated the results that would be expected, using the multi-angle approach, for a generalised exponential (or Schultz) particle size distribution. The results, for samples with various polydispersities, are shown in figure 4.2.

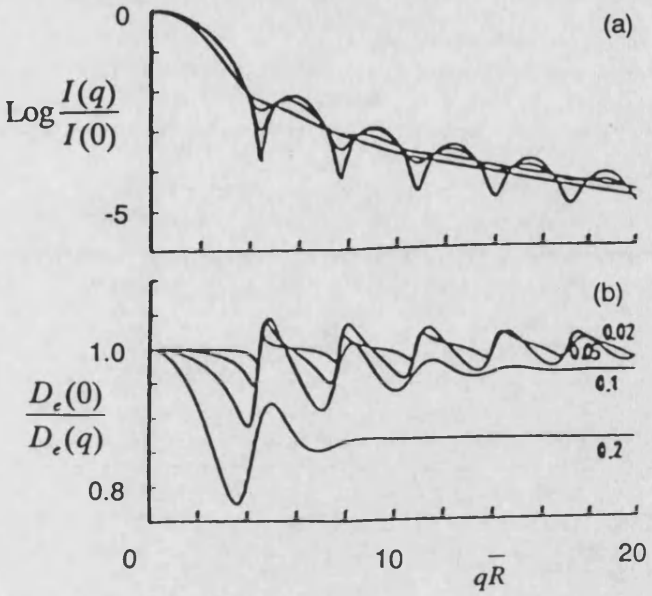

Figure 4.2. Theoretical results for a generalised-exponential particle size distribution, as a function of reduced scattering vector $q\overline{R}$, from Pusey and van Megen.[5] (a) Logarithm of intensity normalised to its low-q value. Curve with the deepest minima is for $\sigma = 0.02$, the other curves are for $\sigma = 0.05$, 0.1 and 0.2. (b) Apparent size, normalised to low-q value. Curves are for $\sigma = 0.02$, 0.05, 0.1 and 0.2.

The oscillatory nature of the curves in figure 4.2(b) is due to the superposition of the form factors, of the large and small particles. As the polydispersity is increased from $\sigma = 0.02$, the oscillations become increasingly damped at higher values of q.

These authors calculated theoretical results for two model distributions.[88] It was found that if the mean particle radius $\overline{R}$ was greater than 170 nm, the intensity form factor $P(q)$ showed significant angular dependence and had at least one minimum in the accessible range of q. In this case, the variation of $D_e(q)$ with q is very sensitive to the sample polydispersity.

4.3.3. Experiment

4.3.3.1. Introduction

The arrangement of the apparatus, used for dynamic light scattering experiments, is illustrated schematically in figure 4.3.

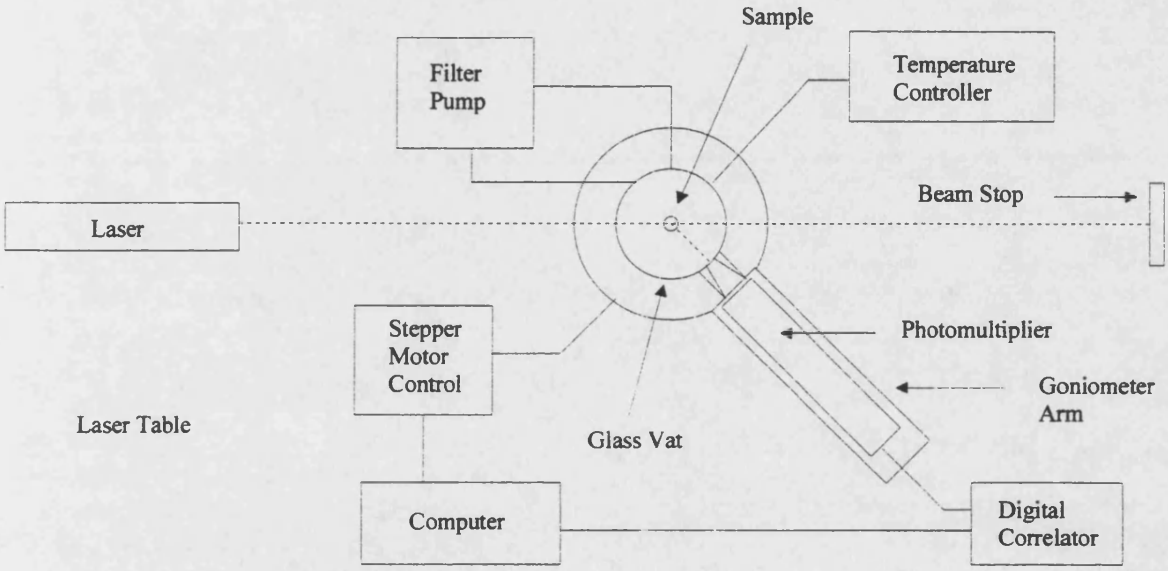

Figure 4.3. Schematic diagram of the dynamic light scattering equipment.

The laser produces a beam of coherent light, which is precisely aligned to pass through the centre of the sample. The electric vector of the incident light is vertically polarised, with respect to the scattering plane (the plane of the diagram). The sample is contained in a glass cell, which is located at the centre of a glass vat filled with water. This maintained at a constant temperature (± 0.1°C) and the beam enters and leaves the vat, through flat optical quality windows. An attenuator is mounted on the exit window, to reduce back reflection of the laser beam and the path terminates at a beam stop. The light scattered by

the sample is detected by a photomultiplier and associated optics, which are mounted on an arm. This can be moved using a computer controlled stepper motor. Using this system, scattering angles of between 10° and 150° can be selected using the computer. The photomultiplier produces a digital signal, based on the fluctuating scattered intensity pattern. The signal is passed to the photon correlator, which determines the correlation function of the scattered light. The computer is then used to abstract information, from the correlation function.

4.3.3.2. The Laser

Both conventional and laser light sources can be used in dynamic light scattering. However, lasers are almost always used in modern DLS measurements, because of the relatively low intensities obtained when light from a conventional source is focused to a point. Also, lasers now often cost less than conventional light sources of equivalent power. The properties of a laser source, which are particularly important are its well-collimated beam, intensity, stability, coherence and single wavelength (or 'laser line') operation. The well-collimated beam gives an intense flux of light, into a single coherence area. Stability is important, as changes in the beam intensity can cause fluctuations in the intensity of the scattered light, which are related to the laser rather than the sample being studied. The wavelength plays a crucial part, in dynamic light scattering theory and having a fixed wavelength is almost essential in interpreting any measurement. The nature of lasers is such that they only operate at specific fixed wavelengths. Hence, only light of certain wavelengths is available for light scattering experiments and the wavelength selected is usually determined by the

nature of the experiments to be performed. It is important that the laser light is not absorbed to any significant extent by the sample.

4.3.3.3. The Photomultiplier

The photomultiplier usually consists of a tube with a window at one end. When a photon enters the window, it collides with a sensitive photocathode, which is usually made of one or more alkali metals. The photon is absorbed and an electron is immediately ejected. The electron is accelerated by a high voltage electric field and then falls onto a sheet of metal (a dynode), which absorbs the electron and ejects several more. These electrons are also accelerated in an electric field, before colliding with a second dynode. This process is repeated over twelve or more dynodes and the original single electron is 'multiplied' into 10^7 or more electrons. These electrons form the electrical pulse, which is the photomultiplier's output. In order for this pulse to be processed by a digital correlator, it must be of a specific amplitude and duration. An electronic unit, called a pulse amplifier-discriminator, provides this function. The relatively small single photon signal, is amplified and converted to a standard logic pulse and at the same time very small photomultiplier pulses are filtered out. The photodetection rate is proportional to the light intensity incident on the photocathode. The two are related by the Poisson (random) nature of the photoelectron emission process.[87] If a photomultiplier is illuminated by a laser source of constant intensity, the photodetections are purely random unrelated events and have a simple Poisson probability distribution[87]

$$P(n) = \frac{(\beta IT)^a}{h!} \exp(-\beta IT), \qquad (4.19)$$

where a is the number of photodetections, which occur during sample time T, I is the (constant) intensity of the laser and β is the efficiency of the detector.

In the present work, the photomultiplier tube was mounted on a goniometer arm, the angle of which was accurately set using a computer controlled stepper motor (10 – 150°). Before reaching the photomultiplier, the light passed through a narrow band filter so only light at the wavelength of the laser was detected. Also mounted on the arm, in front of the photomultiplier, were the detection optics. A lens and a pair of apertures defined an optical axis and careful alignment was necessary to ensure that the photomultiplier was viewing the centre of the probe volume, defined by the laser source. For PCS the quantum efficiency (probability of detecting a photon) of the photomultiplier should be as high as possible at the laser wavelength being used.

4.3.3.4. The Correlator

The correlator is a purpose-built digital computer, which determines $g^{(2)}(\tau)$, the intensity autocorrelation function of the scattered light field. When a correlator receives two time-varying input signals, $I(t)$ and $J(t)$, the correlation function is defined by the function

$$g(\tau) = \lim_{T\to\infty}(T/2)\int_{-T}^{T} I(t)J(t+\tau)\mathrm{d}t\,. \qquad (4.20)$$

In light scattering measurements where the correlator receives two different signals, one derived directly from the laser and the other from the scattered light, $g(\tau)$ represents the cross-correlation function. More often, I and J are the same signal and $g(\tau)$ represents the intensity autocorrelation function of the scattered light. The correlator is usually designed to determine an approximation to the above equation, over a range of values of τ. The arrangement of a simple correlator with five channels, is shown in figure 4.4 below.

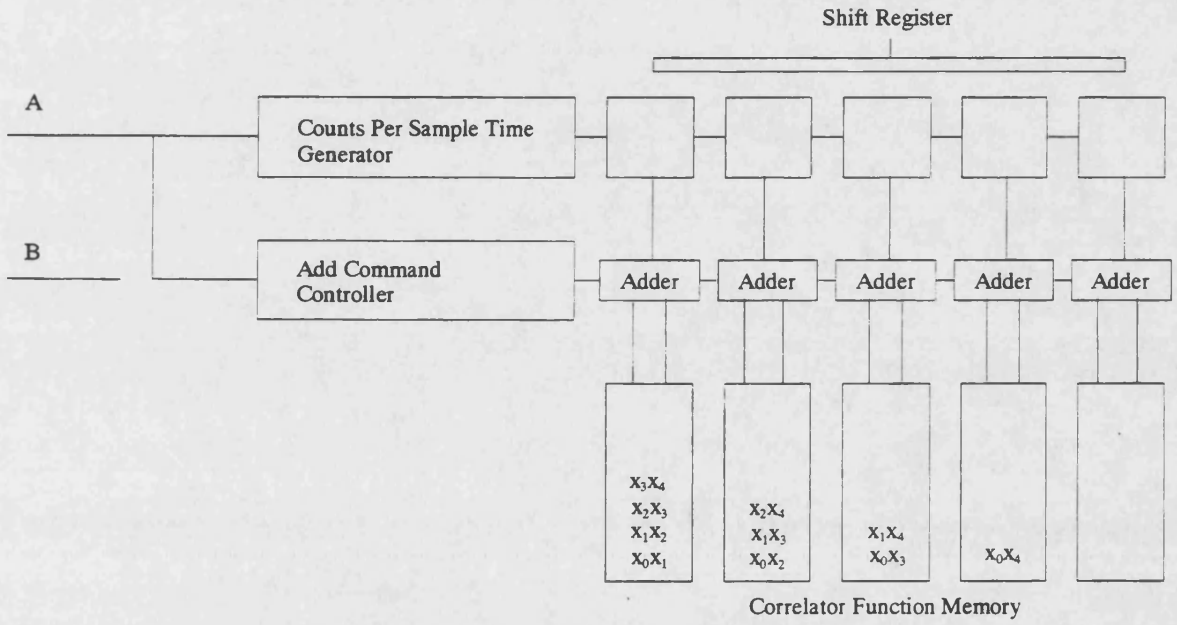

Figure 4.4. Schematic diagram of a simple 5 channel correlator.

Light scattering signals arrive at the correlator as electronic logic pulses, 50ns in length, representing individual photon detections by the photomultiplier. The correlator contains a timing device, which divides time into 'sample times', of equal duration $\Delta\tau$. The signal to be processed is normally fed to input A of the

correlator. The number of pulses arriving here, during each sample time, are counted by the 'counts per sample time register'. At the end of the sample time, all the values stored in the shift register are moved to the right by one element and the number in the 'counts per sample time register' is entered into the now vacant first element. As the values in the shift register are moved to the right, the oldest value is lost. The length of this memory is determined by the number of channels in the correlator.

During the sample time $\Delta\tau$ every pulse representing a photon event, occurring at input A, is passed to the add command generator. This processes the signal and causes the adder, associated with each correlator channel, to add the number stored in the shift register at the head of each channel to the number stored in the channel. If, say, three pulses were counted during the sample time, then the above process will occur three times and the values stored in the shift register will be added to their associated correlator channels three times. Therefore, the total added to each correlator channel during the sample time, will correspond to the shift register value multiplied by three. If the number of pulses counted during consecutive sample times is given by

$$x_0, x_1, x_2, \ldots \tag{4.21}$$

then the values stored in the first correlator channel are given by

$$g(\Delta\tau) = x_0x_1 + x_1x_2 + x_2x_3 + \ldots \tag{4.22}$$

$$= \sum_{i=0}^{N-1} x_i x_{i+1} \tag{4.23}$$

and for the second channel

$$g(\Delta\tau) = x_0x_2 + x_1x_3 + x_2x_4 + \ldots \tag{4.24}$$

$$= \sum_{i=o}^{N-1} x_i x_{i+2} \tag{4.25}$$

the xth channel will contain

$$g(x\ \Delta\tau) = x_0x_x + x_1x_{x+1} + x_2x_{x+2} \ldots \tag{4.26}$$

$$= \sum_{i=0}^{N-1} x_i x_{i+x} \tag{4.27}$$

and this is a reasonable approximation to the true correlation function.

For a real signal the fluctuations are often small statistical fluctuations, that take many thousands of samples to expose the underlying structure. The correlator has to update all the channels, which have a non-zero shift register value, each time a photon is detected. This is normally at least half the channels and often all of them. Therefore, the correlation process is done with dedicated hardware, as a software intensive process is too slow.

The characteristics of a correlator, that are important in terms of light scattering measurements, are the efficiency of operation, the capacity of the shift register counter and the shift register, the range of sample times available and the number of channels. The characteristics of the Malvern correlator, used in the present work were as follows. The number of channels was 128, the shift register capacity 4 bits and minimum sample time 100ns.

As was mentioned earlier, electronic logic pulses arrive at input A and each represents an individual photon detection by the photomultiplier. The total number of logic pulses arriving at input A, during the time of the experiment, is stored in monitor channel A. The signal as it is received is multiplied by all the stored values in the memory, each product adding its result to the contents of the corresponding channel. The resulting sum represents one correlation coefficient. Its value depends on the number of pulses and the length of time of the experiment. The length of time of the experiment is stored in another channel, the samples monitor channel. From these channels a normalisation value, or calculated baseline, can be determined where,

$$\text{Calculated baseline} = A^2 / \text{total samples.} \qquad (4.28)$$

The baseline is also measured by a special group of correlator channels, pushed out in time by the use of a memory extension. The measured and calculated baselines may be compared and in the event of distortion of the correlation function (for example, by dust in the sample) the two baselines will be significantly different. The measured baseline is usually used in calculations.

4.3.4. Results

The multi-angle DLS approach of Pusey and van Megen (described in section 4.3.2.3) was used in the present work, to measure the size and polydispersity of colloidal PMMA particles. The method is illustrated with the results from the one-component colloidal samples, NH31, NH28 and DMM7.

Results for other samples are collected together in tables 3.5, 3.7 and 3.8, in chapter 3.

Measurements were made at various angles, in the range $50° < \theta < 130°$, according to the location of the minimum in the angular intensity profile. At each angle, the effective diffusion coefficient $D_e(q)$ was obtained, from the initial slope of the correlation function. From this the particle radius was calculated. Figure 4.5 shows the results of DLS measurements of a dilute dispersion, in dodecane, of the one-component NH31 sample.

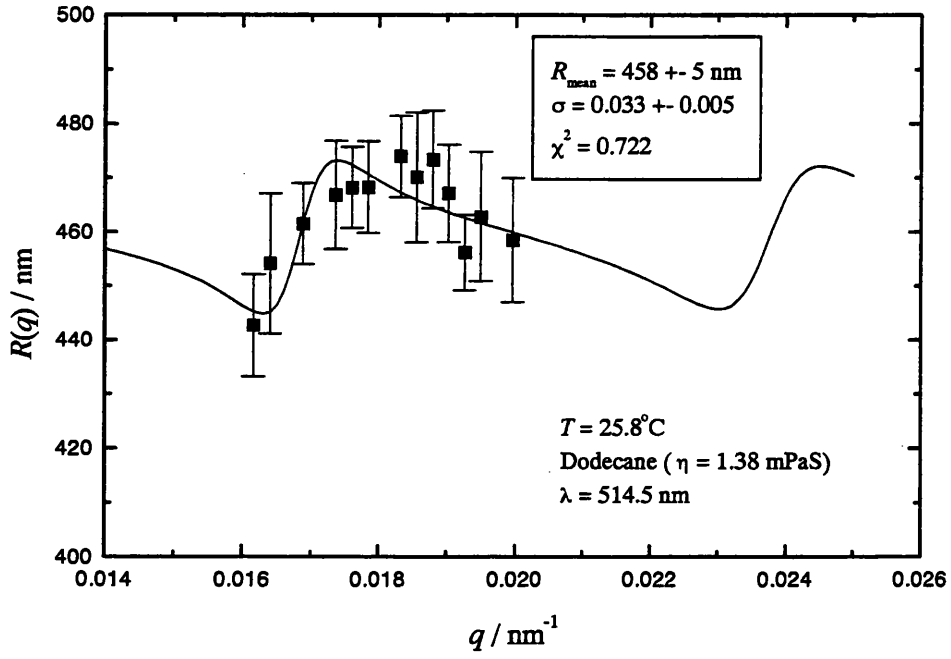

Figure 4.5. Multi-angle DLS measurements for sample NH31, a dispersion of colloidal PMMA particles. The particle radius is plotted vs. the scattering vector q. Black squares indicate experimental points, while the solid line represents the fitted curve.

A Fortran program was used to fit the theoretical curve, to the experimental data.

This provided the mean particle radius (R) and the polydispersity (σ). DLS measurements were also made on the single-component dispersion, NH28. The results are shown in figure 4.6 below.

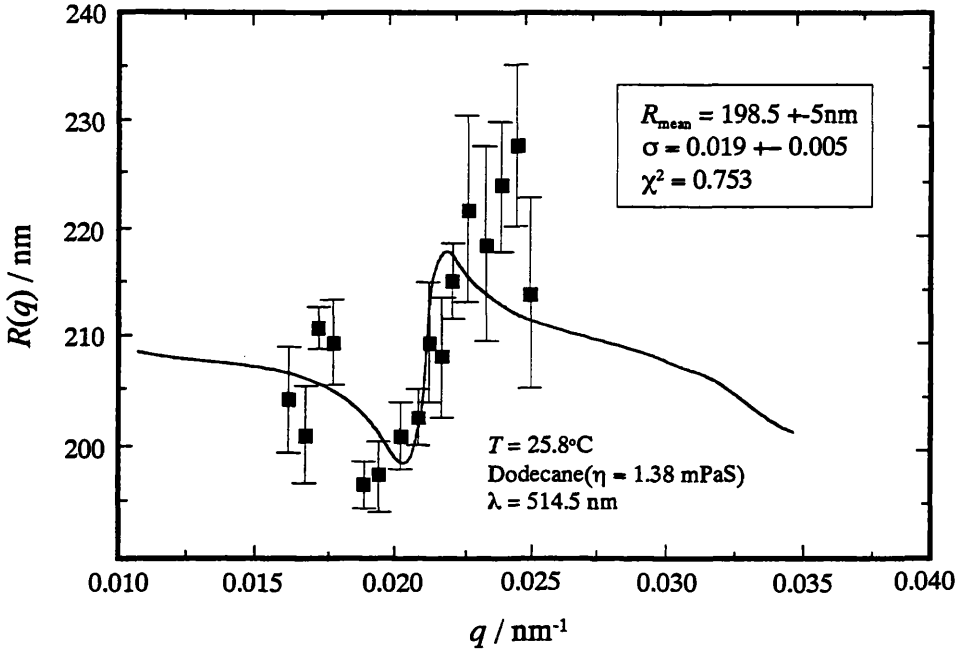

Figure 4.6. Multi-angle DLS measurements for sample NH28, a one-component suspension of colloidal PMMA spheres. The particle radius is plotted against the scattering vector q. Black squares indicate experimental points, while the fitted curve is shown by a solid line.

DLS measurements obtained from earlier work, for the DMM7 sample, are shown in figure 4.7 below.

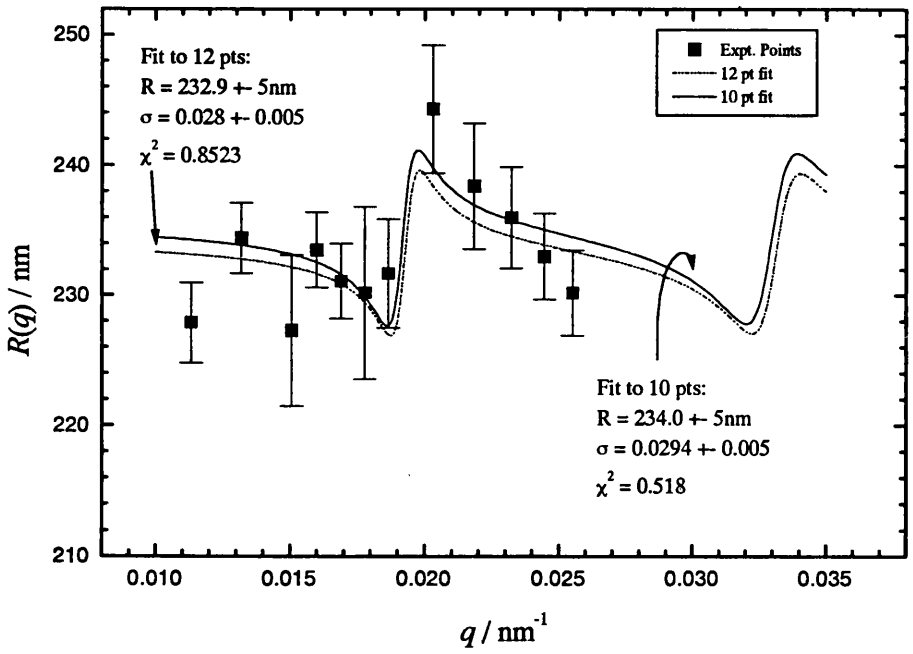

Figure 4.7. Multi-angle DLS results for sample DMM7, a suspension of colloidal PMMA particles, from earlier work. The particle radius is plotted vs. the scattering vector q. Experimental points are shown by black squares and the solid line represents the fitted curve.

The DLS results discussed above are gathered together in table 4.1.

Sample	Mean Diameter d / ± 10 nm	Polydispersity σ / ± 0.01
NH31	916	0.07
NH28	397	0.04
DMM7	466	0.06

Table 4.1 Results of DLS measurements of the one-component colloidal dispersions, NH28, NH31 and DMM7.

4.4. Transmission Electron Microscopy

4.4.1. Introduction

Colloidal particles are generally too small to be directly observed by means of a light microscope. The resolution is limited, mainly by the wavelength of the light used. However, there are several methods, which overcome this difficulty, one of which is electron microscopy. The electron microscope greatly extends the limit of resolution and is important in the study of colloidal systems. In order to resolve sub-microscopic particles, the wavelength of the electromagnetic radiation, must be much shorter than that of light. In the electron microscope, electron beams of wavelength 0.01 nm are produced and focused, using a system of magnetic lenses. A schematic diagram of an electron microscope is shown in figure 4.8.

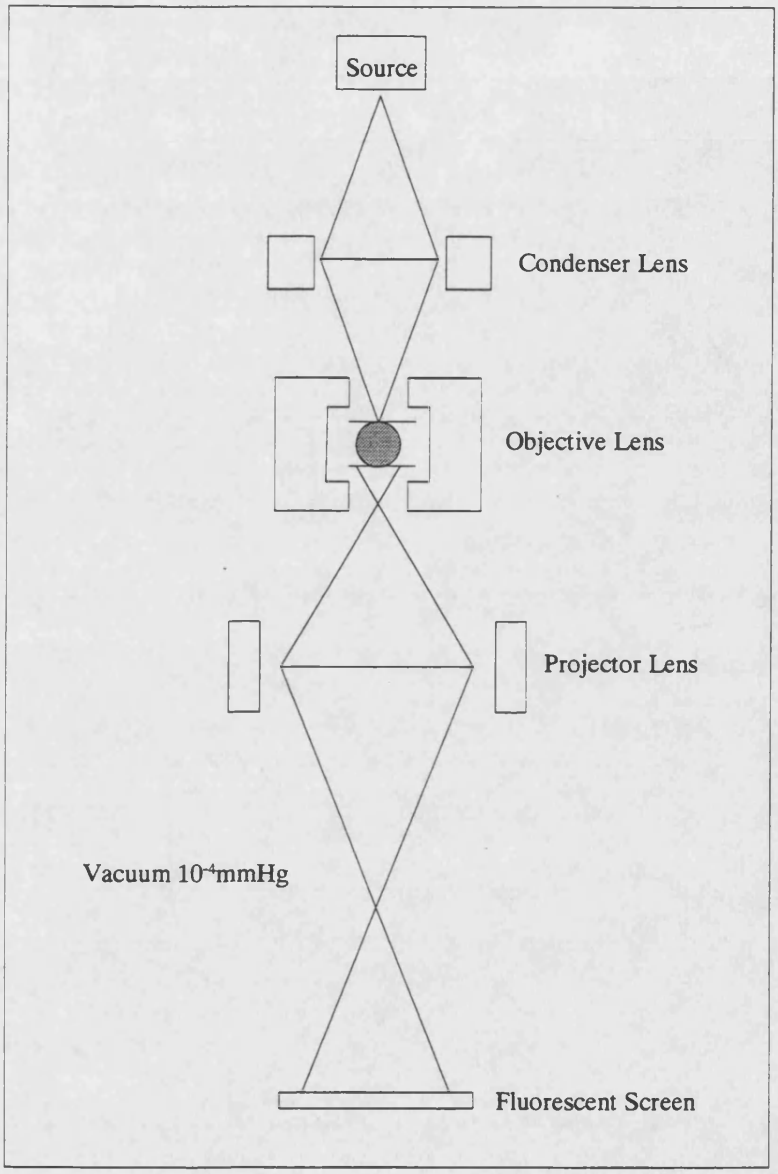

Figure 4.8. Schematic diagram of an electron microscope.

Although a number of different electron microscopes have been developed, in the present work we are concerned with the transmission electron microscope (TEM), which is generally the most useful. In this instrument thin samples are studied by transmitted electrons. The electrons are produced by a thermionic cathode and accelerated by a high voltage electric field. The column of the electron microscope is evacuated and the pressure maintained at 10^{-4}

mmHg, using an efficient pumping system. This minimises collisions, between electrons of the beam and gas molecules, which cause electron scattering. The electrons, emerging from the electron gun, are directed towards the condenser lens. This lens is a relatively weak lens, which focuses the electron beam onto the sample. The condenser is located halfway between the electron source and the sample, so that it forms an image of the source on the sample. The sample is located at the centre of the objective lens. The sample support consists of a fine copper mesh grid, about 3mm in diameter. The objective lens is a strong magnetic lens, which focuses the electron beam onto the sample and is the most critical component of the microscope.

The electrons collide with the sample and most are scattered, although some are absorbed. A narrow circular aperture is situated below the sample, which allows most of the transmitted electrons to pass through. Those electrons scattered at too great an angle, do not pass through the aperture and are eliminated from the beam. This results in a reduction in intensity, corresponding to the points in the sample from which the electrons were scattered. The cumulative effect of this process provides the contrast of the image. In the electron microscope focusing is accomplished, by varying the focal length of the objective lens. This is done by altering the current passing through the coils, which produce the magnetic field. A focused and magnified image of the sample is therefore obtained. The projector lens projects the final image onto the screen or photographic film. The electron intensity varies across the final image, which can be converted into a visual image by means of a fluorescent screen. The image produced can then be viewed directly or observed using a low power optical magnifier.

The electron image can also be viewed using a photographic method, which provides finer details than are possible with the fluorescent screen. The electron beam acts on photographic film, which after development produces a photographic negative (or electron micrograph) of the final electron image. The fine-grained negative provides a detailed image of greater contrast than that produced on the fluorescent screen.

4.4.2. Sample Preparation

The colloidal suspension to be studied was first cleaned, by a process of repeated centrifugation, then a dilute solution was prepared in hexane. A concentration of 0.15% was found to give good results. A single drop of the solution was applied to a microscope slide and the hexane was left to evaporate. When the sample had dried, the slide was placed in a vacuum evaporator and coated with a thin film of carbon. Initially, to enhance the contrast, the samples were shadowed in a vacuum evaporator, at a low angle, using gold. Subsequently, this was found to be unnecessary, as the carbon film alone provided sufficient contrast. This film or carbon replica, containing the sample, was floated off the microscope slide by means of a water meniscus. The slide had previously been washed, in a dilute detergent solution and allowed to dry, to ease the removal of the carbon film. The colloidal PMMA particles were dissolved out of the film, using 1,4-dioxane. This caused the film to break up, into small pieces. Suitably sized pieces were then mounted, on circular copper-mesh grids. These were left to dry thoroughly, in order to prevent the ingress of water molecules into the high vacuum inside the microscope.

4.4.3. Results

Once dry, the samples were inserted into the microscope and closely inspected. Negatives, or electron micrographs, were then produced, of areas of interest. The magnification was typically times 5000 to 10000. Photographs were also taken, at the same magnification, of a calibration grid with 2160 lines per mm. The negatives were developed and prints were made.

The electron micrographs were analysed, by means of a computerised imaging system. Each micrograph was illuminated and an image acquired using a digital camera, connected to a computer. Using the computer, the circular boundaries, of the colloidal particles, were delineated from the rest of the image. Electron micrographs, of different areas of the carbon replica, were analysed so that a large number of particle images were studied. A digitised image was also obtained, of an electron micrograph of the calibration grid, measured at the same magnification as the micrographs of the sample. This allowed the actual particle diameters to be determined, using the computer.

Electron micrographs were obtained (at x 5k) of the samples NH18, NH22 and NH23 and were analysed, using the method described above. For each sample, images of approximately five hundred particles were studied and the mean diameter (d) and polydispersity (σ) were determined. The results are collected together, in table 4.2 below.

Sample	Mean Diameter d / ± 30 nm	Polydispersity σ / ± 0.02
NH18	797	0.09
NH22	728	0.07
NH23	726	0.08

Table 4.2. Average particle diameters and polydispersities, obtained from the analysis of transmission electron microscopy (TEM) measurements.

In comparison with the results obtained by dynamic light scattering, the TEM diameters are slightly smaller. This probably reflects the fact that in the dynamic light scattering experiment the hydrodynamic radius is measured, rather than a bare core diameter.

4.5. Determination of the Phase Behaviour of Colloidal Hard Spheres

4.5.1. Introduction

In order to investigate the phase behaviour of hard sphere colloids, suspensions are required, which exhibit coexisting colloidal crystal and fluid phases. Such samples can be prepared, by careful selection of the concentration, so that the samples span the phase coexistence region of the phase diagram.[8] By measuring the volume of the crystalline phase in each sample, the phase diagram of volume % crystal vs. ϕ_c can be plotted. Extrapolation to 0 and 100% crystal then provides the freezing and melting volume fractions of the sample.[6]

4.5.2. Sample Preparation

The latex samples studied, consisted of index-matched suspensions of colloidal poly(methyl methacrylate) spheres, sterically stabilised by a thin layer of poly(12-hydroxystearic acid). The particles were synthesised in the one-step dispersion polymerisation reaction described in chapter 3. Stock dispersions were prepared in decahydronapthalene (decalin). The PMMA mass fraction of the dispersion was determined, by drying several small samples in a vacuum oven at 45°C. The falling mass of the samples was measured, over a period of several days, until the reading became constant.

The phase behaviour samples were prepared, using PMMA particles from the stock dispersion. A small amount of the dispersion was weighed into a $1cm^2$ cross section glass cell. As was mentioned earlier, carbon disulphide was added to the samples, which in combination with decalin provided a suspension medium, with a refractive index close to that of the particles ($n \approx 1.50$). The resulting index-matched samples could be studied, both visually and by light scattering methods. The following approach was used to index-match the samples. CS_2 was weighed into the cell, containing the colloidal dispersion, until the initially turbid sample became transparent and was approximately index-matched. As was mentioned earlier, the added carbon disulphide is absorbed preferentially into the amorphous PMMA cores of the colloidal particles. The absorption of CS_2 causes the particles to swell slightly, however previous work suggests that the particle radius increases by less than 3%.[54] The sample was left for several hours, to allow the adsorption of CS_2 to fully occur. Further CS_2 was then weighed into the cell, to replace that absorbed by the particles, giving an

accurately index-matched sample. The sample was then centrifuged for two hours, at 2000 rpm, until a distinct boundary was visible between the layer of amorphous sediment formed at the base of the cell and the clear supernatant above. Next, the sample was concentrated, by removing a measured mass of supernatant, to the desired core volume fraction. Core volume fractions were calculated, from the measured PMMA mass fraction of the dispersion and the literature values for the density of PMMA (ρ_{PMMA} = 1.188 gcm^{-3}) and the liquids ($\rho_{decalin}$ = 0.880 gcm^{-3}, ρ_{CS_2} = 1.260 gcm^{-3}). After concentration, the sample was sealed and weighed, in order that the rate of evaporation of the volatile carbon disulphide could be checked. This was usually found to be negligible (approximately 1%), over a period of several months. The particles were redispersed by vigorous shaking, using a mechanical shaker.

4.5.3. Experiment

The NH31 latex sample was found to consist of particles with a diameter of 916 ± 10 nm and a polydispersity of 0.07 ± 0.01, by dynamic light scattering measurements. Using a stock dispersion of this sample, nine index-matched samples were prepared, with core volume fractions ϕ_c = 0.385, 0.395, 0.40, 0.405, 0.410, 0.415, 0.420, 0.425 and 0.43. After vigorous shaking, to ensure that the colloidal particles were fully dispersed, the samples were left undisturbed and observed regularly. After 24 hours, small homogeneously nucleated crystals were visible in each sample. After three days, the crystals in the samples with volume fractions in the range $0.385 \leq \phi_c \leq 0.410$, had settled under gravity to form a distinct lower polycrystalline phase, above which was coexisting fluid. The

samples with volume fractions in the range $0.415 \leq \phi_c \leq 0.430$, remained filled with small colloidal crystals.

In one-component colloidal PMMA particles, the rate of crystallisation normally exceeds the rate of gravitational settling. Hence, the equilibrium phase behaviour can usually be determined under conditions of normal gravity.[8] In a study by Bartlett *et al.*, the phase behaviour of a suspension of PMMA spheres, of diameter 262 nm, was investigated.[52] Essentially the same phase diagram was obtained, under conditions of both time-averaged zero gravity and normal gravity. This suggests that for sufficiently small particles, the effects of gravity on the phase behaviour are minimal. In the present work the phase behaviour of the NH28 ($d = 397 \pm 10$ nm) and DMM7 ($d = 468 \pm 10$ nm) samples, which both consist of relatively small particles, was investigated under conditions of normal gravity as no sedimentation was observed. However, with the larger particles of the NH31 sample ($d = 916 \pm 10$ nm), significant sedimentation was observed over the time scale of the experiment. Several days after redispersing samples, in the coexistence region of the phase diagram, four distinct layers were observed as a result of gravitational settling. Just below the sample meniscus was a layer of clear supernatant, below this a layer of fluid, below this a polycrystalline layer and below this, at the bottom of the cell, was a layer of polycrystalline sediment. The resulting concentration gradients, make the quantitative analysis of the phase behaviour more difficult. In a study reported by Paulin and Ackerson, the phase diagram was determined by measuring the height of each layer boundary, in samples with initial concentrations spanning the phase coexistence region, over a period of several weeks.[53] A boundary height vs. time graph for each sample was plotted and the linear part of the layer boundaries extrapolated to zero time.[53]

This provided the crystal fractions corresponding to those in the absence of settling, which were used to plot the phase diagram. In the present work, the approach of Paulin and Ackerson was used to determine the phase behaviour of the NH31 sample. The height of the layer boundaries in each of the nine samples, were measured over 21 days. The crystal fractions corresponding to those in the absence of settling were then determined as described above. The phase diagram was then plotted, as shown in figure 4.9 below.

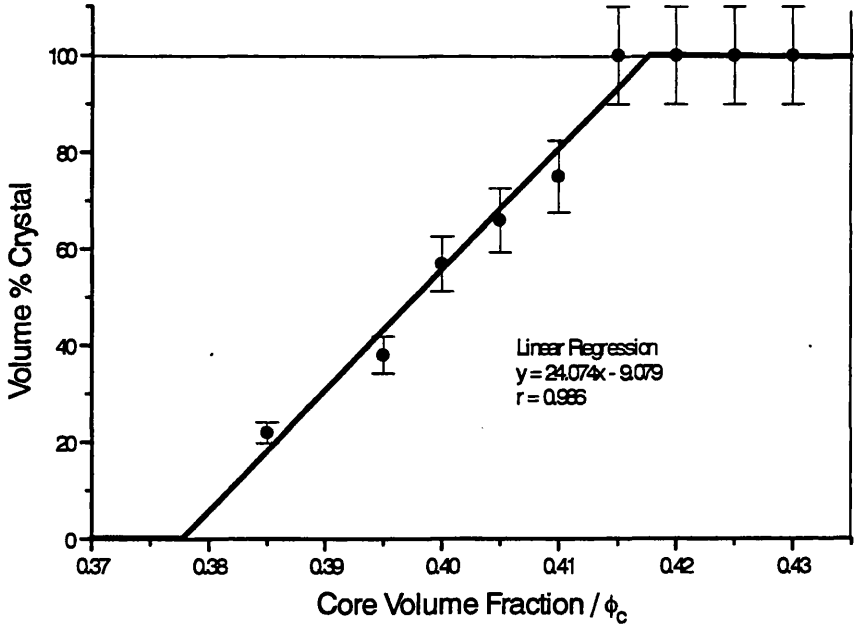

Figure 4.9. Volume % crystal, measured in NH31 phase behaviour samples, plotted as a function of the core volume fraction.

Extrapolation to 0 and 100% crystal provides the freezing and melting core volume fractions, $\phi^c_f = 0.378 \pm 0.005$ and $\phi^c_m = 0.418 \pm 0.005$. These values

do not agree with the theoretical hard sphere values of $\phi_f = 0.494$ and $\phi_m = 0.545$, determined by computer simulation.[46] The difference between the hard sphere and core volume fractions suggests an increase in particle size.[53] The particle size increase may be partly attributed to the solvation of the stabiliser layer, as this was not included in the calculation of ϕ_c, from the mass fraction of PMMA in the stock dispersion. The length of an extended poly(12-hydroxystearic acid) chain has been determined to be 10-20 nm, by small angle neutron scattering.[53] Hence, a similar value is expected for the thickness of the solvated stabiliser layer. Also, as was mentioned earlier, the adsorption of CS_2 by the PMMA cores, is expected to cause the particles to swell.[54] Furthermore, the PMMA cores of the particles also contain approximately 4% copolymerised methacrylic acid and possibly excess stabiliser trapped during the polymerisation.[7] Hence, the cores cannot be assumed to consist solely of PMMA. In the first investigation of the phase behaviour of colloidal PMMA particles, Pusey and van Megen accounted for these discrepancies by scaling the measured freezing core volume fractions, ϕ^c_f, to coincide with the theoretical hard sphere freezing volume fraction ϕ_f.[53] Hence,

$$\phi = \alpha \phi_c, \tag{4.29}$$

where ϕ is the effective hard sphere volume fraction and α is a factor, which incorporates all the uncertainties. In the present work, scaling the measured freezing volume fraction to coincide with the theoretical hard sphere point, gave a value of $\alpha = 1.307 \pm 0.005$ for the NH31 sample. Scaling all the other values by α provided an effective hard sphere melting concentration of $\phi_m = 0.546 \pm 0.005$, which is in excellent agreement with the theoretical hard sphere value of

0.545, determined by Hoover and Ree.[46] This close agreement supports the assumption of a steeply repulsive potential for the PMMA / PHSA system. The quantity,

$$\Delta R = R(\alpha^3 - 1), \qquad (4.30)$$

can be interpreted as an indication of the thickness of the solvated layer. In the present work, for the NH31 sample, a value of 43 ± 2 nm was calculated. Previous studies using the PMMA / PHSA system, suggest that ΔR can vary between about 6 and 34 nm. The value determined in the present work, is slightly higher than the upper value of 34 nm.

The quantity $(\phi_m - \phi_f) / \phi_f$ has been determined for theoretical hard spheres to be 10.3%.[10] Calculation of this quantity for NH31 gave a value of 10.6 ± 0.1 %, which is very close to the hard sphere value. These results are collected together in table 4.3.

The NH28 suspension was synthesised in a dispersion polymerisation and then redispersed in decalin, by the centrifugation process. Dynamic light scattering measurements indicated the average particle diameter to be 397 ± 10 nm and the polydispersity to be 0.07 ± 0.01. In order to investigate the phase behaviour of the NH28 dispersion, seven index-matched samples were prepared, with a range of concentrations ϕ_c = 0.38, 0.39, 0.40, 0.41 0.42, 0.44 and 0.46. After agitation, to ensure complete redispersal, the samples were left undisturbed and observed at regular intervals. Three weeks later, homogeneously nucleated crystallites were observed in all but the ϕ_c = 0.38 sample. After a further four weeks, the following observations were made. No crystals were visible in the ϕ_c

= 0.38 sample, which suggested that this sample was below the freezing transition. In the ϕ_c = 0.39, 0.40, 0.41 and 0.42 samples, the small crystals had settled under gravity. Two distinct regions were observed, a crystalline phase and above, a coexisting fluid phase. In the ϕ_c = 0.44 and 0.46 samples, small crystals were visible throughout the sample volume. The fractions of the volumes of the samples, occupied by the crystalline phases, were measured and the results obtained are shown below.

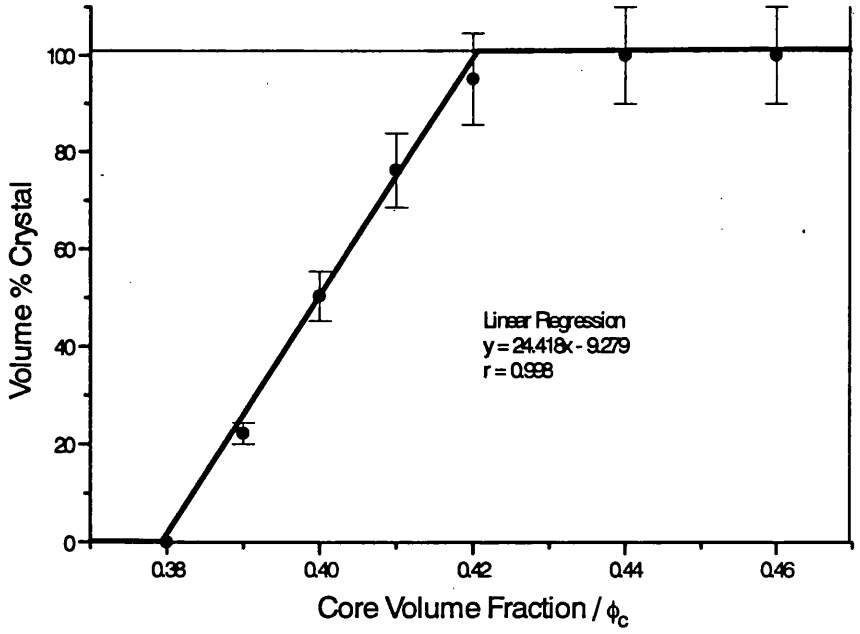

Figure 4.10. Experimentally determined volume % crystal of NH28 samples, vs. core volume fraction.

The freezing and melting concentrations, $\phi^c_f = 0.380 \pm 0.005$ and $\phi^c_m = 0.421 \pm 0.005$, were obtained by extrapolation to 0 and 100% crystal. The scaled effective hard sphere melting volume fraction was found to be $\phi_m = 0.548 \pm 0.005$, which is quite close to the theoretical value of 0.545.[46] A value of 19 ± 2 nm was obtained for the quantity ΔR, which is in the 12 – 34 nm range expected. The value $(\phi_m - \phi_f) / \phi_f$ was also calculated and found to be 10.8 ± 0.1%. This is again in excellent agreement with the hard sphere value of 10.3%.

The DMM7 colloidal dispersion was made prior to the present work. The sample was redispersed in decalin and then dynamic light scattering measurements were made. This provided a number average particle diameter of 468 ± 10 nm. In order to investigate the phase behaviour, seven samples were prepared with core volume fractions spanning the phase coexistence region, ϕ_c =

0.40, 0.41, 0.42, 0.43, 0.44, 0.45 and 0.46. The samples were agitated, to ensure complete dispersion of the colloidal particles, then left undisturbed and observed regularly. After several days no crystals were visible. However, after three and a half weeks crystals were visible in all the samples. In the ϕ_c = 0.40, 0.41, 0.42, 0.43, and 0.44 samples, distinct coexisting fluid and crystalline phases were observed. In the ϕ_c = 0.45 and 0.46 samples, homogeneously nucleated crystals were observed throughout the sample volume. The volume of crystal in each sample was measured and the results obtained are shown in figure 4.11.

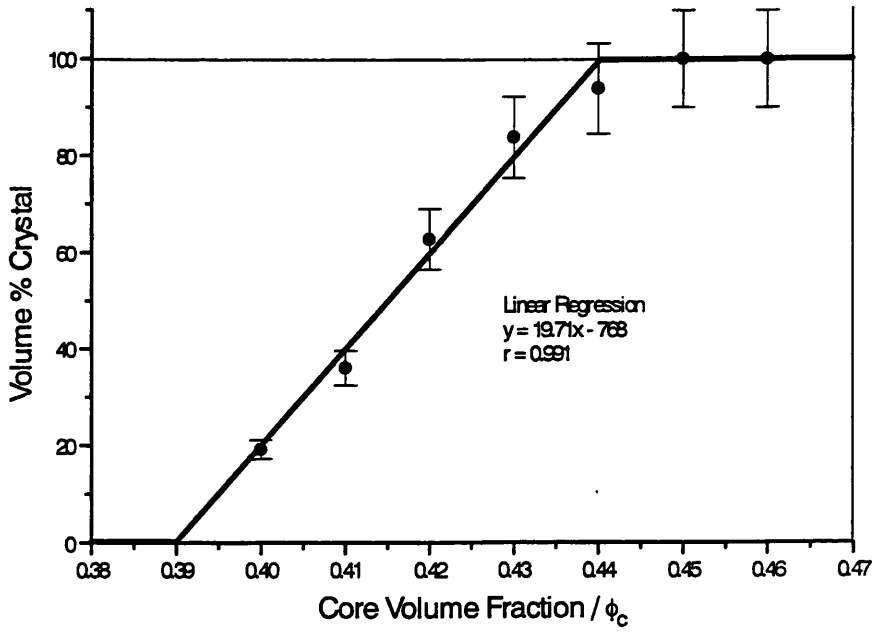

Figure 4.11. Volume % crystal vs. core volume fraction. Phase behaviour samples of DMM7, measured experimentally, in the present work.

Extrapolation to 0 and 100% crystal provided a freezing concentration of ϕ^c_f = 0.390 ± 0.005 and a melting concentration of ϕ^c_m = 0.440 ± 0.005. The

freezing concentration was identified with the hard sphere freezing volume fraction of $\phi_f = 0.494$. The effective hard sphere melting volume fraction was then calculated, by the appropriate scaling of the measured melting concentration. A value of $\phi_m = 0.557 \pm 0.005$ was obtained. This is reasonably close to the theoretical hard sphere value of 0.545, determined by Hoover and Ree.[46] The difference is probably no greater than the experimental uncertainty arising from the imprecise location of the fluid-solid phase boundaries, which change slowly with time due to slow sedimentation of the particles.[5] The effective layer thickness was calculated and a value of $\Delta R = 19 \pm 2$ nm was obtained, which is in the 12 – 34 nm range predicted by previous work. The value of $(\phi_m - \phi_f) / \phi_f$ was determined to be 12.8 ± 0.1%, which is slightly higher than the predicted hard sphere value of 10.3%.

The SPS09 latex sample was prepared prior to the present work and was obtained in order to combine with other samples to make binary mixtures.[10] Previous characterisation work had determined the particle diameter to be 652 ± 10nm and the polydispersity to be low. Also, the freezing and melting concentrations were $\phi^c_f = 0.419 \pm 0.005$ and $\phi^c_m = 0.463 \pm 0.005$. The appropriate scaling of the melting concentration provided a hard sphere value of $\phi_m = 0.546 \pm 0.005$. This is close to theoretical value of 0.545, calculated by Hoover and Ree.[46] Calculation of the effective layer thickness gave a value of $\Delta R = 18 \pm 1$ nm. This within the 12 – 34 nm range determined by previous work. Also, $(\phi_m - \phi_f) / \phi_f$ was calculated to be 10.5 ± 0.1%, which is close to the theoretical hard sphere value of 10.3%.

In table 4.3, the experimentally determined core volume fractions (ϕ^c_f) of the fluid phase at crystallisation and the core volume fraction of the crystal phase

at melting (ϕ^c_m) are given, together with the calculated value of α and the resulting scaled freezing (ϕ^{hs}_f) and melting (ϕ^{hs}_m) hard sphere volume fractions for each one-component suspension, are also shown. In addition, the effective solvated layer thickness ΔR is also listed.

Sample	$\phi^c_f \pm$ 0.005	$\phi^c_m \pm$ 0.005	$\alpha \pm$ 0.005	ΔR / ± 2 nm	ϕ^{hs}_f	$\phi^{hs}_m \pm$ 0.006	$(\phi^c_m - \phi^c_f)/\phi^c_f$ ± 0.1%
NH31	0.378	0.418	1.307	43	0.494	0.546	10.6
SPS09	0.419	0.463	1.179	18	0.494	0.546	10.5
NH28	0.380	0.421	1.300	19	0.494	0.548	10.8
DMM7	0.390	0.440	1.267	19	0.494	0.557	12.8

Table 4.3. Characterisation of the phase behaviour of four one-component colloidal dispersions, NH31, SPS09, NH28 and DMM7. The SPS09 results were obtained in earlier work.

4.6. Conclusions

Colloidal polymer particles were synthesised in a one-step dispersion reaction, as was described in chapter 3. The average size of the particles produced was varied, by changing the initial monomer concentration used in the reaction.[7] The mean diameter (d) and polydispersity (σ) of the particles, was determined by means of dynamic light scattering (DLS). The results are collected together in tables 3.5, 3.7 and 3.8, in chapter 3 and in table 4.1 in this

chapter. Measurements were also made by means of transmission electron microscopy (TEM) and these results are given in table 4.2. The results of the two approaches are very similar, although DLS is slightly more accurate. As the DLS method is more straightforward than the TEM approach, most size and polydispersity measurements were made by means of DLS.

The phase behaviour of the one-component colloidal dispersions NH31, NH28 and DMM7, was investigated. For each dispersion, index-matched samples were prepared with core volume fractions spanning the phase coexistence region ($\phi^c_f \leq \phi_c \leq \phi^c_m$). After redispersing, these samples were left undisturbed and observed regularly over several days, or weeks. Coexisting crystalline and fluid phases formed and the volume of the equilibrium crystal phase was measured. The results are shown in the phase diagrams in figures 4.9, 4.10, 4.11. In each case, extrapolation to 0 and 100% crystal provided the core volume freezing (ϕ^c_f) and melting (ϕ^c_m) concentrations. The freezing concentration was identified with the hard sphere freezing volume fraction, ϕ_f = 0.494, determined by computer simulation.[46] The effective melting volume fraction (ϕ_m) was then calculated, by the appropriate scaling of the measured core volume melting fraction (ϕ^c_m). For each colloidal dispersion, the effective hard sphere melting volume fraction was compared with the theoretical hard sphere value. In each case, close agreement was found. The quantity $(\phi_m - \phi_f) / \phi_f$, was also determined for each sample and again, good agreement with the theoretical hard sphere value was found.

CHAPTER 5

5. STATIC LIGHT SCATTERING

5.1. Introduction

Colloidal particles have characteristic dimensions comparable to the wavelength of visible light. As a result, light scattering techniques are probably the most commonly used experimental methods, for determining the structure and dynamics of colloidal suspensions. Lasers provide an intense source of visible light with defined wavelengths and polarisation.

In the present work, the structures of colloidal crystals were determined by means of static (or conventional) light scattering. In both one-component and binary suspensions of colloidal PMMA particles, crystallisation was homogeneously nucleated, providing a large number of randomly oriented crystallites. These polycrystalline powders were particularly suitable for analysis by static light scattering, which provided the analogue of X-ray powder diffraction patterns.

A quantitative study of the intensity measurements was not undertaken. Instead, the structures were identified from the locations of the peaks in the scattering profile. Static light scattering was also used to determine the particle diameters, in one-component suspensions.

5.2. Static Light Scattering Theory

In static light scattering, the time-averaged intensity of light scattered by a colloidal sample is measured as a function of scattering angle, or of the

scattering vector q, the magnitude of which is given by q,

$$q = |q| = \frac{4\pi n}{\lambda}\sin\frac{\theta}{2}, \qquad (5.1)$$

where λ is the wavelength of the incident light *in vacuo*, n is the refractive index of the suspension medium and θ is the scattering angle, the angle between the incident and scattered light. The geometry of a light scattering experiment is illustrated schematically in figure 5.1 below.

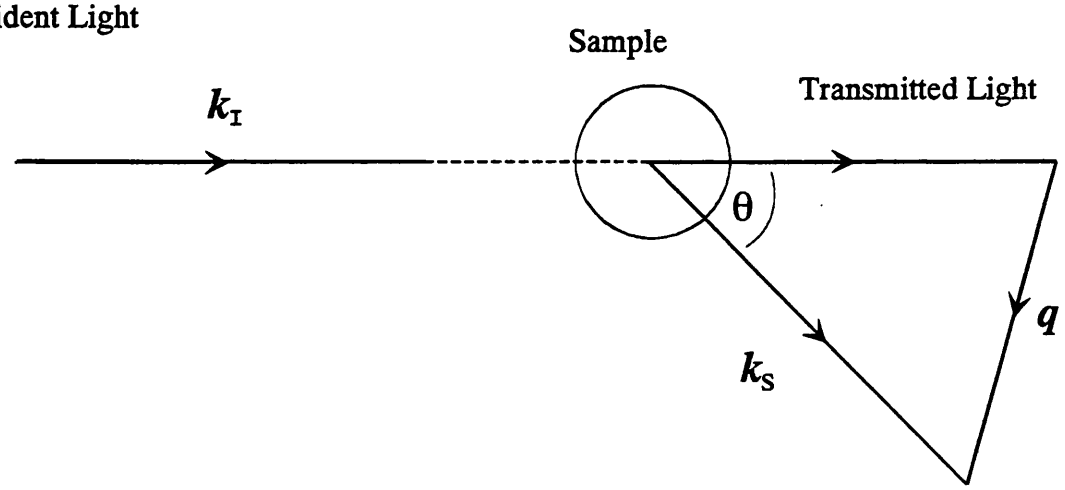

Figure 5.1. Schematic illustration of the geometry of a light scattering experiment. The scattering vector q is the difference between the vectors of the incident and scattered light, k_I and k_S.

The incident light is assumed to be polarised, with its electric vector perpendicular to the scattering plane. It is also assumed that the suspension medium is homogenous, with refractive index n and that the individual particles have a scalar refractive index profile $n_i(r)$, where r is the radial distance from the

centre of the particle. Light scattering then only occurs due to the difference between the refractive indices of the particles and the liquid. Also, the particles are assumed to scatter sufficiently weakly, that only single scattering occurs. In this situation, the amplitude of the electric field of light scattered by a single particle, *i*, has been given as[5]

$$b_i(q) = 4\pi \int_0^\infty dr r^2 [n_i(r) - n](\sin qr)/qr\,, \tag{5.2}$$

The expression for the instantaneous amplitude of the electric field of light, scattered by an assembly of *N* identical particles, is the sum of the light scattered by the individual particles[5]

$$E(q,t) = \sum_{i=1}^{N} b_i(q) \exp[iq \cdot r_i(t)]\,, \tag{5.3}$$

where $r_i(t)$ is the position of the centre of particle *i* at time *t*. The intensity of the scattered light at any given moment is[5]

$$I(q,t) = |E(q,t)|^2. \tag{5.4}$$

The associated average intensity is then given by[5]

$$< I(q) > = \sum_{i=1}^{N} \sum_{j=1}^{N} < b_i(q) b_j(q) \exp[iq \cdot (r_i - r_j)] >\,, \tag{5.5}$$

The angular brackets describe an ensemble average and this equation applies only to systems, which are orientationally invariant, such as a suspension of identical spheres in the fluid phase. A powder of colloidal crystallites, is also orientationally invariant. In this case, a spatial average is obtained over all the randomly oriented crystallites.

For any dispersion of polymer colloids, there will be a distribution of particle radii (R). The distribution may be concisely described in terms of the polydispersity σ, where

$$\sigma^2 = \frac{< R^2 >}{< R >^2} - 1. \qquad (5.6)$$

In this case, equation (5.5) cannot be simplified further. The effects of a finite polydispersity have been discussed in detail, by Pusey.[5]

However, if the system is assumed to be monodisperse, then the field of light $b_i(q)$ scattered by each particle will be identical. Hence, $b_i(q) = b_j(q)$, so that equation 5.5 can be re-written as[5]

$$<I(q)> = N[b(0)]^2 P(q)S(q), \qquad (5.7)$$

where $P(q)$ is the single-particle form factor and $S(q)$ is the static structure factor. $P(q)$ can be written as[5]

$$P(q) = [b(q) / b(0)]^2. \qquad (5.8)$$

$P(q)$ represents the contribution to the scattering intensity, which depends upon the size, shape and refractive index of the individual particles. $S(q)$ is defined by the ensemble average[5]

$$S(q) \equiv \frac{1}{N} \sum_{i=1}^{N} \sum_{j=1}^{N} < \exp[iq \cdot (r_i - r_j)] > . \qquad (5.9)$$

$S(q)$ represents the structure of the sample, in terms of the average spatial arrangement of the particles. For individual spherical particles of radius R and refractive index n_p, equations (5.1) and (5.8) can be readily evaluated to give[5]

$$P(qR) = \frac{9}{(qR)^6} [\, \sin qR - qR\cos qR \,]^2. \qquad (5.10)$$

For a monodisperse system, the structure factor can be determined experimentally by measuring the q-dependence, of the intensity scattered by the concentrated suspension of interest and dividing this by the intensity scattered by a dilute suspension for which $S(q) = 1$. For a concentrated suspension of hard spheres in a fluid state, the main peak in the structure factor $S(q)$ occurs at $qR \approx 3.5$, whereas the form factor $P(q)$ has its primary minimum at $qR \approx 4.49$ (see figure 5.2).

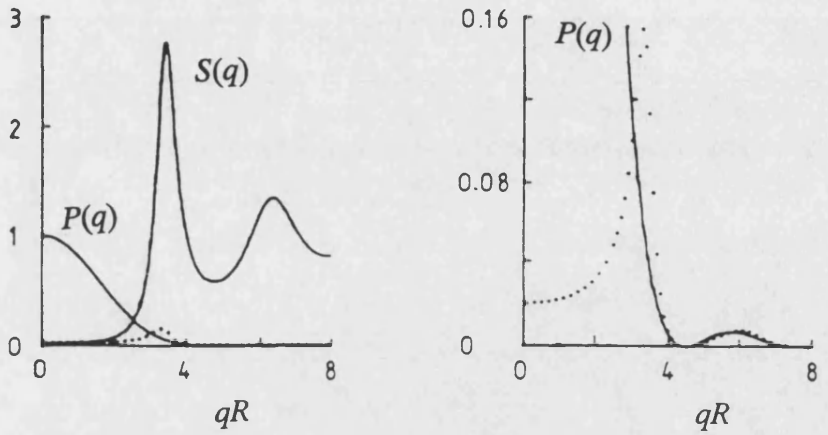

Figure 5.2. From Pusey *et al.*[5] The theoretical form factor $P(q)$, structure factor $S(q)$ and the scattered intensity for identical homogeneous hard spheres at ϕ = 0.47. $S(q)$ was calculated from the Percus-Yevick expression.[55]

At values of qR greater than 4.5, the intensity scattered by the suspension is weak and easily corrupted by background or multiple scattering.[28] Hence, accurate measurements of $S(q)$ can only be reliably calculated up to the first peak. Also, the hard sphere colloidal particles used in experiments are not monodisperse. While the form factor can be weighted approximately to incorporate this polydispersity[5], the experimental uncertainty due to smearing with polydispersity becomes worse at large qR.

In the PMMA / PHSA colloidal system, used in the present work, another factor must be considered. In accurately index-matched suspensions, the PMMA particle core and the PHSA stabiliser layer can have significantly different refractive indices.[5] In this case the particles cannot be regarded as homogeneous. Interference occurs, between the light scattered by the PMMA core and the PHSA stabiliser layer, resulting in a complex form factor. This form factor is a

sensitive function of the suspension conditions.[95] In such cases, the experimental uncertainty can be reduced, by measuring the form factor in a dilute suspension, under conditions that are as far as possible the same as those of the concentrated suspension whose structure factor is required.[95] In the present work, absolute intensities were not measured. Instead, the structure of colloidal crystals, which formed from binary suspensions, were identified from the locations of the peaks in the scattering patterns.

5.3. Light Scattering from Colloidal Crystals

The effective potential between two PMMA / PHSA colloidal particles, although continuous, is very steep and is thought to be a close approximation of the classical hard sphere interaction. Evidence for this assumption comes from the good agreement, between the predictions of hard sphere computer simulations and experiments with binary mixtures of colloidal particles.[76] Due to the short-ranged, non-directional, nature of the hard sphere interaction, the structure of hard sphere colloidal crystals is close packed. Close packed structures can be visualised, in terms of the stacking of planes of hexagonally arranged close packed particles.[90,91] The scattering from a single layer, of hexagonally arranged particles, consists of Bragg rods in reciprocal space, normal to the plane of the layer.[91]

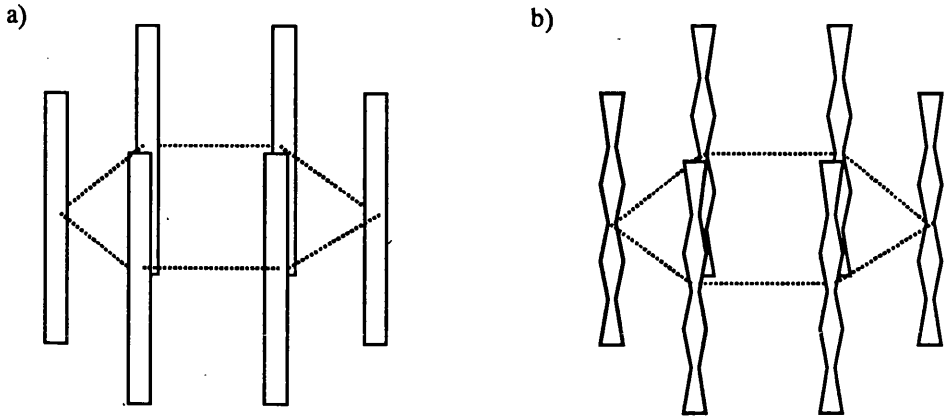

Figure 5.3. (a) Uniform Bragg rods corresponding to a single hexagonal layer and (b) Bragg rods of modulated intensity associated with stacked hexagonal layers.

The Bragg rods are illustrated schematically in figure 5.3. The positions of the rods in the plane of the layer is hexagonal, with a spacing in reciprocal space of $a^* = 4\pi / a\sqrt{3}$, where a is the lattice constant of the original lattice. A system of Bragg rods $\{h,k\}$ can be indexed as shown in figure 5.4.

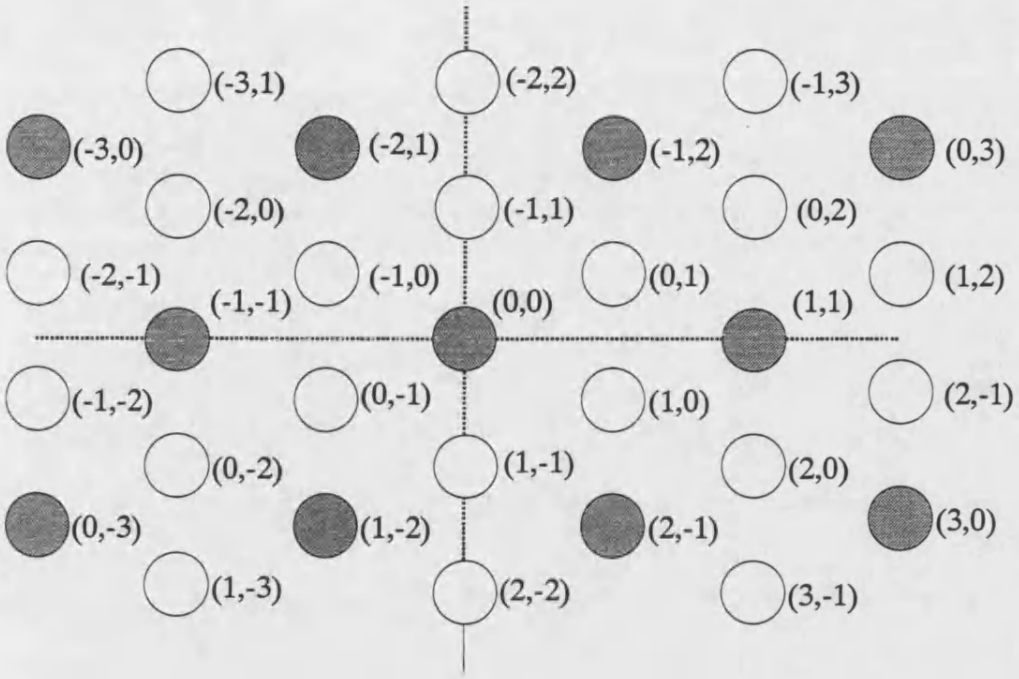

Figure 5.4. Schematic diagram of Bragg rods, in the plane of the layer, with crystallographic indices. Shaded circles correspond to Bragg rods with indices (h - k) = 3n and unshaded circles depict those rods with indices (h - k) ≠ 3n.

As was mentioned earlier, in chapter 2, the stacking of a sequence of layers of hexagonally arranged colloidal hard spheres is expected adopt a degree of randomness.[56] Pusey and co-workers proposed that the probability that layers n and n+2 have different positions can be defined as α, where α = 0 gives hcp, α = 1 gives fcc and α = 0.5 is a completely random stacked close packed structure.

The stacking of the layers produces modulations of intensity, along the Bragg rods, as illustrated in figure 5.3(b). The actual position of the Bragg rods is determined only by the interparticle spacing in the layer and does not change with the stacking sequence. There are two types of Bragg rod, those with indices (h - k) = 3n and those with indices (h - k) ≠ 3n (n is an integer). For the (h - k) =

$3n$ rods the intensity variations are independent of the stacking sequence. The intensity appears as points on the rods, at integral values of l, which correspond to those Bragg reflections common to both fcc and perfect hcp structures. For Bragg rods with indices $(h - k) \neq 3n$, the intensity distribution varies with index l along the lines {hk}, in a manner determined by the stacking probability α. For perfect fcc structures ($\alpha = 1$) there are intensity nodes on the rods, alternately at $l + 1/3$ or $l - 1/3$ with integer l. In the case of perfect hcp structures ($\alpha = 0$) intensity points appear on the rods, at integer l and $l + 1/2$. However, for even a small number of defects in these perfect structures, the reflections in the $(h - k) \neq 3n$ rods are broadened. If the layers are stacked randomly, as is the case for colloidal crystals[56], the reflections become a diffuse scattering background in the powder pattern. For completely random stacking ($\alpha = 0.5$) the intensity oscillates, between 1 at $2l$ even and 9 at $2l$ odd.[56] This is illustrated in figure 5.5 below.

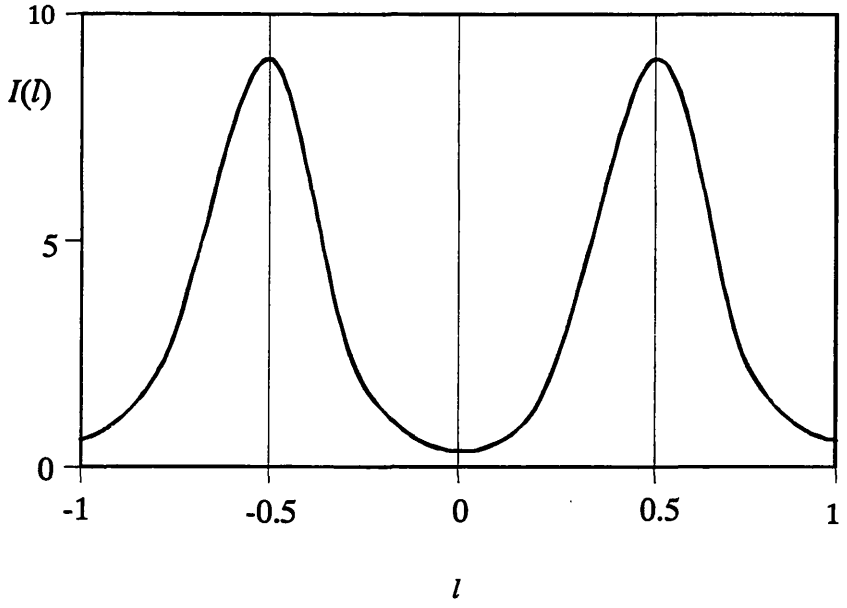

Figure 5.5. Distribution of scattering intensity $I(l)$ along the Bragg rods with indices $(h - k) \neq 3n$, for random close packing ($\alpha = 0.5$).

The reciprocal lattice of a colloidal crystal can be defined as the set of all wave vectors $\boldsymbol{K}$, that yield plane waves with the same periodicity as the colloidal crystal. The light scattered by a colloidal crystal can then be considered in terms of the Von Laue condition, which states that constructive interference will occur provided that the scattering vector q is equal to a vector of the reciprocal lattice. The Von Laue condition can be expressed as

$$q = \boldsymbol{K}_{hkl}, \tag{5.11}$$

where the reciprocal lattice vector $\boldsymbol{K}_{hkl}$ is given by

$$\boldsymbol{K} = h\boldsymbol{b}_1 + k\boldsymbol{b}_2 + l\boldsymbol{b}_3. \tag{5.12}$$

Here (b_1, b_2, b_3) are the primitive vectors of the reciprocal lattice and h, k and l are integers. The wave vectors of the reciprocal lattice can be expressed in terms of $\left\{\frac{Qa_{fcc}}{2\pi}\right\}$, where a_{fcc} is the edge length of an equivalent fcc unit cell, in the direct lattice.[15] There is then a straightforward relationship, between the wave vectors for which constructive interference occurs and the Miller indices h,k,l. For a fcc lattice, scattering occurs from the lattice planes normal to the reciprocal lattice vector, K_{hkl}, with Miller indices h,k,l, when the condition below is satisfied

$$\left\{\frac{Qa_{fcc}}{2\pi}\right\}^2 = h^2 + k^2 + l^2. \tag{5.13}$$

For a hcp lattice, scattering occurs when

$$\left\{\frac{Qa_{fcc}}{2\pi}\right\}^2 = \frac{8}{3}(h^2 + k^2 + hk) + \frac{3}{4}l^2. \tag{5.14}$$

However, constructive interference does not occur for all reciprocal lattice vectors, due to interference arising from the particles in the unit cell. This additional condition for a scattering peak, can be considered in terms of the geometrical structure factor.

$$S_K = \sum \exp[-i(\boldsymbol{K} \cdot \boldsymbol{r}_j)]. \tag{5.15}$$

The structure factor is the sum of all the scattering contributions from the particles j at locations r_j in the unit cell. Depending on the lattice structure, for certain combinations of the Miller indices the structure factor will be zero and no scattering will occur. For fcc lattices, reflections are missing if *h,k,l* are mixed even and odd integers. If *h,k,l* are all odd, the corresponding reflection is altered. For hcp lattices, reflections are missing if $\frac{1}{3}(2h + k) = n$ and l is odd, where n is an integer. In the case of the random stacked close packed structure, characteristic of one-component hard sphere colloidal crystals, the conditions for which reflections are absent are harder to ascertain. Defining the unit cell is rather more complicated. However, providing $0 < \alpha < 1$ the diffraction pattern may be obtained, from a weighted average of the fcc and hcp scattering patterns. For $\alpha = 0.5$, the only scattering peaks in the pattern are those which are present in both the fcc and hcp scattering profiles (see table 5.1).

$\left\{\frac{Qa_{fcc}}{2\pi}\right\}^2$	fcc ($\alpha = 1$) *hkl*	hcp ($\alpha = 0$) *hkl*	rcp ($\alpha = 0.5$) *hkl*
2.67		100	
3	111	002	Present
3.42		101	
4	200		
5.67		102	
8	220	110	Present
9.42		103	
10.67		200	
11	311	112	Present
11.42		201	
12	222	004	Present

Table 5.1. Wave vectors expressed in units of $\left\{\frac{Qa_{fcc}}{2\pi}\right\}^2$, at which reflections can be found for fcc and hcp crystals and for a perfectly randomly stacked close packed crystal.

In the present work, because the stacking in hard sphere colloidal crystals is essentially random ($\alpha \sim 0.5$) the scattering peaks were indexed on the lines, which are present in both the fcc and hcp scattering profiles. Because the index-matched samples had a complicated form factor, structures were identified by the positions of the peaks in the scattering patterns.

5.4. Experiment

In the present work, the structure of hard sphere colloidal crystals was investigated experimentally, by means of the light scattering analogue of powder X-ray crystallography. The equipment used is illustrated schematically in figure 5.6. Approximately 1 cm^3 of the sample volume was illuminated, with an expanded beam of laser light. This volume was expected to contain a large number (~10^6) of randomly oriented crystallites, 25 – 50 μm in size[56], so a large statistical sample was studied. The intensity of the scattered light was measured over a range of angles and this provided orientationally-average scattering data, equivalent to 'powder' diffraction patterns. As mentioned in chapter 1, the colloidal particles were suspended in an index-matching mixture of decalin and carbon disulphide. The resulting samples were almost transparent and exhibited strong single scattering of light, but weak multiple scattering.

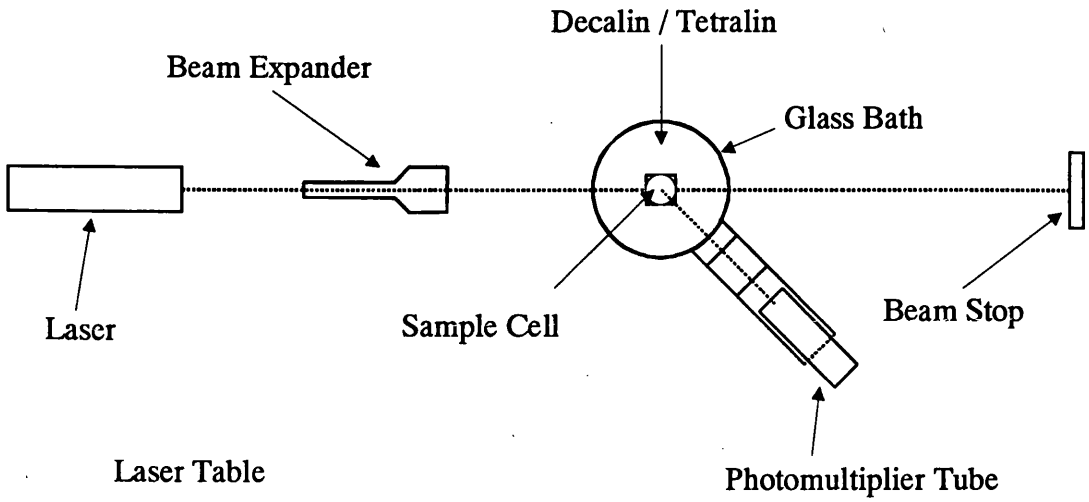

Figure 5.6. Schematic diagram of the arrangement of the static light scattering equipment.

The light scattering apparatus was attached to a purpose-built laser table. The materials used, in the construction of the table, isolated the apparatus from external vibrations. A krypton / argon ion water-cooled laser was used, which produced laser light at discrete wavelengths in the range 488 nm to 647 nm. The path of the transmitted laser beam was terminated at the beam stop. The glass sample cell, which was 1 cm^2 in cross section, was located at the centre of a cylindrical glass bath. The bath was filled with a mixture of decalin and tetralin, at room temperature. The ratio of the two liquids was chosen, so that the refractive index of the mixture ($n \approx 1.52$) closely matched the refractive indices of the colloidal suspension and approximately matched that of the glass sample cell. When filled with liquid, the bath acted as a cylindrical lens, focusing the parallel light scattered by the sample onto the detection optics. These optics consisted of a narrow vertical slit, followed by a diffuser and a photomultiplier tube, all mounted on a goniometer arm. This arm could be rotated around the

axis of the bath, allowing the detection angle to be varied. The movement of the arm was controlled by a computer, which allowed the scattering angle to be accurately selected. Intensity measurements were made at angles from 20° to 140°, at increments of 0.20°, which took just under 15 minutes to complete. The angular resolution of the optics was approximately 0.25°.[56]

5.4.1. Light Scattering from One-Component Colloidal Crystals

Light scattering measurements were made on one-component suspensions, which exhibited coexisting crystalline and fluid phases. Index-matched suspensions were prepared, using fractions of the NH28, NH31 and DMM7 dispersions. As was mentioned earlier, crystals of almost identical hard sphere colloids have a random-stacked close packed structure (rcp).[56] The scattering pattern, of these crystals, can be considered as a weighted average of the fcc ($\alpha = 1$) and hcp ($\alpha = 0$) intensity profiles. For $\alpha = 0.5$, the only peaks in the scattering pattern are those that are present in both the fcc and hcp profiles (see table 5.1). The scattering pattern obtained for the index-matched DMM7 suspension, is shown in figure 5.7 below (the intensity, in arbitrary units, is plotted as a function of the scattering vector q). The sample was prepared, with an effective hard sphere volume fraction, $\phi = 0.55$.

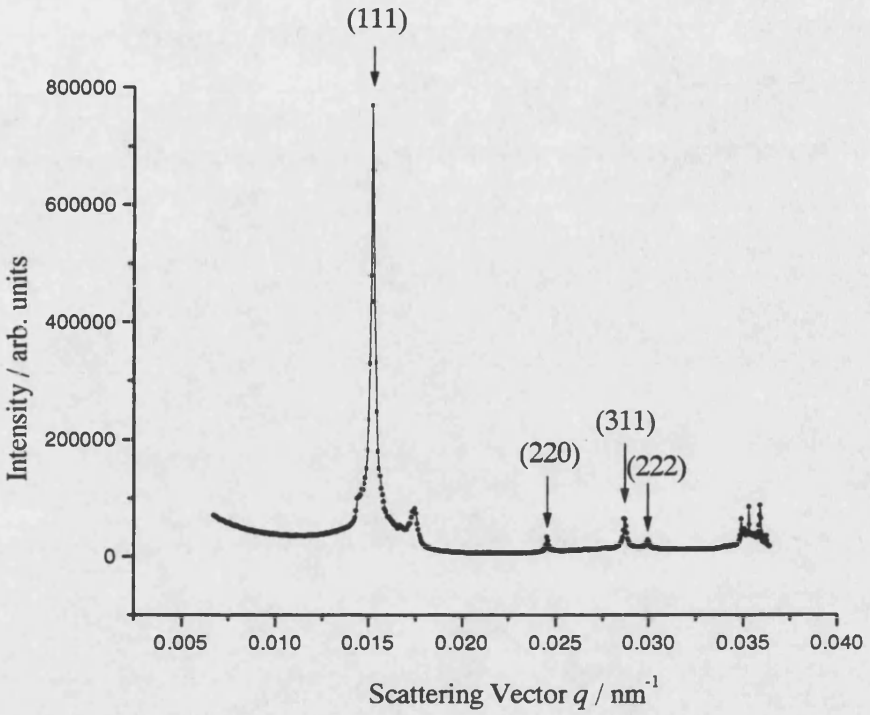

Figure 5.7. Scattering intensity profile of a one-component hard sphere colloidal suspension, DMM7, which exhibited coexisting crystalline and fluid phases. The sample was prepared with a volume fraction $\phi = 0.55$.

As was mentioned earlier, because the form factors of the individual particles are difficult to determine in near index-matched samples, an analysis of the intensities of the scattering patterns was not made. However, structures were identified from the positions of the peaks.[11] In figure 5.7, the sharp Bragg reflection and broad band of diffuse scattering is characteristic of a random-stacked close packed crystal. Pusey and co-workers have explained the features of the scattering pattern, of a one-component colloidal crystal, in terms of the expansion of a sphere, centred in reciprocal space.[56] The features of the real space intensity profile, are directly related to the product of the portion of the

area of the sphere surface, which intersects a region in reciprocal space and the intensity of the region. As size of the sphere is increased, from $q = 0$, a narrowing of intensity is found upon the intersection of the sphere with the six diffraction broadened $\{10l\}$ rods at $l \approx 0$. The diffuse pre-peak, in the scattering of figure 5.7, is due to the magnitude this overlap and not from a peak of intensity in reciprocal space. As the sphere is expanded further, the {001} Bragg peaks are acquired from the 00l line. These peaks are the principal reflections from the close-packed layers. For fcc indexed on a cubic basis, this is one set of (111) layers and for hcp on a hexagonal basis 002. These reflections should be observed for any stacking sequence, since the scattering vector q is perpendicular to the planes. The next peak, in the diffuse scattering (see figure 5.7), corresponds to the intersection of the sphere with the peaks at $l = \pm 1/2$ on the $\{10l\}$ rods.

The measured DMM7 peaks were indexed on the lines of a fcc lattice, as follows. For the intense Bragg reflection at $q = 0.0152$ nm^{-1}, (111). The next peak visible in the scattering profile, at $q = 0.0175$ nm^{-1} is not common to both fcc and hcp structures. However, the following three peaks are. These were indexed as $q = 0.0246$ nm^{-1} (220), $q = 0.0288$ nm^{-1} (311) and $q = 0.0300$ nm^{-1} (222). The corresponding lattice parameter, a = 507 ± 6 nm and also the average particle diameter, $d = 463 \pm 6$ nm, were determined. The scattering at high q values is due to back reflection.

Static light scattering measurements of an index-matched NH28 suspension are illustrated in figure 5.8. The volume fraction was $\phi = 0.56$ and homogeneously nucleated crystallites and colloidal fluid were visible by eye.

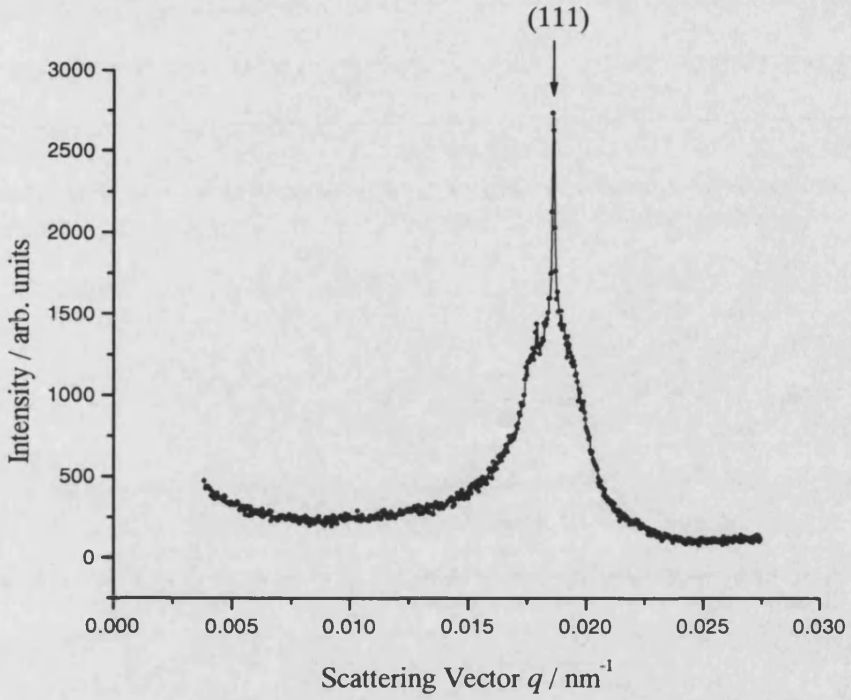

Figure 5.8. Static light scattering measurements, of a one-component dispersion of colloidal hard spheres, sample NH28. The original volume fraction was ϕ = 0.56 and crystals were visible throughout the sample.

The intense Bragg reflection and broad band of diffuse scattering, is consistent with a random stacked close packed crystal. The measured peak, at q = 0.0187 nm^{-1}, was indexed on the (111) line of a fcc lattice. The corresponding lattice parameter was calculated to be 409 ± 6 nm. Also, the average particle diameter, d = 375 ± 6 nm, was determined.

Light scattering measurements were also made on an index-matched sample, prepared with the NH31 dispersion. The effective hard sphere volume fraction, ϕ = 0.55, was between the freezing concentration and glass transition and crystals were observed. The results are shown in figure 5.9.

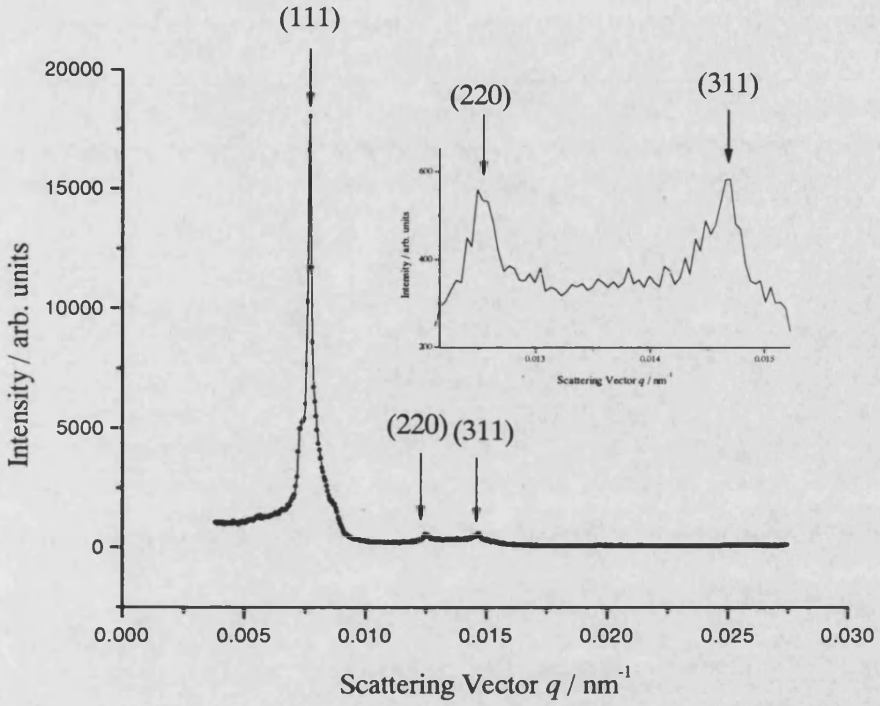

Figure 5.9. Light scattering measurements of a one-component suspension, of colloidal hard spheres, sample NH31. The sample was prepared with a volume fraction $\phi = 0.55$. For clarity, part of the scattering profile is enlarged (inset).

The scattering profile is characteristic of a powder of random-stacked close packed crystallites. The measured Bragg reflections were indexed as follows, q = 0.00782 nm^{-1} (111), q = 0.0125 nm^{-1} (222), q = 0.0147 nm^{-1} (311). The lattice parameter, a = 989 ± 6 nm and the particle diameter, d = 897 ± 6 nm, were calculated.

The measured particle diameters and lattice parameters, determined by light crystallography, are collected together in table 5.2 below.

Sample	ϕ	Lattice Parameter a / ± 6 nm	Diameter d / ± 6 nm
DMM7	0.55	507	463
NH28	0.56	409	375
NH31	0.55	989	897

Table 5.2. Light crystallography measurements, of the lattice parameters and particle diameters, of one-component colloidal dispersions.

A comparison of the particle diameters, obtained by static light scattering measurements, with the diameters measured by dynamic light scattering, is made in table 7.1, in chapter 7. Both approaches give similar results and the accuracy of the static light scattering results is greatest.

5.4.2. Light Scattering from Binary Colloidal Crystals

In the present work, the phase behaviour of binary mixtures of hard sphere colloids was investigated. In mixtures prepared with certain compositions, coexisting crystalline and fluid phases formed. The crystal structures were identified, by light powder crystallography. As well as random stacked close packed crystals of pure A or pure B, examples of the more complex AB_2 and AB_{13} superlattice structures were found. As was mentioned earlier, a quantitative analysis of the intensity data was not performed, due to the paucity of detailed knowledge, of the form factors very close to index-match. The structures were identified, by the positions of the peaks in the scattering profile.

The AB_2 superlattice structure consists of hexagonal layers of large A

spheres, interspersed with hexagonal layers of small B spheres. The structure is illustrated in figure 2.3, in chapter 2. The unit cell comprises vertically stacked layers of A spheres, with B spheres occupying the trigonal prismatic cavities between the A layers. For a hexagonal phase, such as AB_2, diffraction from a plane with Miller indices *h,k,l* occurs for scattering vectors q_{hkl} given by the Bragg equation[17]

$$q_{hkl} = \left(\frac{16\pi^2}{3a^2}(h^2 + k^2 + hk) + \frac{4\pi^2}{c^2} l^2 \right)^{1/2}, \qquad (5.16)$$

where *a* and *c* are the two unit cell lengths, or lattice parameters.

The scattering profile, of a binary mixture thought to contain only crystals with the AB_2 superlattice structure, is shown in figure 5.10 below.

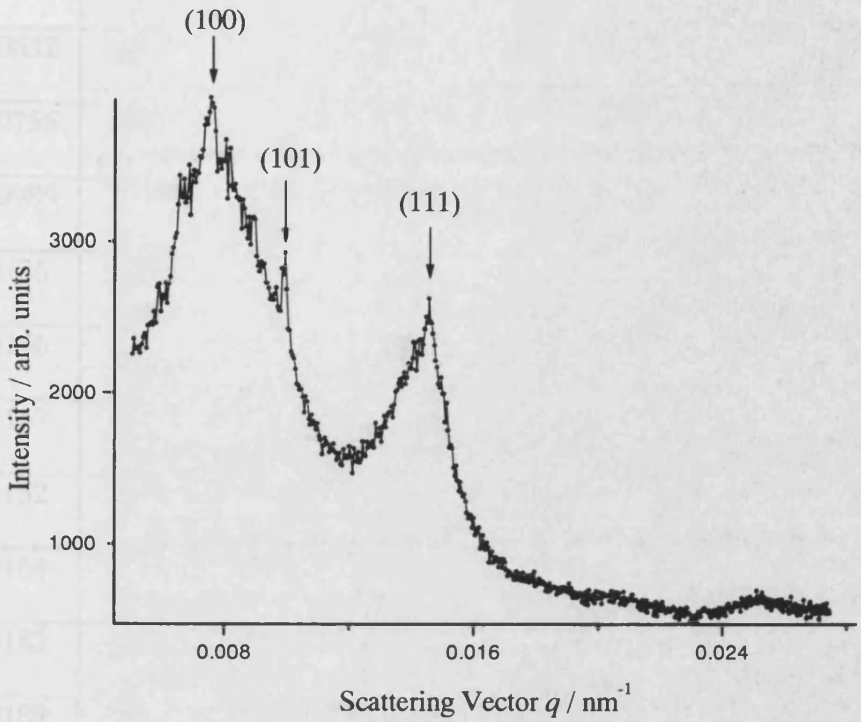

Figure 5.10. Light scattering measurements of sample 61, a binary mixture of hard sphere colloids, prepared with an initial composition: size ratio $\alpha = 0.52$, number ratio $N_B / N_A = 5$ and total volume fraction $\phi_A + \phi_B = 0.494$.

The scattering profile is consistent with the AB_2 structure. The measured Bragg reflections were indexed on a hexagonal phase, as follows: $q = 0.00756$ nm^{-1} (100), $q = 0.00989$ nm^{-1} (101) and $q = 0.0146$ nm^{-1} (111). The corresponding lattice parameters were calculated, using equation 5.16, by means of non-linear least squares fitting. Values of $a = 949 \pm 6$ nm and $c = 989 \pm 6$ nm were obtained. The quantity, $c / a = 1.041 \pm 0.01$ nm, is a measure of the average hexagonal interlayer spacing. The calculated q value of each Bragg peak, indexed on a hexagonal phase with these lattice parameters, is given in table 5.3 below.

q / nm^{-1}	*hkl*
0.00632	001
0.00756	100
0.00989	101
0.0126	002
0.0146	111
0.0147	102
0.0152	200
0.0164	201
0.0182	112
0.0189	003
0.0197	202
0.0204	103
0.0212	211
0.0228	300

Table 5.3. Predicted scattering profile for the AB_2 phase, found in sample 61, indexed on a hexagonal phase, with lattice parameters a = 949 ± 6 nm and c = 989 ± 6 nm.

Some of the predicted Bragg reflections, given in table 5.3, are either weak or absent from the scattering profile (figure 5.10). Nonetheless, the measured peaks are consistent with the theoretical predictions, providing evidence for the AB_2 phase.

The volume fraction of AB_2 in the sample $\left(\phi_{AB_2}\right)$ was determined, using the known particle diameters together with the values obtained for the lattice parameters.

$$\phi_{AB_2} = \frac{\pi(d_A^3 + 2_B^3)}{3ca^2\sqrt{3}}, \tag{5.17}$$

where d_A and d_B are the large and small sphere diameters, respectively. For sample 61, a value of 0.624 was obtained.

Light scattering measurements were also made on mixtures containing the AB_{13} superlattice phase and random-stacked close packed crystals of B. The AB_{13} structure is illustrated in figure 2.4, in chapter 2 and consists of a simple cubic lattice of large A spheres. The cube centres of the lattice are occupied by an icosahedral cluster of 12 small B spheres. A single small sphere is located at the centre of each cluster. In addition, the icosahedra in adjacent subcells are rotated by 90° relative to each other. The unit cell contains eight icosahedral clusters. The scattering profile of a sample thought to contain the AB_{13} phase, is shown in figure 5.11 below.

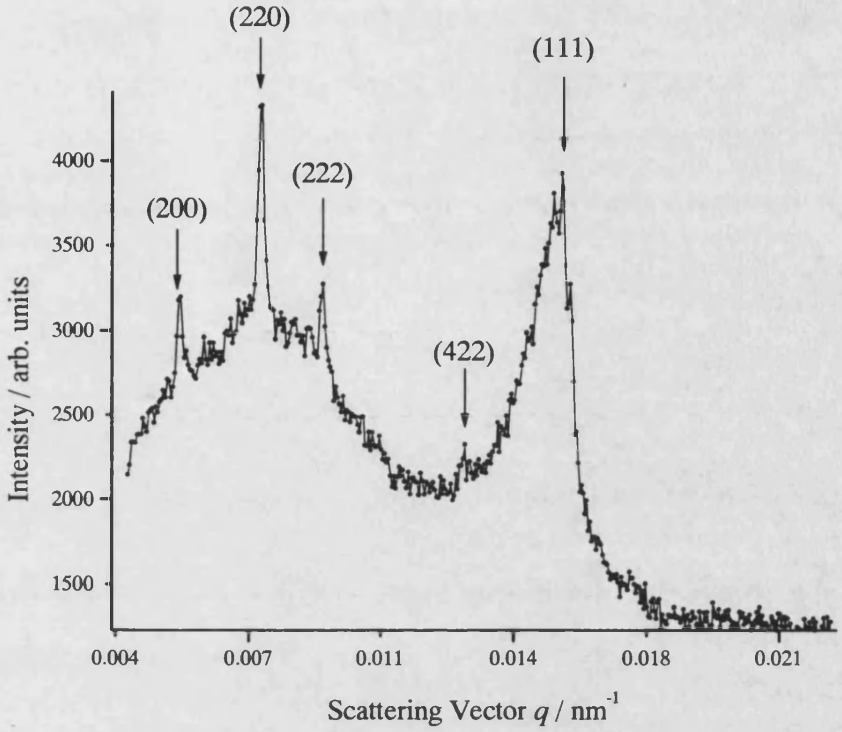

Figure 5.11. Light intensity measurements of sample 10, a binary mixture of hard sphere colloids, with original composition: size ratio $\alpha = 0.52$, number ratio $N_B / N_A = 14$ and total volume fraction $\phi_A + \phi_B = 0.566$.

Again, the structure was identified by the position of the peaks in the scattering pattern. The first four peaks in the profile are consistent with the AB_{13} superlattice structure. These peaks were indexed as follows, $q = 0.00518$ nm^{-1} (200), $q = 0.00731$ nm^{-1} (220), $q = 0.00896$ nm^{-1} (222), $q = 0.0128$ nm^{-1} (422). The measured peak, at $q = 0.0152$ nm^{-1} was indexed on the (111) line of a fcc lattice. This size-broadened peak is consistent with a powder of random close packed B crystals. The lattice constant for this phase was calculated to be ~505 nm.

The Bragg condition, for reflection from crystals with a cubic lattice, can be written as

$$q^2_{hkl} = \frac{4\pi^2}{a^2}(h^2 + k^2 + l^2), \tag{5.18}$$

where a is the lattice constant. According to equation (5.18), a plot of q^2_{hkl} versus $h^2 + k^2 + l^2$, for a cubic phase, should give a straight line, which passes through the origin, with slope $4\pi^2 / a^2$. For each suspension containing the AB_{13} phase, the lattice constant was determined from the measured gradient (see chapter 7). For sample 10, a value of a = 2366 ± 6 nm was obtained. The volume fraction of AB_{13} was also calculated, $\phi_{AB_{13}} = 0.57$, using the lattice parameter and the known particle diameters in the equation below

$$\phi_{AB_{13}} = \frac{8\pi(d_A^3 + 13d_B^3)}{6a^3}. \tag{5.19}$$

For both the AB_2 and AB_{13} superlattice structures, the agreement between the positions of the measured Bragg peaks and those predicted by theory is good. This provides evidence for the formation of the AB_2 and AB_{13} structures, in binary hard sphere colloidal mixtures.

CHAPTER 6

6. THE PHASE BEHAVIOUR OF MIXTURES OF HARD SPHERES

6.1. Introduction

The theoretical phase behaviour of binary hard sphere mixtures has been investigated, by means of both computer simulation and molecular theory. The characteristics of the phase diagram, depend sensitively on the size ratio α. For mixtures with size ratios in the range $0.85 < \alpha < 1.0$, the phase behaviour is well understood. Computer simulation, cell theory and density functional studies give results for this size ratio range that are in good agreement with each other.[96,97,98]

At intermediate size ratios $0.3 < \alpha < 0.85$ the phase behaviour is less well understood. However, computer simulation and cell theory studies, have given a clear picture of the phase behaviour at a number of size ratios.[76,99] The results of these methods are also in good overall agreement with the results of experiments, with binary hard sphere mixtures, carried out with size ratios in this region.[76]

The phase behaviour of highly asymmetric mixtures, with size ratios $\alpha <$ 0.3, has been studied increasingly in recent years and is currently a matter of some debate. In 1991 Biben and Hansen predicted a fluid-fluid demixing transition, for size ratios $\alpha < 0.2$, using integral equation theory.[100] Since then much work has been done, however the question of whether a stable fluid-fluid demixing transition occurs in highly asymmetric mixtures remains unresolved. Computer simulation and experimentation on these mixtures is complicated by the slow equilibration, which occurs at moderate densities of the small spheres.

This chapter is organised as follows. In section 6.2 we review the principal theoretical methods that have been used to study binary mixtures. In 6.3 we summarise the theoretical results, for mixtures with diameter ratios in the range $0.85 < \alpha < 1$ and in 6.4 we summarise the theoretical results for mixtures with diameter ratios in the range $0.3 < \alpha < 0.85$. Finally, in 6.5 the theoretical results for binary mixtures with diameter ratios $\alpha < 0.3$ are summarised.

6.2. Theoretical Methods

6.2.1. Computer Simulation Techniques

In order to study the equilibrium phase behaviour of hard spheres, the relative stabilities of all the different phases are required. Computer simulation methods can be used, to determine the chemical potential or, more generally, the free energy of each phase. The Helmholtz free energy is the relevant thermodynamic quantity, as hard sphere colloids are studied under conditions of constant volume. At equilibrium, the entropy of a given phase is at a maximum, while the free energy ($A = U - TS$) is at a minimum. Hence, the most stable phase, at a particular temperature and density, can be determined by comparing the relative free energies of the competing phases. Unfortunately, even for a hard sphere system, the free energies cannot be obtained directly by computer simulation. Computer simulation methods allow only free energy differences to be determined. In order to compute the free energy of a particular phase, a suitable path must be constructed, which connects reversibly the system in its

actual state, to a reference state of known free energy. The free energy is then evaluated, by integrating the change in free energy difference along this path. This is the basis of the thermodynamic integration method.

In the case of a dense liquid, a reversible path can, for example, be constructed to the dilute gas phase, where analytical results are well known. For the solid phase, several techniques have been developed, which use different reference systems. The earliest approach was the single occupancy (SO) cell method, developed by Hoover and Ree, which used a dilute (lattice) gas as the reference state.[46] This method begins with a lattice gas, with one particle occupying each lattice cell, chosen so that at high densities, the centres of the lattice cells coincide with the average atom positions, in the unconstrained solid. The so called single occupancy (SO) cell model, is essentially the model that is solved approximately in the cell theories (see below).[97,99] The uniform expansion of the SO lattice leads to a dilute gas, so linking reversibly the low density ideal gas (for which the free energy can be determined exactly) and the solid. The free energy of the solid is then obtained by computing

$$F_{\text{solid}}(V_2) - F_{\text{lattice gas}}(V_1) = \int P(V)\mathrm{d}V, \tag{6.1}$$

at constant temperature. Hoover and Ree used this method, to evaluate the absolute free energy of identical hard spheres.[46] These authors were then able to quantitatively establish the freezing transition, in a system of such hard spheres.[46] Subsequently, this method was extended to mixtures by Kofke.[101]

More recently, Frenkel and Ladd have introduced an alternative method to compute the absolute free energy of the solid phase.[57] The approach is again based on the construction of a reversible path, to a state of known free energy, but in this case the reference state is an Einstein crystal, with the same structure as the phase under study, which can be reached by slowly turning on harmonic springs to bind the particles to their lattice sites. By using this approach, in combination with methods for performing thermodynamic integrations over composition, it can be extended to mixtures. An example is the detailed work of Kranendonk and Frenkel, who evaluated the melting curve of substitutionally disordered solid binary mixtures of hard spheres.[96]

Thermodynamic integration was used, to slowly change the size ratio of the particles, at a particular volume fraction. The size ratio $\alpha = 1$ was used as a reference point. The reversible work required, to change the size ratio from unity to a given value of α, then corresponds to a direct measure of the excess free energy, of the solid solution at that composition.

More recently, this approach has been used by Eldridge *et al.* to investigate the stability of the AB_2 and AB_{13} superlattice structures.[102,103] The complete phase diagram for the size ratio $\alpha = 0.58$, which includes the AB_2 and AB_{13} phases, was then determined.[104] Subsequently, in an extensive study, further phase diagrams were computed using the same methods, for binary hard sphere mixtures with diameter ratios in the range $0.58 \leq \alpha \leq 0.625$.[100] Trizac *et al.* also used this approach, to determine the phase behaviour of binary mixtures with diameter ratios $\alpha = 0.414$ and 0.45.[105]

6.2.2. Density Functional Theory

The density functional method provides a useful tool, for the study of the equilibrium properties of inhomogeneous systems, where the one-particle density $\rho(\boldsymbol{r})$ varies in space. The modern version of classical density functional theory (DFT) was developed by Percus.[106] The essence is to approximate the Helmholtz free energy (A), of the inhomogeneous system, using structural and thermodynamic information from the corresponding uniform fluid. Recently, there has been considerable interest in the application of density functional arguments, to the calculation of the hard sphere fluid-solid transition. In this approach (reviewed in references 107, 108 and 109), the crystalline phase is treated as a highly non-uniform fluid, characterised by a rapidly varying equilibrium density $\rho(\boldsymbol{r})$. The Helmholtz free energy of the crystal depends on the density $\rho(\boldsymbol{r})$, where $\boldsymbol{r}$ is a vector specifying the position in space. Hence, the free energy is a functional of the spatially-varying one-particle density $\rho(\boldsymbol{r})$. The free energy functional can be split into two parts, an ideal gas part and an excess part, due solely to the interactions between the particles,

$$A[\rho(\boldsymbol{r})] = A_{id}[\rho(\boldsymbol{r})] + A_{ex}[\rho(\boldsymbol{r})], \tag{6.2}$$

where $\rho(\boldsymbol{r})$ is the density function and A_{id} is the local density form of the free energy for a uniform fluid ideal gas. This is given exactly by

$$A_{id}[\rho(\boldsymbol{r})] = \beta^{-1}\int d\boldsymbol{r}\rho(\boldsymbol{r})\{\ln[\rho(\boldsymbol{r})\beta\Lambda^3] - 1\}, \tag{6.3}$$

where $\beta = (1 / k_B T)$ denotes the inverse temperature and Λ is the thermal de Broglie wavelength. The central quantity of the theory is $A_{ex}[\rho(r)]$, the excess free energy. This is not simply expressible in terms of the densities $\rho(r)$ alone and in practice must be approximated. There are several approximations for the excess free energies. Earlier versions of DFT used the 'truncated-expansion approximation', which was proposed by Ramakrishnan and Yussouff[110] for a one-component system and generalised to mixtures by Haymet and co-workers.[111] In this approach A_{ex} is approximated by a functional Taylor-series expansion. Due to lack of knowledge of higher order correlation functions of liquids, a common approach has been to assume that the higher (than second) order terms are small and can be neglected. The Taylor expansion, truncated at second order, is given by

$$A_{ex}[\rho(r)] = A_{ex}(\rho_L) + \frac{\mu_{ex}(\rho_L)}{k_B T}\int dr\Delta\rho(r) - \frac{k_B T}{2}\iint drdr' c(|r - r'|;\rho_L)\Delta\rho(r)\Delta\rho(r'), \quad (6.4)$$

where ρ_L is the density of the bulk liquid, $\mu_{ex}(\rho)$ is the excess chemical potential, $\Delta\rho(r)$ is the difference between the solid density at point r and that of the bulk fluid and $c(|r - r'|;\rho_L)$ is the direct correlation function of the bulk liquid.

More recently, the third-order terms have been estimated and have been found to be comparable in magnitude to the second order terms.[111] Hence, the convergence of the functional Taylor expansion is not sufficiently rapid, to justify truncation at second order. An alternative approach is the weighted-density approximation (WDA), or modified weighted density approximation

(MWDA).[112,113] These theories are intrinsically nonperturbative and the free energy is approximated by[114]

$$A_{ex}[\rho(\boldsymbol{r})] = \int d\boldsymbol{r}\rho(\boldsymbol{r})\psi[\hat{\rho}(\boldsymbol{r})], \tag{6.5}$$

where $\rho(\boldsymbol{r})$ is the single molecule density, $\psi[\hat{\rho}(\boldsymbol{r})]$ is the Helmholtz free energy density of a uniform system with a density $\hat{\rho}(\boldsymbol{r})$. The weighted density $\hat{\rho}(\mathbf{r})$ is defined by an average of the local density, with respect to a weight function $w(|\boldsymbol{r} - \boldsymbol{r}'|; \hat{\rho}(\boldsymbol{r}))$ according to[114]

$$\hat{\rho}(\boldsymbol{r}) = \int d\boldsymbol{r}' w(|\boldsymbol{r} - \boldsymbol{r}'|; \hat{\rho}(\boldsymbol{r}))\rho(\boldsymbol{r}'). \tag{6.6}$$

The weight function is specified by ensuring that A_{ex} reduces to the free energy of the known fluid, in the homogeneous limit.

The density functional approach has been successfully applied to binary hard sphere mixtures, with diameter ratios in the range ($0.85 < \alpha < 1.0$).[98] In an early study, Barrat, Baus and Hansen investigated the phase behaviour of binary mixtures, with diameter ratios in this range, using a perturbative density functional approach.[115] The results of this work were in qualitative agreement with those of Monte Carlo computer simulations.[96] More recently, Zeng and Oxtoby, and Denton and Ashcroft have reported results, obtained using improved (nonperturbative) density functional theories of binary hard sphere mixtures, with the same range of diameter ratios.[98,114] Zeng and Oxtoby proposed an effective liquid free energy model (ELFEM), while Denton and

Ashcroft used a weighted density approximation. The theoretical predictions of both these approaches are in good agreement with each other and with the computer simulation data.[96]

The predictions from DFT, for the phase diagrams of hard sphere mixtures with diameter ratios in the range $0.85 < \alpha < 1.0$, are in good agreement with the results of computer simulations.[96] For binary mixtures with diameter ratios in the range $0.5 < \alpha < 0.6$, the experimentally determined phase diagrams have been analysed by DFT.[116] The results agree with experiment and with the results of Monte Carlo computer simulations, of hard spheres with the same range of diameter ratios.[105,106] In particular, the AB_2 and AB_{13} superlattice structures are found to be stable at intermediate diameter ratios.[116]

6.2.3. Cell Theory

The cell theory has a long history, which began with the work of Lennard-Jones and Devonshire[117,118] Until the mid-1960s these theories were applied, largely unsuccessfully, to liquids. However, the cell theories may also be applied to solids, with great success.[97] Recently, Cottin and Monson extended the cell theory to treat binary hard sphere mixtures.[97,99]

The approach of Cottin and Monson begins by considering a *n*-component mixture, consisting of N_1 molecules of type 1, N_2 molecules of type 2, ..., N_n molecules of type *n* placed on a lattice characterised with co-ordination number *n*.[119] It is assumed that each cell is characterised by the species of the central particle and by the composition and configuration of the *Z* nearest

neighbours. The configurational partition function of the system is then approximated, as a product of the cell partition functions,[97]

$$Z = (N! / N_1!N_2!\ldots N_n!)\ \Pi\ q_i^{Npi}, \tag{6.7}$$

where N is the total number of particles, q_i is the partition function of cell i and p_i denotes the probability of observing cell i. The p_i's are approximated as,

$$P_i = x_c x_1^{Si1} x_2^{Si2} \ldots x_n^{Sin}, \tag{6.8}$$

where x_c is the mole fraction of the species of the particle present, at the centre of the cell i, x_i is the mole fraction of species i and S_{ij} is the number of particles of type j in the nearest neighbour shell of cell i. The constraint

$$\sum_j S_{ij} \equiv Z, \tag{6.9}$$

is also required, where Z represents the number of nearest neighbours of particle i. Once the set of cell partition functions has been calculated, at a given density, the total configurational partition function can be determined. From this, the thermodynamic properties of the system can be calculated using the usual relations. Even for a binary mixture, a large number of cell partition functions have to be computed. However, all the cell partition functions can be computed simultaneously, by Monte Carlo integration.[97]

This relatively simple theory, together with the algorithm for evaluating the cell partition functions, makes the determination of the phase diagrams of binary mixtures quite straightforward and results, in close agreement with molecular dynamic simulations, have been obtained.[97,99]

6.3. Binary Mixtures with Size Ratios $0.85 < \alpha < 1.0$

The phase behaviour of binary mixtures of similarly sized hard spheres, with size ratios in the range $0.85 \leq \alpha \leq 1.0$, has been extensively studied by computer simulation[96] and density functional theory[115]. Kranendonk and Frenkel carried out a detailed Monte Carlo computer simulation study, of the phase diagram of binary mixtures with $\alpha \geq 0.85$.[96] The results of this study are in qualitative agreement, with the earlier density functional results of Barrat *et al.*[115] More recent studies, using the weighted density functional method, by Denton and Ashcroft[114] and Zeng and Oxtoby[98], give results that are in good agreement with the Monte Carlo computer simulation predictions. The cell theory predictions of Cottin and Monson are also in good agreement with the more recent DFT and computer simulation results.[97]

Binary mixtures with $\alpha > 0.3$ (for the situation where $\alpha < 0.3$, see sec. 6.5), are expected to be completely miscible in the fluid phase at all concentrations. However, the degree of miscibility in the solid phase is expected to vary, according to the size ratio. When the two components A and B are close in size, complete miscibility in the solid phase is predicted in all proportions.

Hence, for binary mixtures with size ratios in the range $0.94 < \alpha < 1.0$, the phase diagram is of a simple spindle type, as shown in figure 6.1.

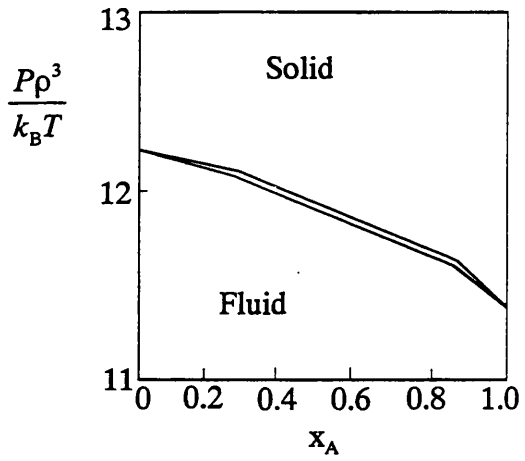

Figure 6.1. Theoretical equilibrium pressure (P) – composition (X_A) phase diagram, calculated from a cell model[119], for a binary mixture of hard spheres with a size ratio $\alpha = 0.97$.

In the phase diagram shown in figure 6.1, X_A is the mole fraction of component A,

$$X_A = \frac{n_A}{n_A + n_B}, \tag{6.10}$$

where n_A is the number of moles of A spheres and n_B is the number of moles of B particles.

The results of the Monte Carlo simulations, density functional and cell theory calculations all concur that, in general, the phase diagram is a spindle

type for binary mixtures with diameter ratios in the range ($0.94 \leq \alpha \leq 1.0$).[96,97,98] At low pressures, the equilibrium phase is a fluid mixture of A and B. At high pressures, both components are miscible in a single crystalline phase. This phase is predicted to be a substitutionally disordered close packed crystal, with both the large and small spheres distributed at random on a common fcc or hcp lattice. In the area between the solidus and liquidus, a solid solution of A and B is predicted to coexist with a fluid phase. In figure 6.1 it can be seen that at any given pressure, the mole fraction of large A spheres is higher in the solid phase, as the larger A spheres have the lower single-component freezing pressure.

For binary mixtures with a size ratio $\alpha \approx 0.94$, the hard spheres are no longer miscible in all proportions in a single solid phase and an azeotropic phase diagram is predicted. The results of cell theory, computer simulation and density functional calculations, predict an azeotropic phase diagram, for size ratios approximately in the range $0.88 < \alpha < 0.94$.[96,97,98] Freezing occurs into two crystalline phases, one rich in large spheres A, the other containing mainly small B spheres. Figure 6.2 shows the azeotropic phase diagram.

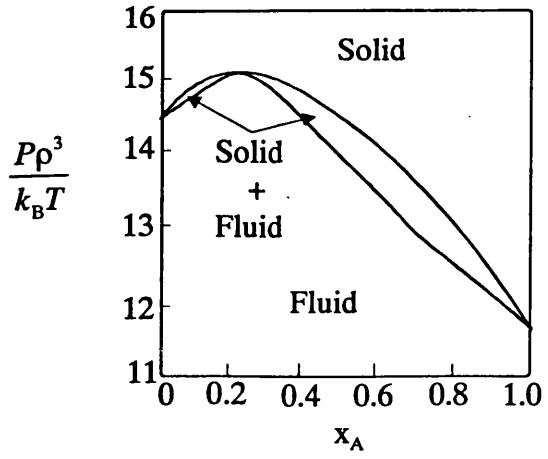

Figure 6.2. Theoretical equilibrium pressure (P) – composition (X_A) phase diagram, calculated from a cell model[119], for a binary hard sphere mixture with a size ratio α = 0.92.

At low pressures the equilibrium phase is a fluid mixture of both components. At low mole fractions of the large spheres, between the solidus and liquidus, a substitutionally disordered solid solution rich in B spheres is predicted to coexist with a fluid mixture of both components. At higher mole fractions of A, between the solidus and liquidus, a substitutionally disordered solid solution rich in A spheres is predicted to coexist with a fluid mixture of both components. At high pressures, the equilibrium phase is predicted to be a substitutionally disordered solid solution of A and B spheres.

As the size ratio is lowered, the diameters of the two hard sphere components becomes increasingly dissimilar and the degree of miscibility in the solid phase decreases. Both the cell theory and DFT find that, for size ratios $\alpha \sim$ 0.87, phase separation occurs in the solid phase and the azeotrope is replaced by a eutectic. The eutectic phase diagram is illustrated in figure 6.3.

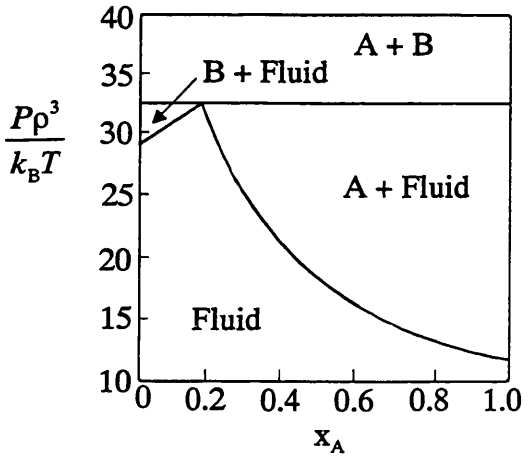

Figure 6.3. The theoretical equilibrium pressure (P) – composition (X_A) phase diagram, calculated from a cell model[119], for a binary mixture of hard spheres with a size ratio $\alpha = 0.85$.

At the size ratio $\alpha = 0.875$ there is partial miscibility in the solid phase and freezing occurs, to give two substitutionally disordered solid phases, one consisting mainly of large A spheres and the other consisting mostly of small B spheres. Barrat *et al.* predict[115] that, while the crystal rich in large spheres still contains a large proportion of small spheres (up to 25% by number), the solubility of the large spheres in the crystal rich in small spheres is low (less than 5%). As the size ratio is reduced to below $\alpha \approx 0.85$, the solubility of the large spheres in a crystal of small spheres decreases to zero. For size ratios $\alpha \leq 0.85$, the substitutionally disordered fcc or hcp phase is found to be mechanically unstable and almost complete immiscibility is predicted in the solid phase. Bartlett proposed a model for the freezing of binary hard sphere mixtures, which are assumed to be immiscible in a single solid phase.[77] Using this model, the phase boundaries of various phases were calculated and complete phase

diagrams, for mixtures with diameter ratios $\alpha = 0.65$ and 0.85, were reported. Both diagrams are of the eutectic type and are shown in figure 6.4.

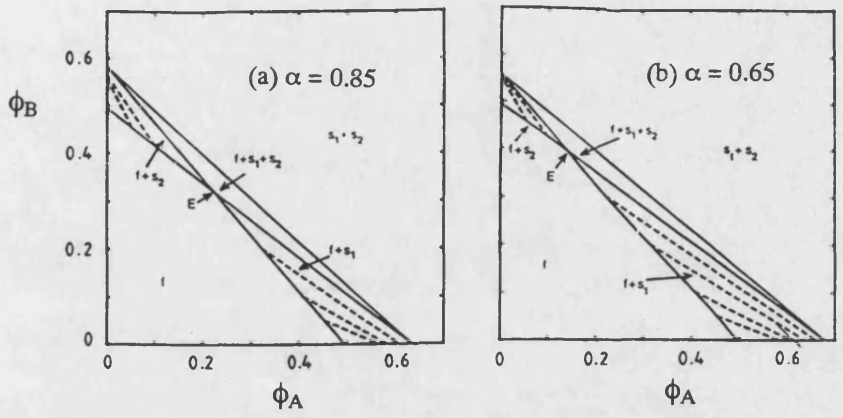

Figure 6.4. From Bartlett.[77] The equilibrium phase diagram of binary mixtures of hard spheres, with size ratios, $\alpha = 0.85$ and 0.65. ϕ_A and ϕ_B are the volume fractions of the large and small spheres respectively. The full lines are phase boundaries and the dashed lines represent the compositions of coexisting fluid and crystal phases. The eutectic fluid is marked by E, f indicates fluid, s_1 refers to the solid phase of the large spheres and s_2 refers to the solid phase of the small spheres.

Figure 6.4 shows that, at low volume fractions, the equilibrium state is a colloidal fluid of both components. At higher concentrations there are two two-phase regions, in which a random close packed solid of component A or B coexists with a binary fluid. With increasing total volume fraction, a three-phase eutectic region is encountered containing a eutectic mixture of A, B and fluid. At higher volume fractions, separate crystals of A and B coexist.

6.4. Binary Mixtures with Size Ratios $0.3 < \alpha < 0.85$

6.4.1. Introduction

For binary hard sphere mixtures with size ratios $\alpha \geq 0.85$, the phase behaviour is reasonably well understood, with computer simulation, density functional theory and cell theory all in good agreement.[96,97,98] However, for $\alpha <$ 0.85 the situation is less clear. As the size ratio is lowered, the formation of ordered solid phases must also be considered. For a binary mixture with a given size ratio (α), number ratio (N_B / N_A) and total volume fraction ($\phi_A + \phi_B$), there is currently no theory capable of predicting which solid phase is the most stable. At intermediate diameter ratios ($0.48 < \alpha < 0.62$) only binary crystals with non-interstitial structures, where each component lies on a crystal sublattice, will be stable. The relative stabilities of all the possible solid phases must be calculated. However, the number of phases under consideration can be considerably reduced, by means of a simple geometric packing argument. Parthé developed the idea, that a binary crystal structure would only be stable, if its maximum volume fraction was greater than that of the separate close packed phases (ϕ_{cp} = 0.7405 for both fcc and hcp structures).[120] Parthé calculated the maximum volume fraction of the NaCl, CsCl, NaTl, NiAs, WC, CaF_2 and the Laves (e.g. $MgCu_2$) crystal structures. For $\alpha > 0.62$, none of the structures was found to have a maximum volume fraction greater than $\phi_{cp} = 0.7405$.[120] Murray and Sanders suggested that the space filling principle alone determines the stability of the binary crystal. On this basis, these authors investigated the stability of

several binary crystal structures, as a function of the size ratio α.[72,73] At intermediate size ratios, Murray and Sanders predicted the non-interstitial AB_2 structure (atomic analogue AlB_2) to be stable.[73] The maximum volume fraction, of the AB_2 structure, was calculated to be 0.779, at $\alpha = 0.577$. Hence, this structure has a maximum volume fraction greater than that of the pure crystals (of A and B), $\phi_{cp} = 0.7405$.[121] Also, these authors found AB_{13}, with an ideal cubic structure (atomic analogue $NaZn_{13}$), to have a maximum close packed volume fraction of $\phi_{cp} = 0.738$, at $\alpha = 0.558$, which is less than that of the pure crystalline phases. However, in order to explain the observation of the AB_{13} structure in a sample of opal, these authors demonstrated that a small modification to the structure increases the maximum volume fraction above $\phi_{cp} = 0.7405$. If the B spheres, in the icosahedral clusters, have a small degree of polydispersity, then the slightly smaller B spheres can occupy the centres of the icosahedra, which increases the maximum volume fraction to $\phi_{cp} = 0.76$.[73]

For binary mixtures with very dissimilar diameters ($\alpha < 0.48$), the formation of crystals geometrically related to interstitial close packed structures, is expected to be important. In a close packed fcc or hcp structure of large spheres, at its maximum packing fraction (the volume fraction when fully compressed, $\phi_{cp} = 0.74$), there are octahedral holes. These can be occupied by the small spheres, if they have a size ratio less than 0.414. There are also smaller tetrahedral holes, which the small spheres can occupy, if they have a diameter ratio less than 0.225. If all the octahedral holes in a fcc crystal are occupied, then structures related to the NaCl structure are generated. Of the interstitial structures of the AB type, NaCl and CsCl have the highest maximum volume

fractions. Based on packing arguments alone, Murray and Sanders expected the AB (NaCl) structure to be stable.[73] The maximum volume fraction was calculated to be 0.793, at $\alpha = 0.414$, which is greater than that of the close packed pure crystal. However, the maximum volume fraction of CsCl is 0.729, at $\alpha = 0.732$, which is less than the maximum packing density of the pure crystal. Hence, in terms of packing arguments alone, this structure will be unstable. Both cell theory and computer simulations predict instability for this structure, in agreement with the space filling calculations.[99,105]

Murray and Sanders also found a series of interstitial structures of the AB_3, AB_4 and AB_5 type to be stable for $\alpha < 0.482$. However, subsequent molecular dynamic calculations and cell theory predictions have found these structures to be unstable.[72,73]

6.4.2. Monte Carlo Simulation

The thermodynamic stability of the AB_2 and AB_{13} superlattice structures has been investigated by Eldridge, Madden and Frenkel, by means of Monte Carlo computer simulation.[102,103] The free energy of the AB_2 phase was determined by simulation and compared with the free energies of the probable competing phases, arising out of Bartlett's immiscible sphere model.[77] The AB_2 phase was found to be stable for size ratios $0.425 < \alpha < 0.62$.[102] This domain of stability is in good agreement with the cell theory results. Cottin and Monson predicted AB_2 to be stable, for size ratios in the range $0.42 < \alpha < 0.59$.[99] The results of Murray and Sanders, based on the space filling principle, also agree

reasonably well with both the cell theory and simulation predictions. Murray and Sanders predicted a range of stability for AB_2 of $0.482 < \alpha < 0.624$.[73] The stability of the AB_{13} structure was also investigated, by Eldridge *et al.*, by means of free energy calculations.[103] The calculated free energy was then compared with the free energies of simpler phases, arising from Bartlett's immiscible sphere model.[77] Eldridge *et al.* calculated AB_{13} to be thermodynamically stable for size ratios $0.48 < \alpha < 0.62$.[103] In comparison, Murray and Sanders predicted AB_{13} to be stable in the range $0.53 < \alpha < 0.58$.[73] The results of Eldridge *et al.* predict the lower limit of stability to be somewhat less than that found by Murray and Sanders. Cell theory predicts AB_{13} to be stable in the range $0.54 < \alpha < 0.61$.[99] Again, this domain of stability is somewhat smaller than that found by Eldridge and co-workers.[103]

More recently, Eldridge *et al.* calculated the complete phase diagram, for a mixture of hard spheres with size ratio $\alpha = 0.58$.[104] To predict the phase diagram by simulation methods, the free energies and equations of state of all the competing phases were required. The competing phases considered were the binary fluid, pure crystals of A and B and the superlattice structures AB_2 and AB_{13}. The Gibbs free energies were calculated by thermodynamic integration. To compute the free energy of the binary fluid, the work needed to compress the fluid mixture from the ideal gas phase to the required volume fraction was calculated. This was done by means of the semi-empirical equation of state of Mansoori *et al.*[122] For the solid phase the method of Frenkel and Ladd was used.[57] This required Monte Carlo simulations. The pressure-composition diagram calculated by Eldridge and co-workers is shown in figure 6.5(a).

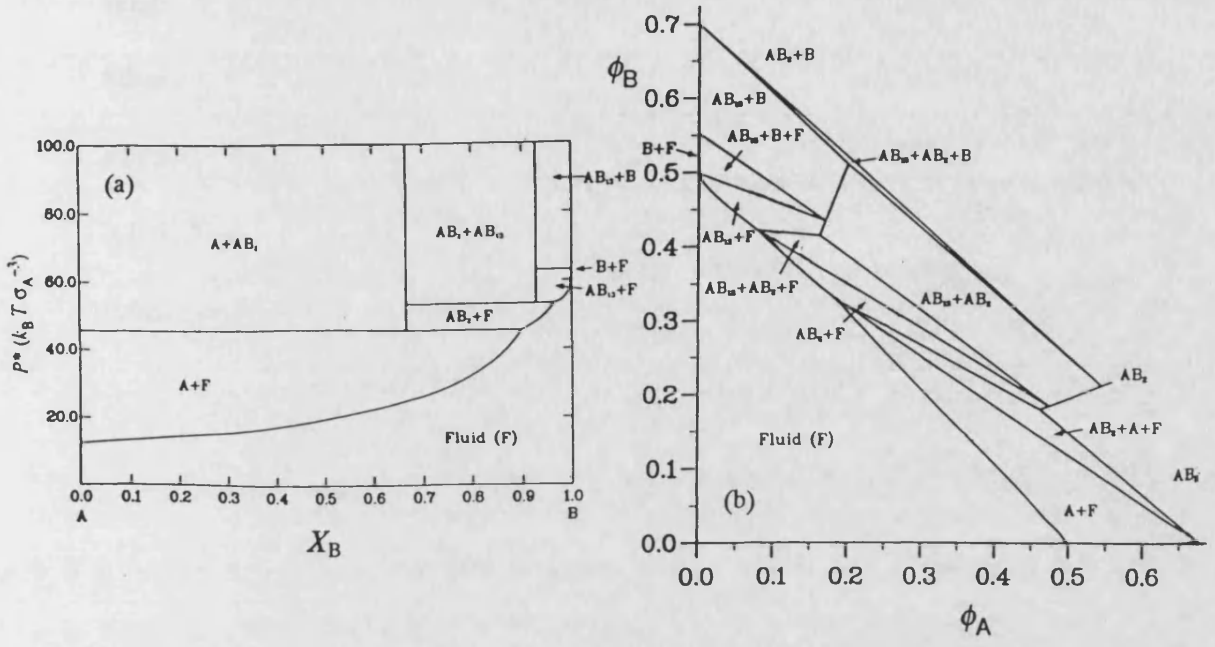

Figure 6.5. Equilibrium phase diagrams, for a binary mixture with a size ratio α = 0.58, calculated by simulation.[104] (a) P-X_B diagram, (b) constant volume representation. From Eldridge *et al.*[104]

In figure 6.5(a), X_B is the mole fraction of small B spheres,

$$X_B = \frac{n_B}{n_A + n_B}, \tag{6.11}$$

where n_B is the number of moles of small B spheres and n_A is the number of moles of A particles. To enable a comparison, of the simulation predictions, with results from experiments, the phase diagram was also calculated at constant volume (fig. 6.5(b)).

In a recent detailed study, Eldridge and co-workers calculated the constant volume phase diagrams for binary mixtures of hard spheres, with a

range of intermediate size ratios.[76] The Monte Carlo simulation approach adopted was the same as that used previously to determine the $\alpha = 0.58$ phase diagram.[104] Phase diagrams were calculated for size ratios in the range $0.60 \leq \alpha \leq 0.625$. The phase diagrams for size ratios $\alpha = 0.50$, 0.54, 0.59, 0.60, 0.61 and 0.625 are shown in figure 6.6 below.

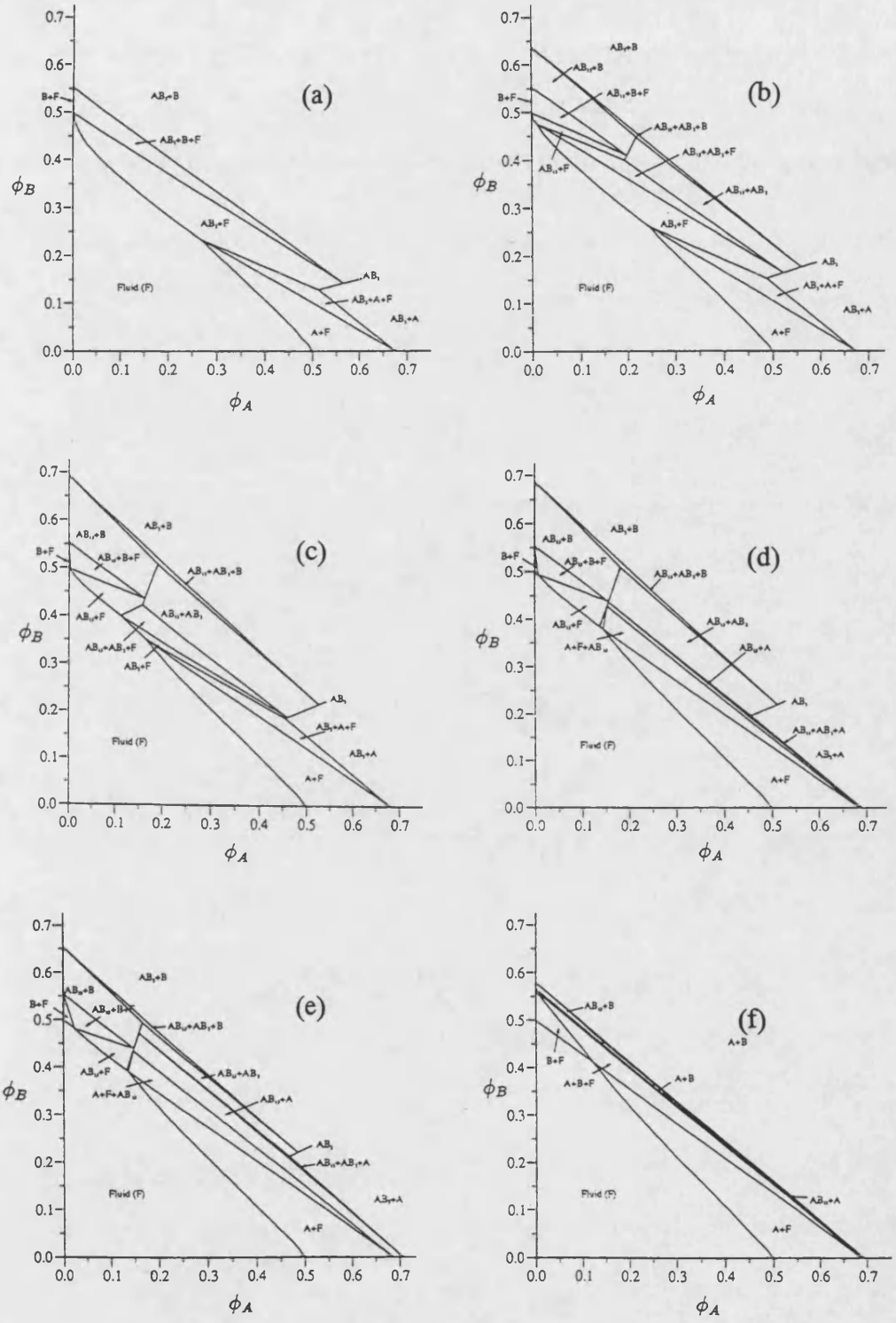

Figure 6.6. From Eldridge *et al.*[76] Constant volume simulation phase diagrams of a binary mixture of hard spheres with size ratios, (a) $\alpha = 0.50$, (b) $\alpha = 0.54$, (c) $\alpha = 0.59$, (d) $\alpha = 0.60$, (e) $\alpha = 0.61$ and (f) $\alpha = 0.625$.

The simulation phase diagram was also calculated, for $\alpha = 0.62$ and the experimental results of Bartlett were also plotted on the phase diagram (see fig. 2.5, chapter 2).[76] As can be seen from figure 6.6, the shape of the phase diagram changes drastically with small changes in the size ratio α. For $\alpha = 0.50$, the dominant phase is the AB_2 superlattice structure. The AB_2 phase is expected to have a lower limit of stability of $\alpha = 0.48$, according to packing arguments alone.[73] As was mentioned earlier, the cell theory and computer simulation predict a lower limit of $\alpha = 0.42$.[96,97] The absence of AB_{13} from this phase diagram, is in qualitative accord with the lower limit of $\alpha \approx 0.54$, predicted by both packing arguments and the cell theory.[99,73] Both the AB_2 and AB_{13} superlattice structures feature strongly in the simulation phase diagrams, for size ratios $\alpha = 0.54 - 0.62$. This is consistent with the space filling predictions, of a maximum volume fraction for AB_2 of $\phi_{cp} = 0.779$, at $\alpha = 0.577$ and for AB_{13}, $\phi_{cp} = 0.738$ at $\alpha = 0.558$.[73] In the simulation phase diagram at $\alpha = 0.625$, AB_2 is not predicted and AB_{13} is found only at high densities. At intermediate volume fractions, the stable phases are crystals of pure A and B. This is reasonably consistent with the computer simulation predictions, of a upper stability limit of $\alpha = 0.62$ for both these structures. This also agrees well with the upper limit of $\alpha = 0.624$, for AB_2, predicted by geometric packing arguments. However, for the upper limit of $\alpha = 0.583$, for AB_{13}, the agreement is less good.

Recently, in order to investigate the stability of the AB (NaCl) phase, Trizac and co-workers calculated equilibrium phase diagrams, for binary hard sphere mixtures.[105] These authors utilised the same method as Eldridge *et al.*[76] Phase diagrams were determined, at size ratios $\alpha = 0.414$ and 0.45, by means of

Monte Carlo computer simulation. These size ratios were chosen, partly because Murray and Sanders predicted AB (NaCl) to be stable, for mixtures with size ratios in the range $0.24 < \alpha < 0.458$.[73] Also, the maximum volume fraction of AB is predicted to be $\phi_{cp} = 0.793$ at $\alpha = 0.414$.[73] The phase diagrams calculated by Trizac *et al.* are shown in figure 6.7 below.

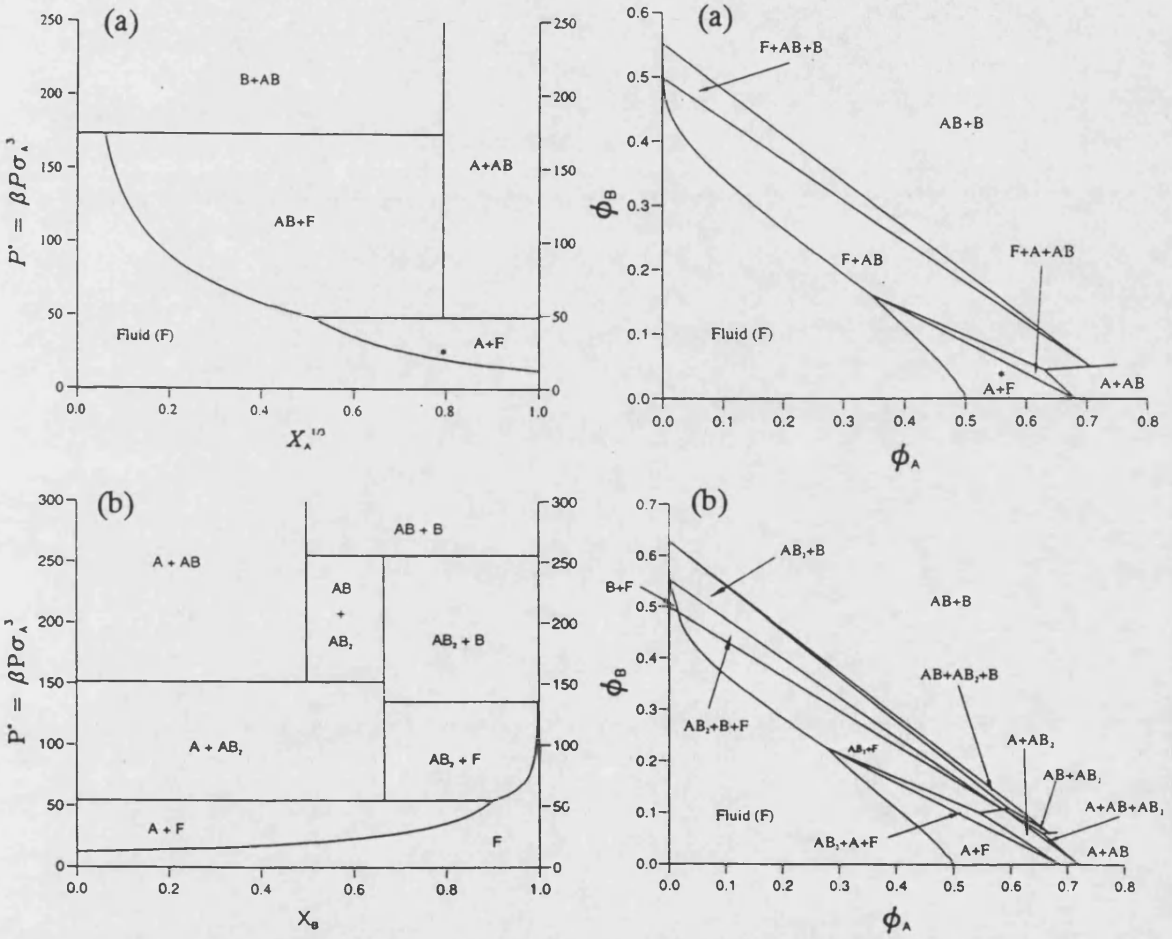

Figure 6.7. For a binary mixture of hard spheres, (a) P-$X_A^{1/3}$ and constant volume phase diagrams, at $\alpha = 0.414$ and (b) P-X_B and constant volume phase diagrams, at $\alpha = 0.45$. Calculated by Trizac *et al.*[105]

At $\alpha = 0.414$ AB is the major solid phase, which is consistent with the packing argument of Murray and Sanders. At $\alpha = 0.45$, AB is found only at high total volume fractions. At intermediate densities, the AB_2 phase dominates the phase diagram. This does not agree with the lower limit of stability for AB_2 of $\alpha = 0.482$, calculated by Murray and Sanders on the basis of packing arguments.[73] However, both the cell theory and computer simulation predict a lower limit of stability of $\alpha \approx 0.42$, which is consistent with figure 6.7.

6.4.3. Cell Theory

As was mentioned earlier, Cottin and Monson have successfully applied the cell theory to binary mixtures, which form substitutionally disordered solid solutions, with size ratios in the range $0.85 \leq \alpha \leq 1.0$.[97] These authors have also extended the cell theory to binary mixtures with intermediate size ratios, which form substitutionally ordered solid solutions.[99] As described earlier (section 6.3), Cottin and Monson used Monte Carlo integration to compute the cell partition functions at a given density.[99] Using this approach, these authors calculated the excess free energy and pressure of both the AB_2 and AB_{13} superlattice structures, as a function of volume fraction. The results obtained for AB_{13}, at $\alpha = 0.58$, were compared with the simulation results of Eldridge *et al.*[104] Very good agreement was found, particularly at high volume fractions. The results obtained, for AB_2, at $\alpha = 0.45$, were also in good agreement with Monte Carlo simulation predictions.[102] Motivated in part by this success, Cottin and Monson

calculated the complete pressure-composition phase diagram, for a binary mixture of hard spheres with size ratio $\alpha = 0.58$ (figure 6.8).

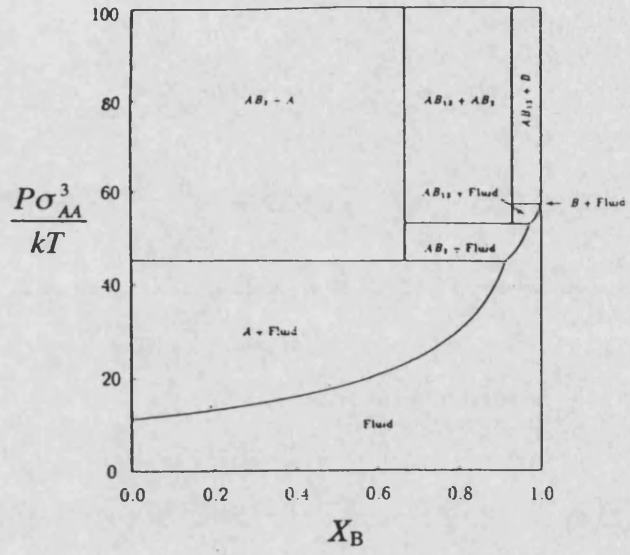

Figure 6.8. Theoretical pressure-composition phase diagram, calculated from a cell model[99], for a hard sphere mixture with a size ratio $\alpha = 0.58$. X_B is the mole fraction of small B spheres.

The semi-empirical equation of state of Mansoori *et al.* was used for the binary fluid, allowing the free energy to be known analytically.[122] The cell theory was used to describe the ordered solid solutions. At each size ratio, these authors not only considered as many individual AB_n phases as possible, but also the fact that they may be coexisting with other phases.[99] Cottin and Monson observed that overall, there is very good agreement between the equilibrium phase

behaviour, determined using the cell theory approach and the diagram obtained by means of the simulation methods.[104] Cottin and Monson also determined several complete phase diagrams, for binary mixtures with size ratios in the range $0.42 \leq \alpha \leq 0.73$.[99] The overall agreement with the simulation results of Eldridge *et al.* was found to be very good. The pressure-composition phase diagram at $\alpha = 0.42$, determined by the cell theory approach, is shown in figure 6.9.

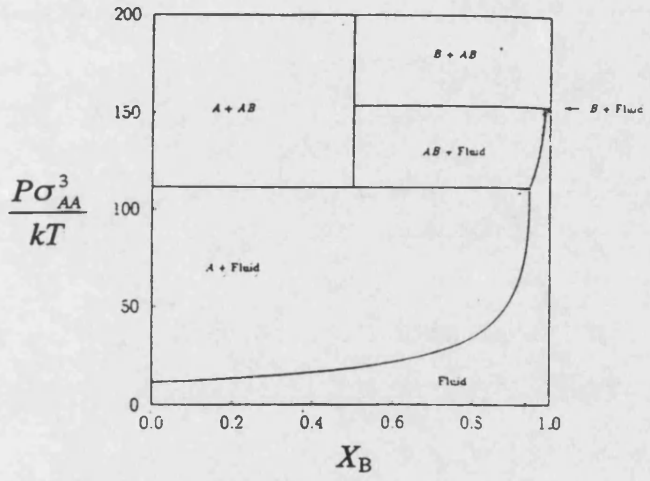

Figure 6.9. The theoretical pressure-composition phase diagram, calculated from a cell model[99], for a binary hard sphere mixture with a size ratio $\alpha = 0.42$.

This phase diagram can be compared with the *P-X* diagram at $\alpha = 0.414$, determined by Trizac *et al.* by means of Monte Carlo simulation.[105] Overall the agreement between the results of the two methods is very good. The small quantitative differences are probably a consequence of the slight difference in the size ratio, at which the two phase diagrams were determined, given the sensitive nature of the diagrams to small changes in α.[99] Cottin and Monson

determined the stability of the AB, AB_2 and AB_{13} solid phases, by calculating the pressure-composition phase diagrams for a range of size ratios. For the AB (NaCl) structure, these authors found the domain of stability to be $0.2 \leq \alpha \leq 0.42$.[99] The lower limit of stability is comparable to the value of $\alpha = 0.24$, determined by Murray and Sanders on the basis of geometric packing arguments.[73] The upper limit is lower than the packing argument value of $\alpha = 0.458$.[73] Cottin and Monson found the AB_2 structure to be stable, for size ratios in the range $0.42 < \alpha < 0.59$. For AB_{13} the range of stability was determined to be $0.537 < \alpha < 0.583$.[99]

6.5. Asymmetric Binary Hard Sphere Mixtures ($\alpha < 0.30$)

6.5.1. Introduction

The phase behaviour and structure of highly asymmetric binary hard sphere mixtures ($\alpha < 0.3$) is still the subject of much debate. A central issue is whether a stable fluid-fluid demixing transition occurs in this model system. In 1964, Lebowitz and Rowlinson showed that, within the Percus-Yevick (PY) closure of the Ornstein-Zernike equation, binary mixtures are completely miscible in all proportions in the fluid phase.[123] Recently, this result was challenged by the work of Biben and Hansen.[100,124] Using an improved integral equation approach, these authors predicted that binary hard sphere mixtures would phase separate, when the size ratio is less than 0.2 and the volume fraction of each species is comparable.[100] Since this ground breaking work, there

has been a great deal of interest in the phase behaviour of highly asymmetric binary mixtures. In contrast with the situation for binary mixtures with lower size asymmetry, computer simulation has not been widely utilised, to determine the phase behaviour of highly asymmetric mixtures. Direct simulations are difficult, due to the slow equilibration that occurs, above a certain density of the small spheres and few direct simulations have been carried out.[125,126]

The current experimental situation, with regard to demixing, is also unclear. Phase separation has been observed, in asymmetric binary colloidal mixtures, but it has proved difficult to distinguish between a fluid-fluid and a fluid-solid transition.[127,128]

The driving force for a demixing transition, in a binary hard sphere mixture, must be entropic in nature. In additive hard sphere mixtures, $\sigma_{AB} = (\sigma_{AA} + \sigma_{BB}) / 2$, depletion has been proposed as a mechanism for the (possible) demixing transition. As was mentioned earlier (in chapter 2), the first theoretical treatment of the depletion mechanism (in a colloid-polymer mixture) was the simple geometrical model of Asakura and Oosawa (AO).[30] In this model, depletion occurs when the large-sphere interparticle separation is less than the small sphere diameter. The unbalanced osmotic pressure, of the small particles, then pushes the large particles together. The depletion force is strongly attractive, at very short distances, but is also quite long range in nature. As the depletion mechanism is concerned with the low density limit, it is uncertain whether depletion can explain demixing in mixtures of finite concentration. Nonetheless, many authors have adopted a depletion approach, to the study of highly asymmetric binary mixtures. The recent theoretical and experimental

approaches to the study of the phase behaviour, of highly asymmetric hard sphere mixtures, are summarised below.

6.5.2. Theory and Experiment

Lekkerkerker and Stroobants investigated the phase behaviour, of asymmetric mixtures of hard spheres, in terms of the depletion mechanism, by means of a free volume statistical mechanical model.[129] For a mixture with a size ratio $\alpha = 0.1$, a fluid-fluid spinodal instability was predicted. Subsequently, Poon and Warren[44] and Dinsmore *et al.*[45] applied this free volume approach, to a hard sphere mixture with size ratio $\alpha = 0.14$. These authors found fluid-fluid demixing to be metastable, with respect to fluid-solid phase coexistence. In another approach, Rosenfeld investigated the phase behaviour of mixtures, with size ratios $\alpha \leq 0.25$, by means of a fundamental measures density functional theory.[130] Fluid-fluid phase separation was found, when the volume fractions of the large and small spheres was similar. Xu and Barentin studied the phase behaviour of a mixture, with a size ratio $\alpha = 0.1$,[131] using the modified weighted density approximation (MWDA), proposed by Denton and Ashcroft.[114] The fluid-solid phase diagram was calculated and a broad fluid-solid coexistence was found.[131] More recently, Dijkstra *et al.* studied the phase behaviour of a mixture of hard cubes on a lattice, by means of grand-canonical Monte Carlo (GCMC) simulations.[132,133] For cubes with a size ratio of $\alpha = 0.33$, these authors found evidence for a demixing transition.

Also, Biben, Bladon and Frenkel reported a numerical simulation study, of the depletion effect in hard sphere mixtures.[134] Monte Carlo (MC) simulations were performed, on mixtures with a size ratio of $\alpha = 0.1$ and a spinodal instability was predicted. Similarly, Dickman, Attard and Simonian reported a detailed study of the entropic forces in binary hard sphere mixtures.[135] These authors performed Monte Carlo simulations, of mixtures with size ratios of $\alpha = 0.1$ and 0.2 and the results were in good agreement with those of Biben, Bladon and Frenkel.[134] Very recently, a direct Monte Carlo computer simulation study for the actual two-component system, was carried out by Buhot and Krauth.[125] For mixtures with a size ratio $\alpha = 0.1$ a depletion effect was found, but no phase separation. For $\alpha = 0.05$, an increased depletion effect was found, but again no phase separation was observed. For $\alpha = 0.033$, phase separation was found.

The phase behaviour of hard sphere mixtures has also been investigated by Dijkstra, van Roij and Evans, based on the depletion, model.[126,136] An approximation to the effective Hamiltonian, based on pairwise additive depletion potentials, was used in simulations of mixtures with size ratios of $\alpha = 0.033$, 0.05, 0.1, 0.2 and 1.0. These authors found a fluid-fluid demixing transition for $\alpha \leq 0.1$. However, this transition was found to be metastable with respect to the fluid-solid transition, at all the size ratios studied. Dijkstra *et al.* also carried out direct simulations for hard sphere binary mixtures with $\alpha \geq 0.05$, for sufficiently low volume fractions of the small spheres.[126] Good agreement was found, between the simulation results and the predictions from the effective Hamiltonian.

Using another theoretical approach, Coussaert and Baus showed that the failure of the Percus-Yevick approximation to predict demixing, in a highly asymmetric mixture of hard spheres, arises because only the first three virial coefficients predicted by this theory are accurate.[137] When the fourth and fifth virial coefficients, from the results of Saija *et al.*,[138,139] were incorporated into the hard sphere equation of state, in the manner of the Percus-Yevick inspired rescaled virial expansion, thermodynamically stable fluid-fluid demixing was found for size ratios up to $\alpha = 0.15$ and 0.45.[137] However, in a recent erratum, the fourth and fifth virial coefficients were instead taken from Enciso *et al.*[140] Consequently, demixing was found to occur for pressures, which exceeded, by two orders of magnitude, the pressure for which a fluid-solid transition is expected to occur in the one-component system.[137] In conclusion, Coussaert and Baus found the demixing transition to be metastable, with respect to freezing into a partially frozen solid phase.

Evidence for the existence of a demixing transition, in asymmetric hard sphere mixtures, also comes from experiments on asymmetric sterically stabilised and charge stabilised colloidal suspensions. Sanyal *et al.* studied the phase behaviour of aqueous binary suspensions, of charge stabilised colloidal polystyrene spheres, with size ratio $\alpha = 0.2$.[127] The Coulomb interaction was screened out, so that the particles behaved as essentially hard spheres. Some evidence for phase separation was found, although the results were complicated by sample sedimentation.

More recently, van Duijneveldt, Heinen and Lekkerkerker investigated the phase behaviour of binary mixtures of colloidal silica particles, with a size ratio

$\alpha = 0.167$.[128] The silica particles were sterically stabilised, with octadecyl alcohol and were suspended in cyclohexane. Evidence of phase instability was found in a fairly narrow concentration range, at volume fractions between 0.25 and 0.35, for the small spheres and between 0.05 and 0.20, for the large spheres.

Another experimental study of phase separation, in binary mixtures of charge stabilised polystyrene particles, was recently reported by Kaplan and co-workers.[43] These authors prepared mixtures, using commercially prepared charge stabilised polystyrene particles. Nine binary mixtures, of nearly hard sphere colloidal suspensions, were prepared with size ratios in the range $0.069 \leq \alpha \leq 0.294$ and with a range of volume fractions. Bulk demixing was observed into two disordered phases, for samples with size ratios in the range $0.07 \leq \alpha \leq 0.14$ and at total volume fractions greater than 0.3.

More recently, Imhof and Dhont reported a study of the phase behaviour, of a binary mixture of colloidal silica particles, with size ratio $\alpha = 0.107$.[141] Charged silica spheres were dispersed in dimethylformamide (DMF), with a high degree of screening, to obtain a hard sphere interaction. Mixtures were prepared, with a range of volume fractions. The phase behaviour of the samples was observed, over one to two days and the phase diagram was determined. Phase separation was observed, at high volume fractions, into a large-sphere colloidal crystal and a coexisting fluid. These authors noted that this work was one of the first studies to observe a phase separation.

Another detailed study, of the phase behaviour of nearly hard sphere binary colloids, was recently reported by Dinsmore, Yodh and Pine.[142] These authors performed experiments with mixtures of aqueous suspensions, of charge

stabilised polystyrene spheres, with diameter ratios in the range $0.083 \leq \alpha \leq 0.149$. At sufficiently high volume fractions of the small spheres, separation into coexisting fluid and solid phases was observed in the bulk of certain samples. Two phase fluid coexistence was not observed in any samples, even at low size ratios.

CHAPTER 7

7. RESULTS

7.1. Introduction

The phase behaviour of binary colloidal mixtures was investigated, using the model PMMA / PHSA system, described in chapter 2. The particles were suspended in a near refractive index-matching mixture of carbon disulphide and decalin. This provided almost transparent samples, which could be observed directly and by static light scattering, even at high volume fractions. In an index-matched sample, the attractive van der Waals forces are expected to be minimised, so that the effective potential between two PMMA colloidal particles is steeply repulsive. Experimentally, this potential has been found to be indistinguishable from a hard sphere interaction.[76]

Stock solutions of the individual components were prepared, with known effective hard sphere volume fractions (ϕ), which were determined using the method described in chapter 2. Binary mixtures were then composed, with size ratios α = 0.42 ± 0.01, 0.52 ± 0.01 and 0.72 ± 0.01, by combining the stock solutions. The diameters of the colloidal particles, measured by static and dynamic light scattering, together with the diameter ratios of the binary mixtures, are given in table 7.1. The particle sizes and diameter ratios, obtained by both approaches, are in good agreement. As the static light scattering measurements were determined with the greatest accuracy, these are referred to in the remainder of the chapter.

Sample	Mean Diameter / nm		Diameter Ratio (α)	
	SLS ± 6	DLS ± 10	SLS ± 0.01	DLS ± 0.02
NH31	897	916	0.42	0.43
NH28	375	397		
NH31	897	916	0.52	0.51
DMM7	463	466		
DMM7	463	466	0.72	0.70
SPS09	641	670		

Table 7.1. Particle diameters, measured by static and dynamic light scattering and the diameter ratios of the binary mixtures prepared.

The samples NH31 and NH28 were synthesised during the present work, as described in chapter 3, while the samples DMM7 and SPS09 were prepared previously.

The binary mixtures were left undisturbed and observed at regular intervals. The effects of gravity were minimised, as described in chapter 2, by the continuous slow rotation of the particles, in the vertical plane, at a rate of one revolution every 24hrs.[52] Periodically, the rotator was stopped in the vertical position and the samples were removed for study. After study the samples were replaced and rotation was resumed. When crystals formed, the structure was investigated by means of static light scattering (chapter 5). In near index-matched samples, the form factors of the

individual particles are difficult to determine[10], so the crystal structures were identified by the positions of the scattering peaks in the powder pattern.

The rest of this chapter is organised as follows. In sections 7.2, 7.3 and 7.4, detailed results are presented, of the fluid-solid phase behaviour of binary mixtures with size ratios 0.42, 0.52 and 0.72. A comparison is made between the experimental results of the present work and the theoretical predictions of Madden and Eldridge[76] and Bartlett[77], in section 7.5. Finally, in section 7.6 the results are summarised.

7.2. Binary Mixtures with a Size Ratio $\alpha = 0.42$

Mixtures with a size ratio of $\alpha = 0.42 \pm 0.01$, were prepared by combining the large A particles ($d = 897 \pm 6$ nm) of suspension NH31, with the smaller B particles ($d = 375 \pm 6$ nm) of the NH28 sample. A total of twenty-one samples were made, at seven different number ratios (N_B / N_A), with total volume factions in the range $0.525 \leq \phi_A + \phi_B \leq 0.565$. In a one-component system, suspensions with volume fractions in this range crystallise rapidly.[8]

In mixtures prepared with a number ratio $N_B / N_A = 0.5$, coexisting fluid and crystalline phases were observed. Crystals were visible to the naked eye in a ~5 mm layer, at the base of the sample cell. In sample 106, crystallisation was complete after ~18 days of slow tumbling, which is significantly longer than the two days characteristic of one-component A samples. A light powder diffraction pattern, of sample 106, prepared with composition, $\alpha = 0.42$, $N_B / N_A = 0.5$ and $\phi_A + \phi_B = 0.534$, is shown in figure 7.1.

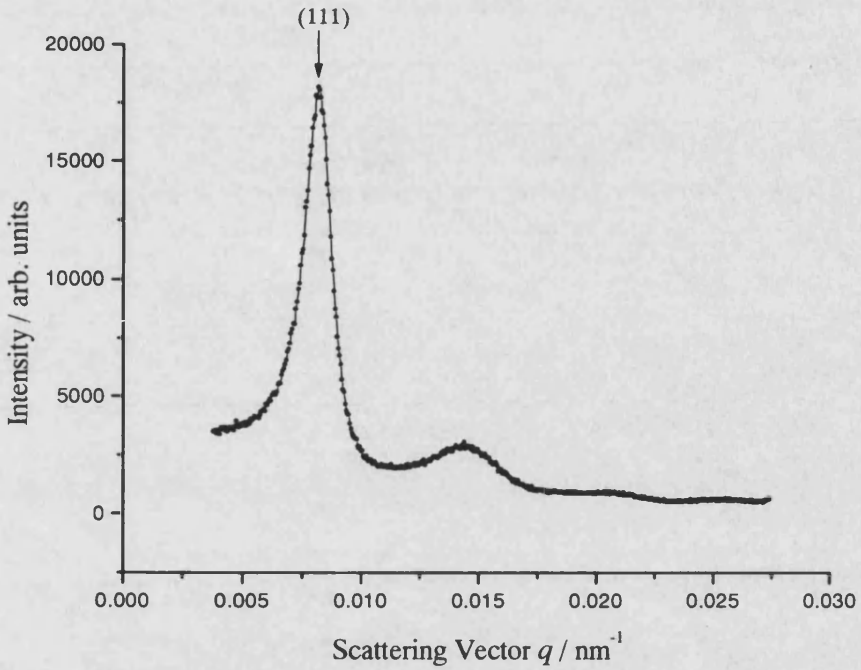

Figure 7.1. Static light scattering measurements of sample 106, a binary mixture of colloidal hard spheres, with an initial composition: size ratio $\alpha = 0.42$, number ratio $N_B / N_A = 0.5$ and total volume fraction $\phi_A + \phi_B = 0.534$.

The scattering profile is consistent with a powder of random stacked close packed crystals, with a size broadened Bragg reflection and a broad band of diffuse scattering. The measured Bragg reflection, at $q = 0.00818$ nm^{-1}, may be indexed as the (111) line of a fcc lattice. The corresponding lattice constant, a = 934 ± 6 nm, suggests that the sample contains crystals of large A particles and a coexisting fluid enriched in small spheres. The volume fraction of A crystals in the sample was calculated, from the measured lattice constant and the known particle sizes, to be 0.659 ± 0.01. The lattice constants and crystal volume fractions are collected together in table 7.2, at the end of this chapter.

Coexisting crystal and fluid phases were also observed, in mixtures prepared with a number ratio $N_B / N_A = 1$. Crystallisation was complete after slow tumbling for ~18 days and crystals were observed by eye, in a ~4 mm layer at the bottom of the sample cell. A light powder pattern of sample 110, with an original composition, $\alpha = 0.42$, $N_B / N_A = 1$ and $\phi_A + \phi_B = 0.537$, is shown in figure 7.2 below.

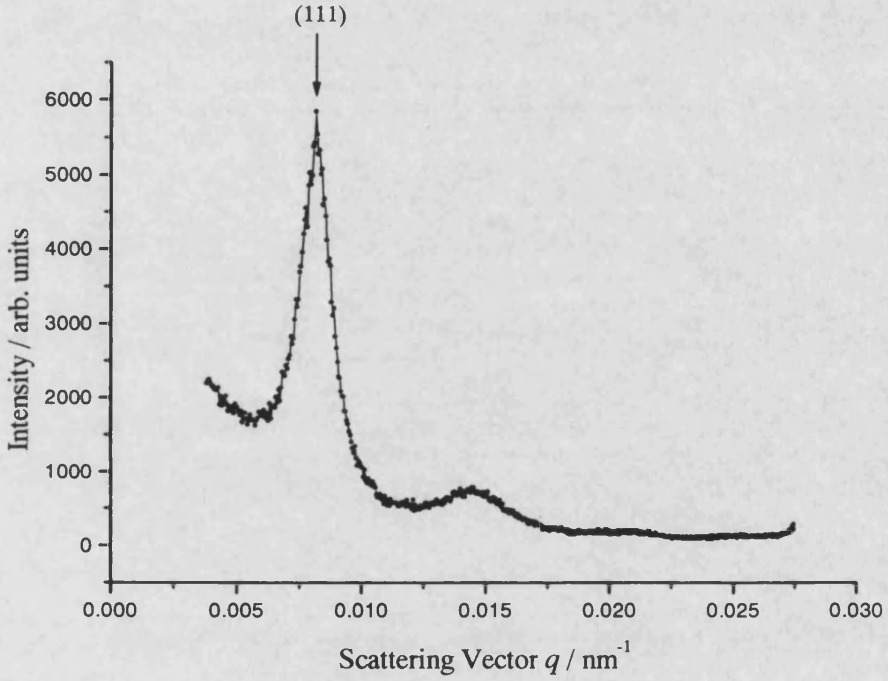

Figure 7.2. Light scattering measurements of a binary mixture of hard sphere colloids, sample 110, prepared with an initial composition: size ratio $\alpha = 0.42$, number ratio $N_B / N_A = 1$ and total volume fraction $\phi_A + \phi_B = 0.537$.

The main peak, at $q = 0.00824$ nm^{-1}, was indexed as arising from the (111) line of a random stacked close packed structure. The lattice parameter, $a = 932 \pm$

6 nm, suggests that the sample contains crystals of large A spheres and a coexisting fluid enriched in B particles.

Similarly, mixtures prepared with a number ratio $N_B / N_A = 2$, formed coexisting crystal and fluid phases. Again, crystallisation was complete after ~18 days and crystals were visible in a ~4 mm layer at the base of the sample cell. Figure 7.3 shows the scattering pattern of sample 113, prepared at this number ratio, with composition $\phi_A + \phi_B = 0.557$.

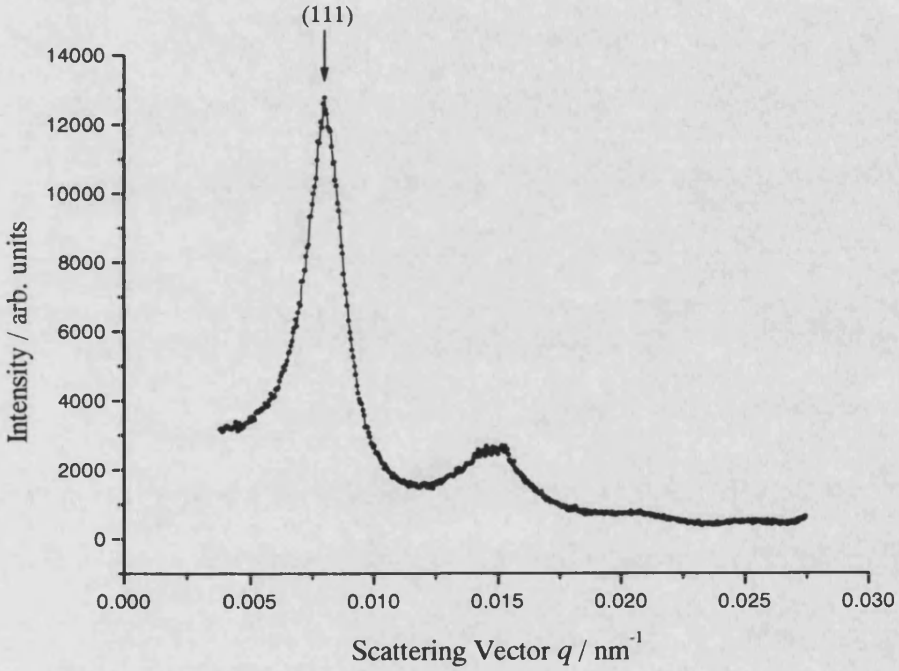

Figure 7.3. Light scattering results for sample 113, a binary colloidal mixture with original composition: size ratio $\alpha = 0.42$, number ratio $N_B / N_A = 2$ and total volume fraction $\phi_A + \phi_B = 0.557$.

The size broadened Bragg reflection, at $q = 0.00824$ nm^{-1} and broad band of diffuse scattering, is characteristic of a powder of random stacked close packed crystals. For this and similar measurements, at this number ratio, the Bragg peak was indexed as the (111) line and the lattice parameter was calculated (see table 7.2). The lattice parameter for sample 113, $a = 948 \pm 6$ nm, is consistent with a close packed structure of large A spheres.

In mixtures prepared with a number ratio $N_B / N_A = 8$, a few crystals were observed, only in the sample with the lowest total volume fraction. Attempts to determine the structure of the crystalline phase were unsuccessful, due to the very small amount of crystalline material visible. The scattered intensity profile obtained for the sample (115) with the lowest volume fraction, is shown in figure 7.4.

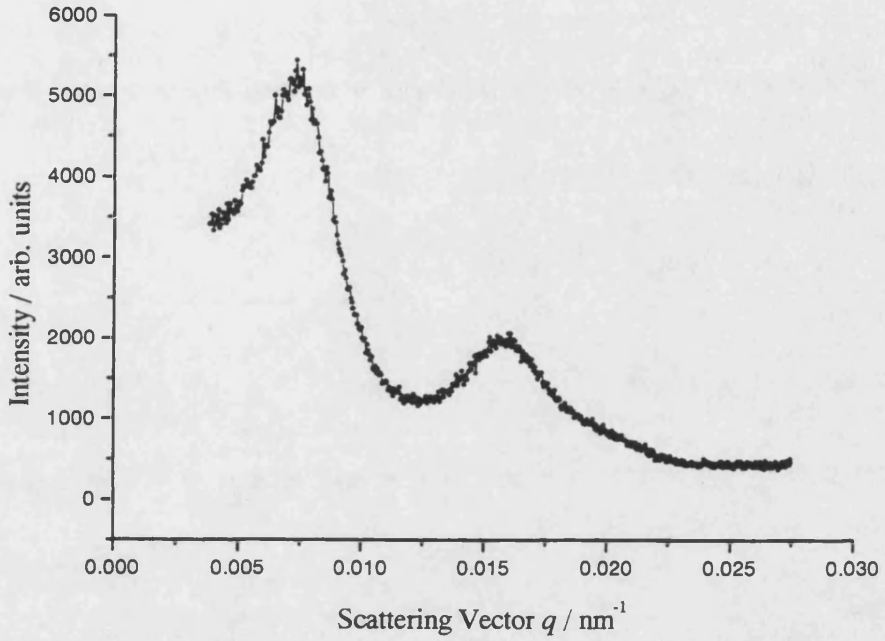

Figure 7.4. Light scattering measurements of sample 115, a binary mixture of colloidal hard spheres, with an initial composition, $\alpha = 0.42$, $N_B / N_A = 8$ and $\phi_A + \phi_B = 0.532$.

In contrast to figure 7.3, the scattering is dominated by the large fraction of amorphous material, with the sharp peaks expected for the crystals not visible. In an effort to identify the crystallites, the scattering volume illuminated by the laser was decreased in size, but the results were inconclusive.

Similarly, mixtures prepared with number ratios $N_B / N_A = 13$ and 26 remained totally amorphous. Even after slow tumbling for 256 days, no crystals were visible.

By contrast, in mixtures prepared with a number ratio $N_B / N_A = 52$, colloidal crystals and a coexisting fluid formed. Crystals were observed in a ~4 mm layer at the bottom of the sample. In sample 126, the formation of B crystals was complete after 38 days of slow tumbling. In comparison, in a one-component B sample, full crystallisation took 21 days. The scattering profile of sample 126 is shown in figure 7.5.

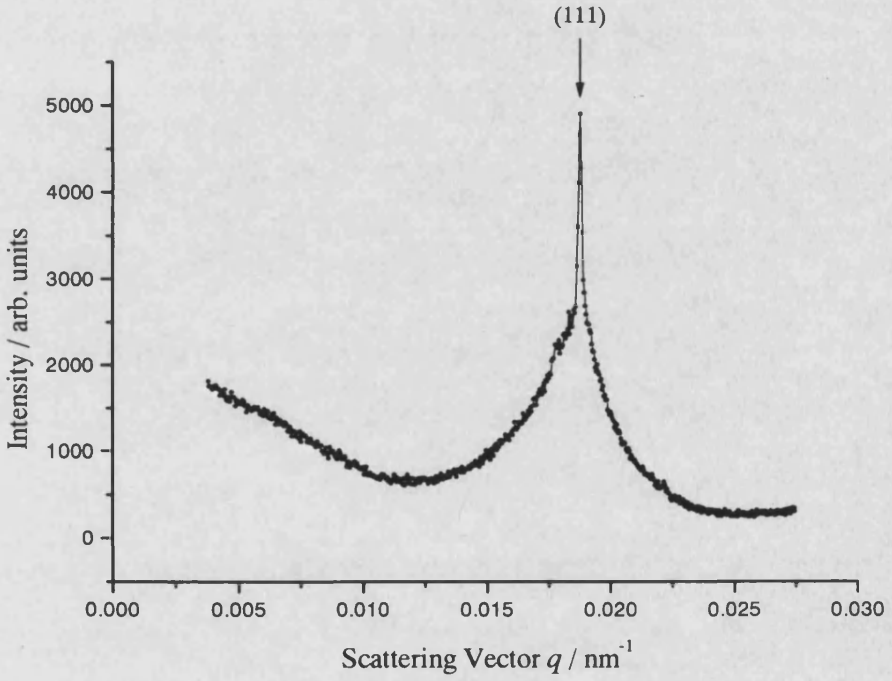

Figure 7.5. Static light scattering measurements of sample 126, a binary colloidal mixture, with an original composition: size ratio $\alpha = 0.42$, number ratio $N_B / N_A = 52$ and total volume fraction $\phi_A + \phi_B = 0.573$.

The measured Bragg peak, at $q = 0.0187\ nm^{-1}$, was indexed as the (111) line and the lattice parameter was calculated. The value obtained, $a = 401 \pm 6$ nm, suggests that the sample contains crystals with a close packed arrangement of small B spheres. The lattice parameters, calculated from the scattering from other mixtures prepared at this number ratio, are assembled in table 7.2. As the volume fraction is increased, there is a significant decrease in the lattice parameter. For instance, the sample with the lowest total volume fraction, $\phi = 0.523$, has a measured lattice parameter of 416 ± 6 nm, while the sample with the highest total volume fraction, $\phi = 0.573$, has a lattice parameter of 401 ± 6 nm. This behaviour is consistent with an osmotic compression of the crystal, with increasing volume fraction.

The phase behaviour of the binary mixtures, prepared with a size ratio $\alpha = 0.42$, is summarised in the constant volume phase diagram, in figure 7.6.

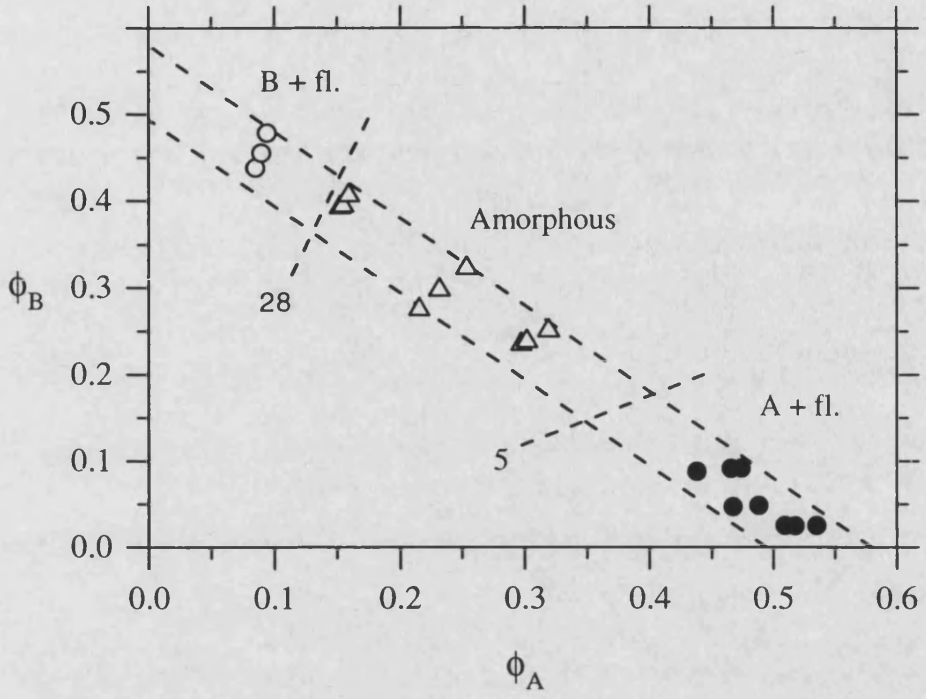

Figure 7.6. Constant volume phase diagram summarising the phase behaviour of binary mixtures of hard sphere colloids, with a size ratio $\alpha = 0.42 \pm 0.01$. The following phases were observed: ●, A + F; Δ, amorphous; ○, B + F. The approximate positions of the phase boundaries are marked by dashed lines and the two lines radiating from the origin depict the AB_5 and AB_{28} stoichiometries.

As can be seen from figure 7.6, the phase diagram contains three distinct regions. The approximate positions of the phase boundaries are indicated by dashed lines, with number ratios $N_B / N_A = 5$ and 28.

Mixtures rich in A, with number ratios $N_B / N_A = 0.5$, 1 and 2, are indicated by solid circles in figure 7.6. In these samples, coexisting crystal and fluid phases formed. The crystal structure was identified as an ordered arrangement of large A particles (however, see also Appendix).

By contrast, at intermediate number ratios, mixtures prepared with N_B / N_A = 8, 13 and 26 remained largely amorphous for the duration of the experiment. These samples are indicated by the open triangles in figure 7.6.

In mixtures rich in B, with number ratio $N_B / N_A = 52$, coexisting fluid and crystal phases were observed. The crystal phase was a random close packed structure of B particles and the fluid phase was enriched in A particles. Open circles in figure 7.6 indicate these samples.

7.3. Binary Mixtures with a Size Ratio $\alpha = 0.52$

Mixtures were prepared with a size ratio $\alpha = 0.52 \pm 0.01$, by combining the large A spheres ($d = 897 \pm 6$nm) of the NH31 suspension, with the small B spheres ($d = 463 \pm 6$nm) of the DMM7 colloidal dispersion. Twenty-eight samples were prepared at eight different number ratios, in the range $0.5 \leq N_B / N_A \leq 100$, with total volume fractions in the range $0.494 \leq \phi_A + \phi_B \leq 0.581$.

Mixtures rich in A, prepared with a number ratio $N_B / N_A = 0.5$, appeared to remain in metastable fluid or glassy states. Figure 7.7 shows the measurement of the scattering, from sample 15, with original composition: $\alpha = 0.52$, $N_B / N_A = 0.5$ and $\phi_A + \phi_B = 0.513$.

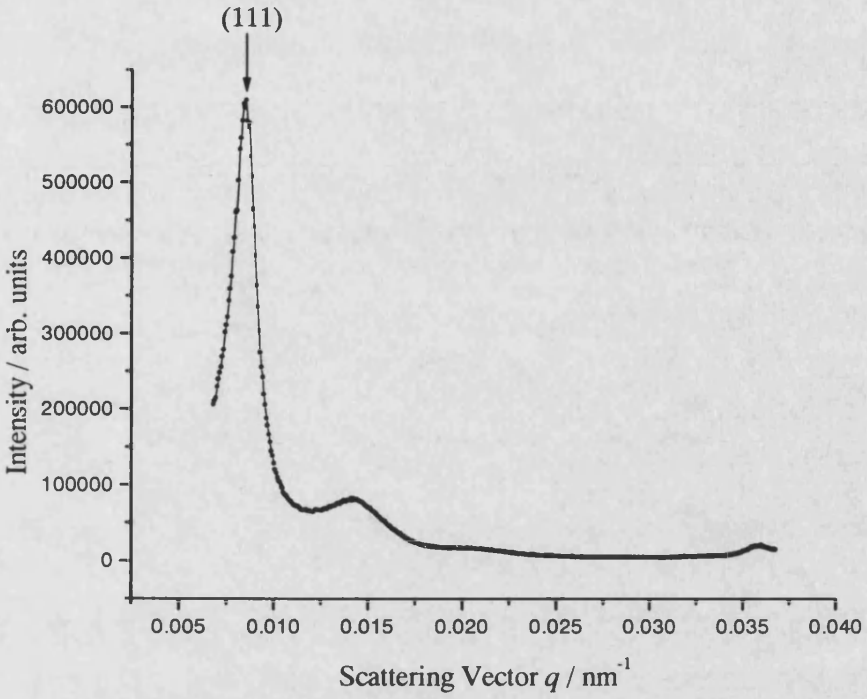

Figure 7.7. Light scattering measurements of sample 15, a colloidal mixture of hard spheres, with original composition: size ratio $\alpha = 0.52$, number ratio $N_B / N_A = 0.5$ and total volume fraction $\phi_A + \phi_B = 0.513$.

Although no crystals were observed by eye, the narrowing of intensity in the scattering, at low q, is consistent with a powder of small crystallites. The measured lattice constant, $a = 914 \pm 6$ nm, is consistent with the formation of crystals of A particles and a coexisting fluid enriched in B spheres.

Similarly, mixtures prepared at $N_B / N_A = 1$ and 2, also appeared to remain in amorphous or glassy states, up to 3.5 months after redispersing. The measured scattering patterns were similar to figure 7.7. However the narrowing of intensity, at low q, was less pronounced, which suggests that these samples are probably amorphous.

By contrast, coexisting crystal and fluid phases formed in mixtures prepared with a number ratio $N_B / N_A = 5$. The rate of crystallisation was slow and full crystallisation took 78 days to complete. Crystals were observed by eye, in a narrow (~3mm) layer, at the centre of the sample cell. The suspensions were analysed by powder light crystallography, which provided strong evidence for the formation of the AB_2 superlattice phase. The AB_2 structure consists of hexagonal layers of large A spheres, interspersed with hexagonal layers of small B spheres. The structure is illustrated in figure 2.3, chapter 2. The unit cell comprises vertically stacked layers of A spheres, with B spheres occupying the trigonal prismatic cavities between the A layers. The distinctive light powder diffraction pattern of the crystalline phase of sample 62, prepared with size ratio $\alpha = 0.52$, $N_B / N_A = 5$ and $\phi_A + \phi_B = 0.509$, is shown in figure 7.8.

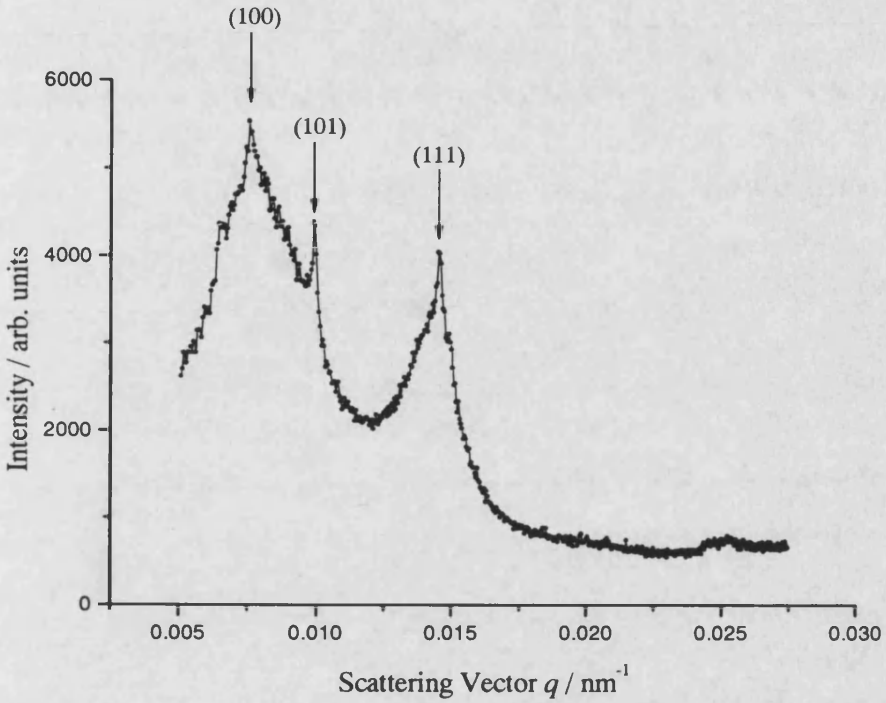

Figure 7.8. Light scattering measurements of sample 62, a binary mixture of colloidal hard spheres, with original composition: size ratio $\alpha = 0.52$, number ratio $N_B / N_A = 5$ and total volume fraction $\phi_A + \phi_B = 0.509$.

The measured Bragg reflections were indexed on a hexagonal phase, as follows: $q = 0.00759$ nm^{-1} (100), $q = 0.00987$ nm^{-1} (101) and $q = 0.0145$ nm^{-1} (111). The average hexagonal interlayer spacing, c / a, was calculated to be 1.041 ± 0.01 and the volume fraction of AB_2 in the sample was calculated to be 0.624 ± 0.01. This analysis was repeated, for the other scattered intensity profiles obtained at this size ratio. The results are given in table 7.5, at the end of the chapter.

In comparison, in mixtures prepared with a number ratio of $N_B / N_A = 8$, a few small crystals were observed only in the sample with the lowest volume fraction. The initial scattering profiles, for all the samples, were consistent with a metastable colloidal fluid. However, after almost 200 days evidence appeared in the light scattering for AB_2, for the mixture with the lowest total volume fraction. Then, after 349 days, AB_2 was also observed in the scattering for the two mixtures prepared with higher densities. A scattering profile, of sample 5, prepared at this size ratio, is shown in figure 7.9 below.

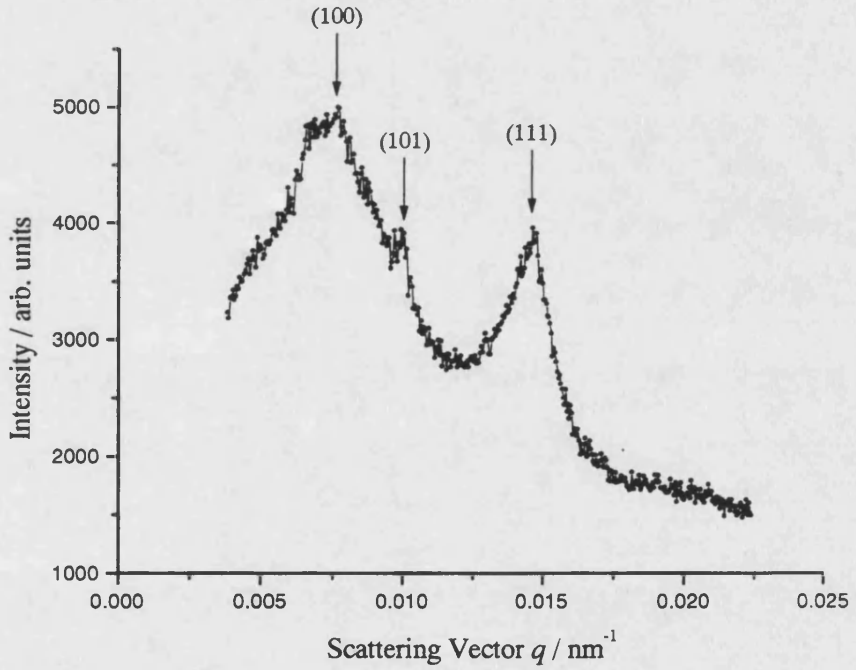

Figure 7.9. Measurements of light scattering from sample 5, a binary colloidal mixture prepared with a size ratio $\alpha = 0.52$, number ratio $N_B / N_A = 8$ and total volume fraction $\phi_A + \phi_B = 0.522$.

The Bragg peaks are indistinct, precluding accurate measurements. However, the peaks have been indexed and a comparison with the scattering profile in figure 7.8, shows striking similarities.

In mixtures prepared with a number ratio $N_B / N_A = 14$, coexisting crystal and fluid phases were observed. After ~18 days crystals were visible in a ~13 mm layer, at the centre of the sample cell, together with coexisting colloidal fluid. A study of the powder diffraction patterns of the crystalline phase, indicated the presence of B crystals. However, after ~116 days of slow tumbling, a second crystal phase was observed by eye, near the top of the crystalline layer. Light scattering measurements of this phase were consistent with crystallites of the AB_{13} superlattice phase. The AB_{13} structure is illustrated in figure 2.4, in chapter 2. The structure consists of a simple cubic lattice of large A spheres. The cube centres of the lattice are occupied by an icosahedral cluster of 12 small B spheres. A single small sphere is located at the centre of each cluster. In addition, the icosahedra in adjacent subcells are rotated by 90^0 relative to each other. The unit cell contains eight icosahedral clusters.

Although AB_{13} was clearly visible in the scattering profile after ~116 days, crystallisation took at least 130 days to complete. This is shown in figure 7.10 below.

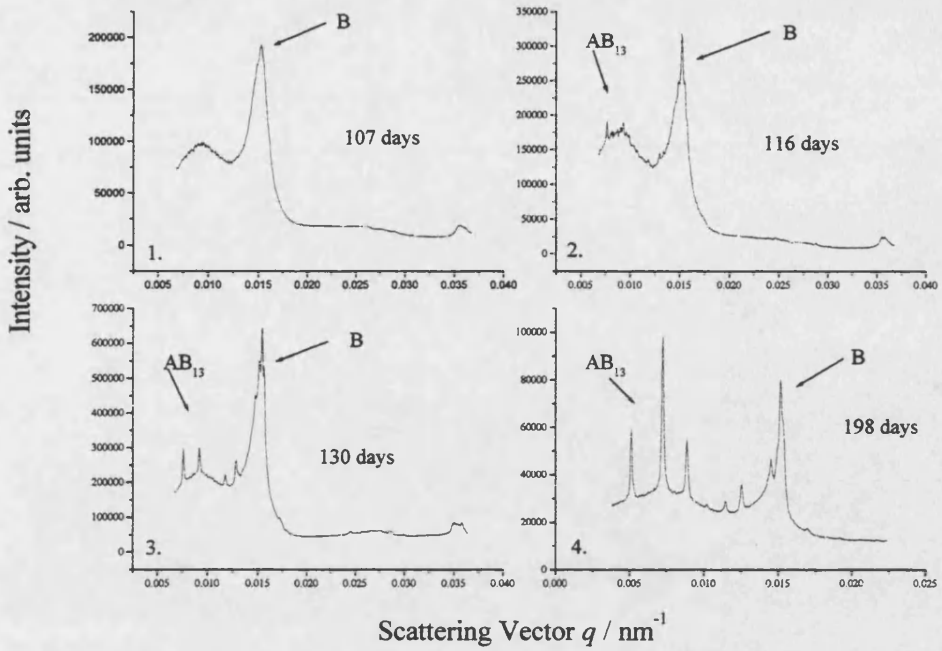

Figure 7.10. Light scattering measurements of sample 8, a binary mixture of colloidal hard spheres, prepared with size ratio $\alpha = 0.52$, number ratio $N_B / N_A = 14$ and total volume fraction $\phi_A + \phi_B = 0.521$. (1) after 107 days, (2) after 116 days, (3) after 130 days and (4) after 198 days.

The powder diffraction pattern shown in figure 7.10(4), is enlarged in figure 7.11 below.

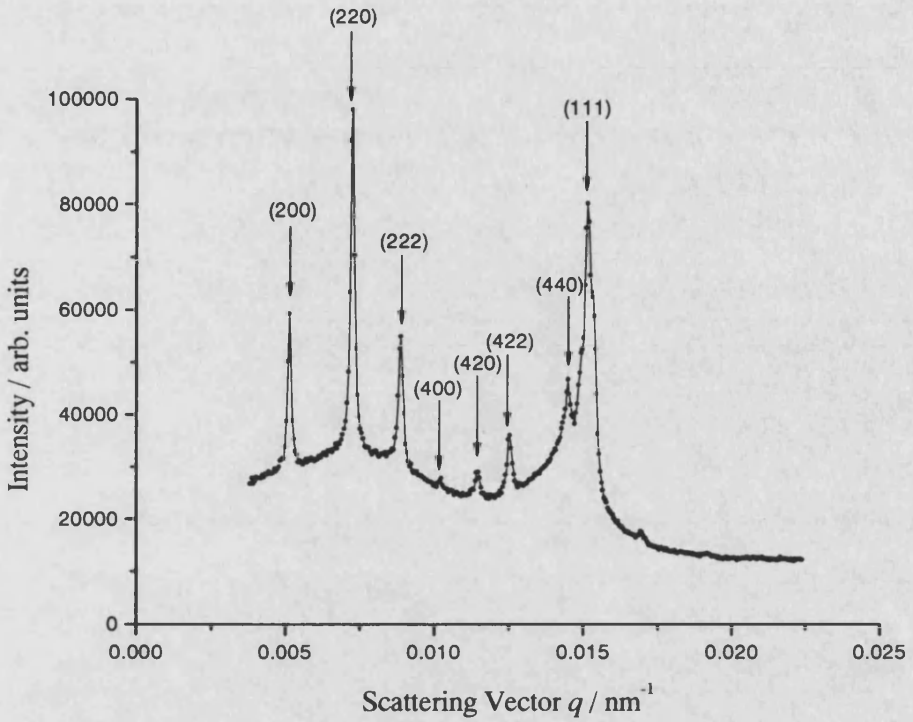

Figure 7.11. Light scattering measurements of sample 8, a colloidal mixture, with original composition: size ratio $\alpha = 0.52$, number ratio $N_B / N_A = 14$ and total volume fraction $\phi_A + \phi_B = 0.521$. The low q scattering is consistent with the AB_{13} superlattice structure, while the Bragg reflection at the highest q value arises due to the (111) line of a random stacked close packed crystal.

The intense Bragg peak at $q = 0.0152$ nm^{-1} corresponds to the (111) line, of the scattering arising from a random stacked close packed crystal. The lattice parameter was calculated ($a = 506 \pm 6$ nm) for this and other similar scattering patterns (see table 7.4) and suggests that the sample contains crystals of B particles. The sharp Bragg reflections at lower q values, are consistent with the AB_{13} superlattice structure. These peaks were indexed as follows, $q = 0.00508$ nm^{-1} (200),

q = 0.00725 nm^{-1} (220), q = 0.00886 nm^{-1} (222), q = 0.0102 nm^{-1} (400), q = 0.0114 nm^{-1} (420), q = 0.0125 nm^{-1} (422) and q = 0.0145 nm^{-1} (440).

As was mentioned in chapter 5, for a cubic phase, a plot of q^2_{hkl} versus $h^2 + k^2 + l^2$ should be a straight line, with gradient $4\pi^2 / a^2$, which passes through the origin. Figure 7.12 shows a plot of q^2_{hkl} versus $h^2 + k^2 + l^2$, for the indexed Bragg peaks given above.

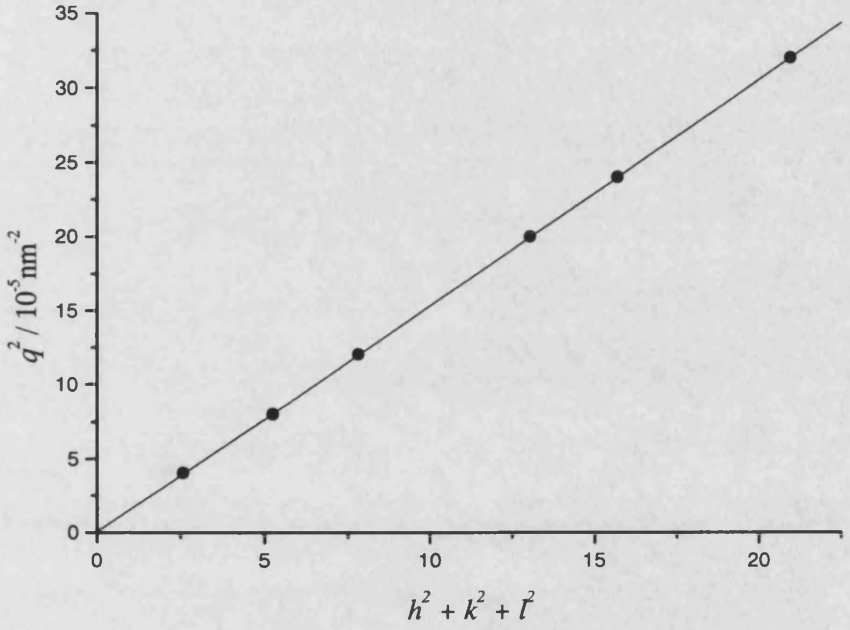

Figure 7.12. Indexing of the AB_{13} phase, of sample 8. q^2_{hkl} is plotted versus $h^2 + k^2 + l^2$ and the gradient is $4\pi^2 / a^2$, where a = 2460 nm, is the lattice constant and $\phi_{AB_{13}}$ = 0.56, is the crystal volume fraction.

From the gradient of the line in figure 7.12 ($4\pi^2 / a^2$), the unit cell length was calculated to be, a = 2460 ± 6 nm. The volume fraction of AB_{13} was calculated to be

$\phi_{AB_{13}}$ = 0.56. This analysis was repeated for the other scattering data, obtained at this number ratio. The results are collected together in table 7.4, at the end of the chapter.

In mixtures prepared with a number ratio N_B / N_A = 30, coexisting crystal and fluid phases formed. Crystallisation was complete after ~8 days of slow tumbling and crystals were visible by eye, in a ~5 mm layer at the base of the sample cell. A scattering profile, of sample 65, is shown in figure 7.13.

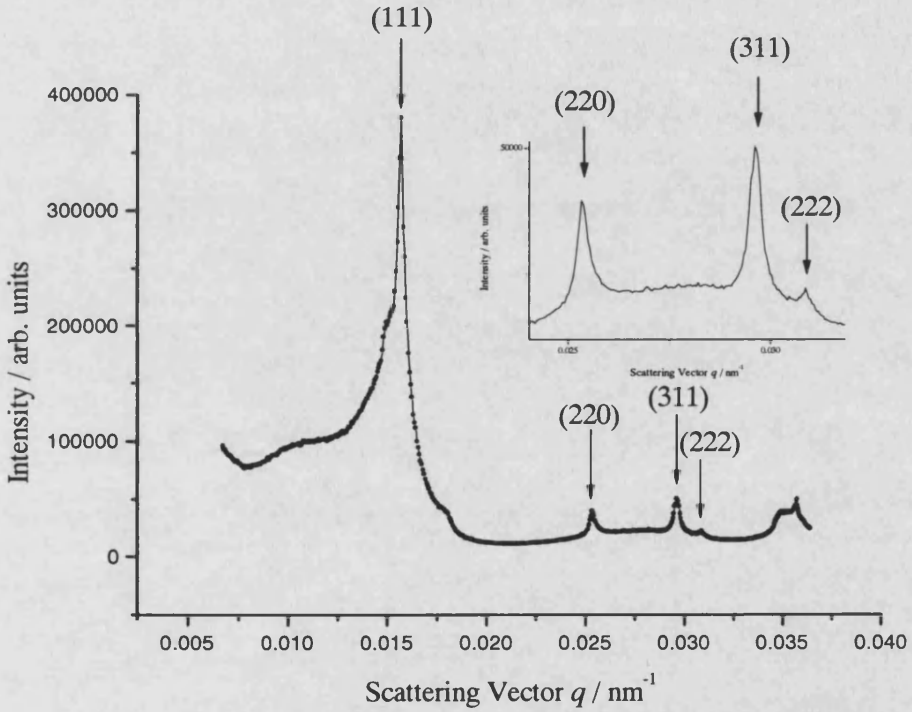

Figure 7.13. Light scattering measurements of sample 65, a binary mixture of hard sphere colloids, with size ratio α = 0.52, number ratio N_B / N_A = 30 and total volume fraction $\phi_A + \phi_B$ = 0.519. For clarity part of the scattering profile is enlarged (inset).

The measured Bragg reflections were indexed as follows, $q = 0.0156$ nm^{-1} (111), $q = 0.0253$ nm^{-1} (220) and $q = 0.0297$ nm^{-1} (311). The sharp peak at $q = 0.0156$ nm^{-1} (111) and subsequent peaks at higher q values are characteristic of a powder of random close packed crystals. The lattice parameter was calculated to be, $a = 489 \pm 6$ nm, which suggests that the crystals consist of small B particles and the coexisting fluid is enriched in A spheres.

Similarly, coexisting crystalline and fluid phases were observed, in mixtures rich in B, with a number ratio $N_B / N_A = 100$. Crystallisation was complete after ~6 days of slow rotational tumbling and crystals were visible by eye, in a ~12 mm layer at the base of the cell. This is slightly sooner than at $N_B / N_A = 30$, possibly because there are fewer A particles to expel from the growing B crystals. An illustrative scattered intensity profile, of the solid phase of sample 22, is shown in figure 7.14.

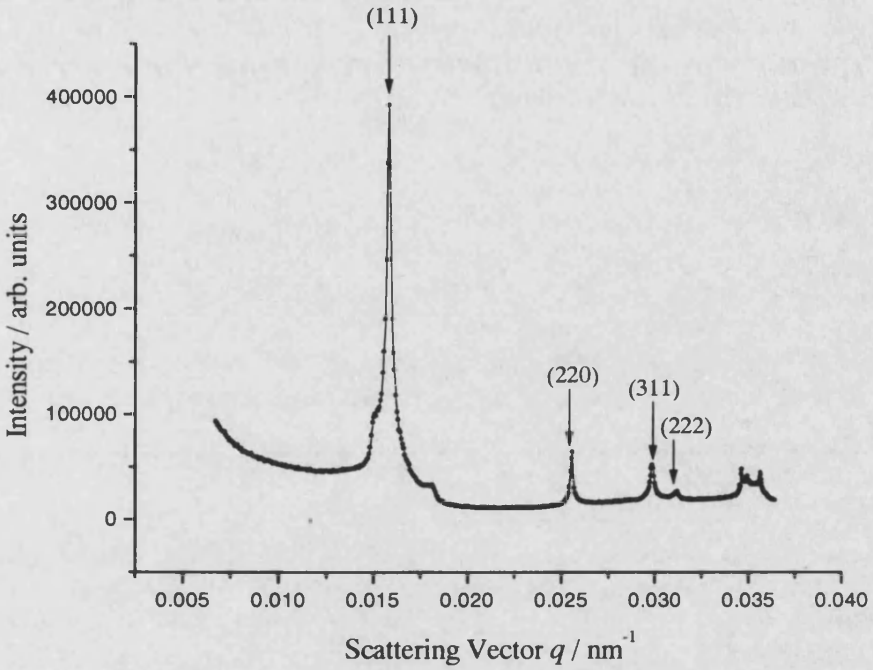

Figure 7.14. Light scattering results for sample 22, a binary hard sphere mixture of colloidal hard spheres, prepared with size ratio $\alpha = 0.52$, number ratio $N_B / N_A = 100$ and total volume fraction $\phi_A + \phi_B = 0.502$.

The sharp Bragg reflection at $q = 0.0158$ nm^{-1} and subsequent peaks, at higher q values, are characteristic of a powder of random stacked close packed crystals. The measured scattering peaks, at, $q = 0.0158$ nm^{-1}, $q = 0.0256$ nm^{-1}, $q = 0.0301$ nm^{-1} and $q = 0.0312$ nm^{-1}, may be indexed as the (111), (220), (311) and (222) lines of a fcc lattice. The measured lattice parameter was determined to be, $a = 484 \pm 6$ nm, which suggests that the sample contains crystals of

small B particles, coexisting with a fluid enriched in A spheres. The calculated lattice parameters are collected together in table 7.4 at the end of this chapter.

The phase behaviour of all the mixtures prepared with a size ratio of α = 0.52, is summarised in the phase diagram in figure 7.15.

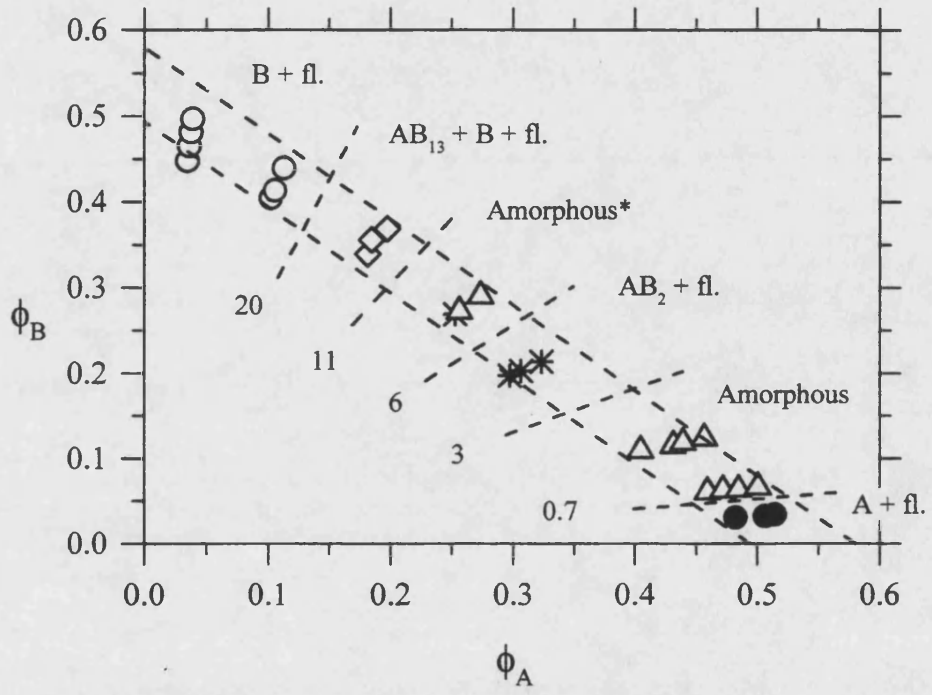

Figure 7.15. The observed phase behaviour of binary mixtures, of colloidal hard spheres, prepared with a size ratio α = 0.52. The samples studied are represented by the points: ●, A + F; ∆, amorphous; ✳, AB_2 + F; ◇, AB_{13} + B + F; ○, B + F and the approximate positions of the phase boundaries are marked by dashed lines. Lines of constant number ratio radiate from the origin. * In the sample with the lowest density, AB_2 formed over a long time.

As can be seen, the diagram contains six distinct regions of fluid-solid phase coexistence. The approximate positions of the phase boundaries are indicated by dashed lines.

In mixtures prepared with a number ratio $N_B / N_A = 0.5$, no crystals were observed by eye. However, the scattering was consistent with the formation of very small crystallites, composed of large A spheres and a coexisting fluid enriched in B spheres. These samples are indicated by solid circles in figure 7.15. Mixtures with number ratios, $N_B / N_A = 1$ and 2, are shown by open triangles in figure 7.15. No crystals were observed in these samples, for the duration of the experiment.

By contrast, in suspensions with number ratio $N_B / N_A = 5$, crystals with the AB_2 superlattice structure and coexisting fluid formed. These samples are marked by stars in figure 7.15.

In mixtures prepared with a number ratio $N_B / N_A = 8$, crystals were visible only in the sample with the lowest total volume fraction. A star in figure 7.15 indicates this sample. The other samples remained amorphous, for the duration of the experiment and are shown by open triangles.

In comparison, mixtures with a number ratio $N_B / N_A = 14$, formed crystals with the AB_{13} superlattice structure together with coexisting B crystals and a binary fluid. These mixtures are indicated by open diamonds in figure 7.15.

Mixtures prepared with number ratios $N_B / N_A = 30$ and 100, are shown by open circles in figure 7.15. In these samples, coexisting crystals of B and a fluid phase formed.

7.4. Binary Mixtures with a Size Ratio $\alpha = 0.72$

Mixtures with a size ratio $\alpha = 0.72 \pm 0.01$, were composed by interspersing the large A particles of the SPS09 sample ($d = 641 \pm 6$ nm), with the smaller B particles of the DMM7 sample ($d = 463 \pm 6$ nm). A total of thirteen different samples were prepared, at five different number ratios, with total volume fractions in the range $0.507 \leq \phi_A + \phi_B \leq 0.576$.

Coexisting crystal and fluid phases were observed in mixtures rich in A, with a number ratio $N_B / N_A = 0.5$. Crystallisation was complete, after ~19 days of slow tumbling and crystals were visible by eye in a ~10 mm layer at the bottom of the cell. An intensity profile, of the scattering from sample 91, is shown in figure 7.16.

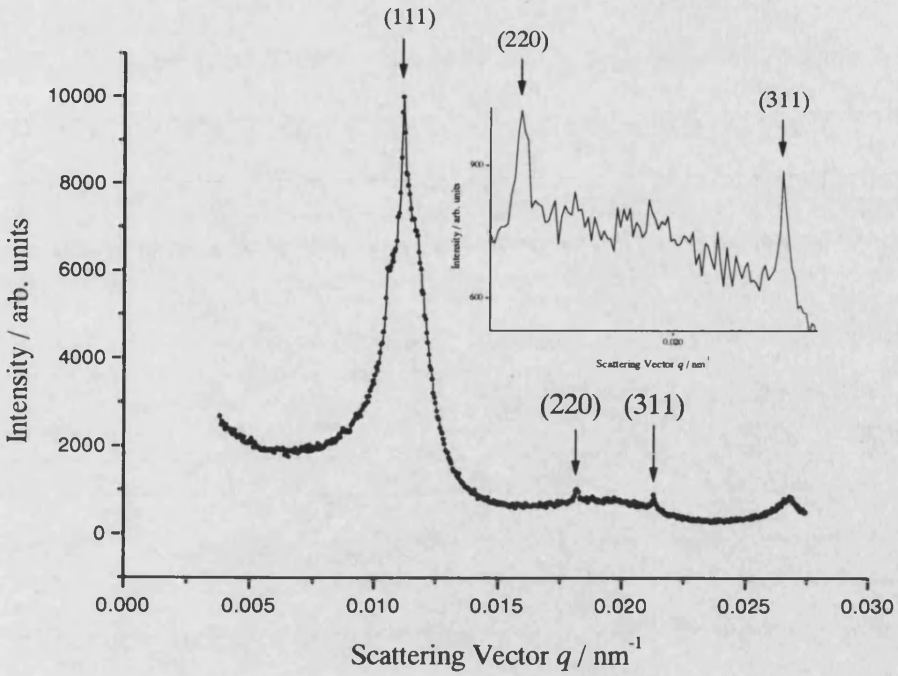

Figure 7.16. Light scattering measurements of sample 91, a binary mixture of colloidal hard spheres, prepared with size ratio $\alpha = 0.72$, number ratio $N_B / N_A = 0.5$ and total volume fraction $\phi_A + \phi_B = 0.529$. The inset diagram shows a magnified area of interest.

The peaks in figure 7.16 were indexed as follows, q = 0.0111 nm^{-1} (111), q = 0.0182 nm^{-1} (220) and q = 0.0213 nm^{-1} (311). The scattering pattern is characteristic of a powder of random stacked close packed crystals. The equivalent fcc lattice parameter was determined to be, a = 671 ± 6 nm (see table 7.7). This suggests that the crystals consist of A particles and the coexisting fluid is enriched in B spheres.

Coexisting crystal and fluid phases also formed in mixtures, prepared with a number ratio $N_B / N_A = 1$. Crystallisation was complete after ~ 19 days and crystals were visible by eye in a ~10mm layer at the base of the cell. A light diffraction pattern, characteristic of the solid phase of sample 94, is shown in figure 7.17.

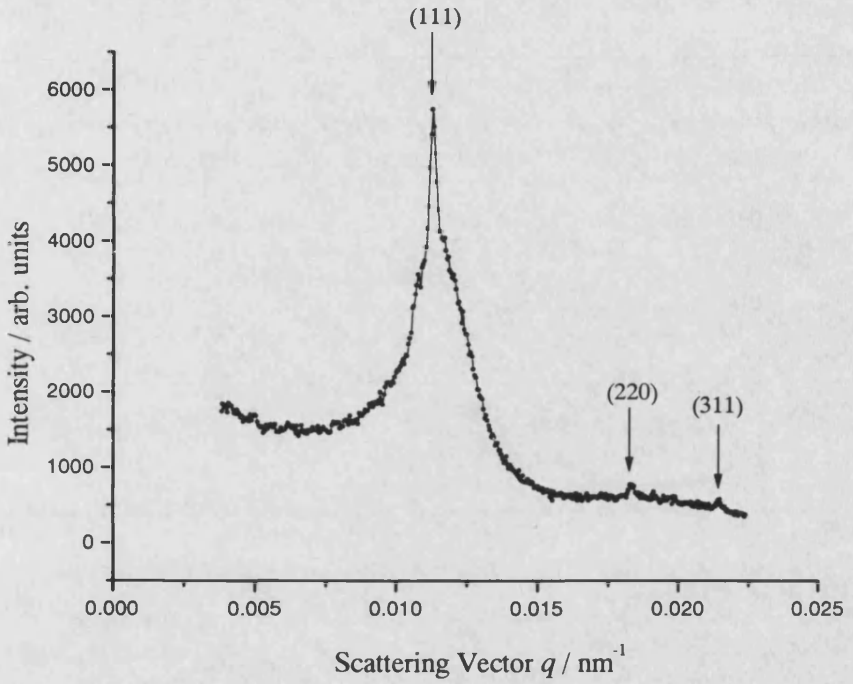

Figure 7.17. Light scattering measurements of sample 94, a binary mixture of hard sphere colloids, prepared with size ratio $\alpha = 0.72$, number ratio $N_B / N_A = 1$ and total volume fraction $\phi_A + \phi_B = 0.527$.

The Bragg reflections in figure 7.17 were indexed as follows, q = 0.0122 nm^{-1} (111), q = 0.0184 nm^{-1} (220) and q = 0.0215 nm^{-1} (311). The scattering pattern is consistent with a powder of random stacked close packed crystals. The peaks indexed as (220) and (311) were insufficiently sharp to use in the calculation of the lattice parameter. The lattice parameter was calculated to be, a = 674 ± 6 nm. Again, this suggests that the crystals are composed of A spheres and the coexisting fluid is enriched in B particles.

By contrast, mixtures prepared with a number ratio $N_B / N_A = 2$, remained in metastable fluid or glassy states. No crystals were observed by eye, after slow rotational tumbling for three months. Figure 7.18 shows the scattering pattern obtained from sample 98.

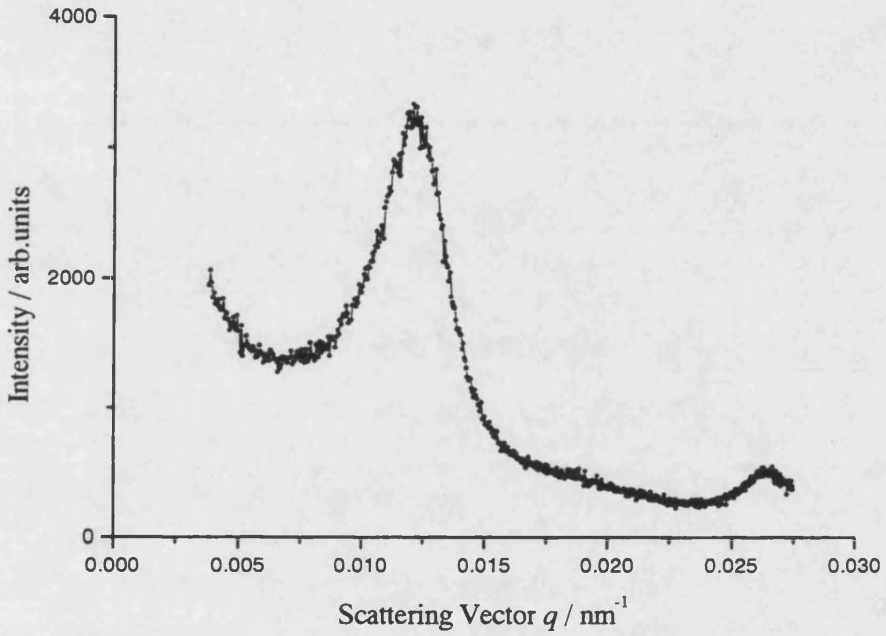

Figure 7.18. Light scattering measurements of sample 98, a binary mixture of colloidal hard spheres, with size ratio $\alpha = 0.72$, number ratio $N_B / N_A = 2$ and total volume fraction $\phi_A + \phi_B = 0.539$.

The scattering pattern is characteristic of a sample that is largely amorphous, with the expected sharp Bragg peaks not visible. Samples prepared with number ratio N_B

/ N_A = 5, also appeared to remain amorphous. The scattering profiles obtained were very similar to figure 7.18.

By contrast, mixtures prepared with a number ratio N_B / N_A = 13, formed coexisting crystal and fluid phases. Crystals were observed by eye, in a ~9 mm layer at the base of the sample cell. A powder diffraction pattern of the crystalline phase, of sample 104, is shown in figure 7.19.

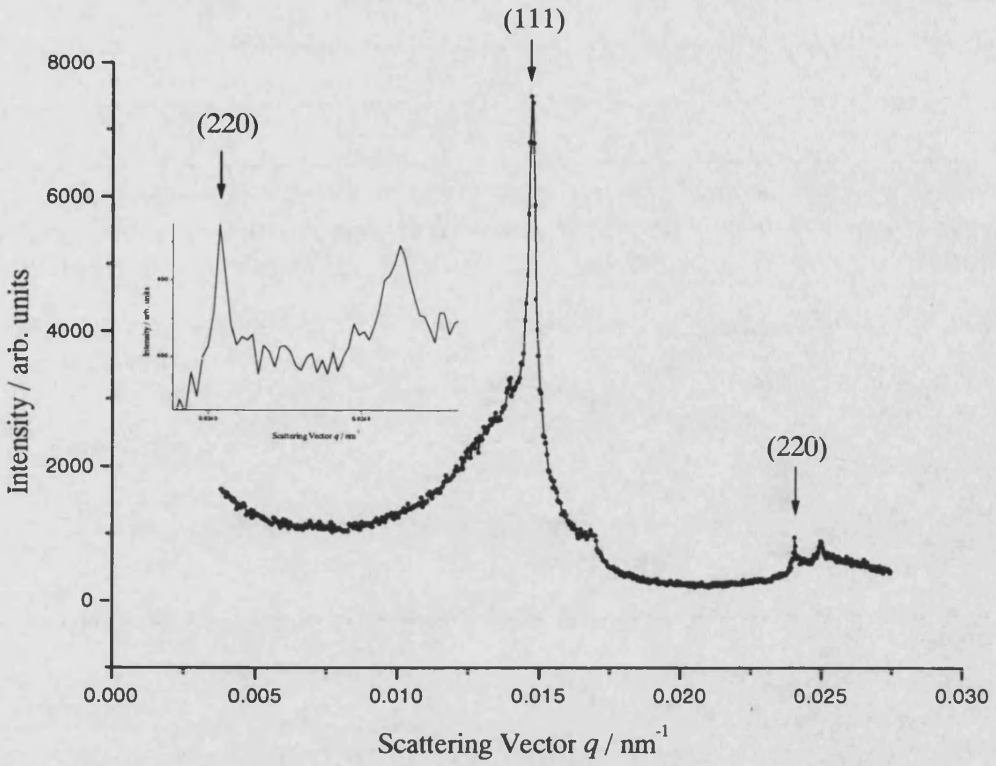

Figure 7.19. Light scattering measurements of sample 104, a binary mixture of hard sphere colloids, with original composition: size ratio $\alpha = 0.72$, number ratio $N_B / N_A = 13$ and total volume fraction $\phi_A + \phi_B = 0.523$.

The intense Bragg reflection at q = 0.0147 nm^{-1} corresponds to the (111) line, while the smaller peak, at q = 0.0240 nm^{-1} corresponds to the (220) line. The scattered intensity is consistent with a powder of crystallites with a random stacked close packed structure. The lattice parameter was calculated to be 518 ± 6 nm (see table 7.7), which suggests that the sample contains crystals of small B particles and a coexisting fluid enriched in A spheres. In sample 104, crystallisation was complete after ~18 days of slow tumbling. In comparison, full crystallisation took 6 days in a one-component B sample.

The phase behaviour, of all the mixtures prepared with a size ratio of α = 0.72, is summarised in the phase diagram in figure 7.20.

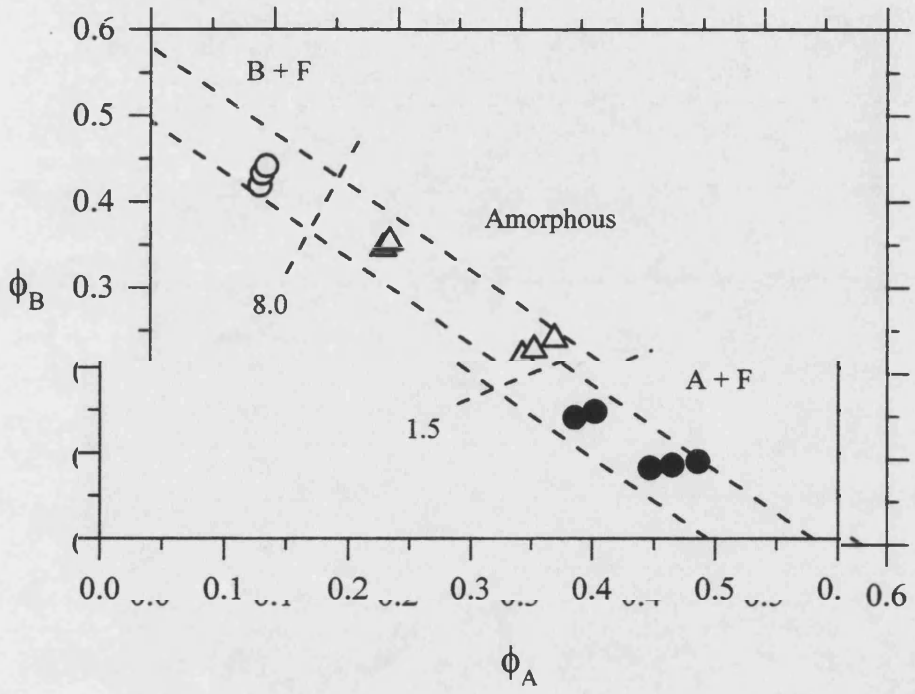

Figure 7.20. Phase diagram summarising the phase behaviour of mixtures, of hard sphere colloids, with a size ratio α = 0.72. The observed phases are: ●, A + F; Δ, amorphous; ○, B + F and the approximate positions of the phase boundaries are marked by dashed lines. The two lines radiating from the origin show the $AB_{1.5}$ and AB_8 stoichiometries.

As can be seen, the phase diagram contains three distinct regions of fluid-solid phase behaviour. Dashed lines mark the approximate positions of the phase boundaries.

In mixtures prepared with number ratios of $N_B / N_A = 0.5$ and 1, crystals of A and coexisting fluid phases formed. These mixtures are indicated by the solid circles in figure 7.20.

At intermediate number ratios, mixtures prepared with number ratios $N_B / N_A = 2$ and 5 remained amorphous. These samples are shown by the open triangles in figure 7.20.

Mixtures rich in B, with number ratio $N_B / N_A = 13$, formed coexisting B crystals and a fluid phase enriched in large A spheres. These samples are indicated by open circles in figure 7.20.

7.5. Comparison with Theory

7.5.1. Binary Mixtures with a Size Ratio $\alpha = 0.42$

Madden and Eldridge have reported equilibrium phase diagrams, obtained by computer simulation, for binary mixtures of hard spheres, with size ratios $\alpha = 0.414$ and 0.45.[105] The experimental observations, for mixtures with a size ratio of $\alpha = 0.42 \pm 0.01$, are compared below with both of these theoretical predictions. This comparison is summarised in table 7.3, at the end of the chapter.

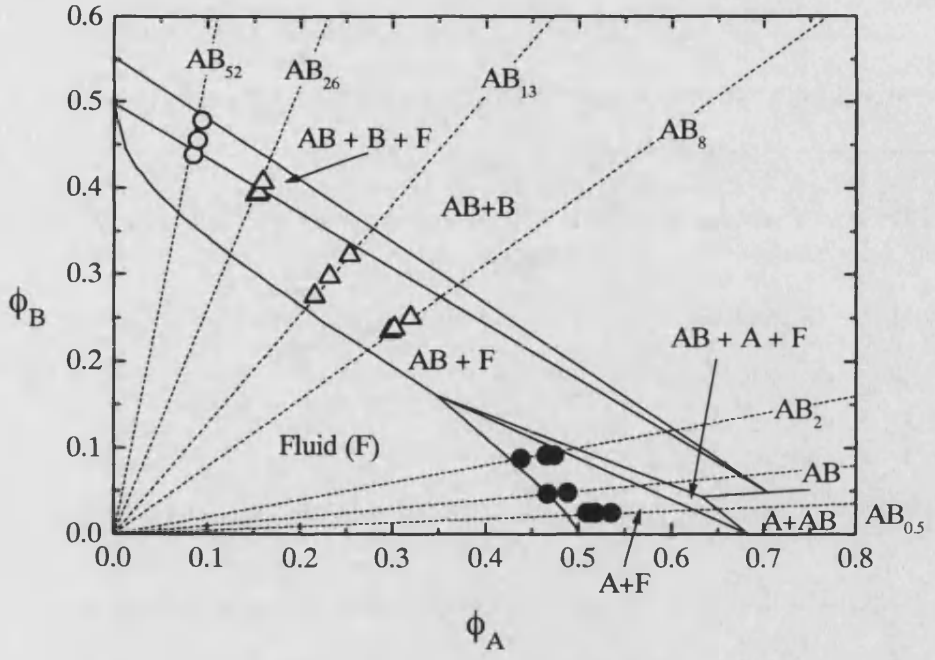

Figure 7.21. The experimental samples prepared in the $\alpha = 0.42 \pm 0.01$ system and the observed phases: ●, A + fluid; Δ, amorphous; ○, B + fluid. The solid lines show the positions of the phase boundaries, calculated by Trizac *et al.* for a mixture of hard spheres, with a size ratio $\alpha = 0.414$.[105]

The theoretical diagram at $\alpha = 0.414$ consists of a single fluid region (F), two regions of fluid-solid coexistence, two three-phase eutectic triangles and two regions of solid-solid coexistence. At the intermediate volume fractions, which are accessible experimentally, samples are predicted to lie in the A + fluid (F), AB (NaCl) + F and the AB (NaCl) + B + F regions of the phase diagram.

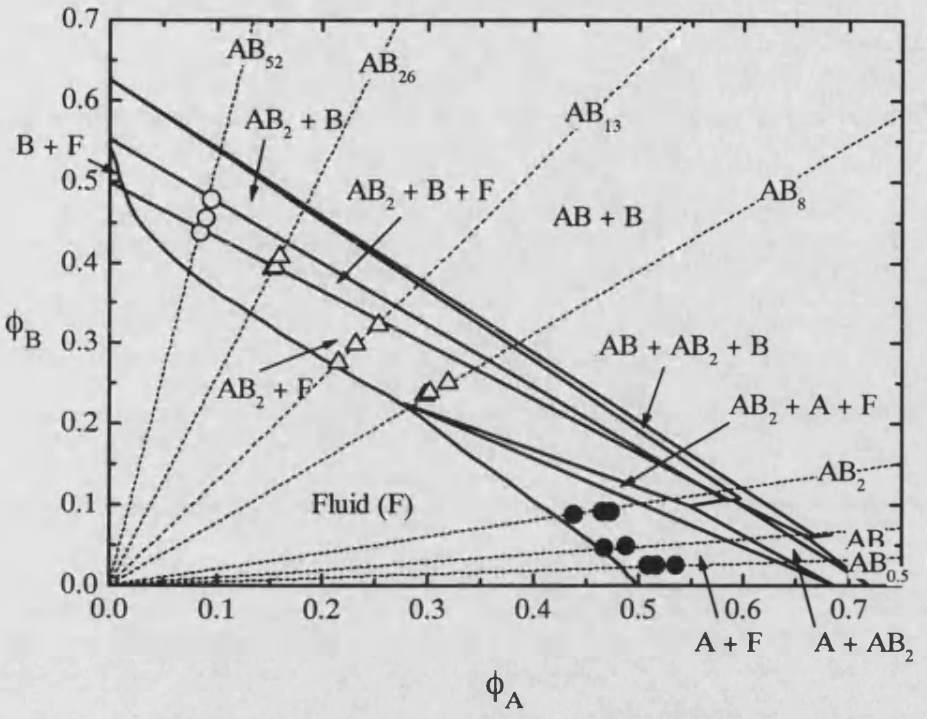

Figure 7.22. The experimental samples prepared in the $\alpha = 0.42 \pm 0.01$ system, with observed phases: ●, A + fluid; Δ, amorphous; ○, B + fluid. The solid lines show the positions of the phase boundaries, calculated by Trizac *et al.* for a mixture of hard spheres, with a size ratio of $\alpha = 0.45$.[105]

In contrast, at $\alpha = 0.45$, the phase diagram contains stable AB_2 structures and AB, with the NaCl structure, is stable only at high densities. As can be seen in figure 7.22, there is a fluid (F) region, three regions of fluid-solid coexistence, four three-phase eutectic triangles and five regions of solid-solid coexistence. At intermediate volume fractions, of relevance to the current experimental work, the

samples are predicted to lie in the A + F, AB_2 + F and AB_2 + B + F regions of the phase diagram.

As can be seen from figures 7.21 and 7.22, mixtures prepared with number ratios $N_B / N_A = 0.5$, 1 and 2 are predicted to lie in the large A + F region, of both theoretical phase diagrams. As was mentioned earlier, in mixtures prepared with these number ratios, crystals of A particles and coexisting fluid formed (see also Appendix). Hence, there is good agreement between experiment and theory for these points.

Experimentally, mixtures prepared with a number ratio $N_B / N_A = 8$ remained largely amorphous. A few crystals were observed, only in the sample with the lowest total volume fraction. In figure 7.21, these samples are predicted to lie in the large AB (NaCl) + fluid region of the phase diagram, at a size ratio $\alpha = 0.414$ or for $\alpha = 0.45$ (figure 7.22), in the large AB_2 + fluid region. Since we were unable to distinguish the identity of the crystal phase, we can not choose between these two predictions.

Similarly, mixtures prepared with a number ratio $N_B / N_A = 13$ remained totally amorphous. After slow tumbling for 256 days, no crystals were visible. In figure 7.21 and 7.22 the three samples, prepared at this number ratio, are predicted to be in the AB (NaCl) + fluid region of the phase diagram, at $\alpha = 0.414$, or in the AB_2 + fluid region of the diagram at $\alpha = 0.45$. Experiment and theory appear to disagree for these points.

Mixtures prepared with a number ratio $N_B / N_A = 26$, also remained amorphous. No crystals were observed, for the duration of the experiment. As can be seen from the calculated phase diagram, at $\alpha = 0.414$ (fig. 7.21), the sample with

the highest density is predicted to be in the AB (NaCl) + B + fluid region, while the two samples with lower densities are predicted to lie just inside the large AB (NaCl) + fluid region of the phase diagram. At $\alpha = 0.45$ (figure 7.22), the two samples with lower densities are predicted to lie just inside the AB_2 + fluid region and the sample with the highest density is predicted to be in the AB_2 + B + fluid region. Again, experiment and theory are not consistent for these points.

By contrast, in mixtures prepared with a number ratio $N_B / N_A = 52$, colloidal crystals and a coexisting fluid formed. The structure of the solid phase was identified as a random stacked close packed arrangement of B particles. At size ratio $\alpha = 0.41$, the sample with the lowest total volume fraction is predicted to form AB (NaCl) + fluid (figure 7.21). The two samples prepared at higher densities are predicted to lie in the AB (NaCl) + B + fluid region of the phase diagram. For the size ratio $\alpha = 0.45$, all three mixtures are predicted to be largely in the AB_2 + B + fluid region (figure 7.22). With the experimental observation of B crystals, there is partial agreement between experiment and theory for these points.

7.5.2. Binary Mixtures with a Size Ratio $\alpha = 0.52$

As was mentioned previously, in chapter 6, theoretical phase diagrams have been determined for binary hard sphere mixtures, with size ratios $\alpha = 0.50$ and 0.54.[76]. Since the experimental diameter ratio lies midway between these two limits, the experimental observations are compared below, with both of these theoretical

these theoretical predictions. The observed and predicted phase behaviour is also summarised in table 7.6.

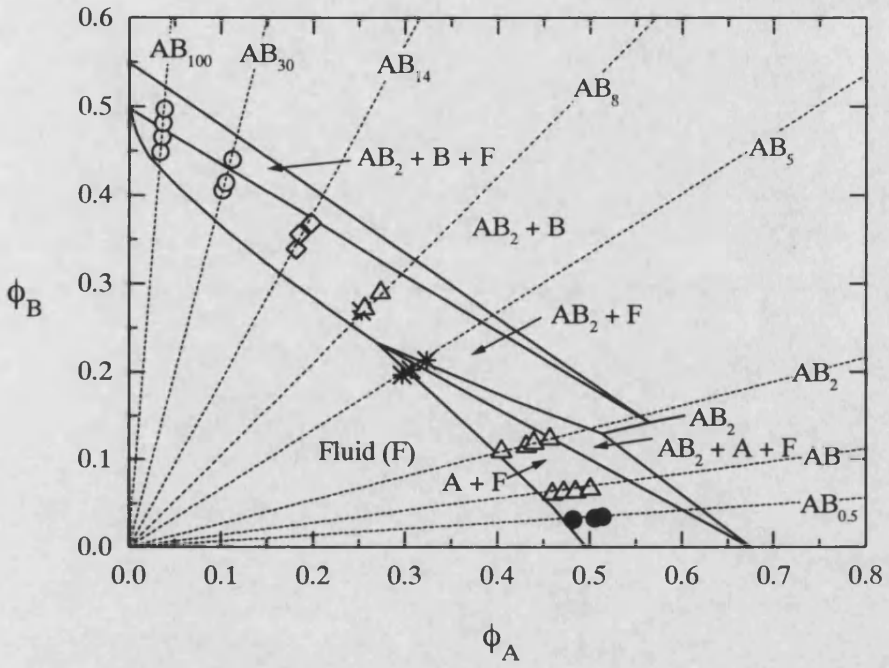

Figure 7.23. The experimental samples prepared in the $\alpha = 0.52 \pm 0.01$ system, with observed phases: ●, A + F; Δ, amorphous; ∗, AB_2 + F; ◇, AB_{13} + B + F; ○, B + F. The solid lines show the positions of the phase boundaries, calculated by Eldridge *et al.* for a mixture of hard spheres, with a size ratio of $\alpha = 0.50$.[76]

The theoretical phase diagram at $\alpha = 0.50$ consists of a fluid (F) region, two crystal-fluid phase coexistence regions, two three-phase eutectic triangles and two solid-solid phase coexistence regions. Similarly, the predicted phase diagram, at $\alpha =$

$\alpha = 0.54$, consists of a fluid region, three fluid-solid phase coexistence regions, four three-phase eutectic triangles and four regions of solid-solid phase coexistence.

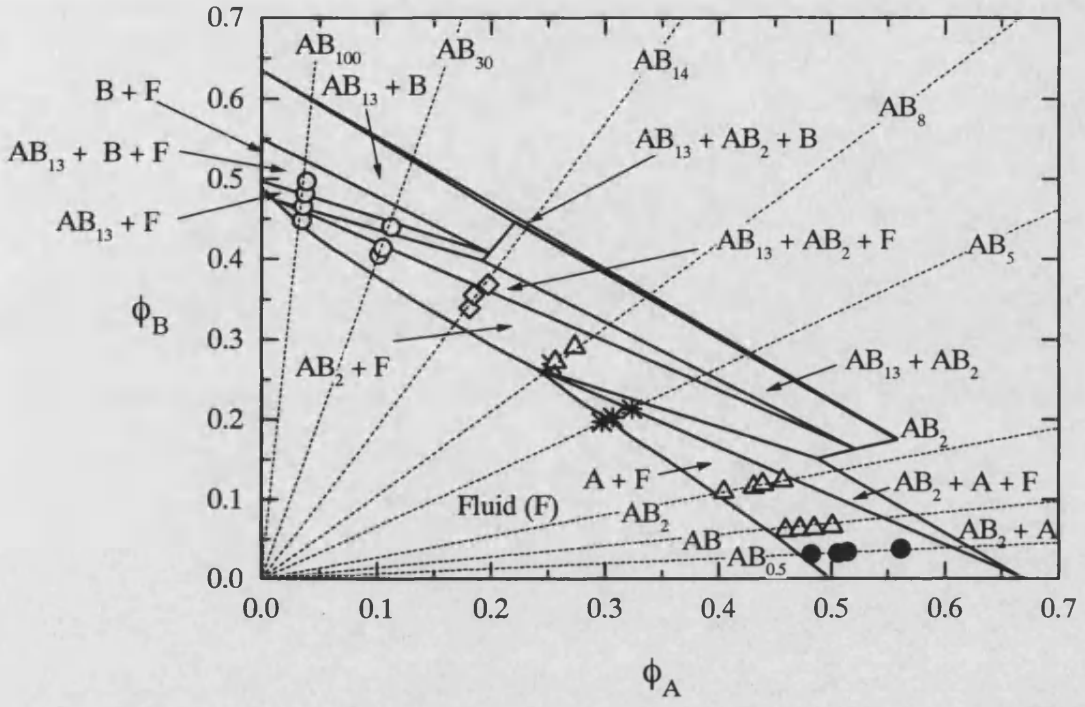

Figure 7.24. The experimental samples prepared in the $\alpha = 0.52 \pm 0.01$ system, with observed phases: ●, A + F; Δ, amorphous; *, AB_2 + F; ◇, AB_{13} + B + F; ○, B + F. The solid lines show the positions of the phase boundaries, calculated by Eldridge *et al.* for a mixture of hard spheres, with a size ratio $\alpha = 0.54$.[76]

Experimentally, mixtures prepared with a number ratio $N_B / N_A = 0.5$, appeared to remain in metastable fluid or glassy states and no crystals were observed by eye. However, static light scattering measurements, of the apparently amorphous phases, suggested that the samples might contain very small crystals of component

A. This is consistent with the theoretical predictions, of A + fluid, for mixtures with size ratios of $\alpha = 0.50$ and $\alpha = 0.54$.

Mixtures prepared with a number ratio $N_B / N_A = 1$ and 2, appeared to remain amorphous, even after slow tumbling for three months. Little evidence was found in the light scattering measurements, for crystals of A. As can be seen from figures 7.23 and 7.24, the samples prepared at this number ratio are predicted to lie in the large A + F region of the phase diagram, at both size ratios. For these samples experiment and theory do not concur. A tendency to form glasses, at large number ratios, has been observed previously at size ratios $\alpha = 0.62$ and $\alpha = 0.58$.[10,11] At $\alpha = 0.62$, mixtures prepared with number ratios in the range $1.2 \leq N_B / N_A \leq 4.0$ remained amorphous.[10] Similarly, samples prepared at $\alpha = 0.58$, with number ratio $N_B / N_A = 2$ did not crystallise.[11]

In mixtures prepared with a number ratio $N_B / N_A = 5$, crystals with the AB_2 superlattice structure formed, together with a coexisting binary fluid phase. Samples with this number ratio, are predicted to be very close to the AB_2 + fluid region of the phase diagram at both $\alpha = 0.50$ (figure 7.23) and $\alpha = 0.54$ (figure 7.24). Hence, for these points, experiment and theory are in qualitative agreement.

Mixtures prepared with a number ratio $N_B / N_A = 8$, remained largely amorphous and no crystals were observed by eye. However, after almost 200 days evidence appeared in the light scattering profile for AB_2. These samples are predicted to lie in the AB_2 + fluid region of both phase diagrams, at $\alpha = 0.50$ and at $\alpha = 0.54$. With the observation of AB_2 in the scattering patterns, there is a degree of agreement with theory, for these points. Previous authors have noted, that the greater

the difference between the sample stoichiometry and AB_2 stoichiometry the more reluctant AB_2 is to form.[76]

In mixtures with a number ratio $N_B / N_A = 14$, crystals with the AB_{13} superlattice structure, coexisting with random close packed crystals of B particles and binary fluid, were found. These samples are predicted to be in the AB_2 + fluid region of the phase diagram, at $\alpha = 0.50$. At $\alpha = 0.54$, the two samples of lower concentration are also predicted to lie in the AB_2 + fluid region of the phase diagram. The sample with the highest concentration is predicted to lie in the AB_{13} + AB_2 + fluid region of the diagram. Experiment and theory are not consistent for these points. It has also been noted previously, that AB_{13} forms whenever it is predicted on thermodynamic grounds and in some cases at compositions where other phases are expected to be more stable.[76]

Coexisting crystal and fluid phases were also found, in mixtures with a number ratio $N_B / N_A = 30$. The crystal phase was identified as a crystal of random stacked B particles. Of the three binary samples prepared at this number ratio, the two samples with the lowest total volume fractions are predicted to be in the AB_2 + fluid region, at $\alpha = 0.50$ (figure 7.23). The sample with the highest volume fraction, is predicted to lie in the AB_2 + B + fluid region. With regards to the formation of B crystals, there is partial agreement between experiment and theory. At $\alpha = 0.54$ (figure 7.24) the two samples prepared with the lowest volume fractions, are predicted to lie in the AB_2 + fluid region of the diagram. The sample with the highest volume fraction, is predicted to lie in the AB_{13} + fluid region. At this size ratio, theory does not agree with the experimental points.

In mixtures rich in B, at number ratio $N_B / N_A = 100$, coexisting crystals of B and a binary fluid phase were observed. Of the four samples prepared at this number ratio, the two with the lower total volume fractions are predicted to lie in the AB_2 + fluid region of the phase diagram, at $\alpha = 0.50$ (figure 7.23). The two samples with higher densities are predicted to lie in the AB_2 + B + fluid region. With the observation of B + F, there is some agreement between experiment and theory. At $\alpha = 0.54$ (figure 7.24), the sample with the lowest concentration is predicted to lie in the AB_2 + fluid region. The sample with the next highest concentration is predicted to lie in the AB_{13} + fluid region, while the two samples with the highest concentrations are predicted to lie in the AB_{13} + B + fluid region. Again, there is some agreement between the theoretical predictions and the experimental observations of B + F.

7.5.3. Binary mixtures with a Size Ratio $\alpha = 0.72$

As was mentioned in chapter 2, the theoretical phase diagram for a hard sphere mixture with size ratio $\alpha = 0.75$ has been calculated by Bartlett, assuming total immiscibility in a single solid phase.[77] The experimental points at $\alpha = 0.72 \pm 0.01$ are compared, in figure 7.25, with the theoretical phase diagram at $\alpha = 0.75$. The observed phase behaviour and theoretical predictions are also summarised in table 7.8.

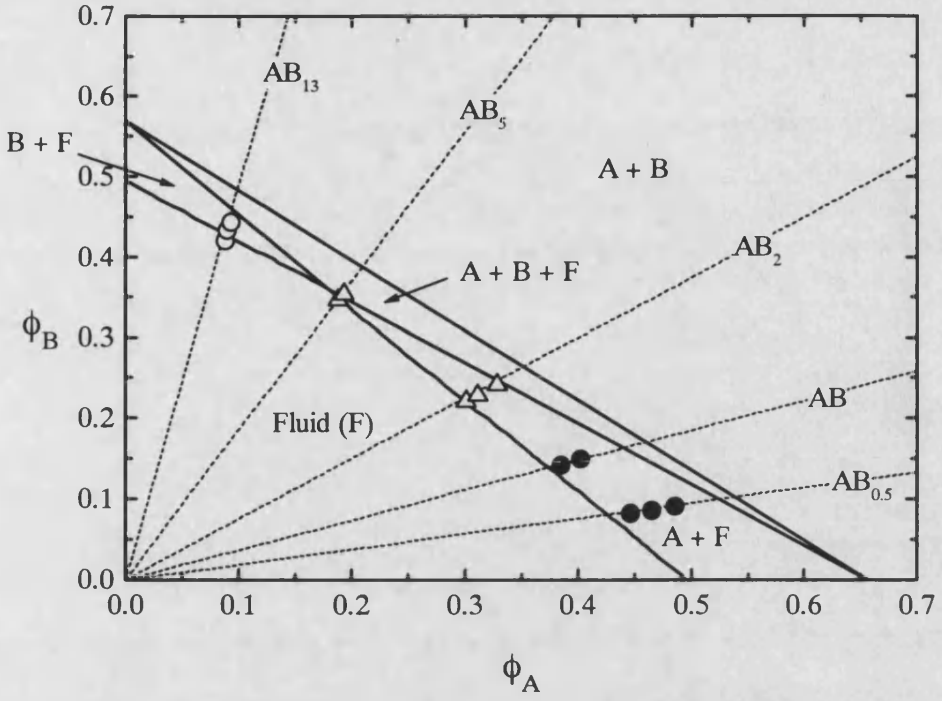

Figure 7.25. The experimental samples prepared in the $\alpha = 0.72 \pm 0.01$ system, with observed phases: ●, A + F; Δ, amorphous; ○, B + F. The solid lines show the positions of the phase boundaries, calculated by Bartlett for a mixture of hard spheres, with a size ratio of $\alpha = 0.75$.[77]

At low volume fractions, the equilibrium state is predicted to be a binary fluid (F). At intermediate volume fractions there are two regions of solid-fluid coexistence, in which crystals of either A or B are in equilibrium with a binary fluid phase. These regions are separated by a three phase eutectic triangle. Within this triangle, a fluid of eutectic composition coexists with two equilibrium solid phases, A and B. The densities and compositions of all three phases remain constant throughout the eutectic region.[77] However, the relative volume fraction of the fluid phase decreases, as the total volume fraction is increased. Hence, the fluid volume fraction is highest at the eutectic point. Calculations have shown that the fluid

remains stable to higher total volume fraction, in the binary mixture than in the one-component case.[77] At higher volume fractions, a region of solid-solid phase coexistence is predicted.

Experimentally, in mixtures with number ratios $N_B / N_A = 0.5$ and 1, coexisting A crystals and a fluid phase formed. As can be seen in figure 7.25, the five samples, prepared with these number ratios, are predicted to lie in the large A + fluid region of the theoretical phase diagram. Hence, experiment and theory are in good agreement for these points.

By contrast, mixtures prepared with a number ratio $N_B / N_A = 2$, remained in metastable fluid or glassy states. No crystals were observed, even after slow tumbling for three months. These three samples are predicted to lie in the large A + fluid region of the phase diagram (figure 7.25). However, a key point of Bartlett's immiscible sphere model is that the increased stability of the fluid phase at the eutectic suggests that glass formation will be most likely to occur in mixtures with the eutectic composition.[77]As the mixtures prepared with a number ratio $N_B / N_A = 2$ are close to the eutectic, the formation of a binary glass may be more likely.

Similarly, the two mixtures prepared with a number ratio $N_A / N_B = 5$, remained amorphous. As can be seen from figure 7.25, both samples are very close to the eutectic point, where preferential glass formation is expected.[77] These observations are qualitatively consistent with the predictions of Bartlett's immiscible sphere model.[77]

In mixtures prepared with a number ratio $N_A / N_B = 13$, coexisting crystals of B and a binary fluid phase formed. The samples prepared at this number ratio, are

predicted to be mainly in the B + fluid region of the phase diagram (figure 7.25). Again, for these points, the theoretical predictions appear to be consistent with experiment.

7.6. Conclusions

In the present work, the phase behaviour of binary mixtures, with size ratios $\alpha = 0.42$, 0.52 and 0.72, was investigated. The phase behaviour, observed at each size ratio, is summarised below.

At the size ratio $\alpha = 0.42$, mixtures rich in A, with number ratios $N_B / N_A =$ 0.5, 1 and 2, formed crystals of A and coexisting binary fluid (also see Appendix). In the opposite limit, in mixtures rich in B, with a number ratio $N_B / N_A = 52$, crystals of B and coexisting fluid were found. By contrast, in samples prepared with intermediate number ratios $N_B / N_A = 8$, 13 and 26, no crystals were observed during the course of the experiment. The observed phase behaviour is summarised in figure 7.6.

In mixtures prepared with a size ratio $\alpha = 0.52$, a more complex sequence of phase behaviour was observed. As at size ratio $\alpha = 0.42$, mixtures rich in A, with number ratios $N_B / N_A = 0.5$, formed A crystals and coexisting fluid. Similarly, in mixtures rich in B, with number ratios $N_B / N_A = 30$ and 100, crystals of B and a coexisting binary fluid phase formed. However, samples with number ratios N_B / N_A = 1 and 2 appeared to remain amorphous. Also, in mixtures with a number ratio $N_B / N_A = 8$, a few small crystals were observed only in the suspension with the lowest total volume fraction. The structure of these crystals could not be determined and

suspensions prepared with higher total volume fractions remained completely amorphous. By contrast, in mixtures with a number ratio $N_B / N_A = 5$, the AB_2 superlattice phase was found, together with a coexisting binary fluid. Also, in samples prepared with a number ratio $N_B / N_A = 14$, a second superlattice phase was found, AB_{13}, coexisting with crystals of B and a binary fluid phase. The observed phase behaviour of the samples prepared, at this number ratio, is summarised in figure 7.15.

At the size ratio $\alpha = 0.72$, mixtures with number ratios $N_B / N_A = 0.5$ and 1, formed crystals of A and a coexisting binary fluid. In suspensions rich in B, with $N_B / N_A = 13$, coexisting crystals of B and a binary fluid phase formed. However, at intermediate size ratios, samples prepared with a number ratio $N_B / N_A = 2$ and 5 remained amorphous for the duration of the experiment. The phase behaviour, of all the mixtures prepared with a size ratio $\alpha = 0.72$, is summarised in figure 7.20.

At each size ratio, the phase behaviour is similar in the regions close to the axes. Mixtures rich in A form crystals of A and a coexisting fluid phase and mixtures rich in B form crystals of B and coexisting fluid. There is also an amorphous region in the phase diagram, at each size ratio. The size of this region increases with decreasing size ratio.

The two superlattice phases AB_2 and AB_{13} were found only at size ratio $\alpha = 0.52$. This suggests that the mixtures with size ratios $\alpha = 0.42$ and 0.72, are beyond the limits of stability for these superlattice phases. Simulation results, for the stability of these phases, are consistent with these observations. As was mentioned in chapter 6, Eldridge and co-workers have predicted the AB_2 phase to be stable in

the range $0.425 < \alpha < 0.62$ and the AB_{13} phase to be stable in the range $0.48 < \alpha < 0.62$.[102,103]

A comparison is made below, between the results of the current work and the earlier work of Bartlett *et al.*[10,11] These authors studied the phase behaviour of binary mixtures of hard sphere colloids, with size ratios $\alpha = 0.58$ and 0.62. The observed phase behaviour is summarised in figure 7.26.

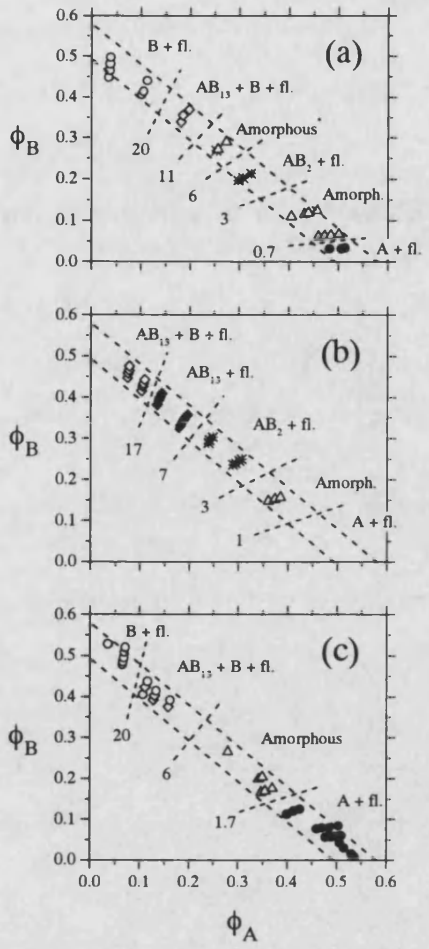

Figure 7.26. Constant volume phase diagrams, summarising the phase behaviour of hard sphere colloidal mixtures, (a) from the present work, with size ratio 0.52 and the earlier results of Bartlett *et al.*, with size ratios 0.58 (b) and 0.62 (c).[10,11] The following phases were observed: ●, A + F; Δ, amorphous; ∗, AB_2 + F; ◇, AB_{13} + B + F; ♦, AB_{13} + F; ○, B + F.

A notable similarity, between the results at $\alpha = 0.62$ and those of the present work, is that pure A or pure B and coexisting fluid, is found in the regions near the limits of extreme composition. At $\alpha = 0.58$, the range of the number ratios of the samples does not extend far enough into these regions, to know whether the same behaviour would be found. However, Bartlett *et al.* have suggested that the same behaviour would be expected.[11]

Another similarity is that amorphous regions were found in the phase diagram, at each size ratio. Also of note, is that the AB_2 and coexisting fluid region occurs at approximately the same number ratios, in the phase diagrams of mixtures with size ratios $\alpha = 0.52$ and $\alpha = 0.58$. The AB_{13} superlattice phase is observed in mixtures, prepared at all three size ratios. As can be seen from figure 7.26, this phase forms over the widest range of number ratios ($N_B / N_A = 9$, 14, 20 and 30) at size ratio $\alpha = 0.58$. Also, the rate of crystallisation of AB_{13} was fastest at $\alpha = 0.58$. In a suspension with a number ratio $N_B / N_A = 20$, crystallisation took 3 weeks to complete. In comparison, at $\alpha = 0.52$ and 0.62, full crystallisation took 3 months. For the AB_2 phase, crystallisation was most rapid at $\alpha = 0.52$, taking approximately 2.5 months to complete. At $\alpha = 0.58$, full crystallisation took around three months and at $\alpha = 0.62$, the AB_2 phase was not observed.

The results of the present work were compared with theoretical predictions. For mixtures prepared with a size ratio of $\alpha = 0.42$, a detailed comparison was made with the computer simulation results of Madden and Eldridge, for hard sphere mixtures with size ratios of $\alpha = 0.414$ and 0.45.[105] Close agreement was found, between the experimental observations and the simulation predictions, over moderate regions of composition. At

intermediate number ratios, several differences were found. In particular, at α = 0.414 simulation predicts crystals with the AB (NaCl) structure and at $\alpha = 0.45$ crystals with the AB_2 superlattice structure are predicted. However, experimentally, crystals with these superlattice structures were not identified (see Appendix).

The phase behaviour of mixtures, prepared with a size ratio $\alpha = 0.52$, was compared with the theoretical predictions of Madden and Eldridge, for hard sphere mixtures with size ratios $\alpha = 0.50$ and 0.54.[76] Close agreement was found in some regions of both phase diagrams. For instance, crystals of A and coexisting fluid were observed, in samples predicted to be in the A + F region, at both size ratios. There were also points of disagreement. For example, mixtures prepared with a number ratio $N_B / N_A = 14$, formed AB_{13} with coexisting crystals of B and a binary fluid. However, at both $\alpha = 0.50$ and 0.54, these samples are predicted to form crystals of AB_2 and coexisting fluid.

For mixtures with a size ratio $\alpha = 0.72$, the observed phase behaviour was compared with the theoretical phase diagram arising from Bartlett's immiscible sphere model.[77] Overall, experiment and simulation were found to be consistent , over wide regions of composition. A difference was found at number ratio $N_B / N_A = 2$, where samples are predicted to lie in the large A + fluid region of the phase diagram. Experimentally, mixtures prepared at this number ratio remained amorphous.

There are several possible sources of error, which have been considered, in previous studies using the PMMA / PHSA, CS_2 / decalin system. Firstly, the stock suspensions, used in the preparation of binary mixtures, have an inevitable distribution of particle sizes. Earlier work has found that one-component colloidal suspensions with a measured polydispersity above a critical value, of $\sigma_c = 0.08$

- 0.12, do not crystallise.[5] Although the polydispersity of the one-component suspensions, used in the present work, to prepare binary mixtures, were below this ($\sigma = 0.04 - 0.07$), the effect of a small degree of polydispersity in binary mixtures has not been studied in detail.

Another matter, is the accuracy of the volume fractions of the experimentally prepared mixtures. An error of approximately 0.01, in the total volume fraction ($\phi_A + \phi_B$), should be considered. Also, although the samples were carefully sealed, liquid was lost over time due to evaporation. By weighing the samples regularly, this depletion was found to be small.

A further consideration, is the closeness of the interparticle interaction to the hard sphere potential. Although steep and repulsive, the interparticle potential is continuous. However, a number of previous studies, on one-component suspensions of this type, suggest that the PMMA particles behave as essentially hard spheres.[8]

Furthermore, as mentioned in chapter 4, during the preparation of index-matched samples, the PMMA cores absorb CS_2, causing the cores to swell.[54] This occurs over several hours and is taken into account, during the sample preparation. However, it is possible that the slow imbibition of CS_2 continues, over the duration of the experiment.

Finally, another influence to consider is the possible shearing effect of the slow rotational tumbling, although previous work suggests that the rate of rotation is sufficiently slow, that the perturbation should be negligible.[76]

Sample No.	N_B / N_A	ϕ_{total}	ϕ_A	ϕ_B	a_{expt} / ± 6 nm	$\phi_{crystal}$
106	0.498	0.534	0.509	0.0250	932	0.659
107	0.481	0.542	0.518	0.0246	932	0.656
108	0.472	0.560	0.535	0.0249	932	0.660
109	1.018	0.514	0.467	0.0469	934	0.655
110	1.007	0.537	0.488	0.0485	932	0.660
112	2.031	0.526	0.438	0.0878	945	0.633
113	1.989	0.557	0.466	0.0913	949	0.625
114	1.960	0.566	0.474	0.0916	946	0.631
115	8.007	0.532	0.297	0.235	-	-
116	8.001	0.540	0.302	0.238	-	-
117	7.956	0.570	0.319	0.250	-	-
118	13.009	0.529	0.232	0.297	-	-
51	12.847	0.483	0.213	0.270	-	-
52	12.883	0.522	0.230	0.292	-	-
53	12.893	0.526	0.232	0.294	-	-
54	12.869	0.541	0.239	0.303	-	-
119	12.949	0.491	0.216	0.276	-	-
120	12.891	0.576	0.254	0.322	-	-
121	26.098	0.545	0.153	0.392	-	-
122	25.815	0.549	0.155	0.394	-	-
123	25.879	0.566	0.159	0.406	-	-

124	52.131	0.523	0.0852	0.438	416	0.543
125	51.334	0.545	0.0899	0.455	-	-
126	51.370	0.573	0.0944	0.478	401	0.610

Table 7.2. Summary of the compositions of binary mixtures, prepared with a size ratio $\alpha = 0.42$ and experimentally determined lattice parameters and crystal volume fractions. Dashes indicate amorphous samples.

Sample No.	N_B / N_A	Phases observed, $\alpha = 0.42 \pm 0.01$	Predicted phases,[105] $\alpha = 0.414$	$\alpha = 0.45$
106	0.498	A + F	A + F	A + F
107	0.481	A + F	A + F	A + F
108	0.472	A + F	A + F	A + F
109	1.018	A + F	A + F	A + F
110	1.007	A + F	A + F	A + F
112	2.031	A + F	A + F	A + F
113	1.989	A + F	A + F	A + F
114	1.960	A + F	A + F	A + F
115	8.007	Amorphous	AB + F	AB_2 + F
116	8.001	Amorphous	AB + F	AB_2 + F
117	7.956	Amorphous	AB + F	AB_2 + F
118	13.009	Amorphous	AB + F	AB_2 + F

51	12.847	Amorphous	AB + F	AB_2 + F
52	12.883	Amorphous	AB + F	AB_2 + F
53	12.893	Amorphous	AB + F	AB_2 + F
54	12.869	Amorphous	AB + F	AB_2 + F
119	12.949	Amorphous	AB + F	AB_2 + F
120	12.891	Amorphous	AB + F	AB_2 + F
121	26.098	Amorphous	AB + F	AB_2 + F
122	25.815	B + F	AB + F	AB_2 + F
123	25.879	B + F	AB + B + F	AB_2 + B + F
124	52.131	B + F	AB + F	AB_2 + F
125	51.334	B + F	AB + B + F	AB_2 + B + F
126	51.370	B + F	AB + B + F	AB_2 + B + F

Table 7.3. A comparison of the observed phase behaviour of colloidal mixtures, with a size ratio $\alpha = 0.42$ and the predicted phase behaviour, of hard sphere mixtures with size ratios $\alpha = 0.414$ and 0.45.

Sample No.	N_B / N_A	ϕ_{total}	ϕ_A	ϕ_B	a_{expt} / ± 6 nm	$\phi_{crystal}$
15	0.482	0.513	0.483	0.0310	914	0.700
16	0.478	0.538	0.506	0.0323	926	0.675
17	0.497	0.548	0.514	0.0341	922	0.683
11	0.993	0.520	0.460	0.0608	929	0.668
12	0.999	0.535	0.472	0.0629	916	0.695
13	0.979	0.548	0.485	0.0633	910	0.708
14	0.992	0.567	0.501	0.0663	883	0.776
2	2.001	0.546	0.431	0.115	871	0.813
3	2.028	0.558	0.439	0.119	891	0.754
4	2.026	0.581	0.457	0.124	878	0.791
61	4.963	0.494	0.297	0.197	969	0.627
62	4.947	0.509	0.307	0.202	1460	0.334
63	4.941	0.537	0.324	0.213	-	-
5	7.979	0.522	0.253	0.269	516	0.535
6	7.964	0.529	0.256	0.272	513	0.545
7	7.960	0.564	0.274	0.290	514	0.541
8	14.032	0.521	0.181	0.340	507, 2374	0.561
9	14.426	0.541	0.185	0.356	504, 2317	0.571
10	14.003	0.566	0.198	0.369	504, 2366	0.571
64	29.759	0.507	0.102	0.405	500	0.588
65	29.444	0.519	0.105	0.414	489	0.627

66	29.247	0.553	0.113	0.440	506	0.567
21	96.857	0.483	0.0347	0.448	486	0.592
22	96.328	0.502	0.0362	0.466	486	0.638
23	95.444	0.519	0.0378	0.482	487	0.639
24	95.686	0.536	0.0390	0.497	511	0.558

Table 7.4. The composition of binary mixtures, prepared with a size ratio $\alpha = 0.52$ and experimentally determined lattice parameters and crystal volume fractions.

Sample No.	N_B / N_A	ϕ_{total}	$c / \pm 6$ nm	$a / \pm 6$ nm	$c / a \pm 0.01$	ϕ_{AB_2}
61	4.963	0.494	988.517	949	1.041	0.624
62	4.947	0.509	989.895	951	1.041	0.621
5	7.979	0.522	992.920	952	1.043	0.617
6	7.964	0.529	987.163	948	1.041	0.626

Table 7.5. The composition of binary mixtures in which the AB_2 phase was found, prepared with a size ratio $\alpha = 0.52$, together with the experimentally determined lattice parameters and crystal volume fractions.

Sample No.	N_B / N_A	Phases observed	Predicted phases[76]	
		$\alpha = 0.52 \pm 0.01$	$\alpha = 0.50$	$\alpha = 0.54$
15	0.482	A + F	A + F	A + F
16	0.478	A + F	A + F	A + F
17	0.497	A + F	A + F	A + F
11	0.993	Amorphous	A + F	A + F
12	0.999	Amorphous	A + F	A + F
13	0.979	Amorphous	A + F	A + F
14	0.992	Amorphous	A + F	A + F
2	2.001	Amorphous	A + F	A + F
3	2.028	Amorphous	A + F	A + F
4	2.026	Amorphous	A + F	A + F
61	4.963	AB_2 + F	F	F
62	4.947	AB_2 + F	A + F	A + F
63	4.941	AB_2 + F	AB_2 + F	AB_2 + A + F
5	7.979	Amorphous	AB_2 + F	AB_2 + F
6	7.964	Amorphous	AB_2 + F	AB_2 + F
7	7.960	Amorphous	AB_2 + F	AB_2 + F
8	14.032	AB_{13} + B + F	AB_2 + F	AB_2 + F
9	14.426	AB_{13} + B + F	AB_2 + F	AB_2 + F
10	14.003	AB_{13} + B + F	AB_2 + B + F	AB_{13} + AB_2 + F
64	29.759	B + F	AB_2 + F	AB_2 + F

65	29.444	B + F	AB_2 + F	AB_2 + F
66	29.247	B + F	AB_2 + B + F	AB_{13} + F
21	96.857	B + F	AB_2 + F	AB_2 + F
22	96.328	B + F	AB_2 + F	AB_{13} + F
23	95.444	B + F	AB_2 + B + F	AB_{13} + B + F
24	95.686	B + F	AB_2 + B + F	AB_{13} + B + F

Table 7.6. Comparison of the observed phase behaviour, of a binary mixture of hard spheres with a size ratio $\alpha = 0.52$, with the predicted behaviour of a binary hard sphere mixture with size ratios $\alpha = 0.50$ and 0.54.

Sample No.	N_B / N_A	ϕ_{total}	ϕ_A	ϕ_B	a_{expt} / ± 6 nm	$\phi_{crystal}$
91	0.503	0.529	0.447	0.0827	680	0.619
92	0.504	0.551	0.465	0.0863	679	0.624
93	0.506	0.576	0.486	0.0904	673	0.639
94	0.999	0.527	0.385	0.142	676	0.633
95	1.003	0.551	0.402	0.149	669	0.653
97	1.987	0.522	0.301	0.220	-	-
98	1.988	0.539	0.311	0.228	-	-
99	1.988	0.569	0.329	0.240	-	-
101	5.000	0.533	0.188	0.346	-	-
102	4.972	0.546	0.193	0.353	-	-

103	12.937	0.507	0.0881	0.419	513	0.543
104	13.0562	0.523	0.0902	0.433	518	0.533
105	12.844	0.536	0.0935	0.442	518	0.527

Table 7.7. Composition of binary mixtures, prepared with a size ratio $\alpha = 0.72$ and experimentally determined lattice parameters and crystal volume fractions.

Sample No.	N_B / N_A	Observed phases, $\alpha = 0.72$	Predicted phases, $\alpha = 0.75$[77]
91	0.503	A + F	A + F
92	0.504	A + F	A + F
93	0.506	A + F	A + F
94	0.999	A + F	A + F
95	1.00276	A + F	A + F
97	1.987	Amorphous	A + F
98	1.988	Amorphous	A + F
99	1.988	Amorphous	A + F
101	5.000	Amorphous	A + B + F
102	4.972	Amorphous	A + B + F
103	12.937	B + F	F
104	13.0562	B + F	B + F
105	12.844	B + F	B + F

Table 7.8. A comparison of the observed phase behaviour, of a mixture of hard sphere colloids with a size ratio $\alpha = 0.72$, with the predicted behaviour of a binary hard sphere mixture with a size ratio $\alpha = 0.75$.

CHAPTER 8

CONCLUSIONS

The aim of the present work was to study the fluid-solid phase behaviour of binary mixtures of colloidal hard spheres, with size ratios α = 0.42, 0.52 and 0.72. These size ratios were chosen, in order to extend our knowledge of binary colloidal mixtures. At α = 0.42, computer simulation phase predictions suggest that mixtures with certain compositions will form crystals with the AB(NaCl) structure.[105] Mixtures prepared with size ratio α = 0.52, are predicted to form both the AB_2 and AB_{13} superlattice phases.[76] At α = 0.72, the theoretical phase diagram has been determined for mixtures, which are assumed to be immiscible in the solid phase.[77] The results of the present work are compared with these predictions and with the results of previous experimental work.[10,11]

The colloidal particles consisted of spherical cores of poly(methyl methacrylate) (PMMA), sterically stabilised by a thin (~10 nm) layer of poly(12-hydroxystearic acid) (PHSA).[7] The suspension medium was a mixture of decalin and carbon disulphide, in a ratio selected so that the refractive index was close to that of the particles ($n \approx 1.51$). The resulting 'index-matched' suspensions were nearly transparent and could be studied both visually and by light scattering, even at high volume fractions. Also, in index-matched suspensions the van der Waals attractive forces are minimised, so that the interparticle interaction is steeply repulsive and close to that of hard spheres.[8]

The PMMA colloidal particles used in the present work, were synthesised in a one-step dispersion polymerisation reaction.[7] Stable suspensions, with a narrow

distribution of diameters ($\sigma < 0.07$) were formed in non-aqueous media. The size of the particles produced was varied, by changing the initial monomer concentration used in the reaction.[7] The size and polydispersity of the polymer particles, were measured by means of dynamic light scattering (DLS) and transmission electron microscopy (TEM).

Dispersion polymerisations were carried out, using three different stabiliser samples. One stabiliser sample was obtained from ICI Paints, a second sample was kindly donated by Bristol University and a third sample was synthesised in the present work. All three samples were analysed, by means of combined gel permeation chromatography (GPC) and viscosity measurements. Molecular weights and polydispersity ratios were determined.

Five dispersion polymerisation reactions were carried out, using the stabiliser sample from ICI Paints. The minimum stabiliser concentration required, to produce a stable dispersion was found to be 10% (by the monomer weight). By comparison, Antl and co-workers found 5% stabiliser to be the optimum for this reaction. This difference in the amount of stabiliser used, could arise due to differences in the stabiliser structures. The glycidyl groups in the stabiliser used by Antl *et al.* may make it more flexible and efficient. Also, these authors used an ethyl acetate-butyl acetate cosolvent, which will increase the solvency of the dispersion medium.

Colloidal PMMA particles were also prepared, using the stabiliser sample from Bristol University. With a stabiliser concentration of 5% (by monomer weight), eight stable suspensions were prepared. The structure of the stabiliser sample from Bristol, was thought to be similar to that used by Antl and co-workers.[7] This is consistent with

the observation that Antl and co-workers also produced stable dispersions, using 5% stabiliser in the reaction.

Dispersion polymerisation reactions were also carried out, using the stabiliser sample synthesised in the present work. In all the reactions, the level of stabiliser was 5% (by monomer weight) and stable dispersions were produced. Again, this concentration of stabiliser was the same as that used by Antl and co-workers to produce stable dispersions. It is also the same level at which the stabiliser from Bristol was used to produce stable colloidal suspensions. In fact, GPC / viscosity measurements suggested that both the stabiliser synthesised in the present work and the stabiliser from Bristol were similar in structure. It also seems likely that both these samples were similar to the sample used by Antl *et al.*

Using the stabiliser synthesised in the present work, twenty stable colloidal PMMA suspensions were produced, in dispersion polymerisations with an initial monomer concentration in the range 41 to 62%. By comparison, Antl *et al.* found the stable monomer range to be 35 to 50%.[7] Similarly, Pathmamanoharan and co-workers found the stable range to be 32 to 44%.[83] Also, in the present work, as the monomer concentration was increased from 41 to 62%, the final size of the polymer particles increased from 301 nm to over 1 μm. In comparison, Antl *et al.* found particle sizes of 180 nm to 2.6 μm (for 35 - 50% monomer) and Pathmamanoharan and co-workers found a range of 40 – 900 nm (for 10 – 28%). These differences, in the stable monomer range and the size of the particles synthesised, could be due to differences in the reaction conditions. For instance, the solvency of the dispersion medium, in the

reactions carried out by Antl *et al.* would be higher due to the use of the co-solvent mentioned earlier.

Stable colloidal PMMA particles, were synthesised in the present work in the one-step dispersion polymerisation reaction described in chapter 3. Stable dispersions were formed in decahydronapthalene (decalin). After cleaning by repeated centrifugation, stock solutions were prepared. Dynamic light scattering measurements were made over a range of angles and the number average particle size and polydispersity of the colloidal particles in the stock solutions was determined.

The colloidal particles were also studied by transmission electron microscopy (TEM). Carbon replicas were made and these were studied using an electron microscope. Electron micrographs were obtained of areas of the carbon replica and of a calibration grid. The micrographs were then analysed by means of a digitised imaging system and the average particle diameter and polydispersity were determined. The results were in good agreement with DLS measurements of the same samples.

The one-component phase behaviour of the PMMA colloidal particles was investigated, by preparing samples with a range of core volume fractions spanning the freezing and melting transitions of the phase diagram. The colloidal particles were suspended in a refractive index-matching mixture of decalin and carbon disulphide, with volume fractions calculated from the experimentally determined PMMA mass fraction. After redispersing, the samples were left undisturbed. Coexisting crystalline and fluid phases formed. The crystal volume in each sample was measured and the one-component phase diagram was plotted. Extrapolation to 0 and 100% crystal then provided the freezing and melting core volume fractions. The phase behaviour of the

NH28 and DMM7 samples was determined in this way. For the larger particles of the NH31 sample the effects of gravity were allowed for, using the approach of Paulin and Ackerson.[53] The freezing concentration was identified with the hard sphere volume fraction, $\phi_f = 0.494$, determined by computer simulation.[46] The effective melting volume fraction was then calculated, by the appropriate scaling of the measured core volume melting fraction. For each colloidal dispersion, the effective hard sphere melting volume fraction was compared with the theoretical hard sphere value. In each case, close agreement was found. The quantity $(\phi_m - \phi_f) / \phi_f$, was also determined for each sample and again close agreement with the theoretical hard sphere value was found.

The fluid-solid phase behaviour, of binary mixtures of hard sphere colloidal particles, with size ratios of $\alpha = 0.42$, 0.52 and 0.72, was investigated. The polydispersity of the particles used was in the range 0.04 – 0.07. In mixtures, crystallisation was significantly slower than in the one-component suspensions and the effects of gravity were minimised, by the continuous slow rotation of the particles.[52] Crystallisation appeared to be homogeneously nucleated, with the formation of small, randomly oriented, crystallites throughout the sample volume. The resulting polycrystalline powders were particularly suitable for analysis by static light scattering, which provided the analogue of X-ray powder diffraction patterns. As has been noted elsewhere, in near index-matched samples the form factors of the individual particles are difficult to determine.[10] Hence, a quantitative study of the intensity measurements was not undertaken. Instead, crystal structures were identified from the locations of the peaks in the scattering profile. The observed phase behaviour is summarised below.

Mixtures with a size ratio $\alpha = 0.42$, were prepared by combining large A particles ($d = 897$ nm), with small B particles ($d = 375$ nm). A total of twenty-one samples were made, at five different number ratios (N_B / N_A), with total volume factions in the range $0.525 \leq \phi_A + \phi_B \leq 0.565$. The observed phase behaviour is shown in figure 7.6. The phase diagram contains three distinct regions. In mixtures rich in A, prepared with number ratios $N_B / N_A = 0.5$, 1 and 2, coexisting crystals of large A particles and a binary fluid phase were identified (see appendix). By contrast, at intermediate number ratios, mixtures with $N_B / N_A = 8$, 13 and 26 remained largely amorphous for the duration of the experiment. Mixtures rich in B, with number ratio $N_B / N_A = 52$, formed coexisting crystalline and fluid phases. The crystal phase was identified as a random close packed structure of B particles.

The observed phase behaviour, of mixtures prepared with a size ratio $\alpha = 0.42$, was compared with computer simulation predictions, for hard sphere mixtures with size ratios $\alpha = 0.414$ and 0.45.[105] Good agreement was found, over limited regions of composition. At intermediate number ratios, the predicted phase diagrams are not consistent with the observed behaviour. Experimentally, the samples remained amorphous, although at $\alpha = 0.414$ AB (NaCl) is predicted and at $\alpha = 0.45$ AB_2 is predicted.

Mixtures were prepared with a size ratio $\alpha = 0.52$, by combining large A particles ($d = 897$ nm), with small B spheres ($d = 463$ nm). Twenty-eight samples were prepared at eight different number ratios, in the range $0.5 \leq N_B / N_A \leq 100$, with total volume fractions in the range $0.494 \leq \phi_A + \phi_B \leq 0.581$. The samples are plotted in the phase diagram, in figure 7.15. As can be seen, the diagram contains six distinct regions

of fluid-solid phase coexistence. In mixtures rich in A, $N_B / N_A = 0.5$, no crystals were observed by eye. However, the scattering was consistent with the formation of very small crystallites, composed of large A spheres and a coexisting fluid enriched in B spheres. Similarly, samples with number ratios $N_B / N_A = 1$ and 2 appeared to remain amorphous and no evidence for A crystals, was found in the scattering profile. In mixtures prepared with number ratio $N_B / N_A = 5$, crystals with the AB_2 superlattice structure and coexisting binary fluid formed. In suspensions with number ratio $N_B / N_A = 8$, crystals were visible only in the sample with the lowest total volume fraction. The other samples remained amorphous for the duration of the experiment. By contrast, in mixtures with a number ratio $N_B / N_A = 14$, crystals with the AB_{13} superlattice structure found, coexisting with B crystals and a fluid phase. Mixtures rich in B, with number ratios $N_B / N_A = 30$ and 100, formed coexisting crystals of B particles and binary fluid.

The phase behaviour of mixtures, prepared with a size ratio $\alpha = 0.52$, was compared with the theoretical predictions of Madden and Eldridge, for hard sphere mixtures with size ratios of $\alpha = 0.50$ and 0.54.[76] Close agreement was found, in several regions of both phase diagrams. For example, crystals of A and coexisting fluid were found, in samples predicted to lie in the A + F region, at both size ratios. There were also significant differences. Mixtures prepared with a number ratio $N_B / N_A = 14$, are predicted to form crystals of AB_2, at both $\alpha = 0.50$ and 0.54. However, these samples formed AB_{13}, with coexisting crystals of B and a binary fluid.

Mixtures with a size ratio of $\alpha = 0.72$, were composed by combining large A particles ($d = 641$ nm), with smaller B particles ($d = 463$ nm). A total of thirteen different samples were prepared, at five different number ratios, with total volume

fractions in the range $0.507 \leq \phi_A + \phi_B \leq 0.576$. The experimentally observed behaviour is shown in figure 7.20. As can be seen, the phase diagram contains three distinct regions of fluid-solid phase behaviour. In mixtures prepared with number ratios of $N_B / N_A = 0.5$ and 1, crystals of A and coexisting fluid phases formed. By contrast, at intermediate number ratios, samples with number ratios $N_B / N_A = 2$ and 5 remained amorphous. However, mixtures rich in B, with number ratio $N_B / N_A = 13$, formed coexisting B crystals and a fluid phase enriched in large A spheres.

The phase behaviour of hard sphere mixtures prepared with a size ratio of $\alpha = 0.72$, was compared with the theoretical phase diagram for $\alpha = 0.75$, arising out of Bartlett's immiscible sphere model.[77] Altogether, good agreement was found between experiment and simulation.

The present work extends the results of previous studies, of the freezing behaviour of binary mixtures of hard sphere colloids. Mixtures with size ratios $\alpha = 0.42$, 0.52 and 0.72, were investigated as a function of dispersion volume fraction and number ratio. A diverse range of fluid-solid phase behaviour was found. At least four crystal phases A, AB_2, AB_{13} and B were identified, at different suspension compositions.

The observed phase behaviour at $\alpha = 0.42$ and 0.52 was compared with the computer simulation predictions of Eldridge and co-workers. At these size ratios, partial agreement was found between experiment and simulation. The observed behaviour at $\alpha = 0.72$, was compared with the predictions for a mixture of hard spheres with size ratio $\alpha = 0.75$, arising out of Bartlett's immiscible sphere model. At this size ratio, good overall agreement was found, between experiment and simulation.

Experimentally, at each size ratio, an amorphous region was found, the size of which increased with decreasing size ratio. This was where the main differences between experiment and theory arose. Non-equilibrium behaviour is not considered in the theoretical methods described above. A study of binary glass formation is a possible direction for future work. Also, as has been observed previously, the AB_2 structure appeared to be reluctant to form from suspensions with compositions differing substantially from $N_B / N_A = 2$. By contrast, the AB_{13} structure formed when it was predicted and at other compositions.[76] Future work could investigate the mechanism of superlattice formation.

The results of the present work show the rich variety of fluid-solid phase behaviour of binary mixtures of colloidal particles. To a good approximation, these particles interact as hard spheres and so provide an experimental method of studying hard sphere systems. In binary mixtures of colloidal hard spheres, entropically driven freezing occurs into quite complex structures. The study of these colloidal systems can provide insights into the fundamental properties of simple atomic and molecular fluids. The present work provides new information about the binary hard sphere freezing transition.

REFERENCES

REFERENCES

1. Hunter, R. J., *Foundations of Colloid Science, Volume I*, Oxford University Press, Oxford (1986).
2. Russel, W. B., Saville, P. A. and Schowalter, W. R., *Colloidal Dispersions*, Cambridge (1991).
3. Verwey, E. J. W. and Overbeek, J. T. G., in *Theory of the Stability of Lyophobic Colloids*, Elsevier, Amsterdam (1948).
4. Poon, W. C. K., Pusey, P. N. and Lekkerkerker, H. N. W., *Physics World*, **27** (1996).
5. Pusey, P. N., *Liquids, Freezing and the Glass Transition*, Les Houches Session LI, eds., Levesque, D., Hansen, J.-P. and Zinn-Justin, J., Amsterdam: North Holland, 763 (1991).
6. Barrett, K. E. J., *Dispersion Polymerisation in Organic Media*, Wiley, London (1975).
7. Antl, L., Goodwin, J. W., Hill, R. D., Ottewill, R. H., Owen, S. M., Papworth, S. and Waters, J. A., *Colloids and Surfaces*, **17**, 67 (1986).
8. Pusey, P. N. and van Megen, W., *Nature*, **320**, 340-342 (1986).
9. Pusey, P. N., Poon, W. C. K., Ilett, S. M. and Bartlett, P., *Phys. Condens. Matter*, **6**, A29-36 (1994).
10. Bartlett, P., Ottewill, R. H. and Pusey, P. N., *J. Chem. Phys.*, **93**, 1229 (1990).
11. Bartlett, P., Ottewill, R. H. and Pusey, P. N., *Phys. Rev. Lett.*, **68**(25), 3801 (1992).

12. McMillan, W. G. and Mayer, J. E., *J. Chem. Phys.*, **13**, 276-305 (1945).

13. Kirkwood, J. G. and Buff, F. P., *J. Chem. Phys.*, **19**, 774-777 (1951).

14. Schätzel, K. and Ackerson, B. J., *Phys. Rev. Lett.*, **68**, 337-340 (1992).

15. Pusey, P. N. and van Megen, W., *Phys. Rev. Lett.*, **59**, 2083-2086 (1987).

16. Bartlett, P. and Ottewill, R. H., *Langmuir*, **8**, 1919-1925 (1992).

17. Bartlett, P. and Ottewill, R. H., *J. Chem. Phys.*, **96**, 3306-3318 (1992).

18. Kose, A. and Hachisu, S., *J. Colloid Interface Sci.*, **46**, 460-469 (1974).

19. Israelachvili, J., *Intermolecular and Surface Forces*, 2nd ed., Academic (1992).

20. Napper, D. H., *Polymeric Stabilisation of Colloidal Particles*, Academic, London (1983).

21. Vrij, A., *Pure Appl. Chem.*, **48**, 471 (1976).

22. Vincent, B., Edwards, J., Emmet, S. and Croot, R., *Colloids Surf.*, **31**, 267 (1988).

23. Pusey, P. N., Lekkerkerker, H. N. W., Cohen, E. G. D. and de Schepper, I. M., *Physica A*, **164**, 12 (1990).

24. Degiorgio, V., Piazza, R., Bellini, T. and Visca, M., *Adv. Colloid Interface Sci.*, **48**, 61 (1994).

25. Robbins, M. O., Kremer, K. and Grest, G. S., *J. Chem. Phys.*, **88**, 3286 (1988).

26. Monovoukas, Y. and Gast, A. P., *J. Coll. Interface Sci.*, **128**, 533 (1989).

27. Sirota, E. B., Ou-Yang, H. B., Sinha, S. K., Chaikin, P. M., Axe, J. D. and Fujii, Y., *Phys. Rev. Lett.*, **62**, 1524 (1989).

28. Poon, W. C. K. and Pusey, P. N., in *Observation, Prediction and Simulation of Phase Transitions in Complex Fluids*, eds., Baus, M. *et al.*, Kulwer Academic (1995).

29. Edwards, J., Everett, D. H., O'Sullivan, T., Pangalou, I. and Vincent, B., *J. Chem. Soc. Faraday Trans. 1*, **80**, 2599 (1984).

30. Asakura, S. and Oosawa, F., *J. Chem. Phys.*, **22**, 1255 (1954).

31. Feigin, R. I. and Napper, D. H., *J. Colloid Interface Sci.*, **75**, 525 (1980).

32. Joanny, J. F., Leibler, L. and de Gennes, P. G., *J. Polym. Sci. Phys. Ed.*, **17**, 1073 (1979).

33. Gast, A. P., Russel, W. B. and Hall, C. K., *J. Colloid Interface Sci.*, **96**, 251 (1983).

34. Gast, A. P., Russel, W. B. and Hall, C. K., *J. Colloid Interface Sci.*, **102**, 109 (1986).

35. Vincent, B., Edwards, J., Emmett, S. and Croot, R., *Colloids Surf.*, **31**, 267 (1988).

36. Sperry, P. R., *J. Colloid Interface Sci.*, **99**, 97 (1984).

37. Lekkerkerker, H. N. W., Poon, W. C. K., Pusey, P. N., Stroobants, A. and Warren, P. B., *Europhys. Lett.*, **20**, 559 (1992).

38. Widom, B. and Rowlinson, J. S., *J. Chem. Phys.*, **52**, 1670 (1970).

39. Ilett, S. M., Orrock, A., Poon, W. C. K. and Pusey, P. N., *Phys. Rev. E*, **51**, 1344 (1995).

40 Leal Calderon, F., Bibette, J. and Biais, J., *Europhys. Lett.*, **23**, 653 (1993).

41. Courtemanche, D. J. and van Swol, F., *Phys. Rev. Lett.*, **69**, 2078 (1992).

42. Courtemanche, D. J., Pasmore, T. A. and van Swol, F., *Mol. Phys.*, **80**, 861 (1993).

43. Kaplan, P. D., Rouke, J. L., Yodh, A. G. and Pine, D. J., *Phys. Rev. Lett.*, **72**, 582 (1994).

44. Poon, W. C. K. and Warren, P. B., *Europhys. Lett.*, **28**, 513 (1994).

45. Dinsmore, A. D., Warren, P. B., Poon, W. C. K. and Yodh, A. G., *Europhys. Lett.*, **40**, 337 (1997).

46. Hoover, W. G. and Ree, F. H., *J. Chem. Phys.*, **49**(8), 3609-3617 (1986).

47. Alder, B. J. and Wainwright, T. E., *J. Chem. Phys.*, **27**, 1208-1209 (1957).

48. Woodcock, L. V., *Ann. N.Y. Acad. Sci.*, **37**, 274 (1981).

49. Pusey, P. N. and van Megen, W., *Physica A.*, **157**, 705-741 (1989).

50. van Megen, W. and Underwood, S. M., *Nature*, **362**, 616 (1993).

51. Bernal, J. D., *Nature*, **183**, 141 (1960).

52. Bartlett, P., Pusey, P. N. and Ottewill, R. H., *Langmuir*, **7**(2), 213 (1991).

53. Paulin, S. E. and Ackerson, B. J., *Phys. Rev. Lett.*, **64**, 22 (1990).

54. Ottewill, R. H. and Livsey, I., *Polymer*, **28**, 109 (1987).

55. Hansen, J.-P. and McDonald, I. R., *Theory of Simple Liquids*, Academic press, New York (1986).

56. Pusey, P. N., van Megen, W., Bartlett, P., Ackerson, B. J., Rarity, J. G. and Underwood, S. M., *Phys. Rev. Lett.*, **63**, 2753 (1989).

57. Frenkel, D. and Ladd, J. C., *J. Chem. Phys.*, **81**, 3188 (1984).

58. Woodcock, L. V., *Faraday Discuss.*, **106**, 325-338 (1997).

59. Bolhuis, P. G., Frenkel, D., Mau, S.-C. and Huse, D. A., *Nature*, **388**, 236 (1997).

60. Woodcock, L. V., *Nature*, **385**, 141 (1997).

61. Verhaegh, N. A. M., van Duijneveldt, J. S., van Blaaderen, A. and Lekkerkerker, H. N. W., *J. Chem. Phys.*, **102**, 1416 (1995).

62. Elliot, M. S., Bristol, B. T. F. and Poon, W. C. K., *Physica A*, **235**, 216-223 (1997).

63. Zhu, J., Li, M., Rogers, R., Meyer, W., Ottewill, R. H., STS-73 Space Shuttle Crew, Russel, W. B. and Chaikin, P. M., *Nature*, **387**, 883 (1997).

64. Hansen, J.-P. and Verlet, L., *Phys. Rev.*, **184**, 151 (1969).

65. Toxvaerd, S., *J. Chem. Phys.*, **69**, 4750 (1978).

66. Hansen, J.-P., *Phys. Rev. A: Gen. Phys.*, **2**, 221 (1970).

67. Hoover, W. G., Ross, M., Johnsen, K. W., Henderson, D., Berker, J. A. and Brown, E. C., *J. Chem. Phys.*, **52**, 4931 (1970).

68. Alder, B. J., Hoover, W. G. and Young, D. A., *J. Chem. Phys.*, **49**, 3688 (1968).

69. Alder, B. J., Young, D. A., Mansigh, M. R. and Salsburg, Z. W., *J. Comput. Phys.*, **7**, 361 (1971).

70. Honda, K., *Prog. Theor. Phys.*, **55**, 1024 (1976).

71. Sanders, J. V. and Murray, M. J., *Nature*, **275**, 201 (1978).

72. Sanders, J. V., *Phil. Mag. A*, **42**(6), 705-720 (1980).

73. Murray, M. J. and Sanders, J. V., *Phil. Mag. A*, **42**(6), 721-740 (1980).

74. Bartlett, P. and van Megen, W., in *Granular Matter an Interdisciplinary Approach*, ed., Mehta, A., New York: Springer-Verlag, 195 - 257 (1994).

75. Hachisu, S. and Yoshimura, S., *Nature* (London), **283**, 188-189 (1980).

76. Eldridge, M. D., Madden, P. A., Pusey, P. N. and Bartlett, P., *Mol. Phys.*, **84**(2), 395-420 (1995).

77. Bartlett, P., *J. Phys.: Condens. Matter*, **2**, 4979 - 4989 (1990).

78. Candau, F. and Ottewill, R. H., in *An Introduction to Polymer Colloids*, Kulwer Academic Publisher, Netherlands (1990).

79. Blackley, D. C., *Emulsion Polymerisation*, John Wiley & Sons, New York (1975).

80. Candau, F. and Ottewill, R. H., *Scientific Methods for the Study of Polymer Colloids and their Applications*, Kulwer, 35 – 72 (1990).

81. Cairns, R. J. R., Ottewill, R. H., Osmond, D. W. J. and Wagstaff, I., *J. Colloid. Int. Sci.*, **54**, 45 (1976).

82. Williamson, B., Lukas, R., Winnik, M. A. and Croucher, M. D., *J. Colloid Int. Sci.*, **119**, 559 (1987).

83. Pathmamanoharan, C., Slob, C. and Lekkerkerker, H. N. W., *Colloid Poly Sci*, **267**, 448 (1989).

84. Lee, K., Winnik, M. A., Jao, T., *Journal of Polymer Science: Part A: Polymer Chemistry*, **32**, 2333 (1994).

85. *CRC Handbook of Chemistry and Physics*, ed., Lide, D. R., London: CRC Press, 174 (1999).

86. Tseng, C. M., Lu, Y. Y., El-Aasser, M. S. and Vanderhoff, J. W., *Journal of Polymer Science: Part A: Polymer Chemistry Edition*, **24**, 2995-3007 (1986).

87. Pusey, P. N. and Vaughan, J. M., *Light Scattering and Intensity Fluctuation Spectrocopy*, 48 (1975).

88. Pusey, P. N. and van Megen, W., *J. Chem. Phys.*, **80**, 3513 (1984).

89. Yoshimura, S. and Hachisu, S., *Progr. Colloid & Polymer Sci.*, **68**, 59-70 (1983).

90. Wilson, A. J. C., *X-Ray Optics, Proc. Roy. Soc. London A*, **180**, 277 (1942), (Methuen, London, 1949).

91. Guinier, A., *X-Ray Diffraction*, Freeman, New York (1963).

92. Clark, S. M., Rennie, A. R. and Ottewill, R. H., *Langmuir*, **13**, 1964 (1997).

93. Brindley, G. W. and Mering, J., *Acta Crystallogr.*, **4**, 441 (1951).

94. Bartlett, P. and Pusey, P. N., *Physica A*, **194**, 415 (1993).

95. Ottewill, R. H., *Colloidal Dispersions*, ed., Goodwin, J. W., Royal Society of Chemistry: London, 143 (1981).

96. Kranendonk, W. G. T. and Frenkel, D., *Mol. Phys.*, **72**(3), 679-697 (1991).

97. Cottin, X. and Monson, P. A., *J. Chem. Phys.*, **99**(11), 8914 (1993).

98. Zeng, X. C. and Oxtoby, D. W., *J. Chem. Phys.*, **93**(6), 4357 (1990).

99. Cottin, X. and Monson, P. A., *J. Chem. Phys.*, **102**(8), 3354 (1995).

100. Biben, T. and Hansen, J.-P., *Phys. Rev. Lett.*, **66**(17), 2215 (1991).

101. Kofke, D., *Mol. Simul.*, **7**, 285 (1991).

102. Eldridge, M. D., Madden, P. A. and Frenkel, D., *Mol. Phys.*, **80**(4), 987-995 (1993).

103. Eldridge, M. D., Madden, P. A. and Frenkel, D., *Mol. Phys.*, **79**, 105 (1993).

104. Eldridge, M. D., Madden, P. A. and Frenkel, D., *Nature*, **365**, 35 (1993).

105. Trizac, E., Eldridge, M. D. and Madden, P. A., *Mol. Phys.*, **90**(4), 675-678 (1997).

106. Percus, J. K., *Phys. Rev. Lett.*, **8**, 462 (1962).

107. Oxtoby, D. W., in *Liquids, Freezing and The Glass Transition*, Les Houches Session LI, eds., Levesque, D., Hansen, J.-P. and Zinn-Justin, J., Amsterdam: North Holland, 147 (1991).

108. Evans, R., in *Fundamentals of Inhomogeneous Fluids*, ed., Henderson, D., New York: Dekker (1992).

109. Hansen, J.-P., in *Observation, Prediction and Simulation of Phase Transitions in Complex Fluids*, eds., Baus, M. *et al.*, Kulwer Academic, 167 (1995).

110. Ramakrishnan, T. V. and Yussouff, M., *Phys, Rev. B*, **19**, 2775 (1979).

111. Haymet, A. D. J. and Oxtoby, D. W., *J. Chem. Phys.*, **84**, 1769 (1986).

112. Denton, A. R. and Ashcroft, N. W., *Phys. Rev. A*, **39**, **426**, 4701 (1989).

113. Curtin, W. A. and Ashcroft, N. W., *Phys. Rev. Lett.*, **56**, 2775 (1986).

114. Denton, A. R. and Ashcroft, N. W., *Phys. Rev. A*, **42**(12), 7312 (1990).

115. Barrat, J. L., Baus, M. and Hansen, J.-P., *Phys. Rev. Lett.*, **56**(10), 1063 (1986).

116. Xu, H. and Baus, M., *J. Phys.: Condens. Matter*, **4**, L663-L668 (1992).

117. Lennard-Jones, J. E. and Devonshire, A. F., *Proc. Roy. Soc.* (London), **A163**, 53 (1937).

118. Lennard-Jones, J. E. and Devonshire, A. F., *Proc. Roy. Soc.* (London), **A165**, 1 (1938).

119. Cottin, X., Paras, E. P. A., Vega, C. and Monson, P. A., *Fluid Phase Equilibria*, **117**, 114-125 (1996).

120. Parthé, E., *Z. Kristallogr.*, **115**, 52 (1961).

121. Rogers, C. A., *Proc. Lond. Math. Soc.*, **8**, 609 (1958).

122. Mansoori, G. A., Carnahan, N. F., Starling, K. E. and Leland, T. W., *J. Chem. Phys.*, **54**, 1523 (1971).

123. Lebowitz, J. L. and Rowlinson, J. S., *J. Chem. Phys.*, **41**, 133 (1964).

124. Biben, T. and Hansen, J.-P., *Europhys. Lett.*, **12**(4), 347-352 (1990).

125. Buhot, A. and Krauth, W., *Phys. Rev. Lett.*, **80**(17), 3787 (1998).

126. Dijkstra, M., van Roij, R. and Evans, R., *Phys. Rev. Lett.*, **81**(11), 2268 (1998).

127. Sanyal, S., Easwar, N., Ramaswamy, S. and Sood, A. K., *Europhys. Lett.*, **18**(2), 107-110 (1992).

128. van Duijneveldt, J. S., Heinen, A. W. and Lekkerkerker, H. N. W., *Europhys. Lett.*, **21**(3), 369-374 (1993).

129. Lekkerkerker, H. N. W. and Stroobants, A., *Physica A*, **195**, 387-397 (1993).

130. Rosenfeld, Y., *Phys. Rev. Lett.*, **72**(24), 3831 (1994).

131. Xu, H. and Barentin, C., *J. Phys.: Condens. Matter*, **7**, L13-L17 (1995).

132. Dijkstra, M. and Frenkel, D., *Phys. Rev. Lett.*, **72**(2), 298 (1994).

133. Dijkstra, M., Frenkel, D. and Hansen, J.-P., *J. Chem. Phys.*, **101**(4), 3179 (1994).

134. Biben, T., Bladon, P. and Frenkel, D., *J. Phys.: Condens. Matter*, **8**, 10799-10821 (1996).

135. Dickman, R., Attard, P. and Simonian, V., *J. Chem. Phys.*, **107**(1), 205 (1997).

136. Dijkstra, M., van Roij, R. and Evans, R., *Phys. Rev. E*, **59**(5), 5744 (1999).

137. Coussaert, T. and Baus, M., *Phys. Rev. Lett.*, **80**, 4832 (1998).

138. Saija, F., Fiumara, G. and Giaquinta, P. V., *Mol. Phys.*, **87**, 991 (1996).

139. Saija, F., Fiumara, G. and Giaquinta, P. V., *Mol. Phys.*, **92**, 1089 (1997).

140. Enciso, E., Almarza, N. G., Calzas, D. S. and Gonzalez, M. A., *Mol. Phys.*, **92**, 173 (1997).

141. Imhof, A. and Dhont, J. K. G., *Phys. Rev. Lett.*, **75**(8), 1662 (1995).

142. Dinsmore, A. D., Yodh and A. G., Pine, D. J., *Phys. Rev. E*, **52**(4), 4045 (1995).

143. Hunt, N. A., Jardine, R. S., Bartlett, P. B., *Phys. Rev. E* (submitted).

APPENDIX

As was described in chapter 7, in binary mixtures prepared with a size ratio $\alpha = 0.42$ and number ratios $N_B / N_A = 0.5$, 1 and 2, coexisting crystal and fluid phases were observed. Static light scattering measurements of these samples were interpreted as evidence for an ordered arrangement of large A particles. However, further analysis suggests these measurements are also consistent with the AB(NaCl) and AB(NiAs) superlattice structures. All three structures can be visualised in terms of the stacking of hexagonal layers of large A particles. In the AB(NaCl) structure the A particles are arranged in a fcc lattice. The small B particles occupy all the interstitial octahedral sites in the large sphere lattice and form a fcc sublatice. In the AB(NiAs) structure, the large A particles adopt a hcp arrangement, with the octahedral interstitial sites occupied by B particles. In this structure, the B particles form a cubic sublattice. The lattice parameter, for both large and small sphere arrangements, is the same and both structures have the same reflection conditions. However, the intensity of scattering is a function of particle size. Hence, at the size ratio $\alpha = 0.42$, the scattering profile of this structure is expected to be dominated by the much larger A particles, to the extent that the scattering is very similar to that from a fcc arrangement of A particles alone. Hence, the AB(NaCl), AB(NiAs) and fcc A structures are difficult to distinguish by means of light scattering alone. In order identify the particle arrangement, accurate intensity measurements are required. As was mentioned earlier, in the present work such measurements were not made, due to the complex form factor near index match. The light scattering data obtained is consistent with each of the three structures described

above, however further work is required to identify the exact nature of the particle arrangement.

Recently, the phase behaviour of binary mixtures of colloidal particles, with a size ratio of $\alpha = 0.38 \pm 0.01$, has been investigated.[143] The particles consisted of PMMA cores, sterically stabilised by thin layers of PHSA, like those used in the present work. In addition, the small particles were fluorescently labelled. The binary phase diagram was found to be very similar to that studied in the present work, at $\alpha = 0.42$, with fluid / A and fluid / B coexistence near the limits of extreme composition and a large amorphous region at intermediate number ratios. In mixtures prepared with the AB stoichiometry ($N_B / N_A = 1$) crystals and coexisting colloidal fluid formed. Static light scattering measurements were consistent with a hexagonal arrangement of A particles, as found in the AB(NaCl), AB(NiAs) and fcc A structures. In order to investigate further the crystal structure, the arrangement of the small fluorescent particles, within the crystals of A particles, was studied by means of fluorescence confocal scanning laser microscopy. The small particles were found to be in a fcc arrangement, which suggests that the small particles were occupying the octahedral holes in the large sphere crystal. However, the structure could not be positively identified as either AB(NaCl), AB(NiAs) or fcc A.